

Forces at the nanoscale: interactions in atomic force microscopy and dielectrophoresis

Adam Marc Sweetman, MSci (Hons)

Thesis submitted to the University of Nottingham
for the degree of Doctor of Philosophy

November 2009

Abstract

Interactions at the nanoscale are governed almost exclusively by electromagnetic forces, but the interplay between different scaling laws produces a vast array of behaviours. We investigate radically different systems spanning almost three orders of magnitude of length scales, and use a variety of experimental techniques to determine the forces present in each regime, and the interplay between them.

An important prototypical surface in SPM science has been the Si(100) surface, which due to its unstable buckling and complex electronic structure has fostered considerable debate in the surface science community. We have used small amplitude, high sensitivity combined qPlus STM/AFM to investigate tip – sample interactions on the Si(100) surface at low-temperature in UHV, with a focus on the chemical, and electronic properties of the system and how these are modified by the probe. We present the first atomic resolution combined force/tunnel current results on the surface and show that great care must be taken in interpreting either pure AFM or pure STM data.

We also examine tip – sample interactions on arrays of thiol passivated spin-cast nanoparticles in both UHV and ambient conditions and show for the first time how minor modifications to the experimental parameters can radically alter the data collected, most likely due to the thiol – surface – tip interaction. We also present SKPM and voltage spectroscopy of the same samples and show the importance of electrostatic interactions in correct height determination of these network arrays, in parallel with the caution that must be maintained in interpreting CPD data.

A key mechanism for the manipulation of meso-scale objects in solution is Dielectrophoresis, which offers strong material and size specificity and a high degree of spatial control. In the final experimental chapter we investigate the effect of inhomogenous electric fields on nanoparticles in aqueous solution, and reveal how previously uninvestigated electrochemical effects can become important even at high frequencies, and may offer a new and exciting route for the control of self organised nanowires in solution.

List of publications

- A. Sweetman, S. Gangopadhyay, R. Danza, N. Berdunov, and P. Moriarty
qPlus Atomic Force Microscopy of the Si(100) Surface: Buckled, Split-off, and Added Dimers
Appl. Phys. Lett. 95, 063112 (2009)
- A. Sweetman, P. Sharp, A. Stannard, S. Gangopadhyay, and P. Moriarty
AFM of self-organised nanoparticle arrays: frequency modulation, amplitude modulation, and force spectroscopy
Proc. SPIE Vol. 7041, 704102 (2008)
- A. Sweetman, L. Ridgway, J. Sharp, G. E. Georghiou, and P. Moriarty
Electrochemical and AC electroosmotic effects during dielectrophoretic assembly of gold nanoparticles
J. Phys. Chem. C in preparation.
- A. Sweetman, E. Spadova, A. Stannard and P. Moriarty
Height and contact potential measurements of gold nanoparticle networks by NC-AFM and SKPM
Surf. Sci. in preparation.

Acknowledgements

The four or so years it takes to complete a PhD can be both rewarding and frustrating, but not always in equal measure! Although it can sometimes feel like it, no PhD is ever just one person's work and I would like to acknowledge some of the people who have made this thesis possible.

First and foremost, my supervisor Phil, for unfailing support and encouragement. His overwhelming enthusiasm whenever I managed to coax the universe into producing a particularly pretty picture, or patience and understanding when I failed to understand some particularly basic piece of physics, or broke some expensive piece of equipment, have made him the best PhD supervisor I could have hoped for.

Many of the results obtained in this thesis were obtained at great physical and mental cost, for at the "coalface" of nanoscience sometimes the best tool at our disposal is sheer pigheaded perseverance and stubbornness. Therefore I must thank some of my co-workers, in particular Subhashis, Rosanna and Peter who have thrown themselves into the meat grinder that is SPM with great aplomb.

The Nottingham nanoscience group itself has been a particularly close knit place to work, and I have never been at a loss for someone to talk to, be it on the intricacies of AFM operation, experimental failures, or The Metal God. There are too many members of the group who deserve mention, both past and present, but in particular I extend my thanks to (in no particular order) Andy (units one and two), Alex, Louise, Chris, Matt, Peter, James S., Alina, Claire, Karina and Ed, who all contributed in their own unique way.

I also thank my friend Jon, for numerous inspirational conversations throughout the years, and Joe, for teaching me just enough tricks to get my shattered frame through the last six months. Dan and Toby must also get a mention for never failing to inform and amuse.

Por ultimo, gracias a mi amorcita Sandra, por todo.

“One could not be a successful scientist without realizing that, in contrast to the popular conception supported by newspapers and mothers of scientists, a goodly number of scientists are not only narrow-minded and dull, but also just stupid.”

James D. Watson

Contents

Abstract	i
List of publications	iii
Acknowledgements	iv
1 Introduction	1
1.1 Introduction	1
1.2 Top-down versus bottom-up	3
1.3 Scanning probe microscopy (SPM) and atomic manipulation . . .	6
1.4 Self-assembly	7
1.5 Thesis outline	10
2 Scanning Probe Techniques	11
2.1 Introduction	11
2.2 Scanning tunnelling microscopy (STM)	12
2.2.1 Principle of operation	12
2.3 Atomic force microscopy (AFM)	22
2.3.1 Contact mode AFM	23
2.3.2 Noncontact AFM (NC-AFM)	24
2.3.3 AM-AFM and FM-AFM	26
2.3.4 Principle of operation	27
2.3.5 Force spectroscopy	32
2.3.6 Parameters in NC-AFM	36
2.3.7 qPlus AFM	38
2.3.8 Contact potential difference/Kelvin probe force microscopy	39

2.4	Equipment summary	42
2.4.1	Omicron VT STM/AFM	43
2.4.2	Omicron LT STM/AFM	43
2.4.3	Omicron VT/Kelvin probe AFM	45
2.4.4	Asylum research AFM	45
3	Electrokinetic manipulation of particles in solution	48
3.1	Introduction	48
3.2	Dielectrophoresis (DEP)	49
3.2.1	Theoretical overview	50
3.2.2	Effective dipole moment method	53
3.2.3	Calculation of DEP force	58
3.2.4	Detail of the force dependence on K	59
3.3	Electrokinetic effects	61
3.3.1	Electrical double layer	62
3.3.2	Electric polarisation	63
3.3.3	Diffuse and Stern layer capacitance	64
3.3.4	Electroosmosis	66
3.3.5	AC electroosmosis (ACEO)	67
3.3.6	High frequency electrothermal flow	69
3.4	AC electrochemical effects	70
3.5	DEP equipment	71
3.5.1	Electrode array/PCB	71
3.5.2	Scanning electron microscopy (SEM)	75
4	Materials review	76
4.1	Si(100)	76
4.1.1	STM imaging of Si(100)	79
4.1.2	AFM of Si(100)	85
4.1.3	Defects	87
4.1.4	Preparation	88
4.1.5	C_{60} on Si(100)	89
4.2	Colloidal gold	92
4.2.1	Charge stabilised gold nanoparticles	92

4.2.2	Thiol stabilised gold nanoparticles	93
4.3	Pattern formation using thiol-stabilised particles	93
4.4	DEP self organisation of charge stabilised nanoparticles	95
5	Combined qPlus STM/AFM of Si(100)	98
5.1	Sample preparation	98
5.2	Large amplitude NC-AFM imaging	100
5.3	Small amplitude NC-AFM imaging	108
5.4	Imaging of defects	109
5.4.1	Boron induced defect	109
5.4.2	1+2DV defect	113
5.5	Setpoint variation	116
5.5.1	Apex variation	125
5.6	Asymmetric scans	128
5.7	Force spectroscopy	131
5.8	Imaging of C ₆₀ on Si(100)	135
5.8.1	Preparation	136
5.8.2	Imaging	136
5.8.3	Force spectroscopy of C ₆₀	141
5.8.4	Signal coupling in the Omicron qPlus implementation	144
5.9	Conclusions and analysis	145
5.10	Further work	147
6	NC-AFM and KPFM of spun cast nanoparticle networks	148
6.1	Topographic imaging	148
6.2	Apparent height of nanoparticle networks	150
6.2.1	Analysis of apparent heights	155
6.2.2	Network modification	159
6.2.3	Origin of the “sub-layer”	159
6.3	Force spectroscopy	162
6.4	Contact potential difference measurements	164
6.4.1	Voltage spectroscopy	164
6.4.2	Kelvin probe	165
6.5	C12 capped nanoparticles	166

6.5.1	In situ annealing and imaging	167
6.5.2	Analysis of measured CPD	182
6.5.3	Comments on the determination of absolute and relative CPD by AM-KPFM	183
6.6	Conclusions	186
6.7	Future work	187
7	Electrokinetic assembly of nanoparticles in solution	188
7.1	Experimental preparation	188
7.2	Frequency variation	189
7.3	Growth dynamics	191
7.4	Growth thresholds	194
7.5	Wire retraction	195
7.6	Electrochemistry/Electrode damage	206
7.6.1	Estimation of permittivity and conductivity	207
7.6.2	Electrical measurements	209
7.7	Origin of morphological changes	211
7.7.1	Double layer effects: ACEO flow/Electrochemistry	212
7.7.2	Origin of the controlled retraction	214
7.7.3	Origin of the spontaneous retraction	215
7.8	Origin of dynamics/plateau	216
7.8.1	Fractal nature	216
7.8.2	Depletion	216
7.8.3	Electrochemical	217
7.8.4	Origin of high frequency cutoff	217
7.9	Conclusions	218
7.10	Future Work	219
8	Conclusions	220
8.1	Conclusions	220
	Bibliography	222
	List of figures	251

Chapter 1

Introduction

“When facing a single tree, if you look at a single one of its red leaves, you will not see all the others. When the eye is not set on one leaf, and you face the tree with nothing at all in mind, any number of leaves are visible to the eye without limit.

But if a single leaf holds the eye, it will be as if the remaining leaves were not there.”

Takuan Soto

In this chapter a broad introduction to the topics investigated in this thesis is presented

1.1 Introduction

Over the last twenty-five years nanoscience has developed from embryonic beginnings to a fully-fledged cross disciplinary field of academia, with research now being carried out in fields as diverse as power generation [1], catalysis [2], drug delivery [3] and metamaterials [4]. During this time, developments in optical, electron, and scanning probe microscope techniques have allowed new and varied insights into the workings of the physical world on the sub-micron to atomic level. However, despite recent advances, attempting to understand how physical and chemical forces operate on, and affect, nanometre sized features is still an active area of research, with many unanswered questions. Even in tightly controlled ultrahigh vacuum (UHV) conditions at low-temperature

there is still debate as to how some of the most commonly used techniques interact with the materials being studied, and what the fundamental limits of such techniques actually are. One of the key goals of nanophysics must be not only to develop control of matter on the nanoscale but also to reach a complete understanding of the forces in play, and critically how they interact. As the size of a system varies, the dominant controlling force can often change due to different scaling behaviours. In general, the observation of unexpected or unexplained behaviour in otherwise well-understood experiments can point the way to new and exciting areas of research, and nanoscience is no exception. On the nanoscale, the forces of interest are almost exclusively electromagnetic in origin. This paring down of the forces in no way reduces the complexity or interest of the systems, however, as subsets of the electromagnetic interactions compete to produce a bewildering range of behaviours. In a very simplified understanding we have four primary modes of interaction (see Fig. 1.1), Pauli repulsion, chemical bonding, van der Waals dipole interactions and net charge electrostatic attraction/repulsion. In this thesis we will engage with each of these, though by the nature of the scaling laws only one or two will compete for domination at any one time.

In addition to developing a fundamental understanding of forces on the nanoscale, a primary motivation is to use the tools at our disposal to build structures. The traditional route for manufacturing nanoscale features, optical lithography, is still the most widely used, despite numerous premature predictions of its downfall [5–7]. The development of increasingly ingenious techniques now mean that sub-wavelength features are routinely produced [8] and used in homes around the world, and it now appears that the fundamental limit for silicon-based electronics may be the very materials they are created from, rather than the technique used to create features. Despite optical lithography’s great success, it still has its acknowledged fundamental limits, and is not suited for general purpose applications, especially manufacturing outside of clean room level facilities. Increasingly large investments are required for diminishing returns [9], and, as such, research into alternative techniques that may be applied more cheaply, or perhaps more widely in different environments continues apace.

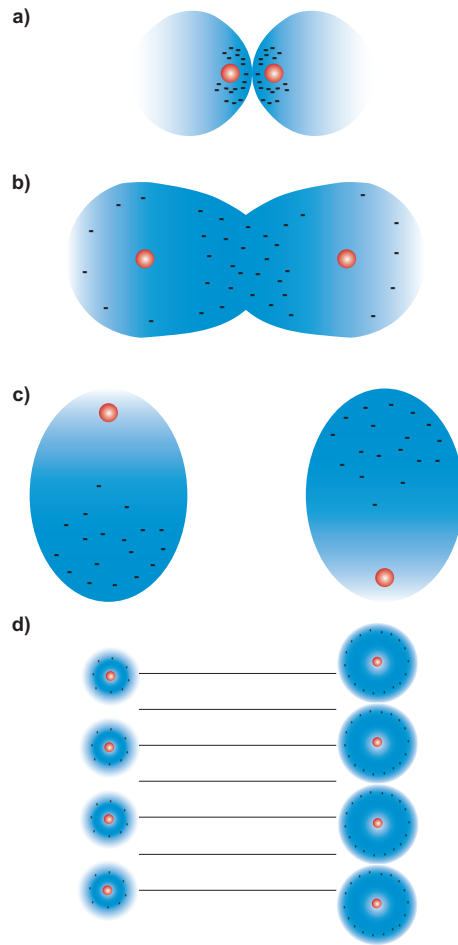


Figure 1.1: Illustrative representation of some of the important forces at the nanoscale: a) short-range Pauli repulsion between two atoms, b) chemical bonding between electron shells, c) mutual induced dipole interaction (van der Waals), d) electrostatic interaction due to a net difference in charge between two surfaces.

1.2 Top-down versus bottom-up

Lithography forms part of what has become known as the “top-down” method of forming small scale features. So called because the fundamental approach is to take a large-scale object (for example a wafer of silicon) and etch away progressively smaller and smaller areas in order to form the required structure (see Fig.1.2 for some examples). This approach can be thought of as carving a sculpture from one huge block of marble – it is required that any imperfections

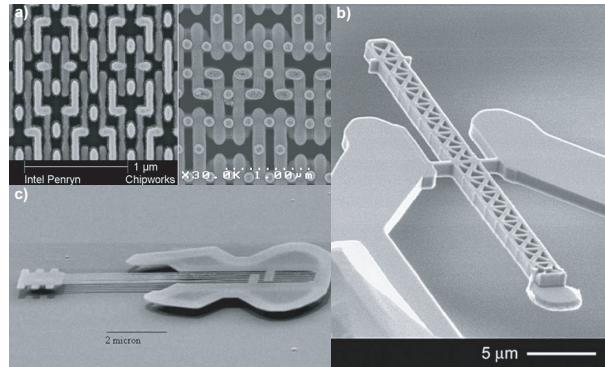


Figure 1.2: Examples of “top-down” methods of fabrication: (a) A commercial Intel “Xeon” chip created using UV lithography imaged by SEM [10]; (b) microscale girder fabricated using focused ion beam (FIB) [11]; (c) “the world’s smallest guitar” fabricated using electron beam lithography [12].

in the marble be small compared to the features to be created on the statue, and the smallest feature must in general be larger than the smallest edge used for carving. In top-down lithography techniques such as focused ion beam (FIB) milling the “statue carving” analogy is taken to its most literal limit.

The other approach to nanofabrication is the so-called “bottom-up” school of thought. Here the philosophy is to take a large number of very small well-defined building blocks (for example single atoms, molecules or nanoparticles) and then assemble them into the required structure. If top-down technology is like carving a sculpture from a block of marble, then bottom-up technology is like building a house from a mass of near identical bricks. The advantage (at least in theory) of bottom-up technology is that as long as the building blocks are well-defined it allows essentially ultimate control over the manufacture of the final product. The problem now is not the fidelity of the material, or how small a feature you can carve, but rather how to get all of the components in the right place at the right time. It is how this final step is to be accomplished that has produced something of a schism in the nanoengineering community [13].

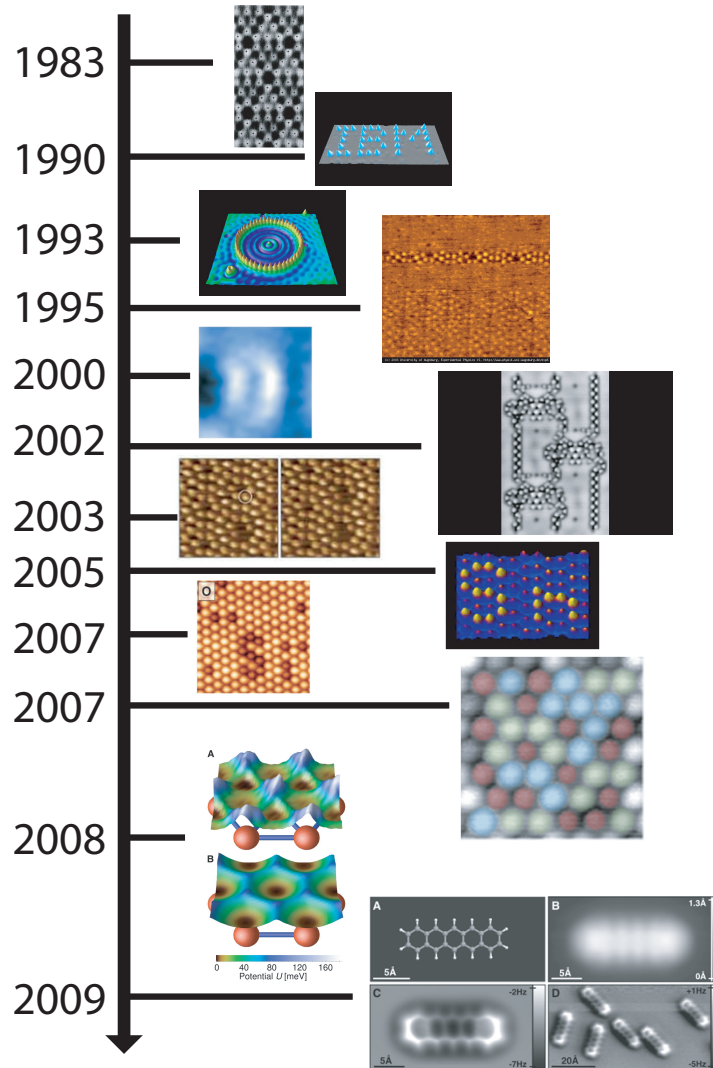


Figure 1.3: A potted history of the rise of the scanning probe microscope: (from top to bottom) the first real space image of the Si(111) 7 x 7 reconstruction taken by STM [14], atomically precise manipulation of individual atoms by STM [15], observation of standing electron waves enclosed in a artificially constructed “quantum corral” [16], first true atomic resolution in NC-AFM [17], “subatomic” resolution achieved using small amplitude NC-AFM [18], an operational logic gate system constructed from individual CO molecules by STM [19], vertical manipulation of an individual silicon atom by chemical forces [20], atomically precise lateral manipulation in NC-AFM [21], atomically precise vertical interchange by NC-AFM [22], chemical identification of individual atoms using NC-AFM [23], direct measurement of the force needed to move an atom by NC-AFM [24], atomic resolution within individual molecules with small amplitude NC-AFM and STM [25]

1.3 Scanning probe microscopy (SPM) and atomic manipulation

Initially some rather outlandish proposals were made regarding atomically precise molecular manufacturing techniques [26] which came to the public's attention in the form of both popular science books [27] and science fiction [28]. Unfortunately, these techniques, even if theoretically realisable, are not a realistic approach for anything other than the most fundamental physics experiments using today's technology. This said, the development of the scanning probe microscope - and, critically, the scanning tunneling microscope (STM) and the noncontact atomic force microscope (NC-AFM), have provided striking demonstrations of atomic resolution imaging and "proof of principle" demonstrations of mechanical single atom manipulation [20]. Fig. 1.3 shows a potted history through some iconic results from SPM most closely related to the work presented in this thesis. Many of these groundbreaking results have been repeated by a number of groups, but require considerable experimental expertise to implement. As demonstrated most strikingly in recent results [25] the combination of AFM and STM into one instrument capable of producing high resolution atomic data from two separate imaging pathways is now routinely realised, and it is expected that this ability to probe both the electronic density of states and the charge density simultaneously with atomic resolution will become a standard tool, that may one day lead towards a more quantitative interpretation of scanning probe data [29].

Of course, the AFM has a multitude of uses far removed from the world of atomic resolution imaging. It has become a standard tool in fields such as materials science and biology, and its ability to not only be tuned to detect the topography of the sample, but also (via appropriate modification) to accurately map other properties such as contact potential [30], friction force [31], magnetism [32], and so on, has led to it becoming a general purpose surface science tool in fields not traditionally associated with nanotechnology. Although bottom-up assembly using scanning probe techniques provides close to ultimate control in terms of precision, it suffers from a number of key drawbacks that make it unlikely to progress beyond prototyping in the research

laboratory. First, most (though not all) experiments of this type must be performed in carefully controlled conditions, such as high vacuum and sometimes at low-temperature. Second, they rely on well-prepared surfaces, and even more importantly well-prepared tips, the creation of which is still as much art as science. Third, and perhaps most critically, it is inherently a serial technique – in order to maintain high precision the components must be positioned in small groups or even one at a time. Therefore, even for well understood systems the assembly of large structures can take many hours of work by a dedicated operator. Finally, they are practically limited to a few tens of nanometres - the construction of high precision features over many microns is not currently practical.

1.4 Self-assembly

An alternative approach to bottom-up assembly is the use of self-assembly or self-organisation. Although technically differentiated - strictly, self-assembly occurs close to thermodynamic equilibrium, while self organisation is a non-equilibrium process - the terms are often interchanged in the literature, and we will not concern ourselves with strict delineation here. Self-assembly and self-organisation rely on some intrinsic or engineered property of either the components or environment that causes the constituent components to come together in an organised way. Strictly, materials such as crystals demonstrate self-organisation in its simplest form, but here we are mainly concerned with the organisation of larger objects, such as molecules and nanoparticles. As has been noted [33], self-organisation is actually ubiquitous on many length scales and is not unique to nanotechnology (see Fig. 1.4 and Fig. 1.5). Although examples of self-organisation are easy to find, discovering examples that reliably work on the nanoscale has been an active area of research, as has been understanding the fundamental properties and force interactions that allow the systems to form.

Under the umbrella of self-organisation we can consider two broad areas of research. Firstly there is research into molecular (or supramolecular) network assembly – where bonds between molecules are utilised to create large

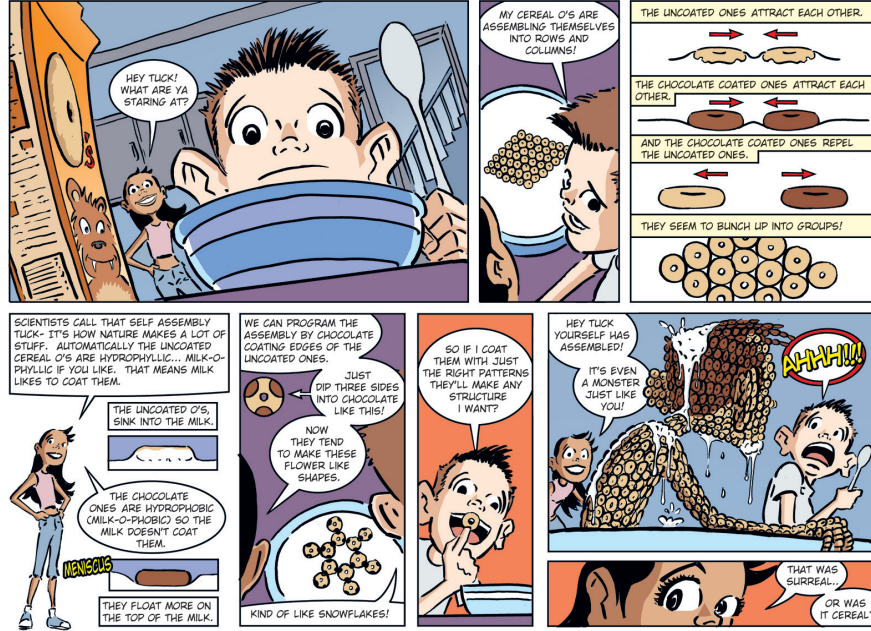


Figure 1.4: Complex behaviour at the breakfast table. Self-assembly and self-organisation are ubiquitous on many length scales, but engineering molecules or nanoparticles to self-assemble into a useful structures remains a challenge for researchers in the field. From [34]

self-assembled networks on surfaces. These systems often utilise the angular dependence of the bonds of the molecules to create repeating structures over large length scales. Schemes of this type have been shown to work both in vacuum [35] and in solution [36] and to demonstrate both conventional long-range order and more complex tiling behaviours. The other approach is to use much larger constituent components (for example nanoparticles) where more typically properties such as the size distribution and the passivation scheme are important, rather than chemical or hydrogen bonding between the particles. By utilising properties of the system, such as fluid dynamics or applied fields, more general purpose schemes of self-organisation may be developed [37]. These schemes can take advantage of the interesting properties of the constituent components, and often the key question is to what extent these may carry forward into creating novel larger scale structures.

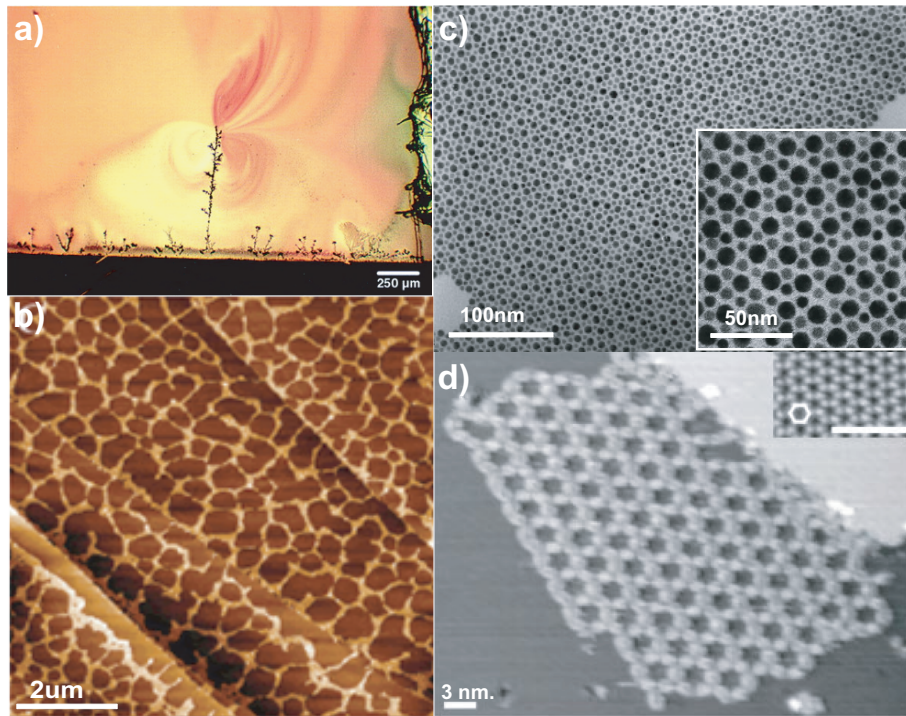


Figure 1.5: self-organisation on a range of length scales relevant to nanotechnology: (a) microwires self organising out of a colloidal suspension under the influence of an inhomogeneous electric field [37], (b) cellular networks formed from a spun cast solution of thiol passivated nanoparticles [38], (c) a close packed network of metallic nanoparticles using two different sizes to create the packing arrangement [39], (d) self-assembly of PTCDI and melamine molecules into a supramolecular network in UHV conditions via hydrogen bonding [35].

1.5 Thesis outline

In this thesis we will cover a wide range of topics, but our fundamental concern will be interactions between objects on the nanoscale. Over the next two chapters we will present a brief literature review of the key topics covered as well as an overview of the experimental techniques and specific instruments used. In the first experimental chapter we will discuss work relating to the investigation of the Si(100) surface in UHV using small amplitude (qPlus) NC-AFM. In addition to examining how the interaction between the tip and the surface modifies the buckled dimer structure at low-temperatures, we will also report on simultaneously acquired tunnel current data in the chemical bonding regime. We also present high resolution imaging of fundamental and boron-induced defects as well as adsorbed C₆₀ on the Si(100) surface using NC-AFM. In this chapter we will primarily be concerned with the van der Waals and chemical bonding forces between a metallic/silicon tip and the silicon surface on the atomic scale. In the second experimental chapter we switch to a larger length scale and use conventional cantilever type NC-AFM to investigate self-assembled nanoparticle networks both in UHV and ambient conditions. We investigate how different types of tip-sample interaction can affect the apparent topography, and also present results of both force and voltage spectroscopy on the same networks. Finally, we also investigate the local contact potential difference across such samples using scanning Kelvin probe force microscopy to simultaneously map topography and contact potential difference. In the final experimental chapter we continue to look at the forces between nanoparticles, but in a radically different environment. We investigate the competing forces that affect structure formation during the self-organisation of microwires in solution via dielectrophoresis (DEP), and discover that as well as dipole interactions, electrically-induced fluid flow and electrochemistry play a key role and can often dominate over the DEP force under certain experimental conditions. Finally, we present general conclusions and look ahead to future work on the topics presented.

Chapter 2

Scanning Probe Techniques

“Science is a way of trying not to fool yourself. The first principle is that you must not fool yourself, and you are the easiest person to fool.”

Richard Feynman

In this chapter a review of the scanning probe techniques used to acquire experimental results in this thesis is presented. We detail some key developments, results and issues related to both scanning tunnelling microscopy and atomic force microscopy

2.1 Introduction

Since its introduction in 1982, scanning tunnelling microscopy (STM) [40,41] has proven to be an invaluable tool in the surface scientist’s arsenal. Although real space imaging with atomic resolution had previously been accomplished [42], this had only been for extremely specialised high aspect ratio systems. With STM, for the first time large-scale real space images with atomic resolution of conducting and semiconducting surfaces became possible. The introduction of the atomic force microscope (AFM) shortly after [43] extended this imaging capability to insulators (although the imaging mechanism is of course fundamentally different).

In this section a brief overview of each of the scanning probe techniques used in the work presented in this thesis is provided. Scanning probe microscopy

spans a huge range of experimental and theoretical advances, so therefore many aspects of the technique not directly used in obtaining results for this thesis will necessarily be excluded.

2.2 Scanning tunnelling microscopy (STM)

STM was the first scanning probe technique introduced [40] and also the first to achieve atomic resolution. Historically, most other scanning probe techniques are therefore considered to be extensions of the STM blueprint. Certainly, many of the conditions needed for successful STM experiments are also required for other scanning probe experiments. Therefore it is helpful for us to consider the STM in some detail before considering other SPM techniques developed later.

2.2.1 Principle of operation

Although it should be noted that there are a number of significant technical obstacles to achieving atomic resolution using STM (including, but not limited to, successful vibration isolation, electronic amplifier and feedback design, tip preparation, and, in many cases, vacuum component design) we will for the purposes of this discussion assume that all practical technical problems have successfully been overcome since the results obtained in this thesis were exclusively obtained on commercial instruments. The review of the technical considerations in the successful construction of an STM may be found in numerous review texts [44–46]. We will instead focus on the basic theoretical principles of operation.

The basic components, found in virtually every STM are (Fig. 2.1):

1. A sharp metal tip, used as the probe with which to investigate the surface. Normally produced by electrochemical etching, or mechanical grinding or pulling [45].
2. The positioning system, capable of moving the tip over a large distance into contact with the surface, and then capable of sub-Ångström positioning and movement once close to the surface.

3. A high sensitivity current-to-voltage (I/V) converter and preamplifier for detecting the tunnel current, typically of sensitivity 10^9 V A^{-1} or better [45].
4. A negative feedback loop capable of regulating the position of the tip based on the tunnel current detected.
5. A digital signal processor for tip positioning, datalogging, signal and image processing, and connection with computer-based control software.
6. Vibration isolation (not shown).

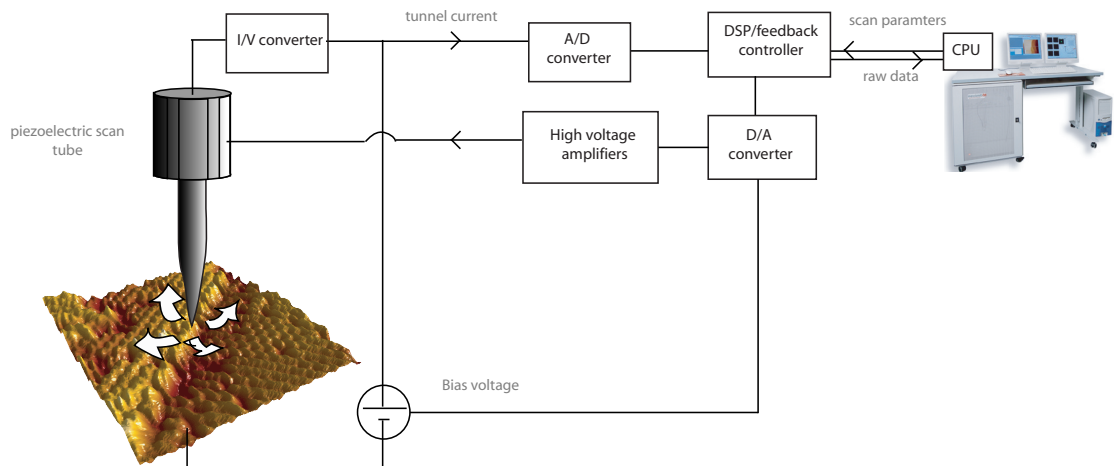


Figure 2.1: Block diagram showing the major electronic components of a modern STM system. Other features such as the vacuum chamber and vibration isolation have been omitted for clarity.

As regards the positioning system, usually a combination of piezoelectrically driven slip sticks or mechanical positioning, and direct piezoelectric actuation is used. In terms of direct actuation, the most common form is now the piezoelectric scan tube, although there are several other designs with their own advantages and disadvantages [45]. The piezoelectric scan tube is essentially a

hollow cylinder made out of piezo ceramic. Usually four electrodes are placed on the surface of the tube, one for each quadrant, whilst the ground contact is made to the inside of the tube. If the same voltage is applied to each of the electrodes the tube will extend in the Z direction such that [45]

$$\Delta L \approx d_{31} \cdot L \cdot \frac{U}{d} \quad (2.1)$$

where ΔL is the change in length of the tube, L is the original length of the tube, U is the applied voltage, d is the tube wall thickness, and d_{31} is the strain coefficient in the direction perpendicular to the polarisation.

If different voltages are applied to the various electrodes then the tube can be made to bend in the X and Y plane or contract/expand in Z. It is by this method that the tip is rastered over the surface. Note that in order to accurately determine the actual extension for a given voltage the piezo tube must be calibrated using a known distance once installed in the scanner. This is typically done by measuring the voltage needed to pass over a structure with a well-defined height, for example an atomic step edge.

In normal operation, the sharp metal tip is positioned near to the sample surface and then slowly brought into near-contact. A bias voltage is applied between the tip and the surface, and when the tip approaches within a few nanometres or so of the sample a small current is detected flowing between them. This so-called “tunnel current” is the mechanism by which the surface is imaged - i.e. the key imaging parameter. For simplicity we will consider the case of a system in vacuum, although it should be noted that the same principles apply for imaging in air, or even fluids.

The tunnel current is an inherently quantum mechanical effect where the potential in the vacuum classically acts as a forbidden region for electrons attempting to travel between the tip and the sample. In general, calculating the tunnel current is not simple, but, with the aid of several simplifying assumptions [47], a qualitative understanding can be reached with basic quantum mechanics. A 1D tip-sample barrier is shown schematically in Fig. 2.2; the essential quantity we need to calculate is the transmission probability for a wave incident on a barrier of a finite height in one dimension.

Following the formalism in both Stroscio [46] and Chen [45] we start with

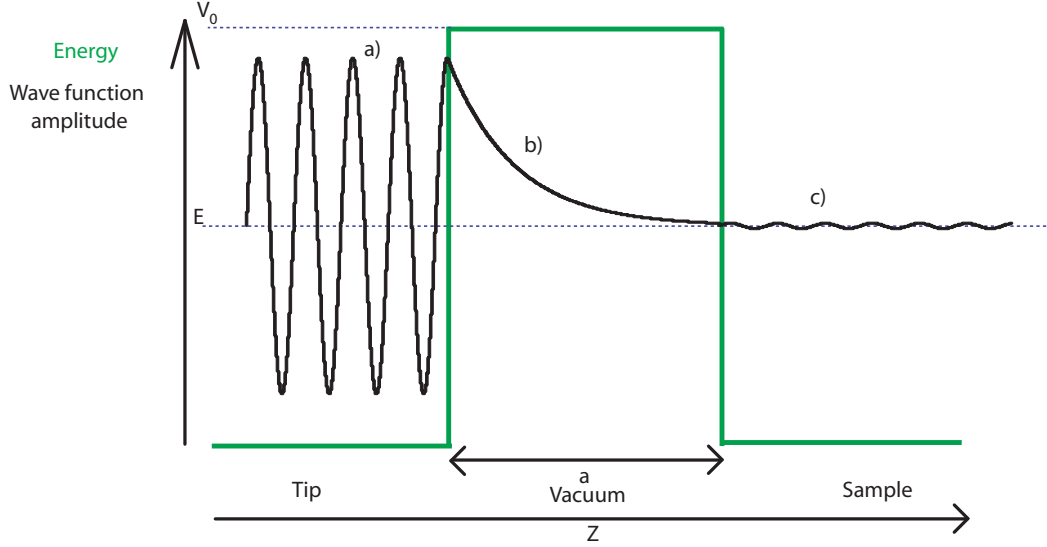


Figure 2.2: Schematic diagram showing a wave incident on a one-dimensional barrier. In region a) we have a travelling wave, in region b) an exponentially decaying wave function, and in region c) a travelling wave, but with diminished amplitude. Note that the associated energy of the electron does not change, only the wave function amplitude, and therefore the probability of finding the electron on the other side of the gap.

the time independent Schrodinger equation;

$$\hat{H}\psi(z) = E\psi(z), \quad (2.2)$$

Which for a particle in one dimension is explicitly

$$\frac{\hbar^2}{2m} \frac{d^2\psi}{dz^2} + V(z)\psi(z) = E\psi(z). \quad (2.3)$$

In region a) of Fig.2.2 the wave function for the electron has a solution of the form

$$\psi(z) \propto \psi_0 e^{\pm ikz}, \quad (2.4)$$

where k , the wave vector of the electron, is defined as

$$k = \frac{\sqrt{2m(E - V_0)}}{\hbar}, \quad (2.5)$$

where E is the energy of the state, V_0 is the potential in the barrier, and m is the effective mass of the electron. Note that the potential in the barrier is not in general constant, but we may replace it with an average value without loss of generality in order to simplify the argument.

Inside the (classically forbidden) rectangular barrier the wave function of the particle has a solution of the form

$$\psi(z) \propto \psi_0 e^{-\kappa z}, \quad (2.6)$$

where

$$\kappa = \frac{\sqrt{2m(V_0 - E)}}{\hbar} \quad (2.7)$$

is the decay constant.

If we assume that the voltage applied is much smaller than the work function of the surface (i.e. very low bias voltages $V \ll \phi$), that is, we assume that we are tunnelling from states near the Fermi level, then we can write κ as

$$\kappa = \frac{\sqrt{2m\phi}}{\hbar}. \quad (2.8)$$

Since the transmission probability is simply the squared modulus of the wave function, we can see that the tunnel current decays exponentially with the barrier width (i.e. tip-sample separation)

$$I \propto e^{-2\kappa a}. \quad (2.9)$$

With work functions of the order of a few electron volts [45], we find that the tunnel current changes by approximately an order of magnitude for every Ångström change in separation between tip and sample. This extremely strong dependence on tip-sample separation is the key to an STM's extremely high-resolution. It is thought that, in general, most tips may have a radius of curvature at the apex of the order of tens to hundreds of nanometres, or may not even have a well-defined apex at all. However the result of this extremely strong distance dependence is that only a small asperity need be sticking out from the bulk of the tip with a well-oriented cluster of atoms in order for

successful atomic resolution imaging to take place - Fig. 2.3 shows a schematic representation.

In general, extending the expression for the tunnel current beyond this simple one-dimensional case is nontrivial. It is, however, worth noting the seminal work of Tersoff and Hamann [47] which provides us with a first approximation with which to interpret STM images. Starting from the work of Bardeen [48], we have an expression for the tunnel current;

$$I = \frac{2\pi e}{\hbar} \sum_{\mu\nu} \left(f(E_\mu) [1 - f(E_\nu + eV)] |M_{\mu\nu}|^2 \delta(E_\mu - E_\nu) \right), \quad (2.10)$$

where $f(E)$ is the Fermi function, V the applied voltage, $M_{\mu\nu}$ the tunnelling matrix between the states ψ_μ (the probe) and ψ_ν (the surface) and E_μ the unperturbed energy of the state ψ_μ .

A number of simplifying approximations are made. It is assumed that the tip itself does not perturb the surface states involved in the tunnelling process (i.e. the weak coupling limit). We also assume that the Fermi functions of tip and sample may be approximated by the Fermi functions at zero Kelvin, and we also assume that (for a conductor) the bias voltage applied is small. Therefore,

$$I = \frac{2\pi e^2 V}{\hbar} \sum_{\mu\nu} \left(|M_{\mu\nu}|^2 \delta(E_\nu - E_F) \delta(E_\mu - E_F) \right). \quad (2.11)$$

If we then reduce the tip wave function to a point at \mathbf{r}_0

$$I = \frac{2\pi e^2 V}{\hbar} \sum_{\nu} \left(|\psi_\nu(\mathbf{r}_0)|^2 \delta(E_\nu - E_F) \right), \quad (2.12)$$

i.e. we find that the tunnel current is proportional to the local density of states (LDOS) of the surface at \mathbf{r}_0

$$I \propto \rho(\mathbf{r}_0, E_F). \quad (2.13)$$

It should be noted that this is the simplest possible interpretation of the tunnelling current. In general, evaluating the tunnelling matrix, and especially

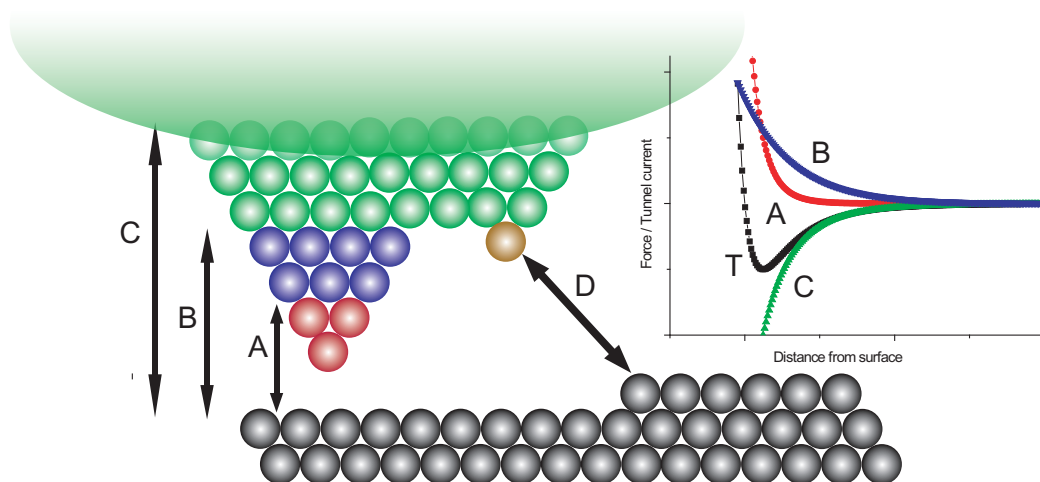


Figure 2.3: Cartoon showing different regions of a tip and their effects. Region A, comprising of only the last few atoms of the tip is primarily responsible for most of the short-range chemical bonding and Pauli repulsion. A slightly larger region (labelled B) is responsible for the bulk of the tunnel current flowing between tip and sample. Region C indicates the region where the long-range van der Waals force due to the bulk of the tip originates. T (labelled inset on the graph) shows the total force modelled by a Lennard-Jones potential as a result of A and C. D shows an asperity demonstrating the effect of a double tip. Although a double tip may not produce a noticeable effect imaging a flat surface, if a larger feature, such as a step edge, is approached, its influence may become apparent.

the tip electronic structure, is extremely difficult. This can be rendered even more demanding in the presence of high temperatures, large biases, or complex nonmetallic systems such as semiconductors and organic molecules. Nonetheless this approach has been shown to work surprisingly well, even producing quantitatively accurate results in certain systems [47].

STM may be operated in several modes. Here however, we shall limit the discussion to the most common - constant current mode. In this mode the current that flows between the tip and sample is regulated by a feedback loop that changes the position of the tip with respect to the sample in order to maintain a constant current. When operated in this mode, the tip height above the surface is roughly constant, and so the shape of the surface is mapped by the path of the tip in three dimensions.

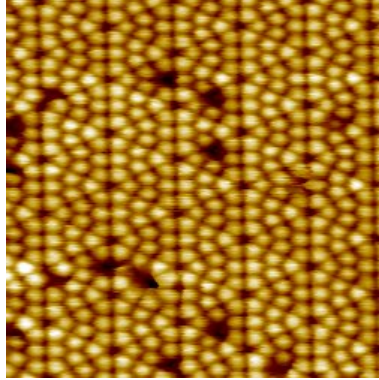


Figure 2.4: Conventional STM image of the Si(111) 7 x 7 reconstruction taken at -0.3 V, 500 pA. Image size 15 x 15 nm.

Although this explanation broadly describes the basic principle of operation, on the atomic scale it is found to be a gross oversimplification. One problem lies in the definition of “topography” at the atomic scale. One definition is that topography corresponds to contours of constant total charge density [49]. However, as we have already seen this is not precisely what STM probes. The charge density is built up from all the electrons below the Fermi level, whereas the tunnel current is weighted towards the Fermi level, but critically depends on the LDOS which can be arbitrarily complicated.

Hence, to a first approximation we consider that we map the local density of states, and not in general the topography. In some cases these have a very close correlation - for example, in the case of the Si(111) surface (see Fig. 2.4) - whereas in others the differences can be striking. For example, on the Si(100)-(2x1) surface, changing the bias voltage to probe filled or empty states causes a shift in the appearance of the silicon dimer rows (see Fig. 2.5), whereas on the GaAs (110) surface (Fig. 2.6) only one of the two types of atoms is imaged for opposite polarities of the bias voltage. A cartoon representation of the bias dependence of tunnelling at different biases is shown in Fig. 2.7

It is also worth noting at this stage that finite voltage, tip size and additional complications (such as band bending at the surface in semiconductors, and even physical surface modification by the probe itself) can significantly modify the image that is observed. In fact, one of the key difficulties in STM is producing a tip that is sharp enough to resolve atomic scale features. Typi-

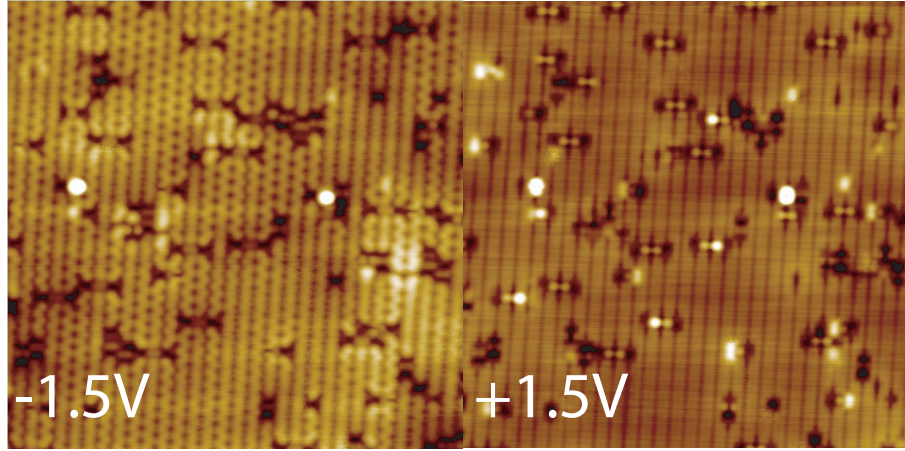


Figure 2.5: Conventional STM image of the same region on the Si(100) surface taken at -1.5 V (left) and +1.5 V (right) at 77 Kelvin. Note the strong differences in both the appearance of the dimer rows and the defects.

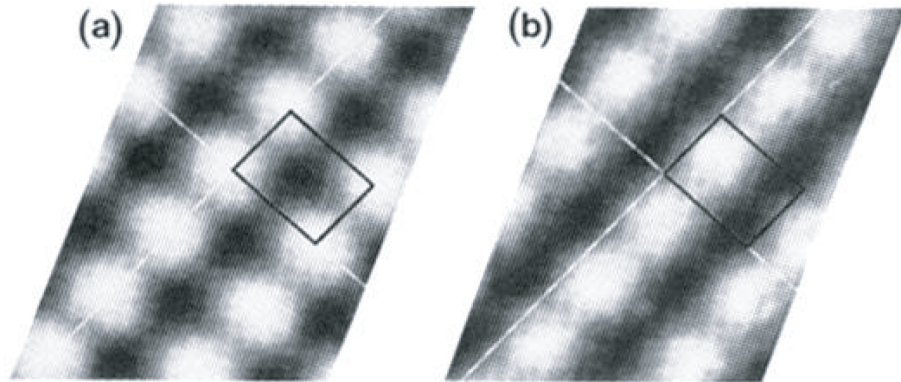


Figure 2.6: Conventional STM image of the gallium arsenide surface at +1.9V (left) and -1.9V (right) taken from [50]. At positive bias only the Ga atoms are visible, while at negative bias only the As atoms are visible. The square box shows the same unit cell in both images.

cally, when the tip is first introduced into the system it is not sharp enough to give atomic resolution, or there may be multiple tips which produce a so-called “double tip” (see Fig. 2.3) effect. The most common techniques by which the tip may be made suitable for atomic resolution imaging are the application of voltage pulses, and controlled tip crashes. Applying a large increase in bias voltage over a short period of time, or controllably crashing the tip into the surface can cause macroscopic changes to the tip structure which may result in

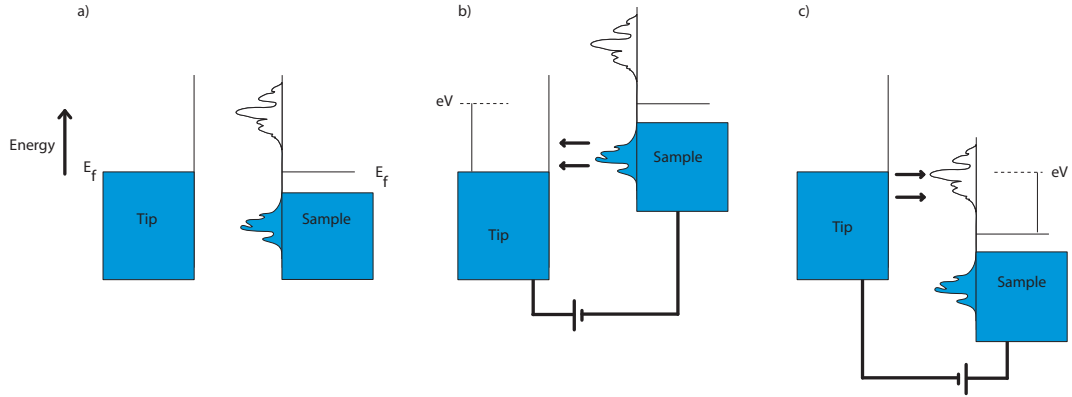


Figure 2.7: Schematic diagram showing the tunnelling between a metallic tip and a sample with a bandgap and complex density of states. In a) the Fermi levels align and no net tunnelling takes place. In b) the sample is biased negatively by $-V$ and electrons tunnel out of the occupied (filled) sample states into the tip. In c) the sample is biased positively by $+V$ and a net flow of electrons tunnel out of the tip into the unoccupied (empty) states of the sample.

the creation of a small sharp asperity suitable for atomic resolution imaging. It is worth noting that depending on initial tip conditions and various other factors this process can take anywhere from several minutes to several days. Tip preparation may also be carried out outside of the STM head using more dedicated procedures such as electron beam bombardment, argon sputtering or high voltage field emission [45], although there are additional difficulties associated with the heating of glued tips (as used in qPlus AFM). However none of these procedures were available on the systems used for atomic resolution imaging at the time.

There are numerous other STM imaging modes that have been covered in extensive detail in several excellent books [44–46]. However one mode that we shall mention in passing is so-called “dynamic STM”. Essentially imaging is identical to conventional STM, but, in addition, the tip is oscillated in the Z direction with small (usually sub-nanometre) amplitude at a frequency far above the bandwidth of the feedback loop. As a result the tunnel current measured is actually the “average” tunnel current over several cycles of the oscillation. Therefore, for a given current set-point the tip’s point of closest

approach is significantly closer to the surface than it would be using conventional STM with the same tip and sample. The advantage of this mode is that most tips (as theoretically modelled) are much stronger mechanically responding to forces in the Z direction than due to lateral forces (i.e. in X/Y). Therefore if the bulk of the force is applied in the Z direction, the tip is able to approach much closer to the surface without being damaged. This imaging technique has led to unprecedented resolution using STM [51], and it is useful to note that a related technique may be used in parallel with atomic force microscopy (AFM) to produce simultaneous tunnel current images. If the STM tip is actually mounted on a cantilever (rather than simply being oscillated by driving the piezo tube) then it is possible to collect information on the tip/sample interaction force simultaneously (see for example [52]).

2.3 Atomic force microscopy (AFM)

Initially, the AFM was developed as a direct extension of the STM to the extent that the first operational AFM used an STM as its height detection mechanism [43]. However, AFM has now developed far beyond being a mere extension of STM into an extensive field in its own right. In addition, the majority of extensions to the SPM technique have since been made as extensions to the AFM, rather than the STM (e.g. [53–56]). Here we present only the briefest history of the AFM, and focus on the specific techniques used experimentally in this thesis, and the key differences between them.

As suggested by its name, the key feedback parameter and detection method in AFM is the force between the tip and the sample. Unlike the tunnel current in STM there are several possible origins for forces between the tip and the surface. The primary mechanisms are Pauli repulsion, short-range chemical forces, slightly longer range van der Waals forces, and, in some cases, long-range electrostatic or magnetic forces [32]. For this reason the feedback design and interpretation of AFM images can be substantially more complicated than that for STM [57].

The key parameter in AFM is the force (or in NC-AFM the force *gradient*) between the tip and sample. In almost all cases this force is detected by the

measurement of the deflection of what is essentially a spring. However, detecting the deflection of the spring may be accomplished in a number of different ways. The usual method is to use a cantilever of some kind with the tip attached at the end roughly at right angles to the cantilever itself. The types of cantilever, tip, and cantilever deflection detection systems are extremely varied (e.g. [58–61], however. In the interests of simplicity we will only consider two primary types, the traditional micromachined silicon cantilever [62–64], and the more recently developed piezoelectric tuning fork (so-called qPlus) [65].

2.3.1 Contact mode AFM

The first AFMs were operated in what is now called “contact mode”. In this method a sharp tip mounted on a cantilever of some kind is brought into contact with the surface. The force between the tip and sample is determined by directly measuring the deflection of the cantilever, the more the cantilever bends the stronger the force. i.e

$$F_{ts} = -k\Delta d \quad (2.14)$$

where F_{ts} is the tip-sample force, and k and Δd are the stiffness and the deflection of the cantilever respectively.

A force/deflection setpoint is chosen and the tip is rastered over the sample, much like STM. This method is in principle extremely simple to interpret and produces what might well be termed “a pure topographic map” of the surface. Unfortunately it has been shown [66,67] that the force between the tip and the sample is usually much higher than the maximum loading stress of an atomically sharp tip. Therefore, except in exceptional circumstances, only “pseudo atomic” resolution may be achieved when a macroscopic area of the tip is commensurate with the lattice of the substrate [68]. Similarly, the imaging of highly reactive substrates (for example semiconductors in vacuum) is virtually impossible, although unit cells may be resolved with the use of special tip coatings [69]. Therefore, we will focus our attention on the so-called noncontact techniques which now routinely allow atomic, or even sub-atomic resolution on a wide variety of surfaces.

2.3.2 Noncontact AFM (NC-AFM)

In order to understand the rationale behind the development of NC-AFM, it is helpful to first consider in some detail the forces between the tip and the sample, and the difficulties involved in accurately mapping them. Fig. 2.3 shows a typical tip-sample force curve (inset). Here we only consider the short-range repulsive and the long-range attractive van der Waals force, and we exclude long-range electrostatic and magnetic forces, although the arguments apply to these in a similar way. A variety of different models exist for determining the forces between the tip and the sample. The two most common are the Lennard-Jones potential (which models the long-range van der Waals attractive force and Pauli repulsion)

$$V_{LJ} = -E_{bond} \left(2 \frac{\sigma^6}{z^6} - \frac{\sigma^{12}}{z^{12}} \right), \quad (2.15)$$

for a bond with energy E_{bond} and equilibrium distance σ , and the Morse potential (which in this form models short-range repulsive and attractive bonding forces)

$$V_{Morse} = -E_{bond} \left(2e^{-\kappa(z-\sigma)} - e^{-2\kappa(z-\sigma)} \right), \quad (2.16)$$

where κ is the characteristic inverse decay length. Note the Lennard-Jones potential (and its separate components) is used to demonstrate the force profiles in Fig 2.3. Often the measured force profiles may differ from the simplified models due to a number of factors (for example tip shape or inhomogeneities in the materials present) [70]. However, the key concept is that in order to obtain high resolution we must probe close to the surface, such that we are able to access the short-range chemical forces. It is thought that it is only by probing those forces which vary strongly on the atomic scale that we are able to obtain clear atomic resolution [66, 67], although it should be noted that the longer range forces have been shown to have variations on this length scale [71, 72]. The problem arises in so much as the force (and force gradient) between the tip and sample in the region we want to probe is so great that if we place the tip in this position in a static environment it will be pulled into

contact with the surface (i.e. a so called 'jump to contact' into the repulsive regime where the tip/sample force will become much greater) due to the finite stiffness of the cantilever. This becomes an issue since in this region the forces are so great that the tip and/or the surface may permanently be deformed by the interaction. If we want to work in the region where we are able to detect the short-range forces, without being drawn into the region where the tip and/or the sample is damaged or modified, it becomes necessary to use so-called dynamic AFM techniques.

Most commonly this is done by vibrating the cantilever, usually at, or near, its resonant frequency (although other schemes exist [61]). By controlling the amplitude of oscillation we are able to ensure that the energy of the cantilever at the point of closest approach is sufficient to retract the tip without it being pulled onto the surface. Thus we are able to probe the short-range forces without permanently deforming the tip and/or surface, without coming into contact with the surface, hence the aforementioned "noncontact" mode.

The advantage of working in this mode can be seen by considering the various instability criteria; in the quasistatic mode we require that the stiffness of the cantilever is greater than the maximum tip-sample force gradient i.e. as given by [66]:

$$k > \max \left(-\frac{\partial^2 V_{ts}}{\partial z^2} \right) = k_{ts}^{max}, \quad (2.17)$$

where typical bond stiffnesses for semiconductor systems are estimated at 100 - 200 Nm⁻¹ [67], with typical silicon cantilevers of stiffness ~ 40 Nm⁻¹ stable static mode attractive imaging is therefore not possible. If we oscillate the cantilever however, then we can avoid a jump to contact by using a sufficiently large amplitude as the relevant stability criteria becomes:

$$kA \geq \max(-F_{ts}). \quad (2.18)$$

However these conditions assume conservative tip sample interactions. If we have hysteresis during the cantilever oscillation (i.e. a nonconservative interaction, with dissipation into the surface) then additional energy needs to be supplied to the cantilever. In the case of nonconservative interactions there

is an additional stability criteria given in approximate form by Giessibl [66] as

$$\frac{k}{2}A^2 \geq \Delta E_{ts} \frac{Q}{2\pi}, \quad (2.19)$$

which arises due to practical difficulties in regulating the amplitude when the energy loss becomes large due to the intrinsic energy loss of the cantilever. This arises as small changes in the tip-sample energy require large changes in the excitation output. Interestingly, this criterion indicates that higher quality factor cantilevers are not necessarily desirable for optimum NC-AFM operation.

2.3.3 AM-AFM and FM-AFM

For NC-AFM there are essentially two modes in which we can operate; amplitude modulation (AM) and frequency modulation (FM). As their names suggest the essential difference is whether we measure the change in amplitude (at a fixed drive frequency), or directly measure the change in frequency of the vibrating cantilever. At this point it is worth noting that amplitude modulation has successfully been used in many situations to access the repulsive regime (i.e. so-called tapping mode [73]). This mode allows imaging in the repulsive regime, while severely reducing wear and damage to both tip and the sample as compared to contact mode. In general, though, this is not well-controlled. That is to say, scanning is effectively a series of “jump to contacts”, and, as such, the technique is generally considered to be a reduced damage (intermittent contact) alternative to contact mode, rather than a “noncontact technique”. It should be noted that under tightly controlled conditions, with very stiff cantilevers and extremely small oscillation amplitudes, atomic resolution imaging has been demonstrated using frequency modulated NC-AFM with positive frequency shifts [74]. However, in this case there is some debate as to whether the tip position is *exclusively* in the repulsive regime or whether it is possible to have positive frequency shifts, and yet remain in the attractive force regime. For the purposes of our discussion we will not consider repulsive mode imaging - when we refer to a “noncontact technique” we will assume that we are operating exclusively on the attractive side of the potential minimum

with negative frequency shifts (for FM mode) or a reduction in amplitude with the appropriate phase difference (for AM mode).

2.3.4 Principle of operation

In this section we will provide a brief overview of the operation of the NC-AFM. We will focus on FM-AFM but note key differences with AM-AFM where relevant.

In NC-AFM the essential principle of operation is that the force between the tip and the sample modifies the effective spring constant of the cantilever system. That is, we essentially have a form of weakly perturbed harmonic oscillator where the Hamiltonian of the cantilever is;

$$H = \frac{p^2}{2m^*} + \frac{kq'^2}{2} + V_{ts}(q), \quad (2.20)$$

(where $p = m^*dq'/dt$, $q'(t)$ the deflection of the cantilever, $q = d$ is the closest point of approach to the sample, A the amplitude of oscillation, and $q(t) = q'(t) + d + A$). The unperturbed motion is given by

$$q'(t) = A \cos(2\pi f_0 t), \quad (2.21)$$

and the resonant frequency

$$f_0 = \frac{1}{2\pi} \sqrt{\frac{k}{m^*}}, \quad (2.22)$$

where m^* is the effective mass and k the stiffness of the cantilever respectively.

The basic principle of operation may be considered thus. We oscillate the cantilever near its resonant frequency, driving the oscillator 90° out of phase. In AM-AFM we excite the cantilever to a given amplitude, and then set the amplitude setpoint to be a fixed fraction of this. As we lower the cantilever towards the surface, the effective resonant frequency of the system is modified as the effective spring constant changes due to the tip's interaction with the surface. In AM-AFM this change in resonant frequency is detected via the change in amplitude of the system. Since the drive frequency does not change

it is now at a different df from the new effective resonant frequency. As such, the response of the cantilever to a given excitation amplitude and drive frequency is modified. Therefore, the feedback system is sometimes called a “slope detection” system, since the relative change in amplitude is proportional to the slope of the Lorentzian (and therefore proportional to the quality factor of the cantilever - see Fig. 2.8). The feedback system is therefore conceptually reasonably simple: the cantilever is lowered until the amplitude is reduced to the amplitude setpoint. The tip is then rastered over the surface and the vertical position of the tip is changed to keep the amplitude of oscillation constant.

One problem with amplitude modulation mode (and the primary motivation for the development of the frequency modulation system) is that changes in the amplitude of oscillation do not happen instantly, they occur on a timescale of [75]

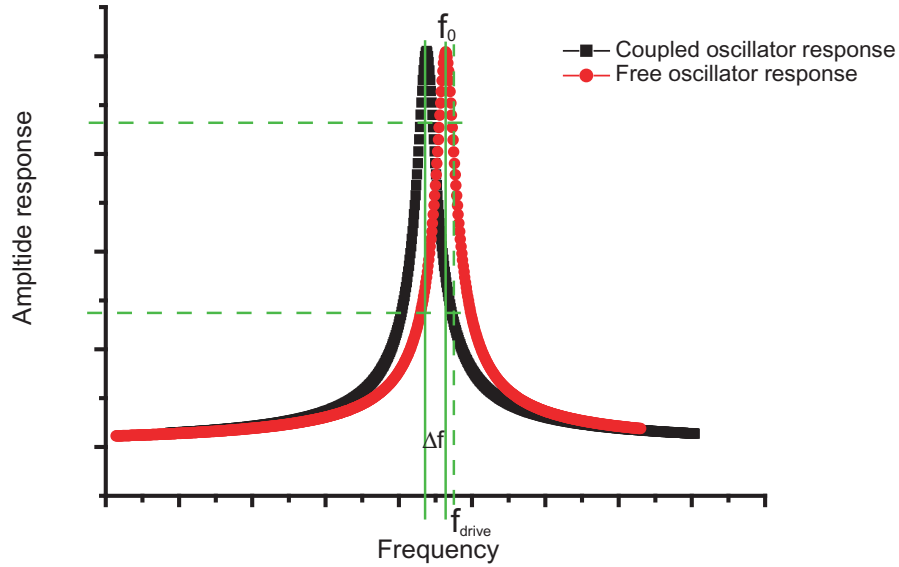


Figure 2.8: Graphs showing the Lorentzian response of a free, and a coupled oscillator. Coupling the oscillator causes a shift in the resonant frequency as described in the text. If we continue to apply a drive frequency at the same initial value, then the amplitude response of the oscillator will be changed as we are “sitting” in a different region of the slope. This is the basic principle by which AM-AFM operates. FM-AFM directly tracks the change in frequency using a phase locked loop.

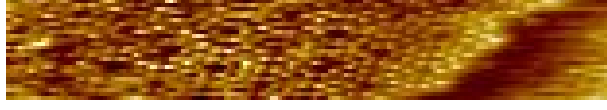


Figure 2.9: Conventional (cantilever based) FM-AFM image taken at the Si(111) 7 x 7 reconstruction over a step edge. $df = -30$ Hz with an effective sample bias of -0.3 V

$$\tau_{AM} \approx \frac{2Q}{f_0}, \quad (2.23)$$

where Q is the quality factor of the cantilever. Therefore, depending on the quality factor and resonant frequency of the cantilever it may be necessary to scan very slowly in order for a feedback mechanism to work properly. Typically in atmosphere with standard silicon cantilevers this is not a serious problem, but in vacuum where the effective quality factor of such cantilevers reach the tens or even hundreds of thousands, the scan speed may become prohibitively slow [75].

In frequency modulated mode the changes to the frequency occur on a timescale of

$$\tau_{FM} \approx \frac{1}{f_0}. \quad (2.24)$$

This decrease in response time has led to frequency modulation mode becoming the preferred method for systems operating in vacuum (although it should be noted that atomic resolution in vacuum with amplitude modulated mode has been accomplished using low Q cantilevers [76]). True atomic resolution using the non contact technique was first achieved using FM-AFM in 1995 [17] on Si(111) using a silicon cantilever and piezoresistive deflection system. Figs. 2.9 and 2.10 show similar images taken using the VT-AFM Omicron system.

Since then, UHV experiments of this type have gone on to produce routine atomic resolution on a wide variety of surfaces [57], as well as much more challenging feats such as both vertical and lateral manipulation on semiconductor surfaces [21, 22]

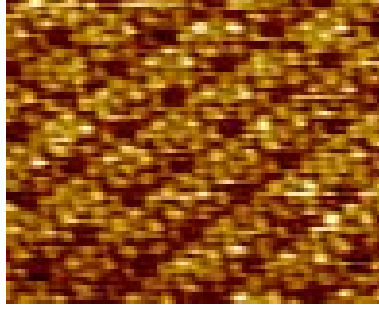


Figure 2.10: Conventional (cantilever based) FM-AFM image taken of the Si(111) 7×7 reconstruction showing a different contrast. $df = -50$ Hz with an effective sample bias of -0.3 V.

FM-AFM operation

The FM-AFM is somewhat more complicated than either the STM or AM-AFM. A schematic block diagram of the major components is shown in Fig. 2.11

It is clear that as well as sharing several key components with the STM, there are a number of important additions. First, we have a cantilever deflection detection system. This usually takes the form of a laser deflection mechanism which works by bouncing a focused laser off the back of the cantilever onto a four quadrant photodetector. Small changes in the position of the cantilever are amplified geometrically into larger displacements on the photodetector and converted into an electrical signal that may be sent back to the feedback and amplitude regulation. Other systems available include laser interferometry [59, 60] and direct detection via the use of piezoresistive cantilevers [58] (see also the discussion of qPlus in the next section). The next addition is the amplitude regulation circuitry which consists of the proportional/integral (PI) feedback system and phase shifter which monitors the amplitude setpoint and adjusts the excitation signal to keep the amplitude constant. Although it is possible to operate FM-AFM in ‘constant excitation’ mode where the amplitude is allowed to vary we will not cover it here as the technique was not used in obtaining results in this thesis. Changes in the gain required due to non elastic interactions of the surface (see below) are converted into the so-called “damping signal”. The deflection signal is also fed

into a phase-locked loop (PLL) which directly detects the change in frequency of the cantilever compared to its free space resonance. This produces the df signal, which is the principal imaging parameter and is fed back into the control electronics and used for feedback. In the simplest case where we are using very small amplitudes and the force gradient is constant over the range of an entire oscillation cycle i.e.

$$k_{ts} = \frac{\partial^2 V_{ts}}{\partial z^2}, \quad (2.25)$$

Then the frequency of the cantilever will be perturbed

$$f = f_0 + \Delta f, \quad (2.26)$$

and the calculation of the frequency shift is simple [57],

$$\Delta f = \frac{k_{ts}}{2k} f_0. \quad (2.27)$$

In general, however, the force gradient may vary significantly over the range of an oscillation cycle in conventional AFM and the calculation of the force from a measured frequency shift is significantly more complicated (see next section). However, if we continue to make the simplifying assumption then it follows that the detuning of the cantilever is proportional to the force gradient between the tip and the sample. Thus the basic principle is that by scanning at a constant frequency shift/amplitude we produce a map of constant force gradient (which we again presume relates to the topography) over the surface. Similar to STM we will find that this interpretation is, at times, overly simplistic.

As noted, nonconservative interactions may cause additional energy loss in the motion of the cantilever, and therefore an increase in the driving signal is required in order to maintain a constant oscillation amplitude. Although this has important considerations in determining the optimum parameters for a cantilever, more importantly, the ‘damping signal’ can provide important additional information as to the nature of the tip-sample interaction [77, 78].

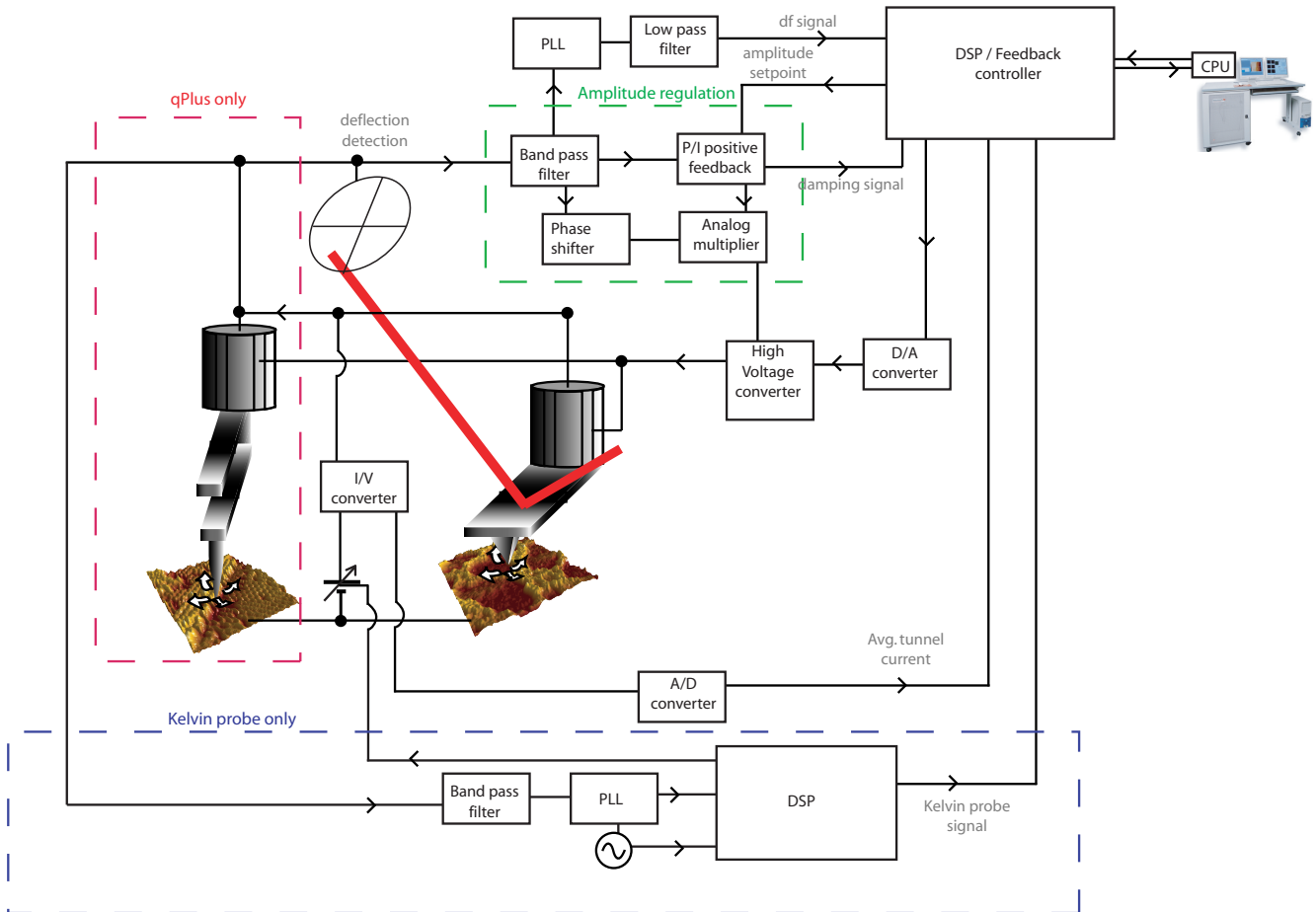


Figure 2.11: Block diagram showing at the major components of a modern FM-AFM system. Additional regions marked qPlus and Kelvin probe indicate features that are only present on the respective modifications to the basic template. Note, for example, the lack of a laser-based deflection system in the qPlus setup and the additional feedback regulation necessary for Kelvin probe. In some systems STM feedback may also be included as an additional regulator branch.

2.3.5 Force spectroscopy

A key ability of the NC-AFM, in addition to providing extremely high resolution topographic images, is the performance of so-called “force spectroscopy” experiments. In this mode of operation the tip is held at a frequency shift set-point (as it would be during a normal scan), but then the feedback regulation is switched off and the tip is moved towards (or away from) the sample, while measuring the frequency shift, damping signal and, for conducting samples, the tunnel current. This mapping of frequency shift against vertical displacement provides a measure of the force profile between the tip and the surface as a function of distance [79]. Its moniker as a “spectroscopic” technique comes from the fact that the force profile over different areas (and even different atoms) on the surface will be different and so, by carefully controlling the experimental conditions, it is possible to, for example, uniquely identify the atomic species on the surface by comparing force profiles [23]. This process may also be used in a slightly modified form to perform single atomic manipulation events and is thus an exciting possible route towards well-controlled atomically precise manipulation of strongly covalently bound surfaces [22]. An understanding of how the force is directly derived from the frequency shift measured is key to understanding these experiments.

For small oscillation amplitudes we have seen that the frequency shift to force conversion is simple. This is rarely true, however, except for cases using sub Ångstrom oscillations (see qPlus next section). For the case where the oscillation amplitude is large compared to the rate of change of the force gradient, a more complex approach first derived by Sader and Jarvis [80] is required.

They first note that Giessibl had earlier calculated a general formula for converting a force profile into a frequency shift [81]

$$\frac{\Delta\omega}{\omega_{res}} = -\frac{1}{\pi ak} \int_{-1}^1 F(z + a(1+u)) \frac{u}{\sqrt{1-u^2}} du, \quad (2.28)$$

where F is the interaction force between tip and sample, ω_{res} is its unperturbed resonant frequency, k is the cantilever stiffness, $\Delta\omega$ is the change in resonant frequency, a is the amplitude of oscillation, and z is the distance

of closest approach between tip and sample.

They then first express the interaction force as

$$F(z) = \int_0^\infty A(\lambda) \exp(-\lambda z) d\lambda, \quad (2.29)$$

where $A(\lambda)$ is the inverse Laplace transform of the force profile, and then substitute the inverse Laplace transform into Giessibl's original equation to obtain

$$\frac{\Delta\omega}{w_{res}} = \frac{1}{ak} \int_0^\infty A(\lambda) T(\lambda a) \exp(-\lambda z) d\lambda, \quad (2.30)$$

where $T(\lambda a) = I_1(\lambda a) \exp(-\lambda a)$ and $I_n(\lambda a)$ is a modified Bessel function [80]. There then follows a complex mathematical deconvolution, to which the reader is directed to the original paper and references therein. Despite the complex nature of the deconvolution, the end result produces a general formula for both the force,

$$F(z) = 2k \int_z^\infty \left(1 + \frac{a^{1/2}}{8\sqrt{\pi(t-z)}} \right) \Omega(t) - \frac{a^{3/2}}{\sqrt{2(t-z)}} \frac{d\Omega(t)}{dt} dt, \quad (2.31)$$

and the interaction potential

$$U(z) = 2k \int_z^\infty \Omega(t) \left((t-z) + \frac{a^{1/2}}{4} \sqrt{\frac{t-z}{\pi}} + \frac{a^{3/2}}{\sqrt{2(t-z)}} \right) dt, \quad (2.32)$$

in terms of the frequency shift of the cantilever in a form that can be easily implemented computationally (where $\Omega(t) = \Delta\omega/\omega_{res}$). The unconventional use of t as the position variable and z as the distance to closest approach can make this formalism confusing at first glance, but Heyde et al. [77] provide a more conventional notation;

$$F(D) = \frac{2k}{f_0} \int_D^\infty \Delta f(z) \left(\left(1 + \frac{A^{1/2}}{8\sqrt{\pi(z-D)}} \right) - \frac{A^{3/2}}{\sqrt{2(z-D)}} \frac{d}{dz} \right) dz, \quad (2.33)$$

where D is the distance of closest approach, A the oscillation amplitude and z is the tip-sample distance.

Comparison with simulated and experimental results in the large and small amplitude limits has confirmed that the deconvolution is accurate to within 5% in the regime of largest error [80]. This algorithm was implemented into a Matlab script [82] and utilised in the deconvolution of spectra taken in the experimental section.

Quantitative determination of the damping per cycle

During force spectroscopy (and indeed during normal scanning) it is conventional to collect data from the instrument damping channel. This provides information related to the dissipation in the approach and retract of the tip from the surface. Normally this channel provides only a voltage related to the gain of the oscillator electronics. However if this signal is *directly* proportional to the drive signal (as is the case for Omicron systems) then Giessibl's equation for the energy dissipation [83] (in eV/cycle) may be used;

$$\Delta E_{ts} = 2\pi \frac{E}{Q} \left(\frac{A_{drive}}{A_{drive}} - 1 \right), \quad (2.34)$$

where A is the excitation amplitude, and we can use the ratio of damping signals instead

$$\Delta E_{ts} = 2\pi \frac{E}{Q} \left(\frac{D'}{D_0} - 1 \right). \quad (2.35)$$

It should be noted that this method requires knowledge of the 'free' damping signal (i.e. far away from the surface) at the exact same amplitude regulation parameters. This can be acquired from spectroscopy points with a range that extends far away from the surface, or from at earlier scans taken at very low frequency setpoint.

2.3.6 Parameters in NC-AFM

There are essentially six key parameters which characterise an FM-AFM experiment; [66]

1. The spring constant of the cantilever.
2. The eigenfrequency of the cantilever.
3. The quality factor of the cantilever.
4. The oscillation amplitude.
5. The frequency shift of the cantilever.
6. The bias voltage between the tip and sample.

It has been shown for a wide range of experimental conditions [66] that two of the key parameters that are freely chosen, i.e. the oscillation amplitude and the frequency shift, may in fact be combined into what has been termed the “normalised frequency shift” for oscillation amplitudes that are large compared to the range of the tip-sample force. This parameter is in many ways a more useful physical quantity by which to compare experiments, since it essentially provides a standardised measure of how close the tip approaches to the sample. It is defined as

$$\gamma(z, A) = \frac{kA^{3/2}}{f_0} \Delta f(z, A). \quad (2.36)$$

It is also a useful (nondestructive) method for calibrating the cantilever’s physical oscillation amplitude with respect to the electrical excitation applied to the piezoelectric actuator, since, as mentioned, it provides a “fixed point” against which the physical position of the tip may be measured as the oscillation amplitude is varied [65].

As first noted by Giessibl [67], the scan parameters used to originally obtain atomic resolution were derived empirically, and were not optimised according to theoretical calculations. It became apparent that the possibility for much greater sensitivity, and a significant increase in the signal to noise ratio, could be made by modifying several of the operating parameters used during scans. The most critical of these was the amplitude of oscillation. It was found that significant improvements might be expected if the amplitude of oscillation was reduced to the same order as the range of the interaction that was to be

observed. In the case of atomic resolution imaging this involved increasing sensitivity to the short-range force whilst simultaneously reducing sensitivity to the much longer range van der Waals and electrostatic forces. Thus, in the case of short-range chemical forces (that are generally accepted to produce the atomic resolution), the amplitude of oscillation needs to be reduced to well under a nanometre. However, of the six key parameters listed above, only the last three are what might be considered “freely tunable” during the course of an experiment (and even then there are severe limitations on what values these parameters can have whilst still maintaining successful imaging). The first three are limited by the initial choice of cantilever, and this became a key driving force in the development of the qPlus NC-AFM technique [57].

2.3.7 qPlus AFM

As noted above, a key requirement in NC-AFM is that the energy of the oscillator be sufficient to withdraw the tip from the potential energy well produced by the tip-surface interaction. The energy of the oscillator is a function of both the stiffness and the amplitude of the cantilever. It was found that with traditional silicon cantilevers (with stiffness of order 10 to 50 N/m) that if the oscillation amplitude was reduced to the same order as the range of the short-range chemical force then the oscillator would not have sufficient energy to retract from the surface and a so-called “jump to contact” event would occur, most likely damaging the tip and/or the surface. Therefore, much stiffer cantilevers were required, the preferred choice for which became a quartz tuning fork, usually with one of the prongs glued down [65]. Commercial quartz tuning forks in this configuration typically have stiffnesses on the order of 1800 N/m [67]. The use of quartz tuning forks, rather than micromachined silicon cantilevers also has a number of secondary advantages. First, the choice of tip material is somewhat arbitrary as any material that can be successfully glued to the end of the prong may in principle be used as a tip [51, 74]. Second, as with other piezoelectric cantilever systems, there is no need for a laser deflection, or laser interferometry, detection system. The deflection of the cantilever may be measured directly via the piezoelectric effect associated with deflection

of the tuning fork. Third, the ability to monitor the tunnel current between the tip and the surface (if a bias is applied and the substrate is conducting) is greatly enhanced, not only because the arbitrary choice of tip material makes it easier to use purely conductive tips, but the measured average tunnel current for an oscillating tip is given by [57]

$$\langle I_t(z, A) \rangle \approx \frac{I_t(z, 0)}{\sqrt{4\pi\kappa_t A}}, \quad (2.37)$$

i.e. proportional to one over the square root of the amplitude. Therefore the use of much smaller oscillation amplitudes produces a proportional increase in the tunnel current signal observed.

2.3.8 Contact potential difference/Kelvin probe force microscopy

Thus far we have only considered the most simple case where the only forces between the tip and the surface are the van der Waals and the short-range repulsive and chemical forces. However, in general, due to differences in mate-

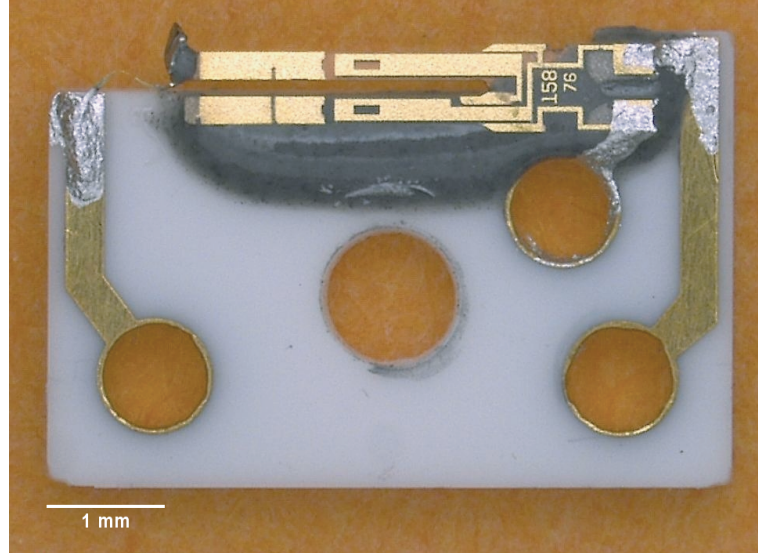


Figure 2.12: Photograph of qPlus sensor design take from [84]. This sensor setup is similar, though not identical to that implemented in the Omicron qPlus system used to acquire results for this thesis.

rial or crystallographic orientation there may be a difference between the work function of the tip and the surface. This difference can give rise to a long range electrostatic force [70]:

$$F_{ES}(z) = -\frac{\pi\epsilon_0 R U^2}{z}, \quad (2.38)$$

where R is the radius of the (spherical) tip, U is the potential between tip and sample and ϵ_0 is the permittivity of free space.

In the case of purely topographic imaging, this force can be minimised by applying a bias to the tip. Typically a so-called “voltage spectroscopy” point is taken, where a measure of the variation of the frequency shift over a range of voltages is plotted. To minimise the contact potential difference (CPD) the bias on the tip is then set to the maximum in the parabola, i.e. the point in voltage space where the frequency shift is minimised - see Fig. 2.13

However, in the case of a spatially inhomogeneous sample (e.g. due to areas of different material, or orientation, or due to defects) the contact potential difference may vary over the surface. In simple terms, this means that the force profile between the tip and the surface is not the same for the different regions of the surface. This means that the profile of constant force gradient taken by the AFM may not in general be the same as the “purely topographic” profile [57]. It has also been shown that the contact potential can vary down to the atomic scale [71] and although the differences on this scale may be small,

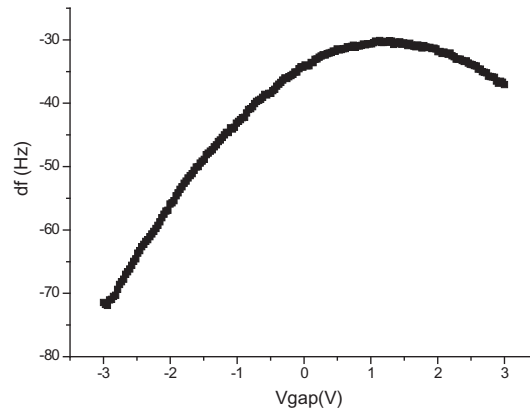


Figure 2.13: Example of a $df(V)$ voltage spectroscopy measurement. In this case the contact potential difference is approximately +1.2V.

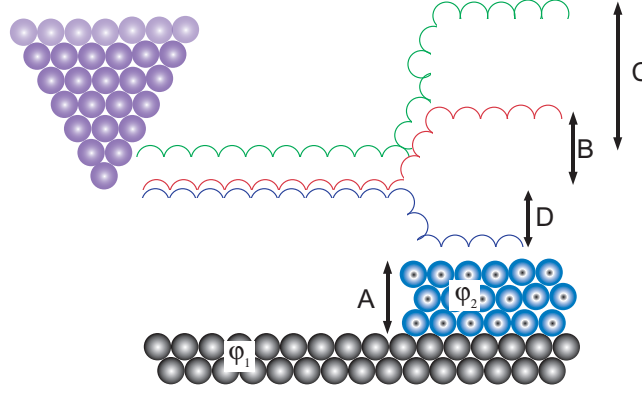


Figure 2.14: Schematic showing how an inappropriate choice of bias voltage can adversely affect topographic imaging during NC-AFM when scanning over regions of a sample with different work functions. The topographic feature has height A, and if we choose a contact potential difference such that the frequency shift is the same over both regions we recover this accurately (trace B). If the tip bias is chosen incorrectly the topography may be exaggerated (trace C) or we may even experience contrast inversion (trace D).

they can still have a strong effect on the imaging process. There are two main approaches to this issue. The first, applicable to one or two phase systems, is to apply a tip bias at the voltage that produces the same frequency shift for both areas of the surface. Therefore, although the electrostatic force still affects the scan, and may reduce spatial resolution, the effect of the force is the same on both regions of the sample. As such the measured profile should correspond more accurately to the actual topography of the surface. A more sophisticated technique (and absolutely necessary for height measurements on a three (or more) phase system [85]) is so-called Kelvin probe force microscopy (KPFM) [30].

The concept of measuring the contact potential of the surface with a probe had previously been introduced [86]. However, implementing it as a real-time detection/correction mechanism to be run in parallel with conventional NC-AFM is significantly more complicated [30]. In Kelvin probe force microscopy, an additional feedback loop is introduced - see Fig. 2.11 - and a small “dither voltage” is applied to the tip, typically at a higher harmonic of the cantilever’s resonant frequency [87] (although a range of frequencies can be used). A lock-

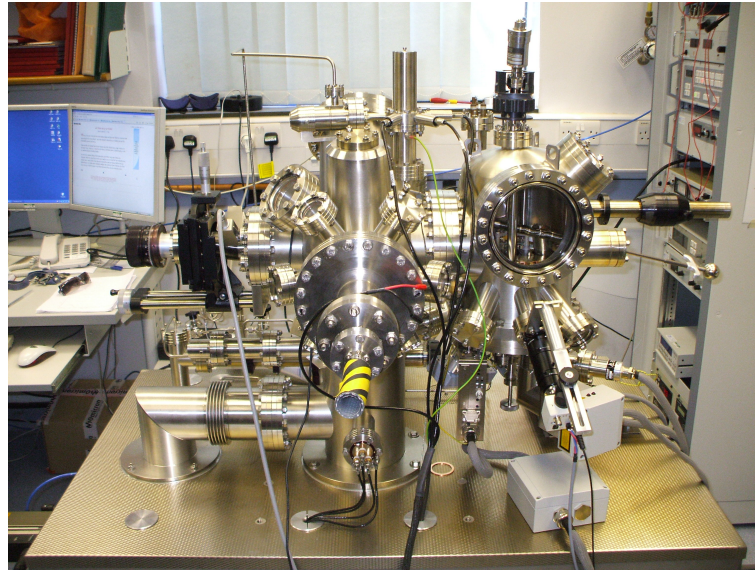


Figure 2.15: Photograph of the Omicron VT STM/AFM used during investigation of the spun cast nanoparticle networks.

in amplifier is used to monitor the deflection of the cantilever, and detect any variation in the resonant frequency (either by amplitude modulation or frequency modulation techniques) *specifically* as a result of the application of the dither voltage. A feedback loop then modifies the DC offset of the dither voltage so as to minimise the frequency shift modulation detected. Thus, as the tip scans over the surface, the bias voltage applied to the tip is constantly changing. If a region is scanned with a different contact potential difference, then the measured frequency shift due to the dither voltage will increase and the feedback loop will change the bias voltage to compensate. The bias voltage applied is recorded as a separate signal path and produces the ‘Kelvin’ image. As such, in addition to allowing accurate topographic measurements over compositionally inhomogeneous surfaces, this technique also provides a simultaneous map of the contact potential difference of the surface. Fig. 2.14 shows a schematic representation of how the electrostatic contribution due to varying contact potential can interfere with topographic imaging.

2.4 Equipment summary

In this section a brief description of the specific SPM instruments used to acquire the results presented in this thesis is given. We note their primary capabilities and which results were acquired with each system.

2.4.1 Omicron VT STM/AFM

The Omicron variable temperature scanning tunnelling microscope/atomic force microscope (VT STM/AFM) is a compact commercial UHV instrument used during the investigation of the spun cast nanoparticle networks in this work (see Fig. 2.15 and 2.16). The chamber is usually pumped by a single ion pump with a titanium sublimation pump (TSP), with the option of roughing the chamber with a rotary pump/turbo molecular pump combination during bake out and/or the introduction of noble gases. The head itself allows conventional etched tungsten wire STM tips, and conventional micromachined silicon cantilevers to be mounted. Via a system of complex sample plate designs, the head itself allows a wide range of temperatures to be accessed during scanning. Use of a liquid helium flow cryostat, and the combination of indirect and direct heating, allows temperatures between 25 Kelvin and 1200 Kelvin to be accessed (although it should be noted not on the same sample, without removing it from vacuum and switching sample plate type). In addition, the chamber is equipped to deposit organic molecules, C₆₀, or silver, and has an argon sputter gun that can be used for tip preparation. The manipulator arm also has the facility for both direct and indirect sample heating to over 1200 Kelvin. In the course of the experiments contained in this thesis only the conventional AFM aspects of the instrument was used. No variable temperature work was carried out and no in situ-deposition took place.

2.4.2 Omicron LT STM/AFM

The Omicron low-temperature qPlus AFM/STM is another commercial UHV instrument used primarily in the investigation of the Si(100) substrate and C₆₀ absorbed on the Si(100) substrate. The instrument comprises two sepa-

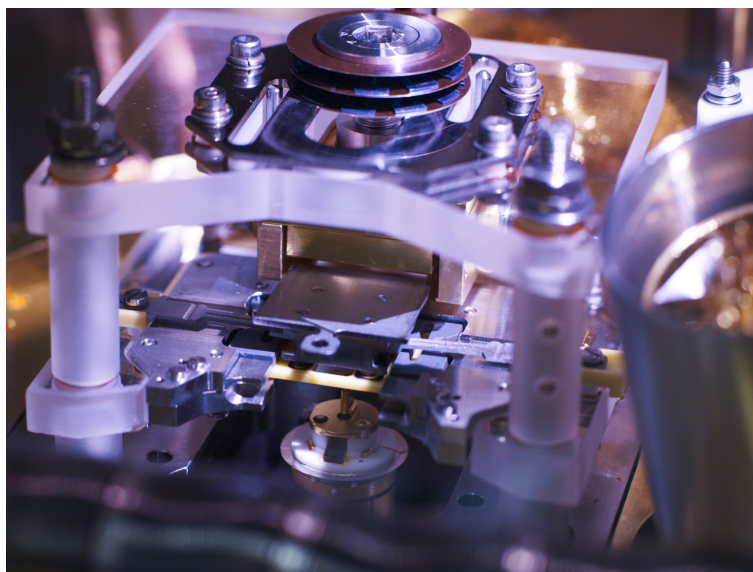


Figure 2.16: Photograph of the VT STM/AFM head. Note that in this image an STM tip is mounted rather than in AFM cantilever.

rate vacuum chambers connected via a gate valve (see Fig. 2.17 and 2.18). On the left of Fig. 2.17 is the preparation chamber which is equipped to allow deposition of C_{60} and silver. It also has a variety of complementary surface science analytical tools available including a XPS/UPS analyser and a LEED system for checking surface reconstructions. The manipulator arm also allows both direct and indirect heating for the preparation of samples and the cryogenic cooling of samples during investigation with the other instruments. To the right of Fig. 2.17 is the chamber containing the STM head. The instrument is surrounded by a two-stage bath cryostat, allowing temperatures down to 5 Kelvin to be reached. The outer “jacket” cryostat is filled with liquid nitrogen and the inner cryostat may be filled either with liquid helium or liquid nitrogen. Throughout the course of experiments the cryostat was filled exclusively with liquid nitrogen – therefore all results were taken at 77 K. The head itself (shown in Fig. 2.18) is a combination STM/qPlus AFM allowing both standard tungsten wire STM tips, and qPlus AFM tips to be loaded. Since the qPlus tips used have electrochemically etched tungsten wires glued to the quartz tuning forks, all of the STM images presented were in fact taken using qPlus tips in STM mode. As with the VT system, both chambers were

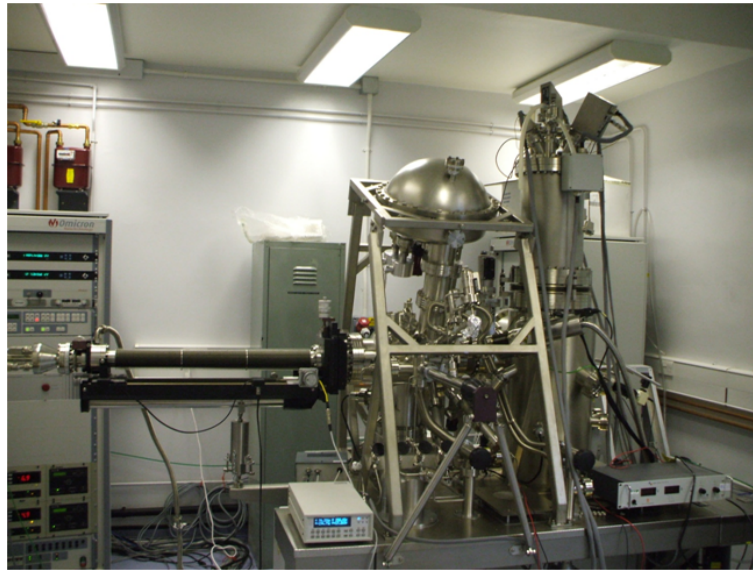


Figure 2.17: Photograph of the Omicron LT system used during investigation of the Si(100) surface.

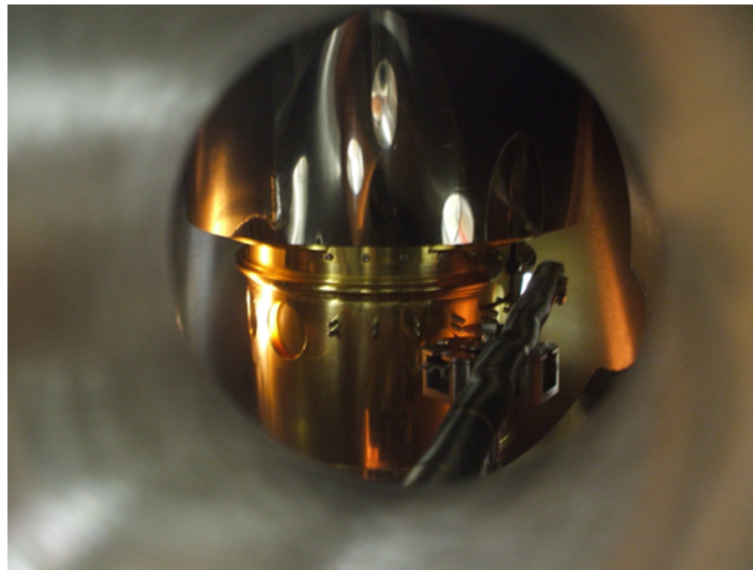


Figure 2.18: Photograph inside the chamber of the LT system showing the heat shields of the cryostat that surround the STM/AFM head during normal low-temperature operation.

pumped with combination of ion pumps and TSPs, with the option for rotary and turbo molecular pumping.

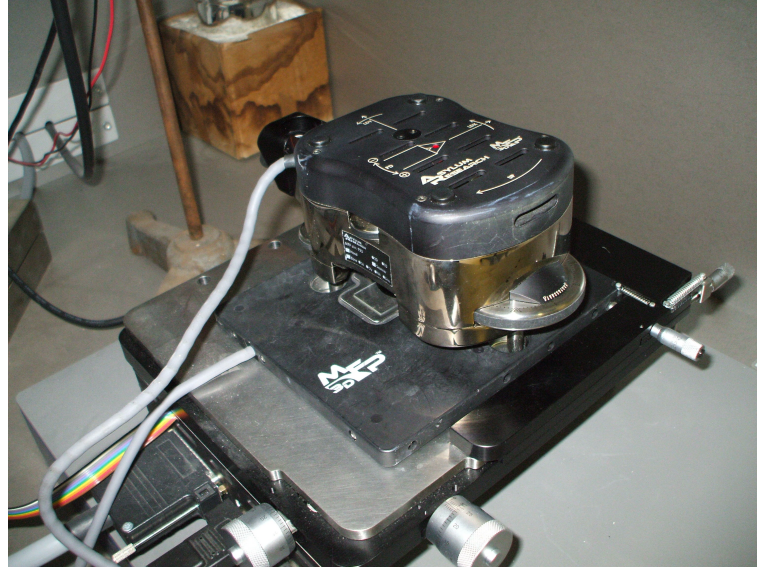


Figure 2.19: Photograph of the Asylum system MFP 3D AFM unit used to obtain images of nanoparticle networks in ambient conditions.

2.4.3 Omicron VT/Kelvin probe AFM

This instrument (located at the CEA in Grenoble, France) is at its core identical to the Omicron VT AFM detailed above. Although it has significant additions on the other chambers, with a variety of other analytical techniques, and dedicated prep. chamber. The key difference is that the AFM head itself is set up to perform Kelvin probe measurements. In all other ways, it is functionally identical to the VT AFM. All Kelvin probe work presented was carried out on this instrument.

2.4.4 Asylum research AFM

The Asylum research MFP3D AFM is a commercial ambient environment instrument capable of operating in contact mode, tapping mode, and amplitude modulated noncontact modes. Although set up to provide an extremely diverse range of scanning probe experiments (including indentation, electrical lithography, conductivity and force measurements) in this case the instrument was exclusively used to perform tapping mode and noncontact imaging of nanoparticle samples in atmosphere.

Chapter 3

Electrokinetic manipulation of particles in solution

“The difference between what the most and the least learned people know is inexpressibly trivial in relation to that which is unknown.”

Albert Einstein

In this chapter we introduce and explore the phenomena of dielectrophoresis and alternating current electroosmosis, and how they relate to the self assembly of conducting microwires from solution under the influence of strong inhomogeneous electric fields

3.1 Introduction

The ability to accurately control particles in solution, from millimetre sized beads down to particles of just a few nanometres, is a long-standing [88], but still incredibly vibrant, field of research. Although many groundbreaking experiments in the field were first conducted in the middle of the 20th century [89], in many ways it was the surge of interest in nanophysics during the early 90s which kickstarted a new wave of research devoted to developing methods for accurately controlling sub-micron particles in solution using electric fields [90]. One specific area of research which attracted a great deal of attention was the manipulation of metallic colloidal solutions. The discovery

that such solutions could be made to form complex self organised fractal structures that were both conducting and self repairing simply via the application of high electrical fields generated a great deal of interest [91]. However, it is only very recently that a detailed understanding of some of the key mechanisms that govern the formation of these structures has been obtained [92,93]. A key difficulty in understanding this phenomenon (and electrically controlled particle dynamics in fluidic environments in general) is that the events take place in regions of a parameter space where several competing forces overlap, and, in many cases, where the exact dynamics of each individual force are not well understood. This rich interplay between different competing effects produces a fascinating panoply of phenomena, but makes quantitative interpretation of results exceedingly difficult.

It is therefore necessary to begin with a review of the key forces present in these types of experiments. For a comprehensive overview, however, the reader is directed to a number of books and review texts [94,95] that cover much of the work detailed in this overview in much greater detail.

3.2 Dielectrophoresis (DEP)

The manipulation of matter using electric fields has long been of scientific interest (see for example Priestley [96]), as have the more specific effects of inhomogeneous electric fields on neutral matter. However it was not until the pioneering work of Pohl in the 1950's [88,89] that a detailed study of the effect of inhomogeneous electric fields on particulate motion was undertaken. Pohl coined the term *dielectrophoresis* to describe the particulate motion he observed and went on to describe the defining characteristics of the phenomenon. Work using dielectrophoresis to manipulate and separate particles and biological specimens has progressed steadily since Pohl's original observations, but interest in the phenomenon has seen a recent resurgence with respect to applying the technique to the manipulation of nanoscale particles and structures. Advances in the technique now allow for the trapping of single nanoparticles [97], as well as the assembly of micro and nanoscale structures [37,98,99].

3.2.1 Theoretical overview

Before engaging in an overview of the theory behind DEP it is worth defining the phenomenon so as not to confuse it with a multitude of similar (and often related) phenomena. Technically it may be thought of as the induced motion of particles due to the influence of an inhomogeneous electric field. However it is also worth noting the phenomenological definitions from [94], which may be summarised as:

1. Particles experience DEP only when the electric field is non-uniform.
2. The DEP force does not depend on the polarity of the electric field and thus is observed with AC and DC excitations (corresponding to time varying and constant fields)
3. Particles are attracted to regions of stronger electric field when their permittivity, ϵ_2 , exceeds that of the suspension medium, ϵ_1 .
4. Particles are repelled from regions of stronger electric field when $\epsilon_2 < \epsilon_1$.
5. The DEP force acts on uncharged particles - it only requires that the particles may be polarised

With these caveats it is possible to separate the DEP force from effects such as the electrophoretic (EP) force (which only acts on particles with a net charge) in situations where they are both present.

Force on an infinitesimal dipole

The DEP force is the result of the effect of an inhomogeneous electric field on the dipole moment of a particle. Usually this dipole is induced as a result of the electric field. In this section we will look at the derivation of this force and some of the key approximations made. Following the method in Jones [94], we will start by examining the force of an electric field on a infinitesimal dipole.

We consider a dipole of equal and opposite charges $+q$ and $-q$ separated by a vector distance \mathbf{d} and resident in an electric field \mathbf{E} . We make the approximation that the dipole itself does not contribute to the field.

If the field is uniform the only force on the dipole is a torque (see Fig. 3.1). This torque is given by

$$\mathbf{T}^e = \frac{\mathbf{d}}{2} \times q\mathbf{E} + \frac{-\mathbf{d}}{2} \times (-q\mathbf{E}) = q\mathbf{d} \times \mathbf{E}, \quad (3.1)$$

where \mathbf{d} is the vector distance between the charges, q is the charge on each end of the dipole, and \mathbf{E} is the electric field. Using $\mathbf{p} = q\mathbf{d}$, where \mathbf{p} is the vector dipole, gives us

$$\mathbf{T}^e = \mathbf{p} \times \mathbf{E}. \quad (3.2)$$

Note that in this situation there is no overall net force on the dipole.

In the case of an *inhomogeneous* electric field the situation is more complicated. The two charges experience different values of \mathbf{E} . By reference to Fig. 3.2 we can see that the force will be given by

$$\mathbf{F} = q\mathbf{E}(\mathbf{r} + \mathbf{d}) - q\mathbf{E}(\mathbf{r}), \quad (3.3)$$

where \mathbf{r} is the vector position of $-q$ (see Fig. 3.2).

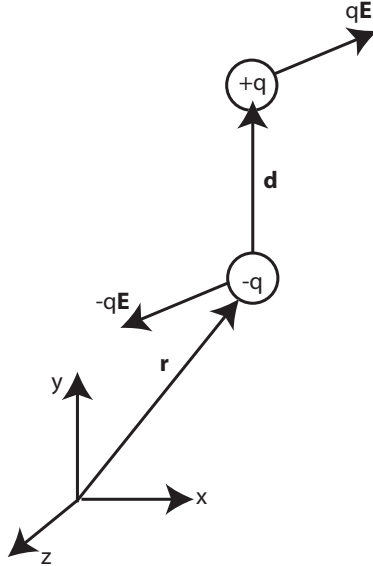


Figure 3.1: Representation of the torque on a small dipole in a uniform electric field

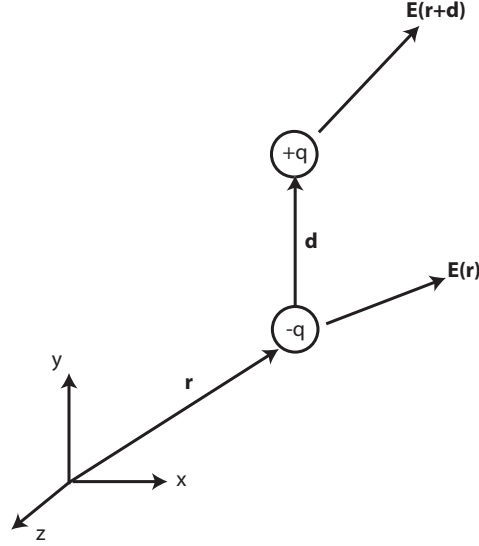


Figure 3.2: Representation of the net force on a small dipole in a nonuniform electric field

If $|\mathbf{d}|$ is small compared to the characteristic length scale of the variation in the electric field then Eqn. 3.3 may be simplified by expanding the expression for the electric field around position \mathbf{r} in the form of a Taylor series and neglecting the higher order terms, i.e.

$$\mathbf{E}(\mathbf{r} + \mathbf{d}) = \mathbf{E}(\mathbf{r}) + \mathbf{d} \cdot \nabla \mathbf{E}(\mathbf{r}) + \dots \quad (3.4)$$

This gives us an expression for the force

$$\mathbf{F} = q\mathbf{d} \cdot \nabla \mathbf{E} + \dots \quad (3.5)$$

Then, in the limit $d \rightarrow 0$ (taking limits to avoid the zero sum limit), we acquire the force on a infinitesimal dipole as

$$\mathbf{F}_{dipole} = \mathbf{p} \cdot \nabla \mathbf{E}. \quad (3.6)$$

However, as noted at the start of the derivation, no attention has been paid to the nature of the dipole. Molecular dipoles may either be permanent (e.g. as for the case for H_2O) or may be induced in the molecule/colloid by the electric

field itself. DEP phenomena are usually concerned with the induced case (though by no means exclusively, and in fact the case of a molecule with both permanent and induced dipole moments is itself of great interest). Therefore, it is worth briefly considering how the effective dipole moment method (see Jones [94]) for evaluating \mathbf{p} works, and in which situations it is valid.

3.2.2 Effective dipole moment method

Again, following the method of Jones [94] we consider a particle suspended in a dielectric fluid. If we impose a uniform electric field on the system, the particle will become polarized by the field - and so a moment is induced across it. This effective dipole moment is aligned parallel to the field and is defined as “the moment of an equivalent, free-charge, point dipole that, when immersed in the same dielectric liquid and positioned at the same location as the center of the original particle, produces the same dipolar electrostatic potential” [94].

From basic electrostatics we know that the electrostatic potential function ϕ_{dipole} due to an effective point dipole of moment \mathbf{p}_{eff} in a dielectric medium of permittivity ϵ_1 is

$$\phi_{dipole} = \frac{p_{eff} \cos \theta}{4\pi\epsilon_1 r^2}, \quad (3.7)$$

where θ and r are the polar angle and radial position. Note that in this chapter we will use ϕ to represent potentials where they are functions of other variables (as in this case), and V to represent potentials when they are applied externally to the system (e.g. from a battery or signal generator).

Calculating the value of this effective dipole moment (and hence the force on a particle) is far from trivial, and varies depending on the type of particle and time modulation of the field. For brevity, the working for three key cases are summarised below. A more detailed analysis (and working for a multitude of further cases) is presented in both Jones [94] and Pohl [88].

Effective dipole moment of dielectric sphere in dielectric medium for a static applied field

We consider a dielectric sphere of radius R and permittivity ϵ_2 , that is suspended in a dielectric fluid with permittivity ϵ_1 , and subject to a *uniform* electric field E_0 . We make the assumption that there is no free charge in the system and that the presence of the particle does not disturb the source of E_0 . Since we have defined a uniform field with no free charges, we are able to use Laplace's equation, and thus we can take assumed solutions for the potential inside and outside the sphere to have the form

$$\Phi_1(r, \theta) = -E_0 r \cos \theta + \frac{A \cos \theta}{r^2}, r > R, \quad (3.8)$$

and

$$\Phi_2(r, \theta) = -Br \cos \theta, r < R, \quad (3.9)$$

where A and B are coefficients to be determined from the boundary conditions (see later working).

In Eqn. 3.8, we note that the first term may be interpreted as being the potential due to the imposed electric field, while the second term is the effect of the induced dipole from the particle. Following standard electromagnetic principles we apply boundary conditions at $r = R$. We note that both the electrostatic potential and the normal component of the displacement flux vector must be continuous across the boundary - i.e.

$$\Phi_1(r = R, \theta) = \Phi_2(r = R, \theta), \quad (3.10)$$

and

$$\epsilon_1 E_{r1}(r = R, \theta) = \epsilon_2 E_{r2}(r = R, \theta). \quad (3.11)$$

Substituting these boundary conditions into Equations 3.8 and 3.9, we obtain the coefficients A and B as

$$A = \frac{\epsilon_2 - \epsilon_1}{\epsilon_2 + 2\epsilon_1} R^3 E_0, \quad (3.12)$$

and

$$B = \frac{3\epsilon_1}{\epsilon_2 + 2\epsilon_1} E_0. \quad (3.13)$$

Now if we compare the equation for the potential from a dipole (Equation 3.7) to the second term in the assumed solution for the potential (Equation 3.8), we can infer that

$$p_{eff} = 4\pi\epsilon_1 A, \quad (3.14)$$

and making the substitution

$$\frac{\epsilon_2 - \epsilon_1}{\epsilon_2 + 2\epsilon_1} = K(\epsilon_2, \epsilon_1), \quad (3.15)$$

where K is known as the Clausius-Mossotti function, we obtain (for the case under consideration, i.e. for the homogeneous dielectric sphere in a dielectric medium)

$$p_{eff} = 4\pi\epsilon_1 K R^3 E_0. \quad (3.16)$$

Note that K is usually interpreted as providing a measure of the strength of the effective polarization of the spherical sphere as a function of ϵ_1 and ϵ_2 [94]. However, as we shall see, the form of K varies from system to system - and, as such, obtaining K is often the key to predicting the behaviour of particles in a given case.

Effective dipole moment of conducting sphere in conducting medium for a static applied field

For the case of a conducting sphere (in a medium with finite conductivity), we consider both particle and fluid to have finite conductivities σ_1 and σ_2 . We may follow the same method as above but must change the boundary conditions at $r = R$ so that the continuous nature of the displacement flux vector is expressed by

$$\sigma_1 E_{r1}(r = R, \theta) = \sigma_2 E_{r2}(r = R, \theta). \quad (3.17)$$

Performing the same substitution as for the dielectric sphere gives us a new expression for the Clausius-Mossotti function.

$$K(\epsilon_2, \epsilon_1) \rightarrow K(\sigma_2, \sigma_1) = \frac{\sigma_2 - \sigma_1}{\sigma_2 + 2\sigma_1}. \quad (3.18)$$

For the case of a nearly perfectly conducting sphere (or the case of a highly conducting sphere in a dielectric medium) we are in the limit of Equation 3.18 such that $K \rightarrow 1$, giving us a maximum value for the effective dipole.

$$p_{eff} \rightarrow p_0 = 4\pi\epsilon_1 R^3 E_0. \quad (3.19)$$

Effective dipole moment of homogeneous sphere in dielectric medium for a time varying applied field

As before, we consider a particle suspended in a fluid. In this case, however, the particle is no longer ideal and exhibits ohmic loss. We consider both particle and fluid to have finite conductivities σ_1 and σ_2 (in addition to ϵ_1 and ϵ_2), and the applied field is now generated by an applied AC excitation of peak magnitude E_0 , unit vector \hat{z} , angular frequency ω , i.e.

$$\mathbf{E}(t) = \text{Re}[E_0 \hat{z} \exp(i\omega t)]. \quad (3.20)$$

As such we need to make the coefficients A and B complex, and modify the boundary condition at $r = R$ to take into account the time dependent accumulation of free electrical charge (i.e. Laplace's equation is no longer applicable). As such we replace Eqn. 3.11 with a charge continuity condition:

$$J_{r1} - J_{r2} + \frac{\partial \sigma_f}{\partial t} = 0, r = R, \quad (3.21)$$

where J_{r1} and J_{r2} are the normal components of the ohmic current outside and inside the dielectric sphere. Note that σ_f is the free electric surface charge and is defined as

$$\sigma_f = \epsilon_1 E_{r1} - \epsilon_2 E_{r2}, r = R. \quad (3.22)$$

Since we assume that the only time varying quantity in the system is the

applied excitation (and hence the electric field strength) we may assume an (imaginary) exponential time dependence for all variables, and make the assumption that $\partial/\partial t \rightarrow i\omega$. This allows us to express the new boundary condition for the normal field components in terms of complex vector phasors [94]

$$\underline{\epsilon}_1 \underline{E}_{r1} = \underline{\epsilon}_2 \underline{E}_{r2} \quad (3.23)$$

where $\underline{\epsilon}_1$ and $\underline{\epsilon}_2$ are the complex dielectric constants defined as $\underline{\epsilon}_x = \epsilon_x + \sigma_x/i\omega$

and the coefficients A and B are found to be

$$\underline{A} = \frac{\underline{\epsilon}_2 - \underline{\epsilon}_1}{\underline{\epsilon}_2 + 2\underline{\epsilon}_1} R^3 E_0, \quad (3.24)$$

and

$$\underline{B} = \frac{3\underline{\epsilon}_1}{\underline{\epsilon}_2 + 2\underline{\epsilon}_1} E_0, \quad (3.25)$$

by the same method as before.

The key result here is that the solutions have essentially the same form as for the steady state, but we are now forced to use the complex forms for the permittivities and electric field. This work leads us to more general forms for the Clausius - Mossotti function and the effective dipole moment, respectively

$$\underline{K}(\underline{\epsilon}_2, \underline{\epsilon}_1) = \frac{\underline{\epsilon}_2 - \underline{\epsilon}_1}{\underline{\epsilon}_2 + 2\underline{\epsilon}_1}, \quad (3.26)$$

and

$$\underline{\overline{P}}_{eff} = 4\pi\epsilon_1 \underline{K} R^3 \underline{\overline{E}}_0. \quad (3.27)$$

3.2.3 Calculation of DEP force

Substituting the expression we have for the effective dipole moment of a particle in an homogeneous electric field into the force of an inhomogeneous field on a infinitesimal dipole gives us a basic expression for the DEP force on the particle

$$\mathbf{F}_{DEP} = 2\pi\epsilon_1 R^3 K \nabla E_0^2. \quad (3.28)$$

An important approximation must be noted at this stage. We have calculated the effective dipole based on the application of a spatially homogeneous (though time varying) electric field, but our expression for the force on a dipole explicitly requires an inhomogeneous field to induce a force. We find [94] that this approximation is valid in the case where the characteristic scale of the inhomogeneities in the field are small compared to the size of the dipole. This is not strictly true for many nanoscale situations, and so in these cases it is necessary to include higher order terms in the derivations in order to obtain an accurate result. Nonetheless, a good understanding of the basic processes involved can be reached from this approximation, so here we continue the derivation again following Jones [94].

From Eqn. 3.28 we can infer that the behaviour of \mathbf{F}_{DEP} is

1. Proportional to the volume of the particle.
2. Proportional to the dielectric permittivity of the medium in which the particle is suspended.
3. Directed along the gradient of electric field intensity.
4. Proportional to the magnitude of K and is directionally dependent on the sign of K .

As noted before, it is the dependence on K that produces some of the most interesting effects in dielectrophoresis, allowing particles and biological samples to be filtered based on their dipole responses to AC fields.

The direct dependence on field gradient also produces an interesting result for practical dielectrophoresis between electrodes on a surface. From Bahaj and Bailey [100], we find a scaling law

$$|\mathbf{F}_{DEP}| = \frac{V^2}{L_e^3}, \quad (3.29)$$

where V is the applied potential across the electrodes (as opposed to Φ the electrostatic potential function), and L is the characteristic length scale of the electrode configuration.

As such, we find that to increase the DEP force we must increase the applied voltage and, *more critically*, reduce the size of the electrodes. As we will see, this scaling law allows dielectrophoresis experiments to be carried out with voltages many orders of magnitude less than those required by Pohl in his original experiments [89, 101].

3.2.4 Detail of the force dependence on K

Expanding the expression we obtained for the complex Clausius-Mossotti function (Eqn. 3.26) gives us the explicit frequency-dependent form

$$\underline{K} = \frac{\epsilon_2 - \epsilon_1 - i(\sigma_2 - \sigma_1)/\omega}{\epsilon_2 + 2\epsilon_1 - i(\sigma_2 + 2\sigma_1)/\omega}, \quad (3.30)$$

From the work of Sauer and Schlogl [102] we have a *time averaged* expression for the force on an homogeneous sphere.

$$\langle \mathbf{F}_{DEP} \rangle = 2\pi\epsilon_1 R^3 \text{Re}[\underline{K}(\omega)] \nabla E_{RMS}^2. \quad (3.31)$$

Now, taking advantage of the work of Benguigui and Lin [103], we also have an explicit expansion for the real component of K ,

$$\text{Re}[\underline{K}] = \frac{\epsilon_2 - \epsilon_1}{\epsilon_2 + 2\epsilon_1} + \frac{3(\epsilon_1\sigma_2 - \epsilon_2\sigma_1)}{\tau_{MW}(\sigma_2 + 2\sigma_1)^2(1 + \omega^2\tau_{MW}^2)}, \quad (3.32)$$

where τ_{MW} is the Maxwell-Wagner charge relaxation time. This term characterises the decay of a dipolar distribution of free charge at the surface of the sphere. It is defined as [94]

$$\tau_{MW} = \frac{\epsilon_2 + \epsilon_1}{\sigma_2 + 2\sigma_1}. \quad (3.33)$$

The key result we extract from this is the general behaviour of $\text{Re}[\underline{K}]$ as the electric field frequency is varied. From Jones [94], the limits are

$$\text{Re}[\underline{K}] \rightarrow \begin{cases} \frac{\sigma_2 - \sigma_1}{\sigma_2 + 2\sigma_1}, & \text{for } \omega\tau_{MW} \ll 1 \\ \frac{\epsilon_2 - \epsilon_1}{\epsilon_2 + 2\epsilon_1}, & \text{for } \omega\tau_{MW} \gg 1. \end{cases} \quad (3.34)$$

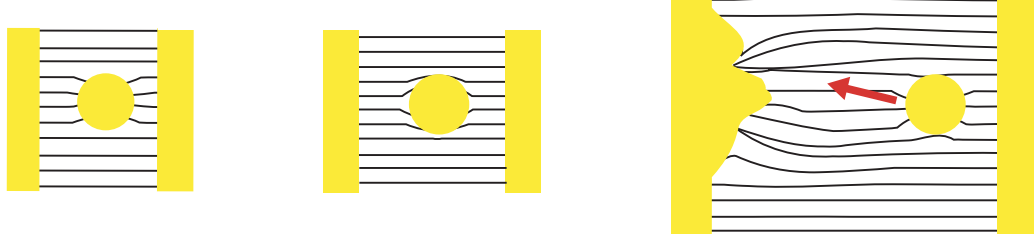


Figure 3.3: Interactions of different particles with electric fields.. From left to right – a conducting particle in a uniform field, an insulating particle in a uniform field, a conducting particle in an inhomogeneous field. Note that for the conducting particle in a inhomogeneous field the result of the DEP force is that it will be drawn towards regions of higher field intensity.

In these limits it is easier to see the effect of frequency on the DEP force. DC conduction dominates in the low frequency regime, while the dielectric polarisation dominates at high frequencies. The ratios of ϵ_1/ϵ_2 and σ_1/σ_2 determine whether the F_{DEP} is positive or negative. For instance, in the case where $\epsilon_1 > \epsilon_2$ and $\sigma_1 < \sigma_2$, $Re[\underline{K}]$ is positive at low frequencies and negative at high frequencies, and vice versa. Since F_{DEP} depends on the sign and magnitude of $Re[\underline{K}]$, this directly influences F_{DEP} 's magnitude and direction. This frequency dependence is especially useful for separating particles, as a slight variation in the dielectric permittivity can allow otherwise similar particles to have differing forces applied to them. For metallic nanoparticles (in water), of the type used in this thesis, the crossover frequency from positive to negative DEP has been shown to be on the order of several GHz [92], even when the effect of salt in the solution and the reduced conductivity of the particles due to plasmon effects have been taken into account. Therefore we expect for the frequency range investigated that the DEP force will be uniformly positive (i.e. $K \sim 1$) during our investigation. Fig. 3.3 shows the effect of spheres of different permittivities in homogeneous and inhomogeneous electric fields.

This short review was designed to outline the key variables for understanding dielectrophoresis. By necessity, it has not expanded on the more com-

plicated scenarios (such as layered particles, or nanoscale dielectrophoresis), although, as we will see, both these topics will need to be engaged with on some level to understand the current and future experimental work.

3.3 Electrokinetic effects

Although Hermansen et al [37] generated a great deal of interest in the area of dielectrophoretically assembled metallic nanoparticles [91], with the benefit of hindsight it is odd that there was no attempt in this paper, or in much of the subsequent literature, to address the role of forces other than DEP in the formation of the structures observed. It was not until 2007 [92, 93] that the first literature emerged that directly addressed these points. This is in many ways surprising because, while these forces are undoubtedly complex, the interplay between dielectrophoresis and various other factors had been commented on in related earlier papers [104]. As we shall see, one of the key phenomena in understanding the formation of these nanoparticle structures is so-called alternating current electroosmosis (ACEO).

Phenomena related to ACEO were first noted and described in 1999 [104] during experiments on latex particles in KCl solution. But it was not until 2002 [105–107] that what might be considered a full theory of the phenomenon was presented in the literature. Perhaps one reason for this is the key dependence on the variations in the electric double layer on both field strength and frequency of applied field [95]. The dynamics of the double layer is a complex and fascinating subject, and understanding the phenomenon is made even more difficult by the comparative dearth of literature dealing with its variation at high frequency. Here we will present a brief overview of the key concepts surrounding the double layer formation, before looking at the background literature surrounding AC electroosmosis.

3.3.1 Electrical double layer

The electrical double layer is a complex phenomenon about which a considerable number of detailed review texts have been written [95, 108–111]. It plays

a key role in the understanding of the electrokinetic behaviour of fluids and colloidal suspensions. Understanding how the double layer is modified under the application of an electric field, and how this in turn alters the polarisation of both electrodes and particles in the solution, is vital to understanding a number of important phenomena. In this section, a brief description of the electrical double layer is given along with an overview of some of the key theoretical and experimental considerations necessary to understand the experimental methodology.

Excluding certain specially prepared experimental situations, any surface will carry a net charge due to the absorption of ions or molecules, or the disassociation of chemical groups at the surface [108]. As such, in general, a surface will have a certain electrostatic surface potential, ϕ_0 , at the interface. If the surface is then immersed in a liquid electrolyte, the potential will attract ions of opposite charge (counterions) and repel ions of like charge (co-ions). In general, charges in the solution will move to screen any overall surface charge, i.e. bulk electro-neutrality is maintained and any surface charge is balanced by an equal and opposite number of excess charges in the double layer that surrounds it. This means that any surface immersed in the electrolyte will be surrounded by a region of liquid with a higher concentration of ions than the bulk. It is this region that is known as the double layer.

The theory dealing with the structure of the double layer is both complicated and, to an extent, still incomplete, especially with regard to large applied potentials [112]. However, a simplified understanding of the double layer structure is helpful in gaining an understanding of its behaviour. In the most simple case, the double layer may be split into two distinct regions. Far away from the surface there is a layer of loosely bound ions screening the charge from the bulk of the solution; this is known as the diffuse layer. However, there is also a thin region between the surface and the diffuse layer containing a region of relatively tightly bound counter ions, normally referred to as the Stern layer [95]. This region may only be one or two solvated ion radii thick, and in this region it is assumed the potential falls linearly with distance from the surface. In contrast, the potential across the diffuse layer decays exponentially with the characteristic length scale given by the Debye length κ^{-1} .

It should be noted that the Stern layer itself may be subdivided into two regions [95], roughly divided between ions that have specifically adsorbed onto the surface, and those that remain hydrated in the solution but tightly bound. However, unusually high charge movement in the Stern layer has been observed despite its apparently fixed nature and has been interpreted as being due to differences in mobility between solvent molecules and low molecular weight ions [111]. For the purposes of our discussion, however, it is sufficient to consider the Stern layer as a collection of more tightly bound ions near to the surface and the diffuse layer as a thicker, but more loosely bound, cloud of ions further away.

3.3.2 Electric polarisation

The result of this charge accumulation at the interface between the surface and the electrolyte is that the system behaves as a capacitor with a nonuniform charge density (potential across the diffuse layer decays exponentially). If a constant potential is applied to the electrode, the result is a change in the charge distribution, which may be considered to be similar to the charging of a capacitor, and, as such, is referred to as the electrode polarisation [95]. The consequence of this in the static case is that most of the applied potential is dropped across the double layer so that in the bulk electrolyte the potential may be very different to that applied to the electrode. If we consider the double layer as a simple capacitor, with capacitance C , in series with the DC impedance of the double layer and the overall reactance of the bulk, then, as the frequency drops to zero (i.e. a DC potential) so the reactance of the double layer tends to infinity and the potential is completely screened from the bulk electrolyte. This can have important effects on electrophoretic manipulation, as it means that, in general, the electrical potential experienced by the bulk of the solution (and therefore particles contained in the bulk solution) is not uniform with varying frequency. This, however, ignores the phenomenon of electrochemical reactions [95] at the electrode surface, which, as we will see, can be extremely important, especially at low frequencies. Conversely, at high frequencies the reactance of the double layer falls to a constant value, deter-

mined by its DC resistance, and the electric field is dropped almost completely across the bulk electrolyte, in a manner determined by the bulk electrolyte properties. The transition between these two regions can give rise to a variety of interesting effects.

3.3.3 Diffuse and Stern layer capacitance

The effective capacitance of the Stern layer is comparatively easy to model, since the potential drops linearly in this region. Therefore, the Stern layer may be modelled as a simple capacitor with capacitance $C'_s = \epsilon_s/d_s$, where d_s is the width of the layer and ϵ_s the relative permittivity of the layer. However, the exponential decay of the potential in the diffuse layer means that we cannot make the same assumption. It is therefore common to define a differential capacitance for the diffuse part which is found by differentiating the Grahame equation [95, 108]. We find that

$$C'_d = \frac{d\sigma_{qd}}{d\phi_d} = \epsilon\kappa \cosh \frac{z\psi_d}{2} \quad (3.35)$$

for low surface potentials (where ψ_d is the dimensionless diffuse layer potential). However, the surface charge and potential are related by $\sigma_d = -\epsilon\kappa\phi_d$, and, therefore, the specific capacitance of the diffuse layer becomes $C'_d = \epsilon\kappa$, where we effectively consider a parallel plate capacitor of thickness κ^{-1} and dielectric permittivity $\epsilon = \epsilon_0\epsilon_r$, commonly called the integral capacitance.

Thus far we have only considered in passing the effect of frequency on the formation of the double layer. When the potential is applied to an electrode, the double layer will necessarily take a finite time to form, since we must consider both effects of diffusion and the final mobility of the ions in the solution. It follows that if we apply an alternating field, then above a certain frequency there will be insufficient time for the double layer to form before the field reverses. At low frequencies, the double layer has time to form completely and so almost all of the potential is dropped across the double layer. Conversely, at high frequencies, the double layer has no time to form at all and so the potential is dropped entirely across the bulk of the solution. Unfortunately, determining where these limiting cases occur, and what the behaviour is in

the crossover region, is nontrivial. We must also consider that, in most true microsystems, the electrodes that we advocate are not true parallel plate capacitors, and that they have a nonuniform geometry to some extent. Ramos et al [104] modelled a simple two-dimensional system as a series of distributed capacitors with values $\Delta C = \epsilon \kappa d \Delta x$ (see Fig. 3.4). The variation in values across each series circuit means that each has a different time constant, and, as a result, there is a spread in the relaxation time for the polarisation of the double layer. The potential dropped across the double layer was derived as

$$\Delta\phi_{DL} = \frac{V_0}{2 + i\omega\pi(\epsilon/\sigma)\kappa x}, \quad (3.36)$$

where V_0 is the magnitude of the potential applied to the electrodes, ω the angular frequency of the applied potential, ϵ and σ the permittivity and conductivity respectively and κ the inverse Debye length. In the derivation it was assumed that the frequency of the applied potential is much smaller than the charge relaxation frequency τ_{MW} .

A number of salient features may be taken from this simplified model. Primarily, and as previously mentioned, the potential dropped across the double layer and the potential across the bulk of the solution are frequency dependent. In addition, the potential across the bulk of the medium is complex and the potential across the electrolyte depends on the position along the electrode surface. Morgan and Green [95] have calculated the normalised potential across the electrolyte and shown that in order to achieve the maximum field in the bulk, the frequency must be higher than the inverse of the time constant given by the product RC .

3.3.4 Electroosmosis

It is well known that if an electric field is applied tangentially to a surface immersed in electrolyte, the charges in the double layer experience a force, and, as a consequence of their motion, a fluid flow is generated. The flow is considered to be zero at the surface and rises to a maximum at the slip plane (i.e. the point at which the fluid is considered to be part of the bulk solution). This is known as conventional electroosmosis, and it can be shown that for an

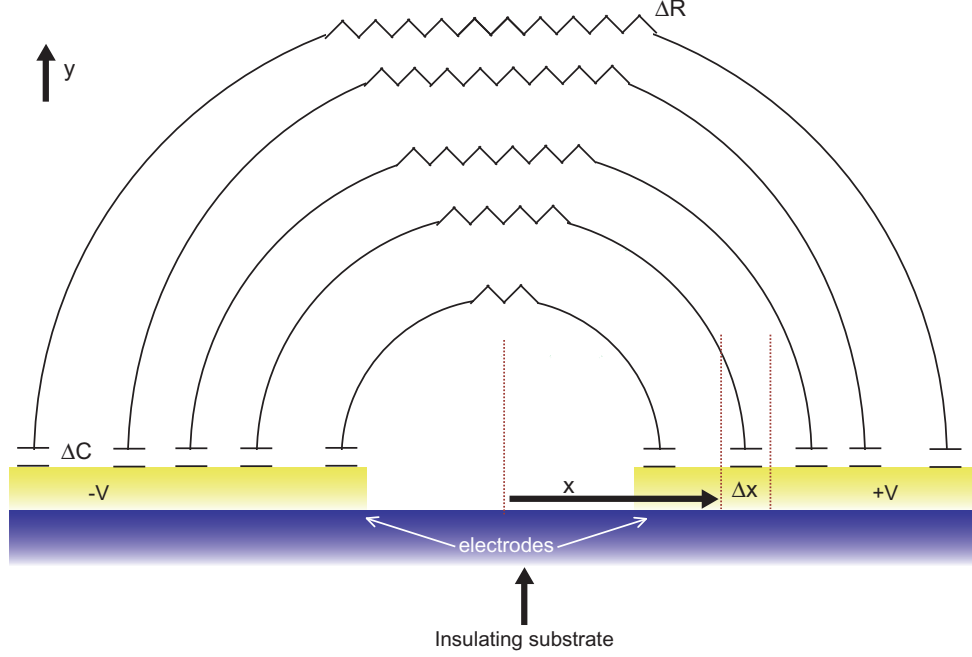


Figure 3.4: Side view of the electrode array on insulating surface (after [104]) showing Ramos et al's model treating the solution and the double layer as a series of C-R-C circuits. The effect of the double layer is represented by the capacitors while the impedance of the bulk solution is represented by the resistors.

infinitely wide two-dimensional electrode the fluid velocity is [95]

$$u_x = -E_x \frac{\epsilon \zeta}{\eta}, \quad (3.37)$$

or in terms of the conductivity of the solution

$$u_x = -\frac{E_x \sigma_q}{\kappa \eta}, \quad (3.38)$$

where η is the viscosity of the fluid and ζ the charge density (zeta potential) in the double layer i.e. the velocity of the fluid is directly proportional to the electric field and the charge density in the double layer. If we reverse the direction of the field then the fluid velocity also reverses direction. Therefore, for uniform geometry and an AC field, there will be no net (time averaged)

fluid displacement.

3.3.5 AC electroosmosis (ACEO)

Only relatively recently [104, 107] has it been recognized that electroosmosis has an AC complement, much in the same way as DEP can be considered to be an AC complement to EP. As DEP only operates when inhomogeneous electric fields are present, but works equally well under AC fields as DC fields, so AC electroosmosis only operates when there are inhomogeneous fields, and is capable of generating net time-averaged fluid flow under the application of AC fields. In this section we briefly review the current understanding of this phenomenon.

AC electroosmosis arises due to effects related to the charging of the double layer. Therefore, an understanding of the mechanism responsible for electrode polarisation is key in order to understand AC electroosmosis. This is because the polarisation process allows us to understand both the potential at the outer edge of the double layer (i.e. the tangential field) and the potential dropped across the double layer (which is related to the charge at the surface).

As we can see from Fig. 3.5 we have a set of two-dimensional electrodes with a gap between them and equal but opposite voltages applied to either side. As a result, an electric field is generated outside of the electrode with a tangential component, \mathbf{E}_t , and an induced charge on each electrode. The induced charges on the electrode experience a force, \mathbf{F}_q , due to the action of the tangential field (this is key to the phenomenon of ACEO since in a uniform geometry there is no tangential field). A key salient feature is that during the other half cycle of the applied AC potential, the direction of the tangential field *and* the sign of the induced charge invert, and, as a result, the direction of the force vector, \mathbf{F}_q , remains the same, giving a non-zero time averaged force. From the equation for DC electroosmosis, we can expect the fluid velocity close to the surface to be proportional to the tangential field and the charge in the double layer. In the setup shown in Fig. 3.5, the tangential component is proportional to the full potential dropped across the medium.

The charge in the diffuse double layer may be represented as the sum of the

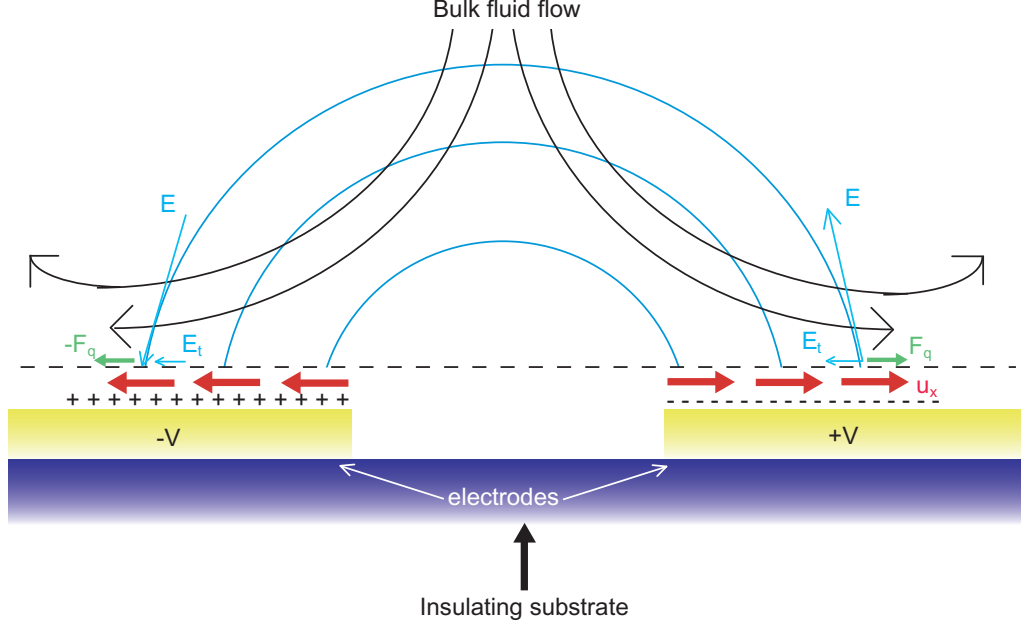


Figure 3.5: Side view of electrodes on an insulating substrate immersed in an electrolyte showing both field lines, the movement of charge and the bulk fluid flow resulting from the ACEO effect due to an inhomogeneous electric field (after [104]).

constant term and time-dependent term related to the applied electric field. From Morgan and Green [95], if we ignore the Stern layer and assume a linear approximation, the time varying charge density in the diffuse layer is

$$\sigma_q = \epsilon\kappa\phi_d. \quad (3.39)$$

This assumes that the charges are able to respond with the applied field. As we have seen, the double layer capacitance is frequency dependent, and therefore so is the AC electroosmotic flow. At low frequencies, the potential is dropped entirely across the double layer, and therefore \mathbf{E}_t is zero. Conversely, at high frequencies, the double layer is unable to respond and \mathbf{E}_t is also zero as there is no induced charge. Therefore, for AC electroosmosis, in the limiting cases of high and low frequency, we have no flow, and there is some intermediate frequency at which the flow will reach a maximum. Using a simplified

expression for the potential dropped across the double layer

$$\phi_d = \frac{V_0}{2(1 + i\Omega)}, \quad (3.40)$$

where $\Omega = (1/2)\pi\kappa x(\epsilon/\sigma)\omega$, then an expression for the time averaged fluid velocity may be derived as:

$$\langle u_x \rangle = \frac{1}{8} \frac{\epsilon\phi_0^2\Omega^2}{\eta x(1 + \Omega^2)^2}. \quad (3.41)$$

3.3.6 High frequency electrothermal flow

As previously mentioned, at high frequencies the magnitude of the AC electroosmotic flow drops to zero. However, there are additional effects that can occur at high frequencies which means that fluid flow does not drop to zero. Primarily, this is because of the so-called high frequency electrothermal flow. In general, the application of an electric field to a fluid will produce a force, but we will only see flows within the body if there are local variations in charge density. Such variations can easily occur due to inhomogeneities in the fluid - for example, from localised heating which can give rise to gradients in permittivity and conductivity. Castellanos et al. [105] and Green et al. [106] investigated these phenomena in some detail, both experimentally and theoretically, and discovered that, in general, the electric, temperature, and velocity fields are coupled. Although this force is important to be aware of, a key finding was that the observed fluid flow velocities due to the electrothermal flow are much smaller [95] than the flows due to ACEO, and so are easily distinguishable. For the experiments described in this thesis, it is not believed that electrothermal flow is an important contributing factor.

3.4 AC electrochemical effects

Although the field of electrochemistry is well-established and well understood, the classical understanding of the phenomenon is usually limited to carefully controlled environments using DC applied fields. Although electro-chemists are well aware that electrochemical effects are present at low frequencies, it is

generally assumed that at high frequencies electrochemical events are no longer significant. However, a careful reading of the literature surrounding microelectrode systems and the manipulation of sub-micron particles in solution reveals a number of comments that suggest damage to the electrode systems (see, for example, [112–115], but rarely is any explanation given, although occasionally steps are taken in order to limit its effects.

A review of the electrochemical literature shows that not only are reactions with gold electrodes expected for aqueous solutions, but that, under the correct conditions, nanoparticles [116], nanorods [117], and nanocubes [118] may be synthesised by electrochemical methods. In general, however, these experiments are done in the classic electrochemical fashion, in a large reaction cell with a control electrode. This is a very different environment from the setup usually used by researchers interested in microfluidic electrically induced flow. The crossover between these two very different areas of research means that there is something of a gap in the understanding between how these phenomena relate to each other. Conventionally, research dealing with electrokinetically induced flow does not consider electrochemical effects, while electrochemically based experiments are usually not concerned with the electrokinetically induced flow that is produced.

3.5 DEP equipment

In order to study the dielectrophoretic assembly of gold nanoparticles in solution into large-scale structures, custom equipment was designed and built in-house, as well as making use of various commercial equipment available in the department. In addition, several iterations of experimental design were required as successive experimental difficulties were encountered. Here an overview of the equipment used during the investigations into DEP assembly is presented.

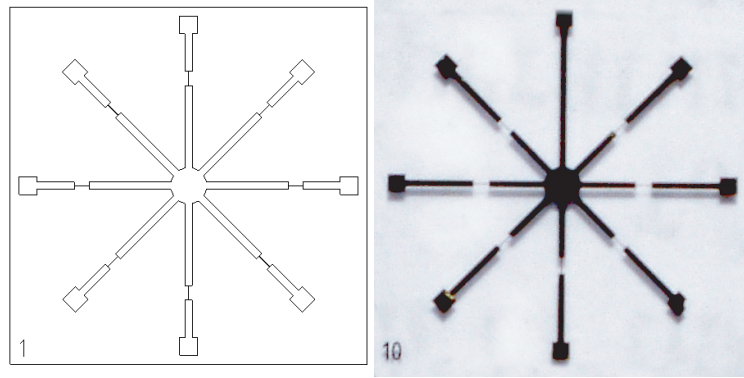


Figure 3.6: (Left) AutoCAD representation of the electrode mask used in DEP experiments. (Right) High contrast photograph taken of gold electrodes on a glass substrate after lithography and lift-off process.

3.5.1 Electrode array/PCB

The first step in designing an experimental setup to probe DEP in solution is the design of the electrode array to be used. An example of the electrode arrays used is shown in Fig. 3.6. The electrode design was created in collaboration with Matthew Suddards, Emmanuelle Pauliac-Vaujour and Philip Moriarty (University of Nottingham). Its unconventional design (most experiments investigating DEP use parallel fingers/plates, or interdigitated fingers) is due to the fact that it was designed as a dual use system both for investigating DEP and for investigating the electrical properties of drop cast nanoparticle networks (separate work carried out by Emmanuelle Pauliac-Vaujour et al. [119]). It features a common ground connection radiating from the centre and seven separate “live” connections that in principle allows seven separate experiments to be conducted on each chip. Several masks were produced, with varying inter electrode distances from $10\ \mu\text{m}$ to $70\ \mu\text{m}$ and macroscopic electrode shapes (square, triangle and hemisphere) to allow a variety of experimental parameters to be investigated. All the results shown in this thesis used $10\ \mu\text{m}$ gaps.

The lithographic mask was created in AutoCAD by Matthew Suddards and produced commercially. This was then in turn used to create vacuum-evaporated metallic electrodes on various substrates, using standard ultraviolet

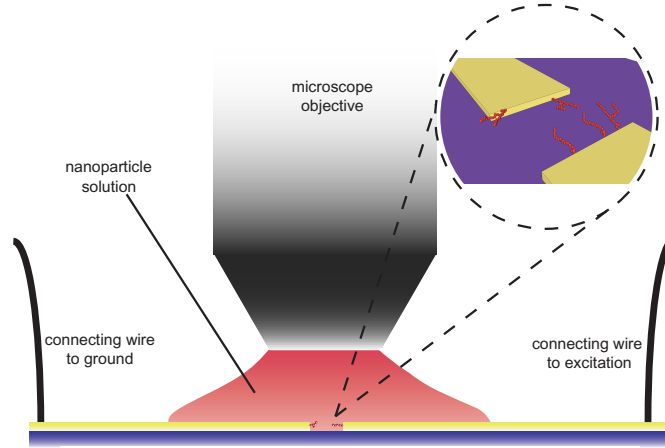


Figure 3.7: Side view of electrode on an insulating substrate with a nanoparticle solution droplet over the gap and optical microscope objective lens brought into contact with the droplet. (Inset) 3D representation of the electrodes and nanoparticle growth in solution.

let photolithographic techniques available in the School’s clean room facilities. Typically, after the photo resist was baked on, a 10 nm titanium adhesion layer was deposited by vacuum evaporation, followed by approximately 100 nm of gold. Excess photo resist was then removed in an acetone ultrasonic wash, leaving behind the metallic electrodes on the substrate. The substrates used comprised of silicon wafers with a 300 nm thermally grown oxide layer (purchased from [120]), and standard microscope slides. Both of these substrates were cut to 1 cm squares and cleaned in a standard four stage solvent wash before being used in the photolithographic process. After the acetone wash to remove the photo resist, the samples were subsequently sonicated in isopropanol and stored in sealed sample boxes.

A large-scale printed circuit board (PCB) was designed and produced with the assistance of Robert Chettle from the Electronics workshop in order to assist in macroscopic connections to the electrode array. A 7 mm diameter hole was drilled in the centre to allow for transmission optical microscopy to be used in the case of the glass substrates. The samples were then fixed to the PCB using standard double sided sticky tape. Electrical connections were made from the electrode pads to the PCB pads using the School’s microbonder.

As experimental work progressed, two subsequent iterations were made to

the PCB design. In the first, the entire design was expanded to allow access in order to use a different optical microscope system. The second, much more complicated change, involved the addition of a high impedance, high gain operational amplifier (circuit design shown in Fig. 3.11, designed by Robert Chettle, University of Nottingham) in order to aid in electrical measurements. In addition, it featured an improved design for connecting the sample to the signal generator and monitoring the signal across the electrode gap via an oscilloscope. The second and third iterations (used for all results presented in this thesis) are shown in Fig. 3.9 and 3.10.

Two optical microscope systems were used for in situ observation of the growth of nanoparticle aggregates. Early preliminary work was performed on a BHM series Olympus microscope located in the School of Physics clean room, whereas the main bulk of the work was performed on an Olympus BX51 due to improved magnification, optical filters and the ability to perform transmission microscopy as well as an improved video capture setup (see Fig. 3.8). All images presented of in situ growth were obtained using the latter instrument.

3.5.2 Scanning electron microscopy (SEM)

Ex situ post experiment observations were also made using a JEOL JSM-7000F SEM located in University of Nottingham clean room. Samples analysed in the SEM were first very gently cleaned (see experimental chapter for details) and

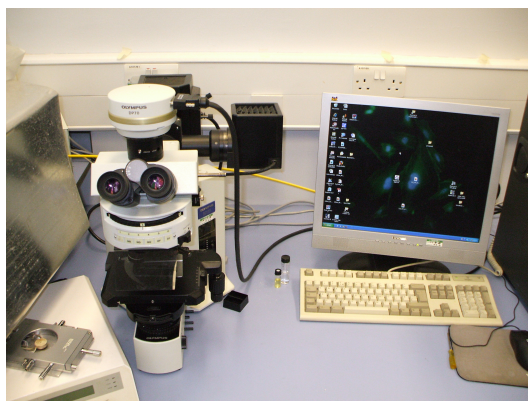


Figure 3.8: Photograph of Olympus BX51 optical microscope used for in situ investigation of microwire self organisation.

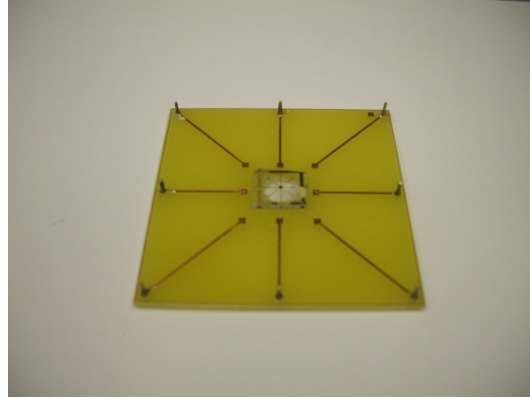


Figure 3.9: Photograph of electrode array from Fig. 3.6 mounted onto PCB (second iteration).

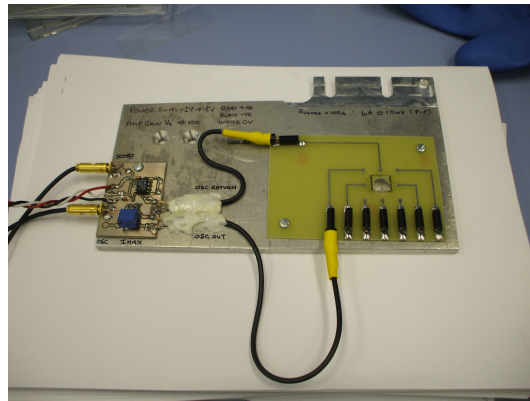


Figure 3.10: Photograph of electrode array mounted on third-generation PCB with improved electrical connections and integral high bandwidth, high gain amplifier for electrical measurements.

then mounted on a standard SEM ‘stub’ and introduced into the instrument without further preparation. All imaging was performed by the author using the standard secondary electron mode of operation.

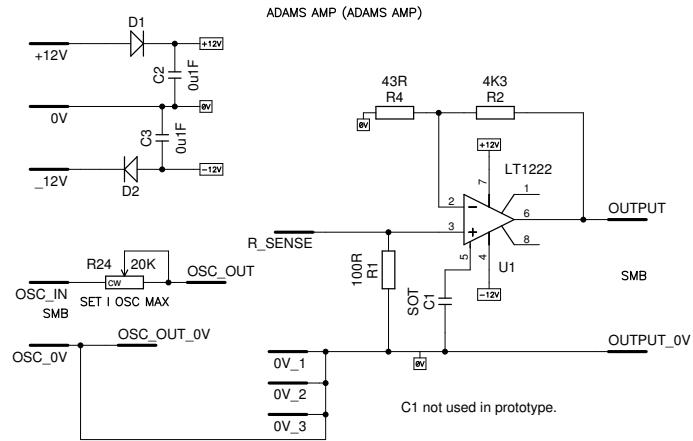


Figure 3.11: Circuit diagram for amplifier integrated into third-generation PCB, circuit design by Robert Chettle, School of Physics and Astronomy electronics workshop.

Chapter 4

Materials review

“A wise man proportions his belief to the evidence.”

David Hume

A brief overview of literature relating to the Si(100) surface, C_{60} on silicon, and both charge stabilised and thiol-passivated gold nanoparticles is presented in this chapter as essential background for the subsequent experimental results chapters

4.1 Si(100)

Silicon is a group IV element which, in its bulk form, takes on a diamond-like face-centred-cubic tetrahedral structure. In the bulk structure, the electron orbitals hybridise creating four sp^3 orbitals. This combination of s and p orbitals forms a tetrahedral shape, thus providing the building blocks for the diamond-like structure. When prepared with the (100) face exposed, a square grid of atoms with 1x1 periodicity is revealed with a surface lattice constant of 3.84 Å. Each silicon atom at the surface has two dangling bonds, and, for this reason, the bare silicon surface is highly reactive forming SiO_x almost instantly if prepared in air or rough vacuum. Only by preparation in UHV may the unreacted surface be investigated.

As with many other surfaces, the bulk-like termination of the Si(100) plane is not a natural ground state. Although surfaces can undergo complex recon-

structions to reach the ground state, the Si(100) reconstruction is conceptually relatively simple. In this case, the topmost layer of atoms on the Si(100) surface pair up to produce rows of dimers, which reduces the number of dangling bonds per atom from two to one. As a result of this dimerisation, there is a strong σ -like bond between the two atoms of the dimer (similar, though not identical to, bonding in the bulk), but also a weak π like interaction between the two remaining dangling bonds. This reconstruction reduces the surface energy by about 1 eV per atom, producing rows of dimers with a (2x1) periodicity. The unit cell of bulk silicon contains two different layers of atoms separated by a quarter of the lattice constant and rotated by 90 degrees with respect to each other, and, as such, atomic steps on the surface are one layer high (if the surface is not miscut). Across terraces, two rotated domains, (2x1) and (1x2), will coexist (i.e. the dimer rows on one step run perpendicular to the rows on the next - see Fig. 4.3).

Although this dimer model explained many of the salient features observed during the investigations of the Si(100) substrate by LEED [121], it failed to explain occasional spots at the quarter position, or photoelectron spectroscopy results that indicated two different states for surface atoms [122]. For these, and other reasons, it was suggested that the dimers on the surface were not in fact symmetric, but were instead buckled, which would give rise to (2x2) and (4x2) periodicities. This physical buckling is caused by a transfer of charge from one end of the dimer to the other in order to lift the electronic degeneracy of the dimer, a so-called Jahn-Teller distortion. Theoretical work [123] indicated that a buckled structure resulted in an energy gain of approximately 260 meV per dimer as compared to a symmetric p(2x1) structure.

Although the majority of theoretical and experimental work indicated that buckled dimers were a true ground state of the system, alternative viewpoints have persisted for decades [124–127]. The first STM imaging of Si(100) in 1985, [122], at room temperature undisputedly confirmed the dimer model, but left the question regarding buckling unsolved, as both symmetric and buckled dimers were observed. The conventional interpretation of the symmetric dimers at room temperature was that they were the time average of a buckled dimer flipping between two stable positions faster than the STM feed-

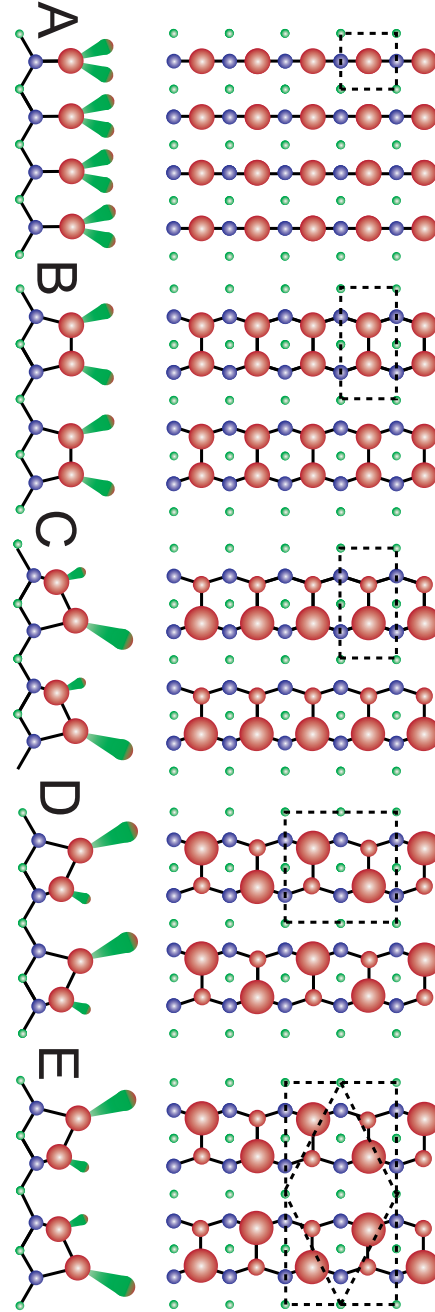


Figure 4.1: The different surface reconstruction units cells of Si(100) viewed from above and along the surface. A: The 1x1 ‘bulk-like’ surface (not observed), B: Symmetric p(2x1), C: Asymmetric p(2x1), D: In phase buckling p(2x2), E: Out of phase buckling c(4x2).

back loop was able to respond. This seemed to be confirmed by subsequent low-temperature observations at 120 K [128] that showed a large increase in the proportion of buckled dimers as the thermal energy of the system was reduced. However, subsequent investigations using STM and LEED at lower temperatures often produced conflicting results (for example: [124, 129–132]), and it quickly became clear that the effect of the probe (be it energetic electrons in the case of LEED or tunnelling electrons and interaction forces in the case of STM) could strongly perturb the surface from its ground state, making interpretation of results extremely difficult. In addition to the probe directly modifying the surface, systematic STM studies have shown that the exact nature of the local density of states must be considered. As is common with many other surfaces, the STM images produced vary strongly with applied bias and have a nontrivial relationship to the actual topography of the surface.

4.1.1 STM imaging of Si(100)

The buckling of the dimers on Si(100) surface is caused by a Jahn Teller-like distortion, and, as a result, charge is transferred from the lower atom to the upper atom. A consequence of this is that the π -like bond between the two dangling bonds is also distorted with the π bonding states localised around the upper atom and the π^* anti-bonding states localised around the lower atom. However, even this quite complicated picture is actually an oversimplification of what is observed during STM imaging, and, as such, it is useful to conduct a brief review of STM imaging of the Si(100) surface.

The calculated [133] and experimentally-estimated [134] energy barrier to flip a dimer is somewhere between 100 and 200 meV, though it is expected there will be a variation in the exact energy depending on the local environment of the dimer in question [122, 123, 133, 135, 136]. As a result, at room temperature a dimer will rapidly flip between the two possible states at a frequency of several MHz [133]. Since STM feedback loops typically have a response frequency on the order of a few kHz [45], the image observed will be a time average over many oscillations. In the first images of Si(100) at room

temperature, it was observed that at negative sample bias (i.e. filled states) that “bean-like” protrusions were observed, and, at positive sample bias (i.e. empty states), rows of double protrusions were observed – both of these structures had a $p(2 \times 1)$ periodicity. Around defects and step edges, buckled dimers were observed, and it is believed that strain effects related to these features stabilise the buckling [122]. Initially, the bean-like protrusions were interpreted as being the result of tunnelling from the centre of the π -like bond, and the protrusions were interpreted as tunnelling from the π^* anti-bonding states, with a degree of localisation towards the troughs between the dimer rows rather than the topographic location of the atoms [45]. However, subsequent theoretical and experimental work [137] has suggested that, in fact, these features are the result of delocalised bulk and surface state contributions as a consequence of using high applied biases. Hata et al [137], for example, found in room temperature experiments that, when using positive or negative biases on the order of 1 V or less, they imaged almost identical rows of protrusions and found that switching to *higher* negative or positive biases resulted in the “bean” or “trough centred” protrusions respectively. First principles calculations also indicated that the filled and empty state images for voltages corresponding to the π and π^* states for thermally oscillating dimers should be almost identical.

At temperatures below ~ 200 K, it was expected that the flip-flopping would be frozen out and the buckled ground state would be observed. This was confirmed by Wolkow [128], but subsequent imaging revealed possible problems with the interpretation of the images - as lower temperatures became accessible in STM, various data became available [126, 130] that suggested the $c(4 \times 2)$ reconstruction may not be the ground state. In order to understand the confusion that has surrounded this topic, it is necessary to outline the properties of Si(100) across a range of temperatures.

In what we might loosely term the “liquid nitrogen regime” (that is to say temperatures of the order of 70 to 100 K), the buckled $c(4 \times 2)$ and $p(2 \times 2)$ structures are routinely observed, but there are a number of salient features which should be noted. First, and similar to observations at room temperature, imaging at high biases can result in a strong contribution from delocalised bulk/surface states, resulting in a $p(2 \times 1)$ like appearance (see Fig. 4.2). Also,

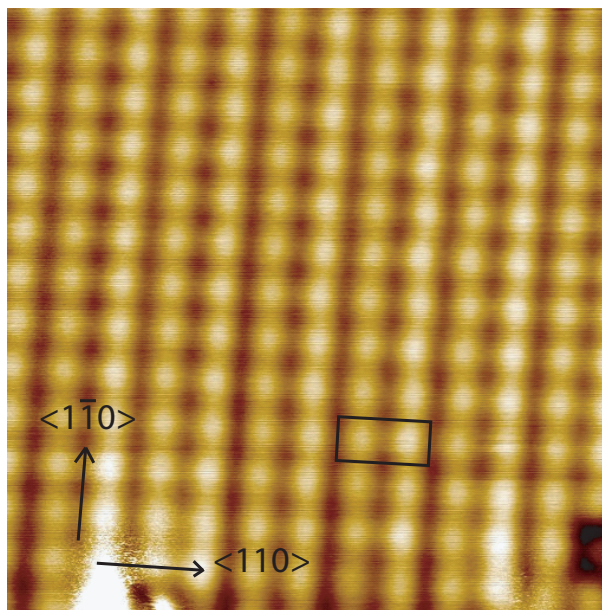


Figure 4.2: Si(100)-p(2x1) imaged at +1.5V, 0.5nA at 77K in conventional STM. Rectangle indicates unit cell. Image courtesy S. Gangopadhyay.

it is extremely common to observe so-called “flicker” dimers (see Fig. 4.3). The conventional interpretation of these is that some aspect of the probe interaction with the surface is causing the dimer to flip between two states while the tip is above it. The three key interaction parameters are the electric field, the tunnelling current, and the mechanical (physical) tip interaction. This topic will be returned to in both the Results and Conclusions chapters, but at this point we note that in conventional STM it has been shown that the most likely cause of this dimer flipping is inelastic electron tunnelling [138–140]. It is thought the electric field may have a small contributing factor and that the chemical bonding effect in conventional STM studies is small. As we will see, this interpretation may not strictly be valid for more complex simultaneous AFM/STM studies.

In an attempt to definitively decide the ground state of the Si(100) surface lower temperature studies were carried out. However, in what we might term the “liquid helium regime” (that is to say between 4 and 10 K), the situation becomes even more complex. Studies were conducted that showed the p(2x1) [125–127], p(2x2) [138,140], and c(4x2) [131,140] reconstructions at low-

temperature. Subsequent systematic studies have shown that to successfully interpret these results we must consider not only the probe surface interaction, but also changes in the electronic and physical structure of the surface below 40 K. Between 60 K and 40 K two important physical properties change for the Si(100) surface. First, the carrier concentration drops sharply [138, 141] to what can be as low as 1% of the concentration at room temperature, as a result both the bulk and surface conductivity drop sharply. Second, the thermal energy of the system drops such that if the dimer is somehow flipped out of its ground state it no longer has enough energy to return to its original configuration on a reasonable timescale [133]. These two changes mean that the surface will react differently to the effect of the probe. In addition, Kawai and Hanrikiyo [139] investigated theoretically the vibration of a dimer excited by the STM current on a p-type substrate, focusing on the degree of electron-vibration coupling [139]. They modelled the effect of the tunnel current as an “effective surface temperature” local to the dimer through which the current was flowing. They found that below approximately 60 K there was a strong non-linear effect on the effective temperature of the dimer due to the tunnel current, with effective temperatures of well over 200 K at moderate tunnel currents of 100 pA or less. However, above 60 K the effect of the tunnel current on the effective temperature tends to zero and thermal, rather than tunnel current, effects dominate.

As with imaging in the “liquid nitrogen regime”, applying a high bias results in contributions from states not localised to the atoms of the dimer, and can result in a p(2x1) like structure. However, imaging at lower biases helps ensure that buckled or flickering dimers are recorded. More complicated is the effect of the reduced carrier availability. This has two primary effects as regards STM imaging: (i) there are fewer carriers available to screen the electric field due to the tip, and as a result, the depletion region caused by the local field is greatly enhanced, causing much greater band bending (especially in more lightly doped samples); (ii) the reduced conductivity of the sample increases the potential for local charging due to the injection of electrons into the surface [141]. Both of these effects are critical to the interpretation of STM imaging of low-temperature Si(100).

One of the primary aims of these investigations was to determine the true ground state of the system. It has been determined theoretically that the energy of the p(2x2) and c(4x2) periodicities differ by only a few meV per dimer, and that the energy difference may in fact be smaller than the accuracy of the simulations [133, 135]. Therefore conflicting STM studies produced a great deal of confusion. However, systematic studies by both Sagisaka and Hata [137, 138, 141] seem to have resolved the mystery, at least on n-type samples. In this work they were able to successfully reversibly transform the c(4x2) phase into the p(2x2) reconstruction by carefully modifying the bias at which they scanned the surface. It was shown that it was possible to exclude mechanical probe-surface interactions, and electric field effects as primary mechanisms for the transformation. They instead found a narrow bias voltage window for the transformation around +1.3 V applied surface bias. Careful $I(V)$ spectroscopy and setpoint-dependent experiments determined that the phase manipulation occurred at a bias voltage which coincided with the energy for the surface π^* state. This fact, along with evidence of the transformation occurring along dimer rows but not across dimer rows (the π^* surface state is localised along dimer rows – see [141] for dI/dV spectroscopic data) strongly suggested that electron ejection directly into the π^* surface state was responsible for the phase manipulation. They postulated that the most likely mechanism is that the electrons are able to enter the surface state but have limited mobility due to the reduced conductivity, and so there is a small charging effect in the region of the tip. This hypothesis is supported by theoretical calculations showing that negative charging of the surface can modify the energy landscape such that the p(2x2) phase becomes more energetically favourable than the c(4x2). It is presumed that the dimers are given the energy to flip by electrons tunnelling inelastically, and return to the p(2x2) state due to the modified potential. In addition, they showed that the threshold voltage for the phase manipulation coincided with the measured location of the π^* surface state at different setpoints as the amount of band bending varied due to the position of the tip.

In addition the number of flickering dimers increased almost linearly with increasing voltage (notwithstanding a dip arising from the “phase manipula-

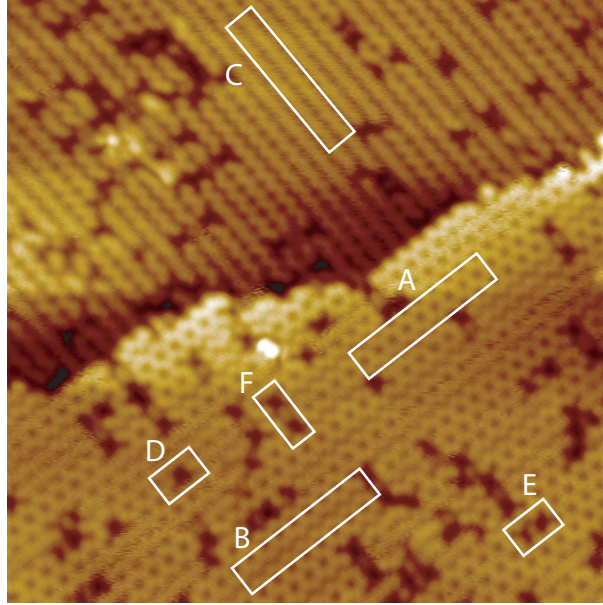


Figure 4.3: Conventional STM image of Si(100) at 77 K (taken with a qPlus tip) showing different features of the surface, including the orthogonal row directions over a step edge. A: c(4x2), B: p(2x2), C: 'flicker' dimers, D: 1DV (dimer vacancy) defect, E: 1+2DV defect, F: Boron induced defect.

tion" energy band), and that they were able to "reset" the surface by scanning at very high (+5 V) voltages. This indicates that by increasing the number, and the energy, of the electrons entering the surface more energy is deposited, exciting the dimers and allowing them to return to their true ground state. This is also supported by the fact that the surface disruption caused by high energy electron injection spread radially as it was not limited to travelling along the row-localised π^* surface state.

Although the results in this thesis were acquired exclusively at 77 K, these liquid helium regime results provide us with important information. Although we know the p(2x2) to c(4x2) phase manipulation and local surface charging due to electron-injection should not be an issue, we must remain mindful of the effects of the tunnel current and electric field during our interpretation of AFM results if an electric field and/or tunnel current is present. With this in mind we will briefly review the current literature regarding the AFM imaging of Si(100).

4.1.2 AFM of Si(100)

In contrast to the vast literature concerning STM imaging of the Si(100) surface there is comparatively little work concerning NC-AFM of the same substrate [66, 142], especially at low temperatures [131, 143]. What is known is that at room temperature the observed topographic images correspond well to low bias STM images, i.e. rows of symmetric dimers are observed [144]. At low temperatures the $c(4 \times 2)$ periodicity has been observed in NC-AFM, helping confirm this state is the ground state. Although, in theory, AFM can be a much “cleaner” probe than STM as an electric field and tunnel current are not required (although this is dependent on the contact potential difference between the tip and the sample – see experimental techniques section), in a typical AFM experiment the mechanical force between the tip and the sample will be much higher than for the typical STM experiment. This creates its own interesting effects with regard to the Si(100) surface.

A detailed experimental and theoretical investigation [131, 133] showed that by carefully varying the interaction force, a $c(4 \times 2)$ to $p(2 \times 1)$ phase transition could be activated. However, the interpretation of this phase transition is very different from the $c(4 \times 2)$ to $p(2 \times 2)$ phase transition, or apparent $p(2 \times 1)$ periodicity, mentioned above for STM. For NC-AFM, the interpretation is that as the AFM tip passes over the dimer it forms chemical bonds with the dangling bonds of the silicon atoms. For the “up” atom of the dimer this has little lasting effect, but if the interaction force during scanning of the lower atom is strong enough then the AFM tip can “pull” the atom up and “flip” an individual dimer. As a result, this atom will be imaged as the “up” atom of the dimer. The $p(2 \times 1)$ structure observed is an artefact of the scanning process as the tip systematically modifies the atoms as it images them at high interaction strengths. Direct confirmation of this theory would be provided by additional low-temperature experiments showing the manipulation of individual or groups of dimers correlated with the scan direction or specific spectroscopic points. A cartoon representation of this process is shown in Fig. 4.5.

An important subtlety of this model is whether the dimer is able to return to its “ground state” or whether the manipulation is permanent. As noted above, it is interesting that in the liquid nitrogen regime the energy barriers are

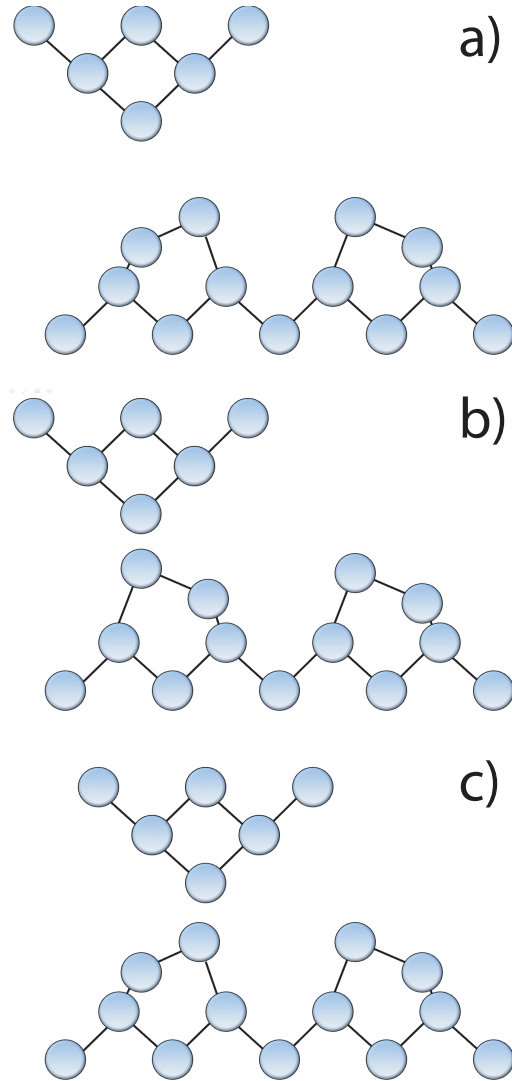


Figure 4.4: Simplified view of the scheme from [131, 133]. a) At low setpoints the probe does not perturb the surface. b) At high setpoints ‘down’ atoms are pulled into a ‘up’ position. c) Each subsequent down atom is pulled up, resulting in a apparent p(2x1) image.

such that the surface is able to “heal” itself. Hobbs and Kantorovich [131, 133] calculated that at or above 70 K, a dimer would have enough thermal energy to return to its ground state on a timescale less than, or on the order of, a single oscillation of a typical AFM tip. As the tip retracts, the dimer flips back to its original state so that on every oscillation the AFM tip will pull

the dimer up again. As a consequence, the effective interaction strength for a down atom averaged over a large number of cycles is reduced compared to that of a true “up” atom. Conversely, at liquid helium temperatures, there is insufficient energy for the dimer to change its state and so once a dimer has been flipped it will stay in that configuration until externally excited in some way, and there should be almost no asymmetry between a true “up” atom and a “down” atom pulled up during the first oscillation.

4.1.3 Defects

In addition to the ideal surface, with its dimer reconstruction and buckling, the Si(100) surface is notable for having a reasonably high proportion of defects. The most common of these are the so-called missing dimer defects, which, as the name suggests, are defects resulting from the absence of one or more dimers in the rows. In their initial investigations using STM, Hamers and Kohler [145], [146] observed three primary types of defects. Type A corresponds to a single missing dimer, type B corresponds to two missing dimers together, and type C, which is not a missing dimer defect, but rather (as is now commonly accepted) the result of adsorbed water [147, 148]. In their theoretical investigation of defects on the Si(100) surface, Wang et al. [149] re-characterised type A defects as 1-DV (dimer vacancy), type B defects as 2-DV, and aggregations of type A and type B defects as 3DV or 1+2-DV, depending on arrangement. The presence of defects on the surface has been shown to increase the local surface strain, and at room temperature it is clear that the presence of defects stabilises the buckling of nearby dimers [146]. It should be noted that if the surface is prepared in the presence of certain contaminants (most notably nickel [150], or tungsten [151]) then a large number of dimer vacancy defects are generated, and they may order into the so-called (2 \times n) phase, in which the defects align themselves perpendicular to the dimer rows to form “trenches” on the surface. To date, room temperature STM and AFM studies [142, 151], appear to confirm the model proposed by Wang et al. [149] for missing dimer defects. The current models for the three main types of defects are shown in Fig. 4.5.

In addition to these “native” defects, defects may also be caused by the

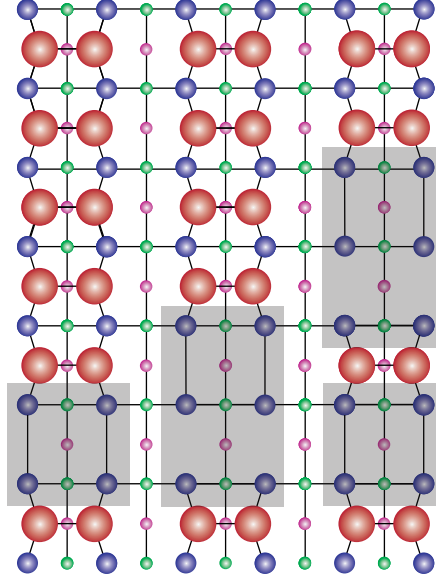


Figure 4.5: Structure of the most common ‘native’ defects on Si(100). From left to right, the 1DV, 2DV and 1+2DV defects shown using the currently accepted re-bonding model.

presence of dopants added to the silicon to increase its conductivity [152, 153]. For example, for p-type substrates the addition of boron can cause characteristic defects as the dopants segregate to the surface after repeated flash/anneal cycles. The exact structure and, critically, also the exact chemical composition of these defects, is still a subject of current research (most notably a recent systematic STM and theoretical study [154]). In that study, previous results and theoretical models were compared with a systematic range of bias-controlled experiments and simulated scans. On the basis of this work, it seems most likely that the structure of these defects is the result of an aggregation of boron dopants forming a substitutional structure at the surface - the most recent model for which is shown in Fig. 4.6.

4.1.4 Preparation

Although there are numerous methods for the preparation of a clean Si(100) surface, the most common is in situ heat treatment of a native oxide terminated surface. Typically, the silicon sample is solvent cleaned ex situ and then

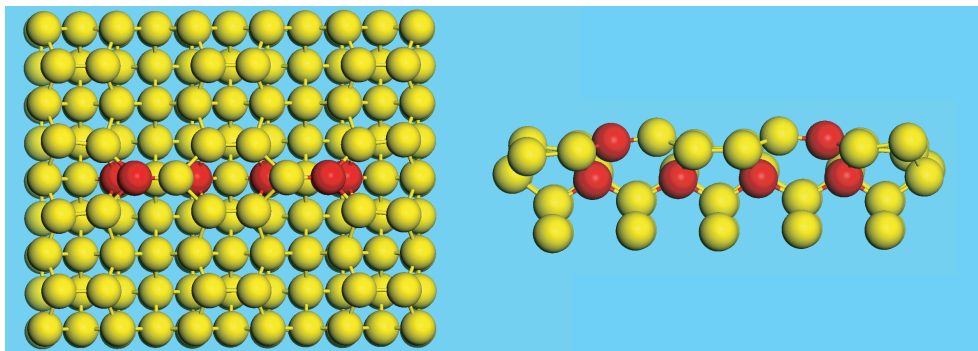


Figure 4.6: Most recent model [154] for the substitutional boron defect shown in plane and side view. Red atoms indicate substitutional boron.

inserted into a vacuum chamber where it is degassed at approximately 600°C for 4 to 12 hours in order to remove the majority of surface contamination from the oxide layer (for example water, and residual solvent). Following degassing, the sample is “flashed” to approximately 1200°C in order to remove the native oxide layer, drive residual carbon contamination into the bulk, and expose the bare silicon substrate beneath. The sample is then quickly cooled to approximately 900°C to allow the surface to reconstruct and then slowly cooled to room temperature. This heating and slow cooling allows contamination that is not removed during the initial flashing to move into the bulk, and also allows defects to diffuse and aggregate, and should lead to large areas of relatively defect free surface. It is critical during this process that the pressure of the vacuum system be kept in the low 10^{-10} mbar range. High vacuum pressures during preparation have been linked to very high defect concentrations, and even large-scale faceting [122].

The highly reactive nature of the surface, and the natural anisotropy caused by the perpendicular arrangement of the dimer rows, has made Si(100) an ideal test substrate for the manipulation of covalently bound molecules at room temperature using STM [155, 156]. An interesting research goal is to extend this ability to NC-AFM. We therefore briefly review previous work on C_{60} on Si(100).

4.1.5 C₆₀ on Si(100)

Fullerenes are large carbon cage molecules, of which the most common by far is C₆₀, also called a “buckyball” after Buckminsterfuller. Discovered in 1985 by Kroto et al. (a discovery for which the Nobel prize was awarded in 1996), C₆₀, as its name suggests, contains sixty carbon atoms. The shape of the molecule is a truncated icosahedron – with twelve pentagon faces and twenty hexagon faces (Fig. 4.7). Each of the carbon atoms in the cage is in an identical bonding configuration and as a result of the bonding some of the π electrons in the cage delocalise, producing a raft of interesting electronic effects [157]. The core-to-core distance across the cage is approximately 7Å and, as such, the molecule has been considered something of an archetypal “nano” building block, and is in many ways an ‘icon’ associated with nanotechnology in general.

Investigations of C₆₀ on the Si(100) surface using scanning probe techniques began in 1992 with the work of Hashizume et al. [158]. Initial investigations indicated that the molecule clearly had a strong bond to the surface, however the exact bonding mechanism was a subject of debate throughout the 90’s with some groups claiming that up to 75 % of the molecules in a monolayer physisorb at room temperature [159–161], and chemisorb only upon annealing. Subsequent investigations [162–164], including a recent systematic experimental study combining UPS/XPS and low-temperature STM on the Si(111) surface [165], indicate that the C₆₀ molecule clearly chemisorbs upon contact with the silicon surface and that earlier experimental results by other groups suggesting initial physisorption were most likely the result of inaccurate calibration. However, it should be noted that the exact bonding configuration does change if the substrate is annealed with C₆₀ attached. Initially when deposited at room temperature the C₆₀ molecule has been shown to bond in the dimer “trenches”. Upon annealing, however, the molecules have been shown to move on top of the dimer rows [163, 166], and apparently increase the strength of the bonding between the cage and the substrate, as STM manipulation events became increasingly difficult [163].

Although atomic and molecular manipulation using the STM is now well into its second decade [15] it is worth noting that almost all the early experiments were conducted at low-temperature on metal surfaces, in order to

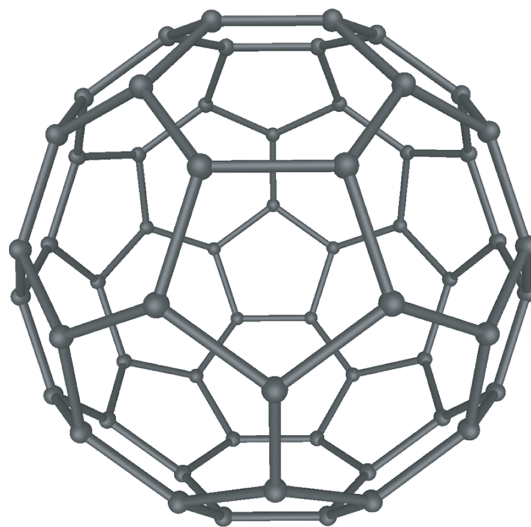


Figure 4.7: Simple ball and stick model of the C₆₀ molecule, after [167]

prevent diffusion of the adsorbates during manipulation. Beton et al [162] demonstrated for the first time controlled molecular manipulation using STM at room temperature for C₆₀ molecules on a silicon substrate. Subsequent theoretical analysis has indicated that it should be possible to manipulate the C₆₀ molecule solely by mechanical means [168]. Although C₆₀ has been successfully manipulated on the Si(100) surface it is difficult to separate the mechanical effect of the probe from the effect of the strong electric field and tunnel current present during manipulation events using STM. Solely mechanical molecular manipulation – as demonstrated on the atomic scale on the Si(111) surface by Oyabu et al [20] – would be another important step towards realising so-called “mechanosynthesis” i.e. direct three-dimensional control of matter at the atomic scale via the exploitation of chemical bonding forces.

Although theoretical studies indicate that it should be possible to image the C₆₀ molecule with sub-molecular resolution [169] thus far only one study of isolated C₆₀ molecules using NC-AFM on a silicon surface is available in the literature [170]. In that study, using conventional silicon cantilevers and the Si(111) surface, individual molecules were resolved, but, in general, image quality was poor with numerous artefacts, and sub molecular resolution was not obtained. It is anticipated, given the noted additional difficulty imaging Si(100) over Si(111) in NC-AFM [144], that imaging the C₆₀ molecule on the

Si(100) surface will present an even greater experimental challenge.

C₆₀ molecules are remarkably stable in terms of their thermal breakdown temperature [171]. As a result, they are reasonably easy to deposit in vacuum and devices such as a Knudsen cell, or a simple tantalum boat can be used to heat a C₆₀ sample until the molecules begin to sublime. Therefore deposition of C₆₀ onto silicon in vacuum is reasonably straightforward, as the clean surface can simply be brought into a beam of thermally sublimed molecules until the required coverage is reached.

4.2 Colloidal gold

It is well known that “nanotechnology” is not a “new invention”. One of the clearest examples of this is the use in ancient pottery and glassware [172,173] of gold nanoparticles to produce a striking red colour. The red colouring is produced due to the plasmon resonance effects in metallic nanoparticles smaller than about 100 nm [174,175]. It is only rather more recently, however, that the scientific investigation of the size dependence of these effects has been formalised in the field of nanoscience.

Colloidal gold is most simply thought of as a suspension of sub micrometre particles of gold in a fluid. The properties of colloidal gold have been of interest in such disparate fields as biological marking [176], far from equilibrium pattern formation [38,177,178], and microelectronics [179]. In this thesis self-organised patterns and micro structure formation of colloidal gold are studied in two very different scenarios. A brief overview of the types of particles used is provided in the following section.

4.2.1 Charge stabilised gold nanoparticles

The conventional method of colloidal gold synthesis was pioneered by J. Turkevich et al. [180] and later G. Frens [181]. Chloroauric acid is dissolved in deionised water and then a reducing agent, such as sodium citrate (and additionally sometimes tannic acid), is added causing the aggregation of gold ions into particles. The size, and the size distribution, of the particles produced is

controlled primarily by the amount and rate of reducing agent added during the process. After the particles are formed, negatively charged citrate ions adsorb onto the surface, which produces a counter ion cloud surrounding the particles causing a repulsive force between them, thus preventing the particles from aggregating and falling out of solution.

4.2.2 Thiol stabilised gold nanoparticles

Although the above method works well for producing suspensions in water, it cannot be used to produce suspensions in other solvents (such as toluene/hexane/dichloromethane). Brust et al. [182] described a new method using tetraoctylammonium bromide (TOAB) that allowed suspension in organic solvents. Here the particles are temporarily stabilised by the presence of the TOAB molecules on the surface, and long term stability may be produced by adding a thiol which strongly bonds to the gold nanoparticle. Particles made in this manner may be precipitated and then redissolved in other organic solvents. The use of PEG-OH as the passivating ligand allows particles of this type to be suspended in water as well as the organic solvents used with standard thiols. The presence of the interacting thiols, and the lack of the charge cloud surrounding the particles, radically alters the properties of the nanoparticle solution both in liquid and during the drying phase. Fig. 4.8 shows a simplified representation of the structure of both types of nanoparticle.

In this thesis, all nanoparticles used were either purchased commercially in the case of charge stabilised particles [183] or synthesised by other members of the group in the case of thiol-stabilised particles [184]. The only exception is for a small batch of charge stabilised gold nanoparticles which were synthesised by the author (with the help of Daniel Marsh, School of Chemistry) in order to create a control solution.

4.3 Pattern formation using thiol-stabilised particles

The ability to organise nanoparticles over large length scales is a well-established but still vibrant area of research. The reasons for investigating these phenomena are varied, but include interests such as the wetting dynamics [38, 182, 185], electrical characterisation [186], nanolithography [187], and nanoscale self organisation [38, 188]. Although many groups have focused on creating large arrays of well-ordered nanoparticles, other groups have found fascinating physics in the description of the formation and properties of self organised nanoparticle networks [185, 189, 190]. Although these networks do not have the local order of a well packed array, it has been shown that they exhibit long-range order and properties not specifically governed by the size of the nanoparticles themselves, but rather the balance of various forces during their formation [191, 192]. In addition, experimental and theoretical work [186] related to charge transport through these networks have shown the importance of considering the degree of nanoparticle connectivity in determining the conductivity of the network.

The morphology of these networks, and the elucidation of the key factors in their formation has been well studied [193] and will not be discussed further here. However, thus far only a limited number of surface science tools have been brought to bear on the investigation of these networks. Most imaging has been performed in atmosphere using tapping mode AFM (see for example Blunt et al. [190]) with some investigation of the chemical specificity using spectroscopic techniques in vacuum [187]. These studies have helped develop an understanding of the various morphologies that are developed during drop deposition and spin casting, but have thus far not yet investigated properties of the network beyond the morphology. It is also important to note that, at least in the case of tapping mode AFM, the very observation of the network can in and of itself be disruptive [190], and thus it is hoped that more sensitive (noncontact) techniques can provide a more comprehensive understanding of the network structure. Additionally, no scanning probe investigations of these networks in vacuum have been carried out, and in order to develop a full under-

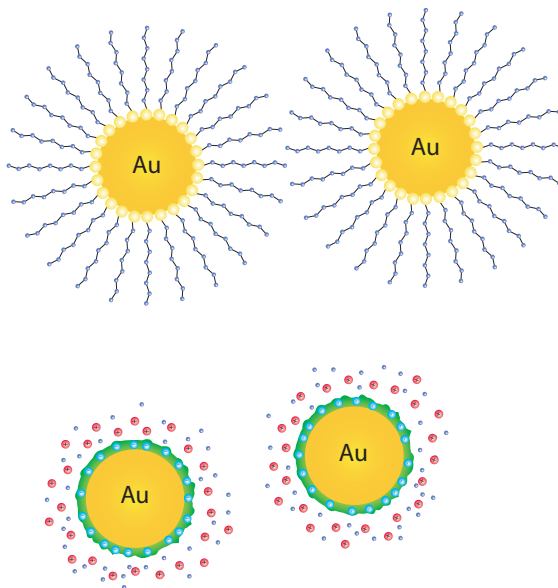


Figure 4.8: Cartoon representation of different gold nanoparticle structures. Top: thiol passivated (sulphur headgroups attached to the gold); Bottom: Citrate (charge) stabilised with citrate coating surrounded by counter-ion ‘cloud’

standing of local charge transport in these networks, further characterisation is necessary as an important step towards using techniques that may be able to image charge transport in situ.

4.4 DEP self organisation of charge stabilised nanoparticles

Although the manipulation of micron scale particles in suspension by dielectrophoresis is a well-established field of research [37, 92, 93, 98, 194], the use of dielectrophoresis to form conducting wires in solution via the self organisation of metallic nanoparticles is a relatively recent development. The first reported experiments in this field were in 2001 by Hermanson et al. [37]. In this heavily cited work they observed the self organisation of gold nanoparticles with diameters of 15 to 30 nm into conducting wires that were able to span gaps of several millimetres with growth rates of up to $50\mu\text{m}$ per second. The key

point to note is that the use of conducting, rather than insulating particles, with metallic electrodes allows aggregations of nanoparticles to effectively “extend” the electrode, and hence the associated distortions in the electric field, out into the solution. Use of insulating particles, or an insulating layer on the electrodes, will still allow aggregation to occur, but the extension of the electrode as a “wire” cannot occur.

It was also reported that the wires were “self-healing”. That is, if a wire broke due to excessive current/heating effects then particles from the surrounding solution would rapidly aggregate at the ends of the broken sections and cause the wire to reform. Hermanson et al. also showed that wires could be made to grow from, and connect to, conducting islands that were not electrically connected due to their effect on the electric field in the gap between the electrodes. In addition, and depending on the parameters used, more fractal shapes, similar in structure to diffusion-limited aggregates, are observed [98]. A qualitative investigation into the parameters affecting the likelihood, speed, and structure of the wires was carried out [194], although this focused on high applied potentials, large gaps, and relatively low frequency applied fields.

Subsequent investigations [98] expanded the parameter space, revealing additional growth modes and noting the effects of parameters such as fluid viscosity on the structure of the formed wires. In addition, simulations modelling the dielectrophoretic force and the aggregation of nanoparticles successfully modelled certain aspects of the wires appearance, such as branched, fractal growth patterns. Other authors [195,196] concentrated their efforts on related schemes to trap very small numbers of (or even individual) nanoparticles in nanometer scale gaps formed by electron beam lithography as a means to investigate the electrical properties of individual nanoparticles. It was also noted that similar experimental conditions applied to other “nanostructures” such as metallic nanorods and semiconducting, layered, and Janus particles produced similar results [197–199].

However, it was not until mid-2007 that systematic investigations [92,93] of the physical forces present during these experiments were carried out. Although phenomena such as fluid flow were noted in the initial investigations [37], the vast majority of subsequent publications chose to focus solely

on the DEP force as the dominant effect. However parallel investigations by Green and Ramos et al. [104] had already noted that forces other than dielectrophoresis could be dominant in the parameter space being investigated. Gierhart et al. [92] investigated the effect of AC electroosmotic fluid flow (ACEO, also known as induced charge electroosmosis (ICEO)) over a range of frequencies and showed that under certain conditions the induced fluid flow could completely dominate dielectrophoretic effects. Bahukudumbi et al. [93] performed related experiments with mechanically prepared micron-sized particles and plotted a phase map for their experimental system showing the relationship between the dominant forces over a range of frequencies and field strengths. However, the strong dependence of both the DEP force and ACEO fluid flow on parameters such as field strength, particle size, electrode shape, and frequency mean that despite these recent advances there is still not a clear “overarching” theory that explains all of the observed results.

Chapter 5

Combined qPlus STM/AFM of Si(100)

“It is always by way of pain one arrives at pleasure.”

Marquis de Sade

In this chapter, results related to imaging of the clean Si(100) surface by combined NC-AFM and STM at 77 K are presented. In addition to clean surface data, successful imaging of defects on the surface is reported, alongside images and spectroscopy that highlight the critical role the tip apex plays in the observed phase. Preliminary results demonstrating imaging with sub-molecular resolution of the C_{60} molecule on Si(100) are also presented.

5.1 Sample preparation

Solvent-cleaned wafers of highly boron doped Si(100) (doping level approximately 2×10^{19} dopants per cm^3 , conductivity $1 \text{ m}\Omega\text{cm}$) were introduced into the UHV system and degassed at 600°C for between three and six hours. The samples were then flashed to approximately 1200°C in order to remove the native oxide layer from the surface, rapidly cooled to approximately 900°C , and then slowly cooled to room temperature. The chamber pressure during the flashing part of the preparation was kept below $5 \times 10^{-10} \text{ mbar}$ with a base vacuum pressure of below $5 \times 10^{-11} \text{ mbar}$. The samples were then introduced

into the scan head inside the low-temperature cryostat for imaging. All images presented in this chapter were taken with a sample temperature of 77K unless otherwise stated.

In the Omicron combined qPlus/STM it is possible to use the qPlus sensor as an STM tip. Therefore, all STM data presented in this thesis were collected using qPlus sensors in conventional STM mode. This also allows for much easier switching between modes as the tip may be withdrawn, STM regulation disengaged, and the AFM regulation switched on. At the time of the experiments, dual regulator environments were unfortunately not supported in the MATRIX control software. Once the AFM regulation has been successfully engaged the tip may be re-approached using the AFM feedback loop without requiring tip and/or sample transfer. The qPlus sensors themselves (purchased pre-glued and pre-etched from Omicron GmbH) were introduced into the system and the scan head without any special tip treatment (for example argon sputtering and/or electron beam bombardment). Therefore it is likely that the tips were covered in an insulating tungsten oxide layer. Although atomic resolution was not initially possible with qPlus tips in STM mode, by applying controlled voltage pulses, and controllably crashing the tip into the surface, atomic resolution in STM mode was routinely obtained. Before AFM imaging could be attempted it was necessary to ensure that excellent STM resolution was first obtained.

Once the tips had been adequately prepared, STM of the surface of the sample routinely demonstrated a well-reconstructed surface with the expected features, i.e. rows of dimers showing buckling and “flicker noise”, with the direction of dimer rows changing by 90° when moving from one terrace to another, as well as a number of vacancy and dopant-related defects. Fig. 5.1 shows a representative image.

Once it had been ensured that the tip and the surface appeared to be in good condition, the tip was withdrawn and STM regulation disengaged, NC-AFM regulation was engaged, and the tip was re-approached in constant frequency shift mode. Once the tip had approached the surface at low df setpoint, voltage spectra ($df(V)$) were taken to measure the contact potential difference (CPD) between the tip and the surface. In general, a bias was

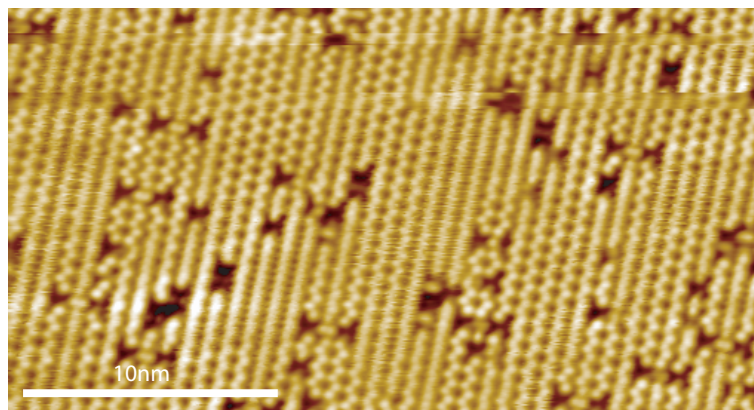


Figure 5.1: Conventional high resolution STM image of the clean Si(100) surface taken using a *qPlus* sensor. Scan conditions: -2V effective sample bias; setpoint 1 nA.

applied to the tip in order to null out this contact potential difference.

In the following sections, the focus is first on results obtained at relatively large oscillation amplitudes that should be directly comparable to previous NC-AFM studies using conventional Si cantilevers. Imaging of various defect structures and comparisons to accepted structural models are presented before results using subnanometre oscillation amplitudes and the effects of varying frequency shift setpoint on the imaging are discussed. Results are also presented which involve signal channels collected in parallel with the topography data, primarily the tunnel current and the dissipation signal. Critically, force spectroscopy data are shown which detail the variation in frequency shift, tunnel current and damping as a function of tip-sample separation. In addition, results showing the effects of possible tip asymmetry are presented alongside the imaging of adsorbed C₆₀.

5.2 Large amplitude NC-AFM imaging

Initial imaging of the surface was carried out using large oscillation amplitudes of 5 to 10 nm. Here amplitude is used in the conventional sense, rather than peak-to-peak amplitude which is used exclusively in the Omicron control software and documentation). The use of large amplitudes allows for a more

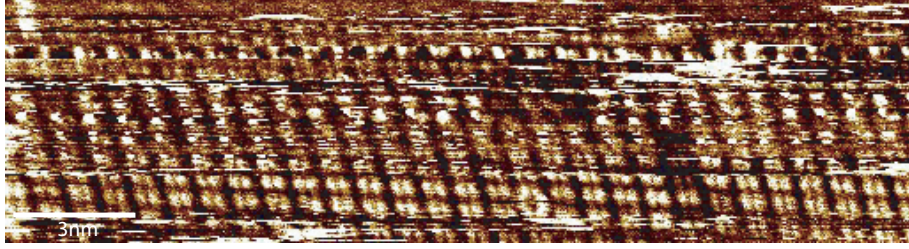


Figure 5.2: First successful NC-AFM imaging of the Si(100) substrate using a qPlus sensor at 77 K. $df = -2.4$ Hz, $A_0 = 8$ nm, $V_{gap} = +0.15$ V

direct comparison with conventional NC-AFM. To the best of our knowledge the first image acquired showing atomic resolution of the Si(100) surface using a qPlus sensor is shown in Fig. 5.2.

Only a couple of rows of unit cells are clearly visible (between noise due to tip instabilities) in this image. However, as more expertise was acquired in both operating the instrument and tip preparation techniques, resolution and tip stability were improved. Fig. 5.3 shows a later scan demonstrating clear atomic resolution across a step edge. Although large patches of noise remain, (most likely due to the tip dropping contamination onto the surface as it scans), a clear $p(2 \times 1)$ periodicity is observed on both terraces along with numerous defects.

The vast majority of imaging performed at high oscillation amplitudes showed the $p(2 \times 1)$ periodicity (that is to say, either no atomic resolution was observed or the $p(2 \times 1)$ periodicity was observed). However, on rare occasions it was possible to observe the $c(4 \times 2)$ phase (see Fig. 5.4).

The most likely reason for this is that in order to obtain atomic resolution without disturbing the surface it is necessary to have a much sharper tip as the background van der Waals contribution must be small enough not to mask the atomic scale variations in force while still being far enough away from the surface not to induce dimer flipping. Fig. 5.4 also shows simultaneous tunnel current data collected during the topographic scan. It is clear that there is a stronger tunnel current associated with some atoms than others even though they appear almost identical topographically. In general it was difficult to acquire high quality tunnel current data alongside atomic resolution topography.

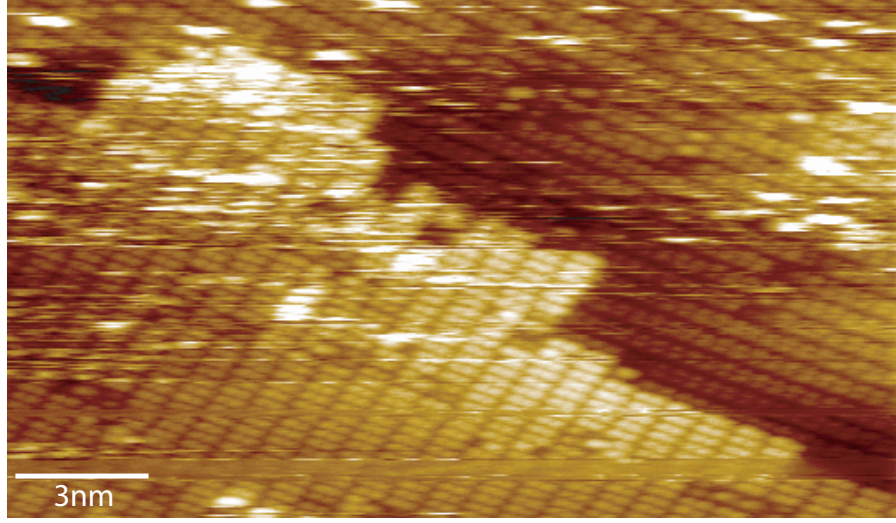


Figure 5.3: Imaging across a step edge using large amplitude showing the $p(2 \times 1)$ phase on the upper and lower terraces. $df = -0.5$ Hz, $A_0 = 5$ nm, $V_{gap} = 0$ V.

One reason for this is that at large amplitudes the tunnel current recorded is a small fraction of the tunnel current that would be recorded were the tip held stationary at the point of closest approach (see Experimental Methods section). Perhaps more important is the fact that the tip bias applied was determined by measuring the contact potential difference between tip and surface. It was found for almost all tips that gave atomic resolution in AFM mode that the contact potential difference varied between 0V and +0.8V, with most contact

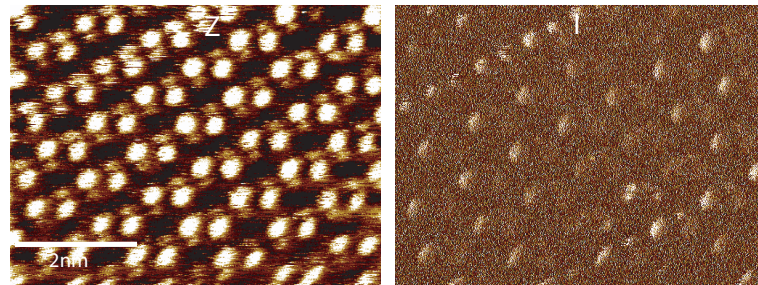


Figure 5.4: Image of the $p(2 \times 2)$ and $c(4 \times 2)$ phases using large amplitude. Note the faint appearance of the lower atoms in the topography, and the very weak (~ 0.1 pA peak current) simultaneous tunnel current signal. $df = -5.9$ Hz, $A_0 = 5$ nm, $V_{gap} = +0.2$ V.

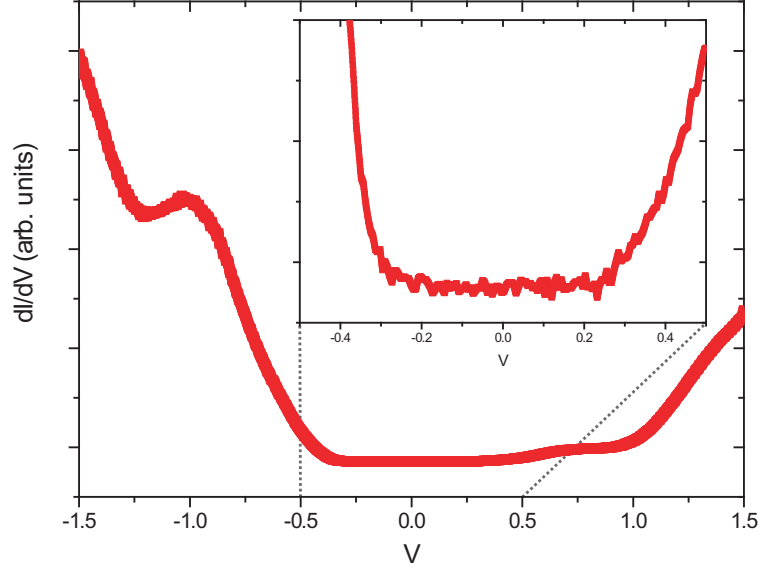


Figure 5.5: dI/dV measurement of the Si(100) $c(4 \times 2)$ surface at 77K showing a lack of states between 0V and 0.25V obtained using a 100mV dither during a scan at +1.5V / 2.5nA. [Data taken by Subhashis Gangopadhyay]

potential differences being between 0V and +0.4V. This places the applied bias in the bandgap of the silicon sample as measured using conventional STM (see Fig. 5.5 for example). As strikingly demonstrated by Sawada et al. [200] and Jelinek et al. [201] the LDOS of a silicon surface can change dramatically in the chemical bonding regime and it may be that the tunnelling data shown here implicitly depends on these changes in the electronic structure. In addition, there is no strict requirement that a tip capable of atomic resolution topography would necessarily have the local density of states required for atomic resolution imaging in the tunnel current at the biases applied. It is, for example, trivial to imagine an atomically sharp, but insulating, tip.

Despite these difficulties, occasionally high resolution data were acquired as shown in Fig. 5.6 and Fig. 5.7. In both, the $p(2 \times 1)$ periodicity is shown over a wide region in the topography, along with a number of associated defects. It is immediately apparent that there are a number of key differences between the tunnel current data and the topography.

In Fig. 5.6 there is very little tunnel current information on dimers making

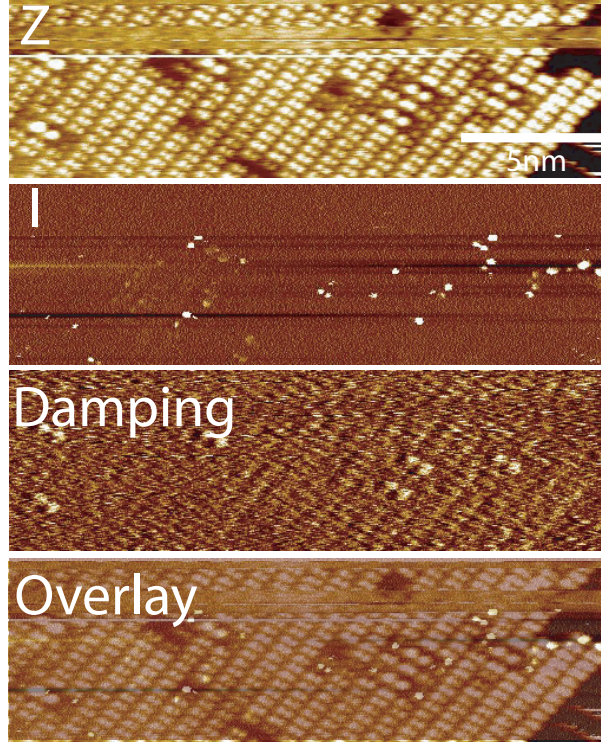


Figure 5.6: Imaging using large oscillation amplitudes showing clear differences between the contrast in Z / damping / I signals. Contrast is enhanced in the tunnel current around a number of the defects on the surface, while the B-Si ad-dimer defects demonstrate enhanced contrast in the damping. $df = -4.8$ Hz, $A_0 = 5$ nm, $V_{gap} = +0.1$ V

up the ‘clean’ surface, however there are clear bright spots isolated around both the corners of the boron induced defects, as well as some of the dimer vacancy complexes and near the step edge. In Fig. 5.7 in contrast, while most (although not all) of the clean surface dimers have a very strong tunnel current signal, the boron induced defects do not seem to have any associated signal, whilst some of the dimer vacancy complexes and areas near the step edge have an extremely strong “diffuse” signal. These features around the defects are indicative of local charging or band bending, and have previously been observed in low bias STM (see Fig. 5.8 [202]). In addition, diffuse areas may be enhanced by the presence of subsurface dopants, which are also observed in low bias STM [203, 204]. More difficult to explain is the appearance of both symmetric $p(2 \times 1)$ and buckled $c(4 \times 2)$ in the tunnel current while only

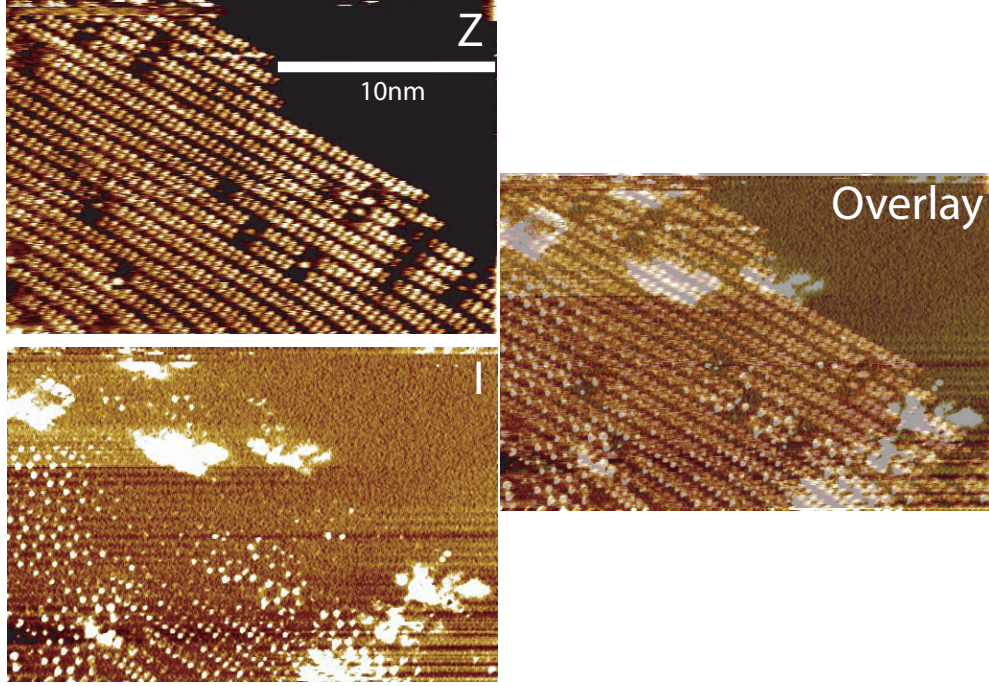


Figure 5.7: Large-scale imaging using large oscillation amplitude with simultaneous tunnel current imaging. Note that due to an apparent difference in tip-sample interaction, resolution on the lower terrace was poor and has been thresholded out. The topography shows a uniformly $p(2 \times 1)$ periodicity, while the tunnel current data shows a mix of buckled and symmetric dimers along with bright regions associated with charging of defects. The overlay demonstrates that the buckled and symmetric dimers in the tunnel current image correspond to the topography. $df = -4.9$ Hz, $A_0 = 5$ nm, $V_{gap} = +0.1$ V.

symmetric $p(2 \times 1)$ is observed in the topography. While either phase might be plausibly explained on its own, it is difficult to interpret the physical origin of both these features in the same image with the same tip and scan parameters. It is conventionally understood that at small positive sample biases tunnelling occurs into the lower atom of the buckled structure while at higher biases there are contributions from the bulk atoms [137]. If the “dimer flipping” model proposed by Kantorovich et al [133] is accepted as the origin of the $p(2 \times 1)$ phase in the topography, then the key information required to interpret the images involves knowing how the local density of states at the dimer varies during the mechanical perturbation, and how the chemical bonding with the tip affects

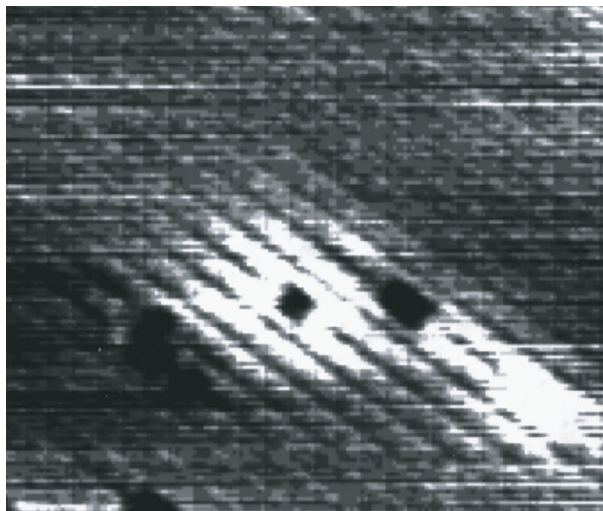


Figure 5.8: Charge around defect imaged at +1.3 V sample bias (at room temperature). Tunneling current 0.2 nA. Image taken from [202]

the LDOS. In addition, it is important to know over what fraction of the total oscillation cycle any modification is present for, and how the modification proportionately affects the topographic and tunnel current imaging. Unfortunately, thus far no detailed combined STM/AFM theoretical studies of the Si(100) surface have been carried out, and it is expected that such simulations will be extremely computationally intensive as simple “perturbation” methods commonly used in simulated STM studies are unlikely to be a valid approximation when considering a system where chemical bonding and mechanical deformation between the tip and the surface is commonplace. We are currently in collaboration with the group of Pavel Jalenik (Czech Academy of Science) to develop first principles calculations to address these issues, but at the time of writing no conclusive results are available. Simple arguments related to the stabilisation of buckling around defects (as seen in room temperature STM and AFM) also cannot adequately explain the images as the $p(2\times 1)$ topography is best interpreted as being due to all of the dimers being flipped during scanning.

Another feature of Fig. 5.6 that has not yet been adequately explained is the failure to image the lower terrace. It was occasionally noticed that step edges seem to interfere with imaging on the lower terrace and although one

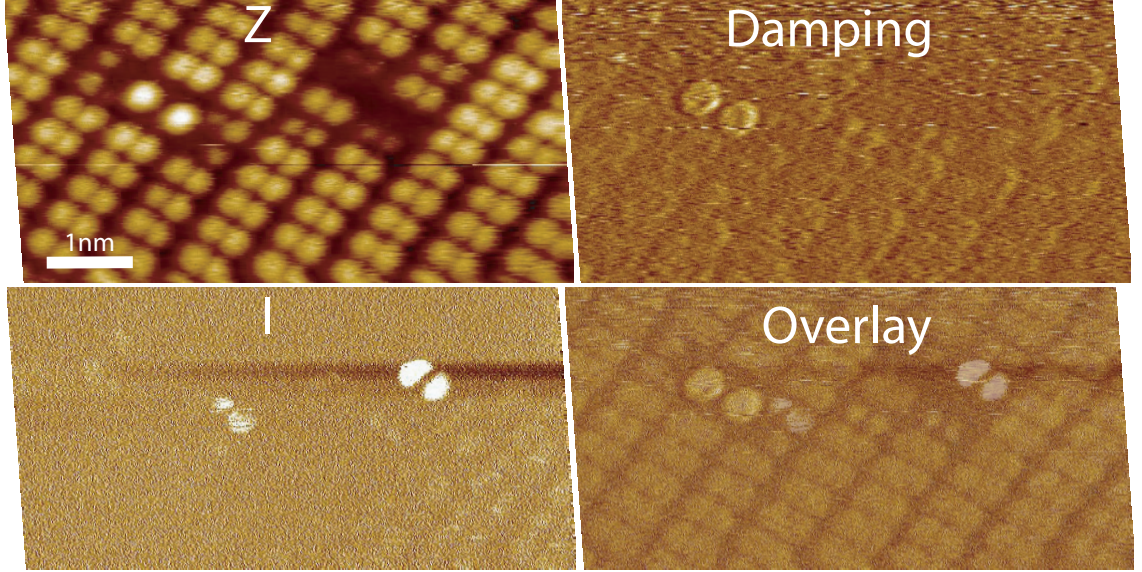


Figure 5.9: High resolution NC-AFM image showing details of two key types of defect on the Si(100) surface. To the left is a boron induced defect, and to the right a complex of 1+2 DV defects. The damping shows strong contrast over the boron defect ad-dimers, while the tunnel current shows an anomalously high tunnel current signal over one of the split off dimers. $df = -5.9$ Hz, $A_0 = 5$ nm, $V_{gap} = +0.2$ V.

other study [205] observed differences in imaging between the upper and lower terraces on the Si(100) surface with NC-AFM, there is no mention of a failure to image the lower terrace. One possible explanation is if the tip had a large radius of curvature with only a small protrusion, then the presence of an upper terrace may prevent the apex from getting close enough to the surface in order to successfully image with atomic resolution - this might also explain the lack of tunnel current signal on the lower terrace. Alternatively, it has been shown on semiconductor surfaces that charge can build up near step edges [206], [207] and so there may be a small difference in contact potential difference close to step edges which could also affect imaging depending on the tip state. A combined qPlus/KPFM study could help eliminate this possibility.

Fig. 5.9 shows a high resolution scan of both a boron induced defect and a number of split off dimer vacancy complexes. Here, similar to Fig. 5.6, we note that the clean surface dimers have a very weak, or no associated

tunnel current signal, whereas the boron induced defect and one of the split-off dimer vacancies do have an associated signal. It is curious that, despite being apparently identical topographically, only one of the split of dimers has an associated strong tunnel current signal. Possible explanations for this disparity include subsurface boron dopants, or possibly effects due to the nearby boron induced defect. Also of interest is the associated damping signal. While there is an associated signal corresponding to the clean surface dimers, it is clear that the boron induced defect has an enhanced signal, indicating a much stronger tip/surface interaction. The detail of the defect structures shown in this image are covered in section 4.1.3 and 5.4.

5.3 Small amplitude NC-AFM imaging

Once imaging had been successfully demonstrated at large oscillation amplitudes, the focus switched to imaging the surface using subnanometre oscillation

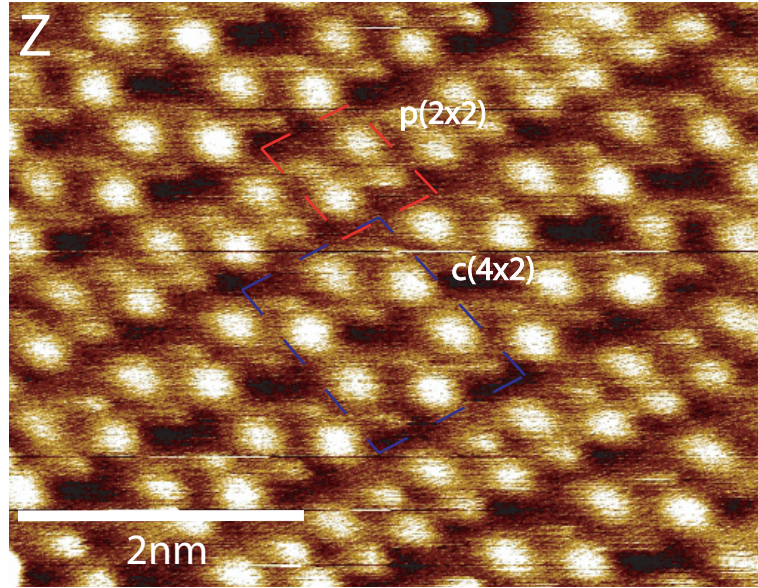


Figure 5.10: *qPlus* NC-AFM image of the Si(100) surface using small oscillation amplitude. Both the $c(4 \times 2)$ and the $p(2 \times 2)$ periodicities are observable, and demonstrate a difference in the apparent intensity of the lower atoms. $df = -10.9$ Hz, $A_0 = 0.35$ nm, $V_{gap} = +0.3$ V.

amplitudes, utilising the ability of the *qPlus* AFM to use oscillation amplitudes on the scale of the length scale of the chemical interaction between the tip and sample. Fig. 5.10 demonstrates similar features to Fig. 5.4 but is of higher quality. It is interesting to note that rows that are in phase with one adjacent row (i.e. a $p(2 \times 2)$ row) image differently from rows in the $c(4 \times 2)$ arrangement. The difference in apparent height between the upper and lower atoms of the dimer is reduced in these rows giving the row a more $p(2 \times 1)$ like appearance. In this image the associated tunnel current data (not shown) featured a “diffuse background” that prevented clear imaging. This may be due to nearby defects similar to the effect seen in Fig. 5.7.

5.4 Imaging of defects

In addition to the clean surface, the various defects observed on Si(100) are of theoretical and experimental interest and have been the subject of previous STM studies [147–149, 151–154, 202, 204, 208]. In this section the imaging of defects on the Si(100) surface with small and large oscillation amplitude NC-AFM is presented, along with a comparison of the images with the most recent structural models.

5.4.1 Boron induced defect

The distinctive ‘double protrusion’ boron induced defect has been the subject of numerous investigations, most recently a combined systematic STM / DFT / simulated STM study [154]. The most recent model proposed in that work, selected from a number of structures investigated using DFT simulations, agrees well with the data from our AFM scans. Fig. 5.11 shows line profiles from a high resolution AFM image and Fig. 5.12 shows a comparison between data taken from line profiles taken across the defect, and data from DFT calculations kindly provided by Z. Liu et al. (private communication). The quoted errors in the theoretical calculation are taken from the range of positions of atoms in a given layer (i.e. from the upmost “up” atom to the lowest “down” atom) and therefore should provide a range in which we would

expect atoms in that layer to lie. It should also be noted that while the experimental values seem to lie consistently at the top of the range of values predicted in theory, if the tip is mechanically interacting with the dimers and imaging each atom as a “up” atom due to mechanical flipping then we would expect the vertical position of the atoms to lie in the upper half of this range.

With this in mind, it should be noted that the apparent heights of the features (for example the difference in height between the clean surface dimers and the “dark” region of the defect or the relative apparent height of the silicon adatoms above the surface) vary with tip condition and scan parameters. Analysis of the depth of the depression (i.e. the difference in height between clean surface atoms on the surface and the dark region of the defect) showed a range of values from around 40 to 85 picometres for large amplitude scans, while for low amplitude scans the same distance was measured to be between 2 and 17 picometres. The height of the silicon adatoms above the clean surface dimers did not seem to show any variation with oscillation amplitude, with a range of values from around 5 picometres to 65 picometres recorded over a range of scan parameters. It should be noted that the limited number of images acquired does not allow for a rigorous statistical analysis, and, as with many features, the most important factor is overwhelmingly likely to be the configuration of the tip apex. All of the values recorded fall within the values allowed for the proposed energy minimised DFT model. That said, only a comprehensive simulated NC-AFM experiment will reveal quantitative information about how the tip distorts the position of the atoms as it images a defect of this type.

In Fig. 5.13 we observe a boron induced defect with high resolution. Here the “dark” region of the defect is also imaged (these features are also imaged, but less clearly, in Fig. 5.9). In addition to the internal structural details, it is obvious that there is a very strong interaction between the tip and the silicon adatoms on top of the defect. This images as both a “scratching” in the topography and an extremely bright signal in the damping image - using the method outlined by Giessibl to estimate the dissipation per cycle [83] provides an estimate of $\sim 100\text{meV/cycle}$ for the clean surface and $\sim 180\text{meV/cycle}$ on the B-Si ad-dimers. Fig. 5.14 shows a sequence of images of the same de-

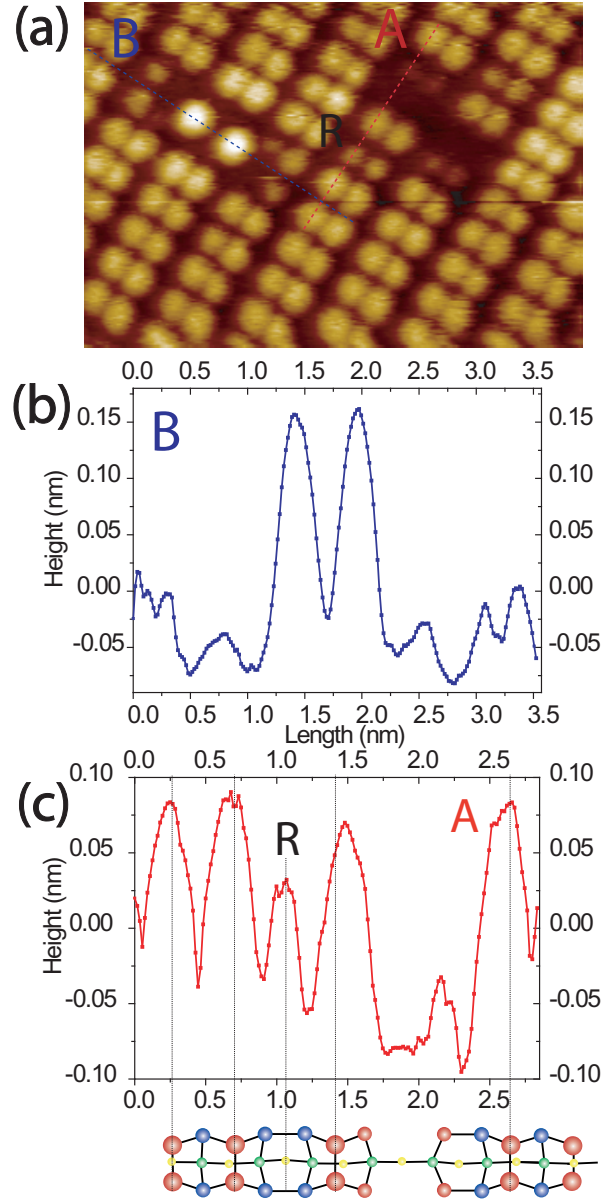


Figure 5.11: Detail of the defect structures shown in Fig. 5.9 b) and c) show line profiles over the boron induced defect and 1+2 DV defect respectively. In c) a comparison with the currently accepted model [149] is shown with the anomalous “recessed” dimer position labelled R.

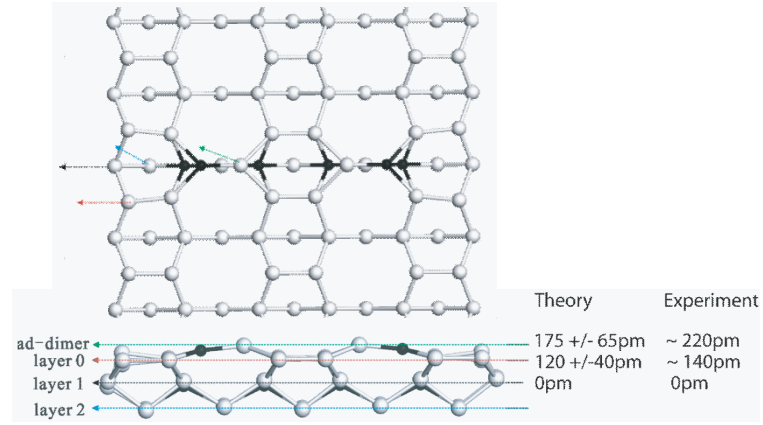


Figure 5.12: Ball and stick model of the most recently proposed structure for the boron induced defect. In the side on view a comparison between experimentally measured and theoretically predicted heights for atoms in the structure is given showing good quantitative agreement. Ball and stick model and atomic position information courtesy of [154]

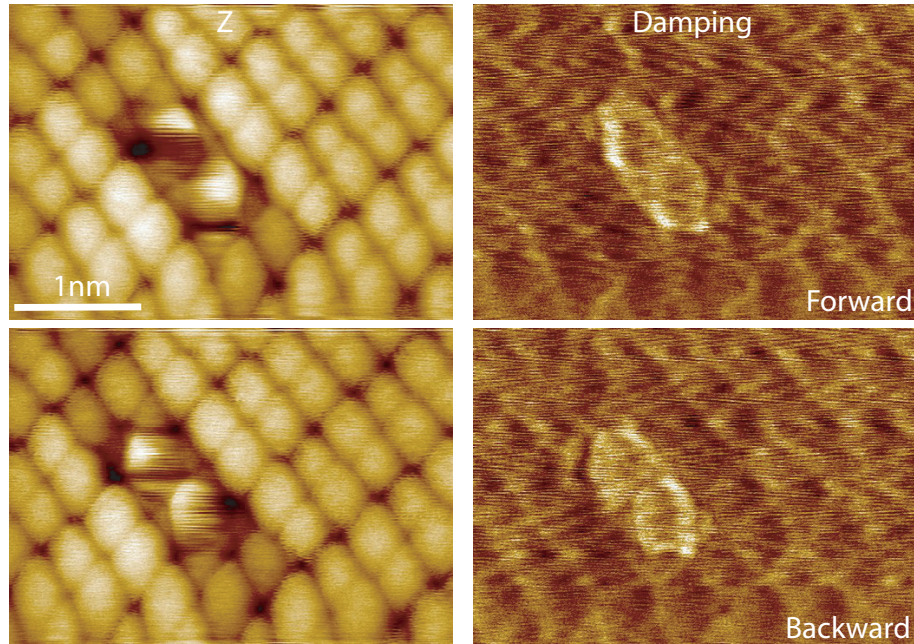


Figure 5.13: Small amplitude imaging of the boron induced defect showing internal structure of the defect, and strong tip - sample interaction in the damping over the Si-B ad-dimers. $df = -18$ Hz $A_0 = -0.25$ nm, $V_{gap} = +0.2$ V.

fect type taken with a different tip. Initially, row resolution is achieved in the topography, while the tunnel current shows a buckled structure. At higher setpoints a symmetric structure is observed around the defect in the topography, while again a mix of buckled structures and symmetric structures is observed in the tunnel current (similar to Fig. 5.7). The highlighted dimers close to the defect show a transition from the $c(4 \times 2)$ to $p(2 \times 1)$ arrangement, whereas dimers in different positions relative to the defect do not show this transition even though topographically the surface images as a $p(2 \times 1)$ unit cell. Fig. 5.16 shows an image of two boron-induced defects at low setpoint with poor topographic resolution, but the tunnel current clearly shows buckled dimers around the defect when only weakly perturbed by the tip. In contrast with Fig. 5.13 no damping contrast was detected.

We generally find good agreement with the most recent proposed model, but an intriguing feature of the imaging of these defects is the failure to observe both the boron and silicon adatoms (i.e. we only see a double, rather than quadruple protrusion). Most likely this is due to the lack of dangling bonds associated with the boron atoms, which might reasonably be expected to reduce the tip-sample interaction. Nonetheless it is curious that they apparently produce no contrast in either STM or AFM images, and this is likely to be a subject of further investigation experimentally and theoretically.

5.4.2 1+2DV defect

In addition to the boron-induced defect, Fig. 5.11 shows line profiles taken over one of the 1+2DV defects, and comparison with the most recent structural model (see section 4.1.3). In the case of the 1+2-DV complex it can be seen that in general there is good agreement with the proposed model, with the exception of the position marked R on the line profile. Here we observe what appears to be a recessed dimer in the gap between the row and the split off dimer.

This feature was not noted in a systematic STM study recently carried out by Schofield et al. [151], but recent high-resolution images taken in our group - see Fig. 5.17 - seem to indicate a similar feature. In addition Fig. 5.18 shows

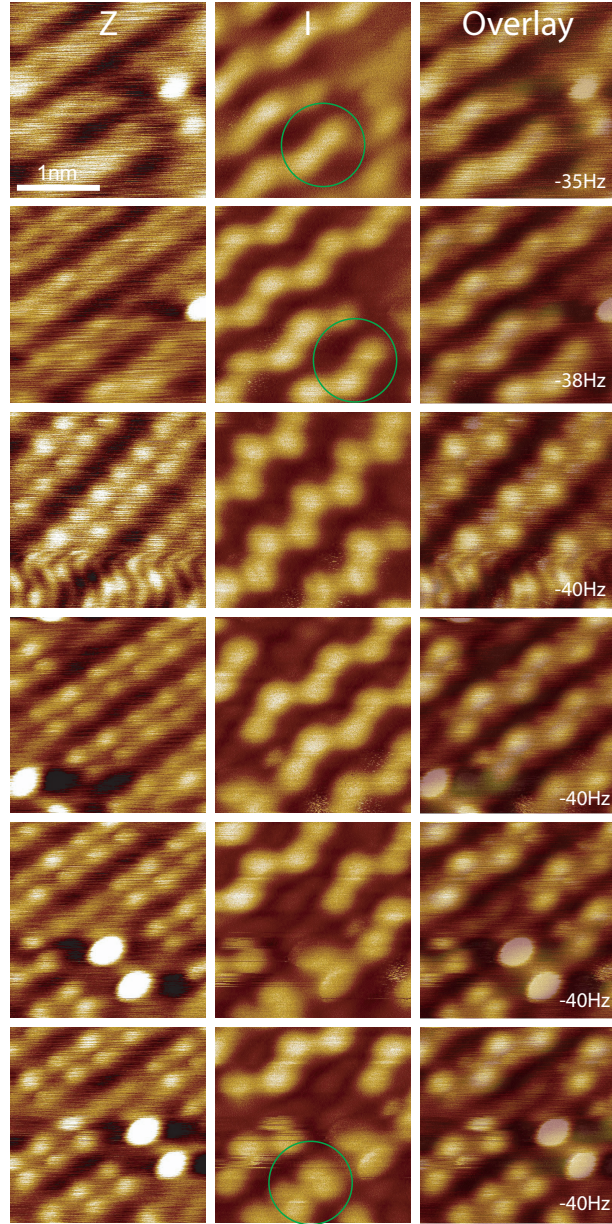


Figure 5.14: Frequency shift (df) setpoint dependent imaging of the B-induced defect with simultaneous tunnel current. At low df diffuse rows appear in Z with a buckled structure in tunnel current. At high df a symmetric structure is imaged in the topography, while a mix of symmetric and buckled dimers appears in the tunnel current similar to images taken at large oscillation amplitudes (see Fig. 5.7). The circle highlights the same dimers throughout, but note this area has drifted out of frame in some of the images. The topographic imaging of the defect appears qualitatively similar to high positive bias STM imaging, while the tunnel current image has appearance closer to low positive, or negative bias imaging (see Fig. 5.15). $A_0 = 0.25$ nm, $V_{gap} = +0.3$ V.

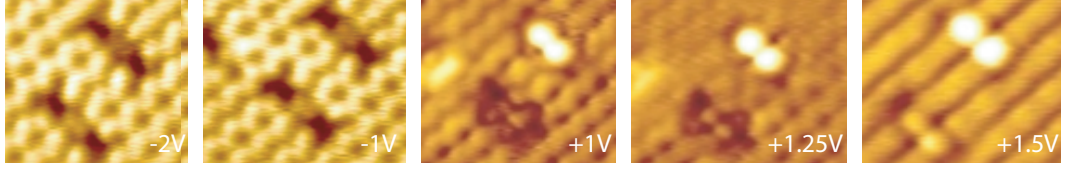


Figure 5.15: Conventional STM of boron induced defects at various bias voltages. Setpoint 500pA. Images courtesy of Subhashis Gangopadhyay

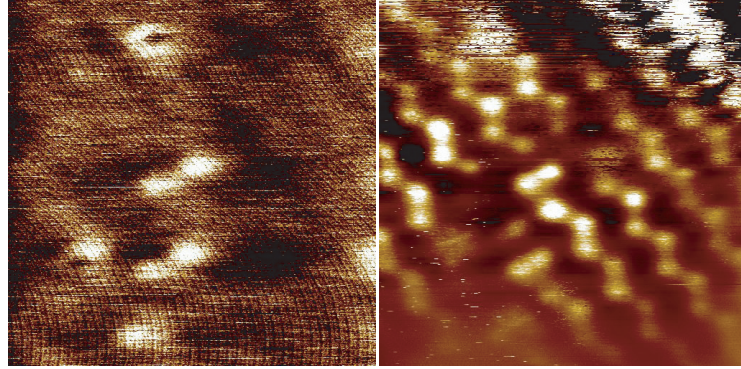


Figure 5.16: Additional image of boron defects taken with small oscillation amplitude. At low setpoint only poor resolution is observed in the topography, but a clear buckled structure is observed in the tunnel current image, confirming a buckled structure around the defects in the absence of a strong tip sample interaction. $df = -6$ Hz, $A_0 = 0.35$ nm, $V_{gap} = +0.35$ V

a series of scans showing an area of the surface with the 1+2 DV complex at different setpoints using the same tip as in Fig. 5.21. The same transition between buckled structure and symmetric structure is demonstrated, but the key feature to note is the appearance of a “recessed” dimer in between the split off dimer and the main dimer row. These observations with both high amplitude AFM, high resolution STM, and *qPlus* AFM seems to suggest that there is a deficiency with the currently accepted model for defects of this type. It should be noted that an earlier model proposed by Ihari et al. [209] did feature a recessed dimer in this position and may provide an explanation for the observed data. We are currently in the process of running DFT calculations to reassess the energetic stability of such an arrangement.

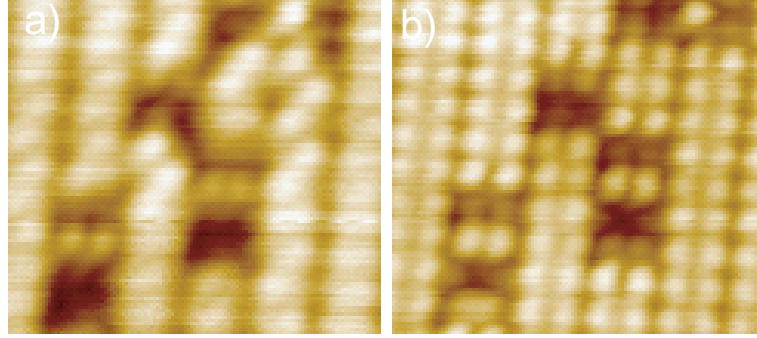


Figure 5.17: Very high tunnel current setpoint imaging of the 1+2 DV in dual bias STM. a) -1.5 V 17 nA, b) + 1.5 V 17 nA. The “recessed” dimer is clearly visible at positive bias voltage, but apparently invisible at negative bias voltages. Image appears courtesy of Subhashis Gangopadhyay.

5.5 Setpoint variation

A primary research goal was the reproduction, and further investigation, of the apparent $p(2\times 1)$ periodicity observed at low temperatures due to mechanical dimer flipping postulated in [133]. A specific objective was to investigate the evolution from the buckled to symmetric structure with varying tip/sample interaction strength. Fig. 5.19 demonstrates this clearly, with a $c(4\times 2)$ periodicity observable at low setpoints and an increasing “ 2×1 ”-like nature becoming apparent at higher setpoints. The asymmetry in the topography even at a higher setpoints has been predicted for scans at 77 K using simulated NC-AFM imaging from DFT simulations (see Fig. 5.20 [133]) and is a consequence of there being sufficient thermal energy for a flipped dimer to “heal itself” (i.e return to its initial configuration) during the parts of the oscillation cycle where the tip is not close enough to the surface to pull the lower atom out of position. The increase in the damping signal with stronger tip/surface interaction is again expected if the dimers are being mechanically flipped. In both the topography and the damping signals, however, a strong asymmetry is observed. While the “up” atoms of the dimers appear to image with roughly the same intensity, the “down” atoms of the dimers image with a stronger apparent intensity when they are on the left-hand side of the row (with respect to the image shown), while, conversely, atoms on the right-hand side of the

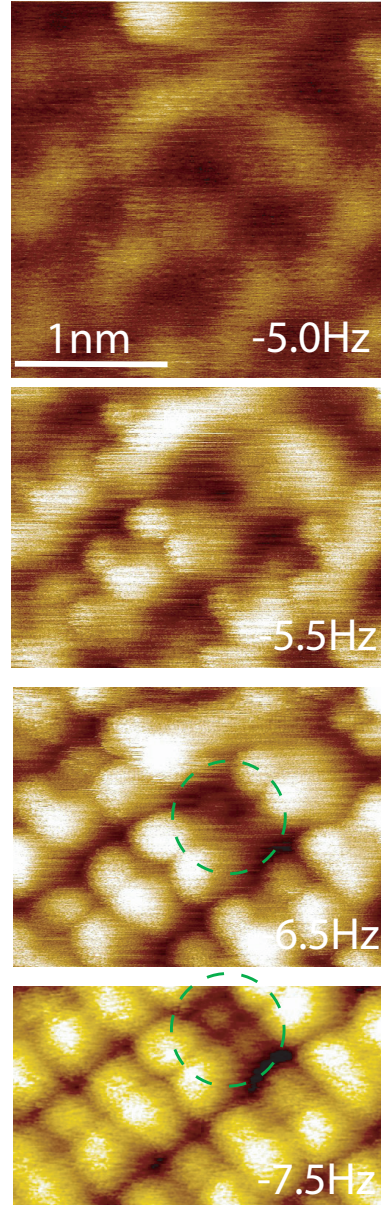


Figure 5.18: Setpoint dependent imaging at low oscillation amplitude of the 1+2 DV defect confirming observation of the “recessed” dimer. Final image has been 3x3 low pass filtered. $A_0 = 0.25$ nm, $V_{gap} = +0.4$ V.

rows appear to be associated with a stronger damping signal.

The same features were present in both forward and backward scans and so are unlikely to be an artefact caused by a strong asymmetry of the tip (see later sections). That said, the clear “square” nature of the imaging in the damping and even the topography (at the highest setpoint shown) indicates that the tip structure is influencing the imaging in a way we do not yet clearly understand. With regards to the simultaneous tunnel current images the first feature to note is the inverted imaging of the dimers themselves. At the voltages used a strong tunnel current signal associated with the gaps between the rows is unusual but not unprecedented [137], but it is difficult to explain why the atoms themselves appear inverted. One possible explanation is that the mechanical flipping of the dimers into a “up” position shuts off the primary tunnelling pathway at positive bias voltages. However this interpretation is not wholly consistent with other observations using different tips where bright spots in the topography correspond to bright spots in the tunnel current. Simulations have indicated that contrast inversion in the tunnel current is a possible consequence of tunnelling in the chemical bonding regime [201] on the Si(111) surface and it is possible a similar effect could be responsible for the features observed here. The second feature of note is the very bright tunnel current signature that apparently has no corresponding feature in either the topography or the damping. A plausible explanation for this is the presence of subsurface boron dopants which have been shown to image as bright double protrusions with some tips at low bias voltages [203]. This feature appears much more localised than in previous STM observations, but it must be remembered that not only is the bias lower, but the tip-sample distance is likely to be over an order of magnitude smaller and so qualitative differences might be expected. Whatever the origin it seems likely to be a subsurface feature as any contamination or surface defect should produce corresponding features in the topography and/or damping.

Although Fig. 5.19 shows excellent agreement with our current understanding of how AFM imaging affects the Si(100) surface it is important to consider how different tips states can affect imaging. In Fig. 5.21 a different sequence is presented. Although a transition from a buckled structure to a near symmetric

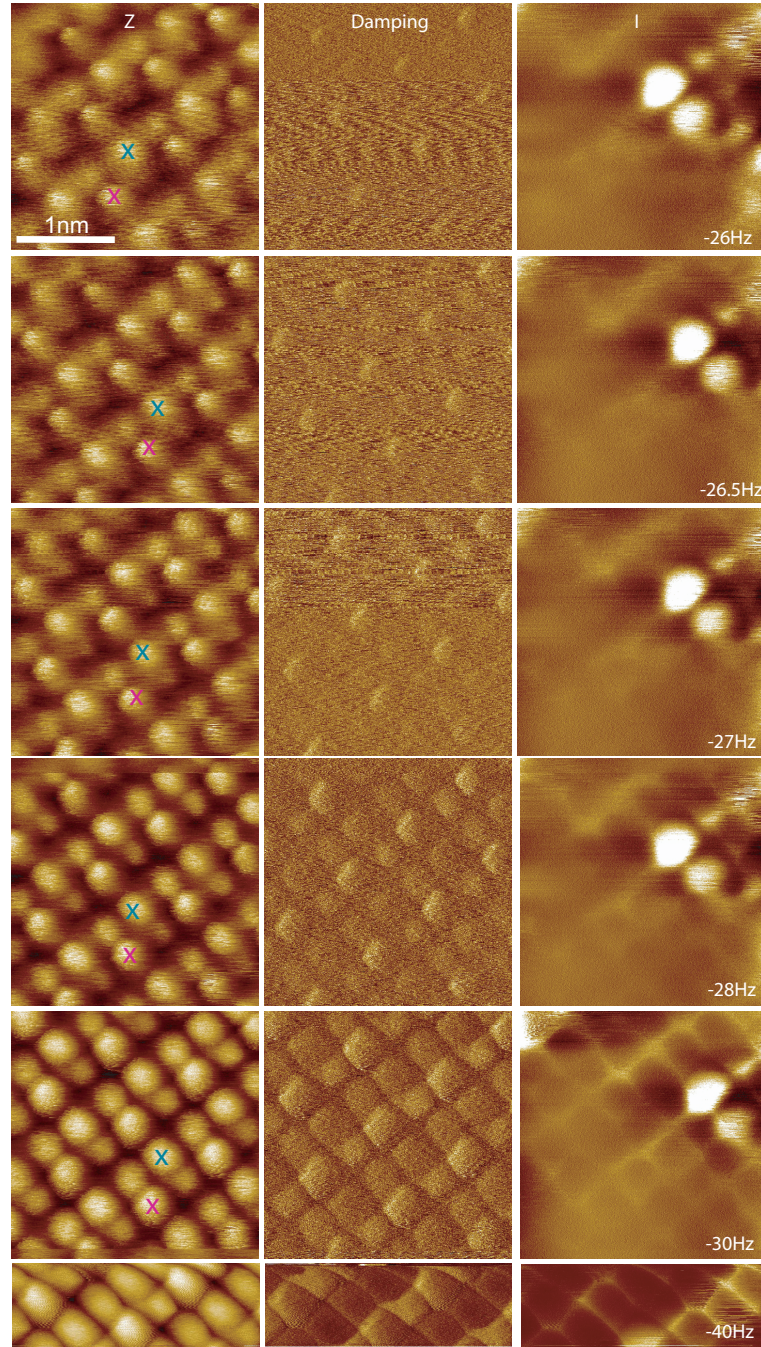


Figure 5.19: Series of images demonstrating the effect of increasing setpoint during imaging. At low setpoints (-26 Hz) a buckled structure is observed in the topography. With increasing setpoint the lower atom intensity increases, as does contrast in the damping and tunnel current signals. X's indicate the same atoms in each image $A_0 = 0.25$ nm, $V_{gap} = +0.8$ V for all images.

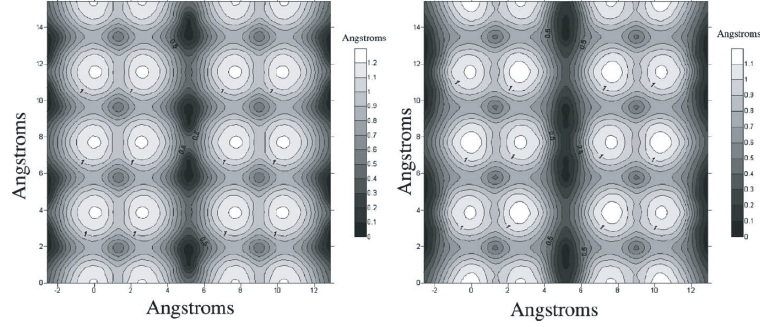


Figure 5.20: Simulated NC-AFM scans of the $c(4 \times 2)$ structure with high setpoint resulting in an apparent $p(2 \times 1)$ structure at 0K (left) and 100K (right). Note the residual asymmetry at 100K. Image taken from [133]

structure is again clearly demonstrated, careful analysis of the transition shows that unlike the previous sequence (where the lower atoms slowly increased in intensity until imaged with almost the same brightness) here the upper atoms that are imaged initially appear to “rotate” until they form the right-hand side of the dimers in the final apparently symmetric scan. This can be seen most clearly by following the two marked atoms through the sequence. Again, a most plausible explanation for this is some kind of tip asymmetry, or possibly even an atomically sharp apex, terminated with more than one dangling bond (as posited in [18] for example). In this sequence faint contrast was observed in the damping at the highest setpoint (see inset of final image) but no tunnel current was detected.

Initially, the key goal of SPM science was to produce atomic resolution, but as work continues on well defined substrates it is clear that the challenge is now not to simply image the surface, but to begin the (much more challenging) task of understanding the interaction between real (as opposed to idealised) tips and the surface. Although we can safely ignore blunt and obvious ‘double’ tips we must acknowledge the role of the tip apex and not cherry-pick data that comfortably fits our assumptions. For example, while in Fig. 5.22 the same experiment was performed as exemplified by Fig. 5.19 and Fig. 5.21, it is clear that the buckled structure is not clearly observed at low setpoint and that atomic resolution is only obtained at high setpoints, and then only a symmetric structure is imaged. An attempt was made to increase sensi-

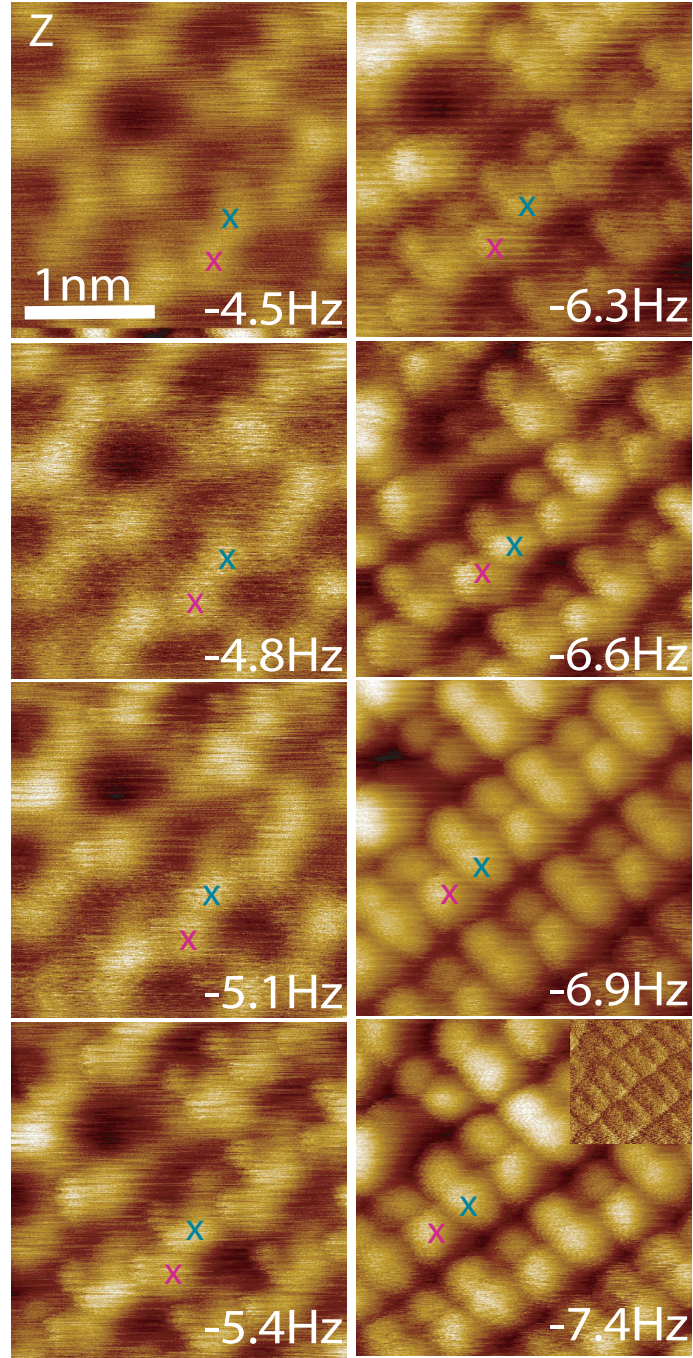


Figure 5.21: Series of images with a different tip showing the buckled to symmetric transition with increasing setpoint. In this instance the transition is less clear, and it is difficult to pinpoint the transition of the lower atoms into the symmetric structure (Inset final image: damping signal after applying 3x3 low pass filter). X's indicate the same atoms in each image. $A_0 = 0.25$ nm, $V_{gap} = +0.4$ V

tivity to short-range forces by reducing the oscillation amplitude by a factor of two, however the subsequent set of images still fails to show the buckled structure and again only the symmetric structure is imaged at high setpoints. A plausible explanation for this is that the tip structure in this set of images was relatively blunt, and so long range van der Waals forces prevented atomic resolution imaging far away from the surface - once close enough to achieve atomic resolution the tip/surface interaction is likely to have been sufficiently strong that only the symmetric structure could be observed.

Similarly, in Fig. 5.23 an intriguing dataset recorded using a different tip is presented. The atomic structure is clear in both topography and tunnel current, although curiously in the topography at low setpoint a diffuse $c(4 \times 2)$ “overlay” is seen on the rows. Comparing the topography and the tunnel current it appears that this diffuse buckled structure corresponds to regions in the tunnel current that seem to image as “down” atoms. As the setpoint is increased the intensity of this “diffuse” structure is reduced and a more conventional $p(2 \times 1)$ periodicity is resolved in the topography, but curiously a buckled structure remains for the most part in the tunnel current. Whilst this imaging is no doubt indicative of an unusual tip structure it vitally demonstrates the need for studies utilising both force and tunnel current information. Were either of the data channels at high setpoint taken in isolation it might be assumed that the tip structure was (from a practical SPM standpoint) functionally “normal”, i.e. atomically sharp and producing an expected structure with atomic resolution. However, by combining both channels it is clear that the tip - surface interaction in this case is far from trivial. Data such as these demonstrate that even greater care must be taken when interpreting images that only provide one of the data channels (for example in conventional STM or NC-AFM). In this case looking at the topography we can say that in light of the other data presented it confirms the buckled to symmetric transition, but the tunnel current reveals that this simple interpretation cannot be the whole story.

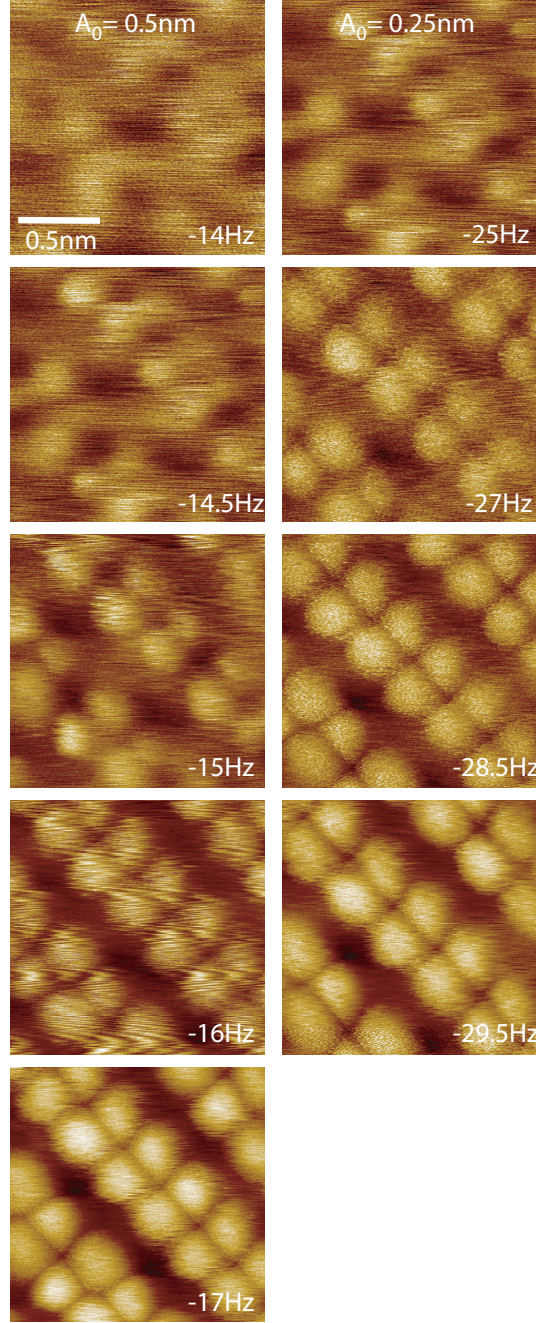


Figure 5.22: Setpoint dependent imaging of the same region with two different oscillation amplitudes failing to show a buckled to symmetric transition. Although a $p(2 \times 1)$ symmetric structure is imaged at high setpoints, at low setpoints the buckled structure is not observed, possibly due to a blunt tip. $V_{gap} = +0.2$ V for all images.

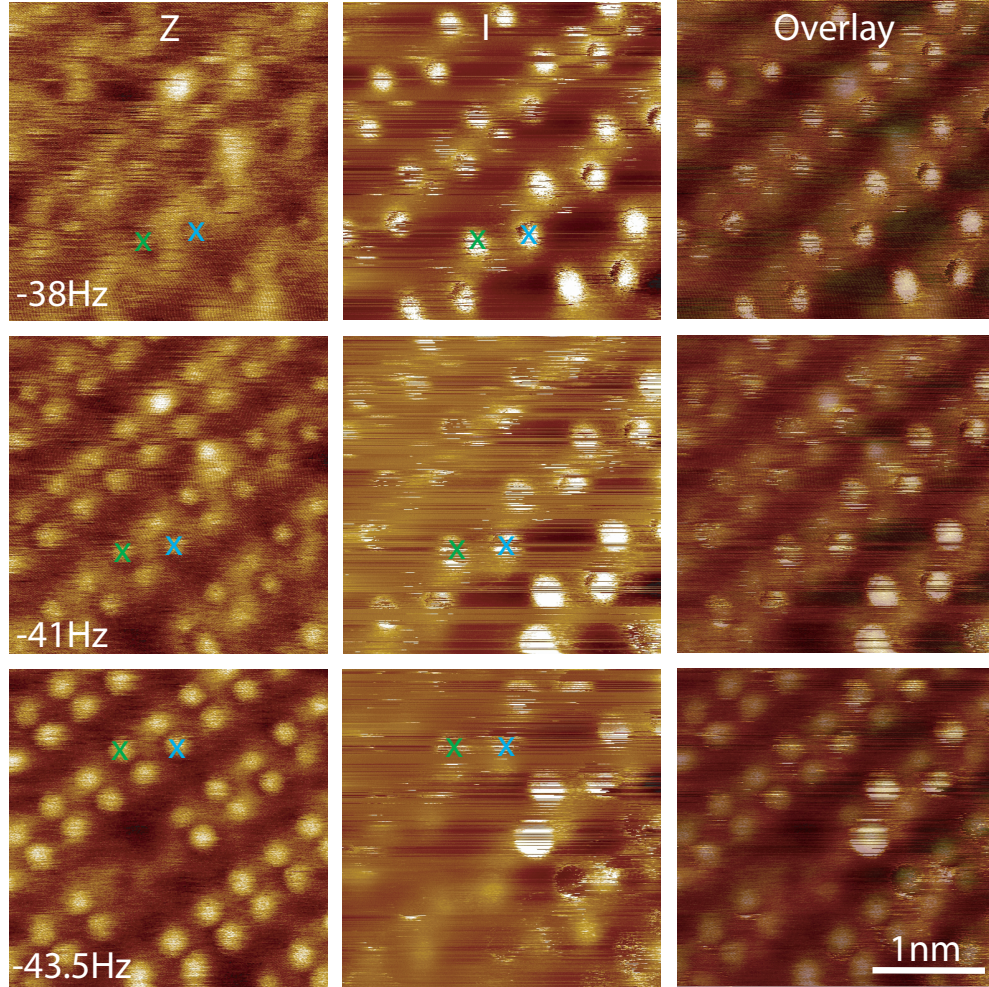


Figure 5.23: Series of images with a tip showing the topographic and tunnel current imaging with increasing setpoint. Note the ‘diffuse buckled’ structure at low setpoint. Due to drift there is a small shift in the observed region. X’s indicate the same atoms in each image. $A_0 = 0.25$ nm, $V_{gap} = + 0.3$ V

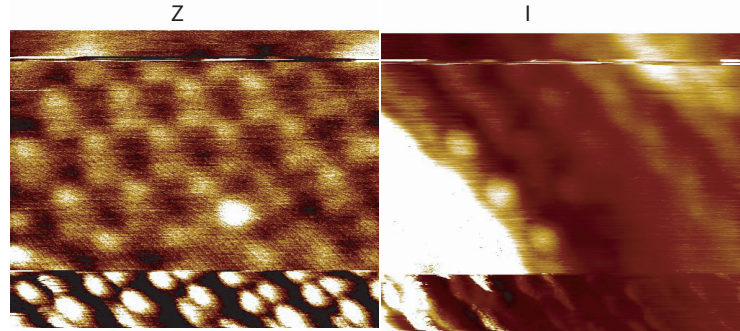


Figure 5.24: Tip event showing a dramatic change from clear symmetric p(2x1) to low resolution buckled p(2x2) structure indicating a strong change in the tip – sample interaction. The corresponding tunnel current data also indicates a large change in the electronic structure of the tip. $df = -7.5$ Hz, $A_0 = 0.35$ nm, $V_{gap} = +0.35$ V

5.5.1 Apex variation

It is well known that apex variations during SPM can result in changes in imaging, but in the case of the Si(100) surface we have the added possibility of not only undergoing a transition in the quality of the imaging (as for most substrates), but, if we are particularly fortunate, a change in interaction strength that shows the buckled to symmetric transition. Fig. 5.24 presents a good (but rare) demonstration of a direct change in tip state on the apparent imaging of the surface. At the bottom of the image a clear p(2x1) reconstruction is observed, but a sudden tip event causes the imaging to change radically and for a buckled structure to be imaged. This clearly demonstrates that a change in the interaction strength between the tip and the surface due to the tip termination changes whether the tip is able to flip dimers as it scans over them. Interestingly, the simultaneous tunnel current image shows that the electronic configuration of the new tip is also radically different as, in addition to the change from symmetric to buckled imaging, bright regions, possibly associated with defects on the surface start to dominate.

Fig. 5.25 provides another striking example of the radical effect tip changes can have on imaging. Initially the p(2x1) structure was observed, but after a tip event an *inverted* buckled structure was observed. Even more inter-

estingly the subsequent series of images taken with increasing setpoint clearly show the inverted buckled structure stating to show protrusions rising from the centre of the depressions. The image then goes through what appears to be an “intermittent phase” (qualitatively similar to a transition shown in [131]) before producing a conventional symmetric-like structure at very high setpoints, with an associated increase in the damping signal. Contrast inversion has been widely reported during noncontact AFM experiments, on both clean substrates [210, 211], and during imaging of adsorbates and molecules [212, 213]. Although there is still some debate as to the mechanism for contrast inversion depending on the system in question, in general the inversion is ascribed to a crossover in the frequency shift curves between two regions as detailed in [213]. It has been shown that in general for constant frequency shift experiments, that contrast inversion requires the force profiles for two sites be different, and not just shifted in the Z plane. It is also not unexpected that by increasing/decreasing the setpoint it is possible to pass through a crossover point and invert the contrast.

Despite the array of features observed during imaging, it is clear that the ability to collect high-quality topography and tunnel current data simultaneously during NC-AFM is vital to understanding the state of the tip. It is expected that as theoretical techniques continue to improve, the information collected during these simultaneous scans will allow a much higher degree of qualitative and quantitative understanding to be reached as to the various tip states that are present during the imaging of surfaces. As noted we are currently in collaboration with the theoretical groups of Pavel and Perez in order to develop simulations incorporating these elements. A knowledge of not only the force interaction, but the overlap of the local density of states, provides a great deal of additional information that is vital in aiding the interpretation of images taken during scanning probe microscopy.

5.6 Asymmetric scans

It was occasionally noticed during scanning that there were strong differences between the forward and backward traces of the topography. The most com-

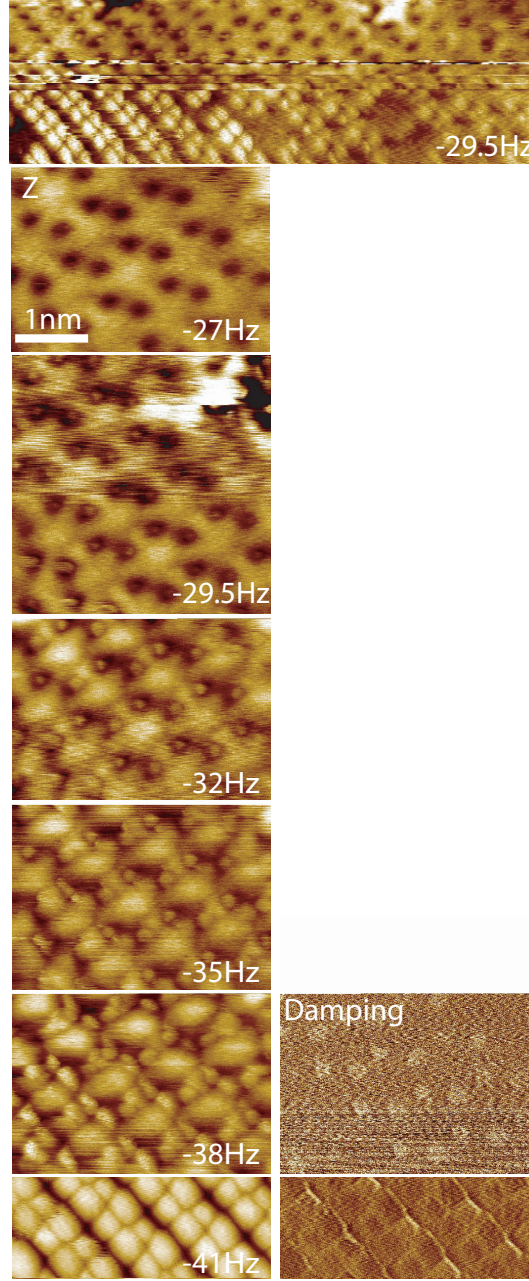


Figure 5.25: Rare example of a sudden tip change causing image inversion, and subsequent setpoint dependent imaging. Initially the symmetric $p(2 \times 1)$ structure was imaged, after tip change an inverted $c(4 \times 2)$ appeared. Subsequent setpoint increases show a “intermittent” phase, but eventually recover the $p(2 \times 1)$ periodicity. At high setpoints a transition from $c(4 \times 2)$ to $p(2 \times 1)$ is also observed in the damping. $A_0 = 0.25$ nm, $V_{gap} = +0.2$ V

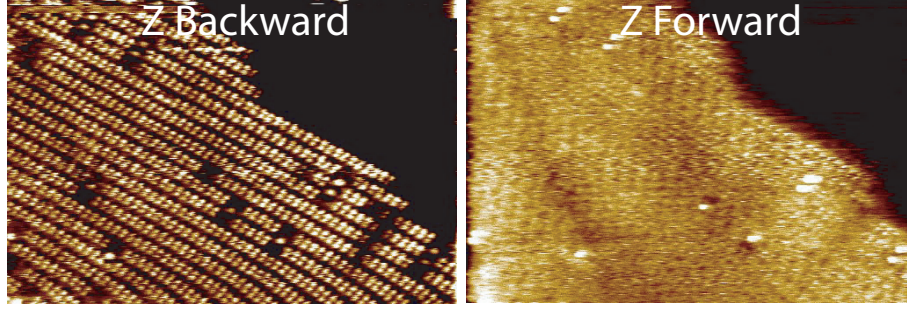


Figure 5.26: Example of asymmetric imaging, clear atomic resolution is observed in the backwards scan, but only a diffuse structure is observed in the forward scan. The diffuse imaging suggests a poorly resolved buckled structure. $df = -4.9$ Hz, $A_0 = 5$ nm, $V_{gap} = +0.1$ V.

only observed example of this is shown in Fig. 5.26, where clear atomic resolution is demonstrated in the backwards scan, but only very diffuse imaging is present in the forward trace (the only clear features being the protrusions associated with the boron induced defects and the step edge). However, on rare occasions differences in forward and reverse imaging were observed which showed atomic resolution in both directions. Examples of this are shown in Fig. 5.27 and Fig. 5.28. This is particularly clear in Fig. 5.28 (large amplitude scan) where on the upper terrace both scans show the $p(2 \times 1)$ periodicity, but on the lower terrace the forward trace shows $p(2 \times 1)$ while the reverse trace shows a $p(2 \times 2)$ structure.

Fig. 5.27 shows a series of small amplitude scans, with simultaneous tunnel current imaging. In the first set of images a buckled structure is observed in both forward and back in the topography and the tunnel current. This is still the case in the next set of images. However, in the final set (at still higher setpoint) in the forward scan a mostly buckled structure is observed, while in the reverse scan a $p(2 \times 1)$ periodicity is observed in both topography and tunnel current. Interestingly, in the tunnel current images a large number of the atoms are associated with “flicker” noise.

In conventional STM “flicker” noise of this type is associated with dimers that are being flipped as the tip passes over them, thus preventing clear imaging of any particular phase. It is not yet understood whether the flickering in these images is the result of the tip being on the threshold of mechanically flip-

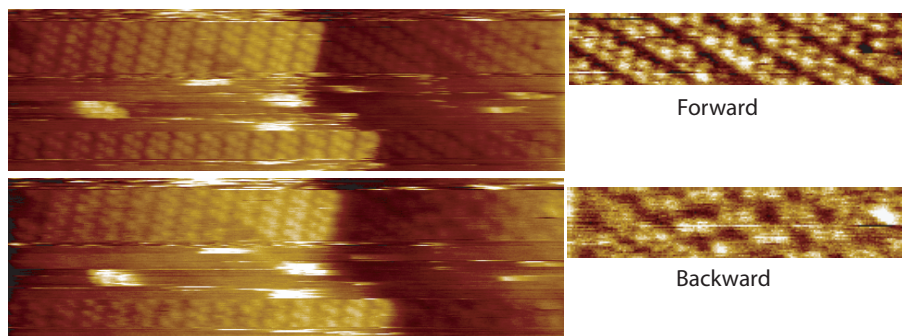


Figure 5.27: Asymmetric imaging with atomic resolution in both directions at large oscillation amplitude, showing $p(2 \times 1)$ in the forward trace, and a buckled structure in the reverse. Curiously on the upper terrace the imaging is approximately the same in forward and reverse with a $p(2 \times 1)$ structure in both. $df = -0.5$ Hz, $A_0 = 5$ nm, $V_{gap} = 0$ V.

ping the dimers, or whether the associated tunnel current is causing the atoms to flip in addition to any influence of the tip, and any interpretation is further complicated by the asymmetry in the imaging between the forward and backward scans. An obvious question to ask is how a rotation of the scan direction would affect the observed asymmetry. Unfortunately, tips demonstrating an asymmetry in scan direction, with atomic resolution in both directions were only rarely observed, and maintaining tip stability during long sequences of experiments proved to be problematic. Additionally, in most experiments we rotated the scan direction so as to minimise the slope of the sample due to issues with feedback ‘overshoot’ at the edge of scans. Therefore, as yet, an investigation on the effect of scan direction on the asymmetry has not been carried out.

5.7 Force spectroscopy

Although NC-AFM and STM imaging provide detailed atomic scale representations of the surface, a valid criticism is that they can fail to provide quantitative information about the interaction between the tip and the sample. One way to offset this shortcoming is to carry out so-called “force spectroscopy” experiments in which various parameters are measured as the tip position is

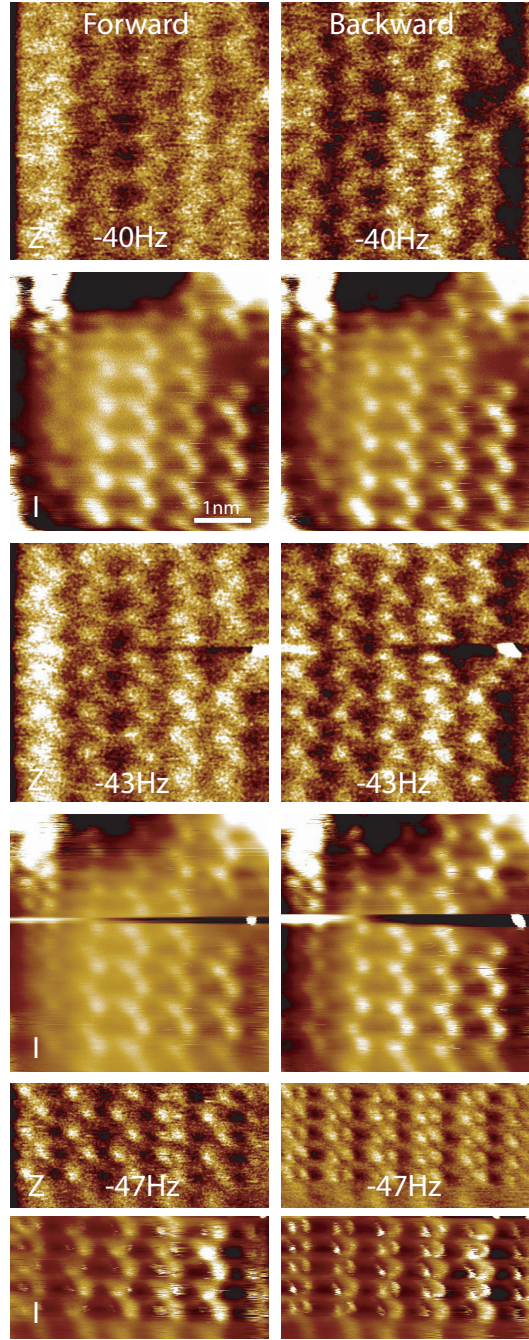


Figure 5.28: Asymmetric imaging observed at small oscillation amplitude with simultaneous tunnel current imaging. At low setpoints a buckled structure is observed in both the topography and tunnel current. At higher setpoints, however, a symmetric structure is observed in the reverse trace in topography and tunnel current, while a mix of buckled and symmetric dimers is seen in the forward trace. Curiously “flicker” noise is observed over some dimers in the tunnel current. $A_0 = 0.35$ nm, $V_{gap} = +0.35$ V.

shifted vertically (or laterally) with respect to the surface. These techniques, when combined with state-of-the-art DFT calculations (as detailed in works such as Sugimoto et al. [22], Ternes et al. [24] and Gross et al. [25]), are beginning to provide *quantitative* information about the tip-sample interaction. As such, spectroscopic measurements were conducted during a number of scans that demonstrated atomic resolution imaging. In addition to the frequency shift, the tunnel current and damping signal were recorded simultaneously. In this section results of our force spectroscopy experiments are presented. All frequency shift measurements have been converted into forces using the Sader deconvolution algorithm detailed in Experimental Techniques section (section 2.3.5).

In Figs. 5.29 and 5.30 spectroscopy data are shown which were taken from scans showing the c(4x2) to p(2x1) transition with increase in setpoint. In Fig. 5.29 several points were taken over an “up” atom and a “down” atom of a dimer and then averaged. A clear difference can be seen between the spectra from each atom. The down atom appears to undergo a sudden increase in the force gradient at a larger tip-sample separation than the up atom. Conversely, on the “up” atom, the tunnel current starts to increase at a larger distance, and reaches a higher value, though this is most likely due to the proximity of the ‘subsurface’ feature in the tunnel current image. In the damping signal the “down” atom sees an increase slightly further away, but for the up atom there is a sudden large increase very close to the surface. According to a recent extensive theoretical investigation of the Si(100) surface using DFT and virtual noncontact AFM it was expected that there would be no dissipation on the up atoms, but a dissipation of approximately 300 meV/cycle on the lower atom [133]. However this investigation only used one stable silicon tip. More recent investigations examining dissipation mechanisms *within* other tip configurations have indicated that dissipation within the tip structure might conceivably be responsible for observed dissipations of up to 600 meV/cycle [78], *even without any relaxations at the surface*. Consequently, although from an idealised view the observed dissipation is difficult to understand, it is perhaps not completely unexpected, and certainly compatible with accepted mechanisms.

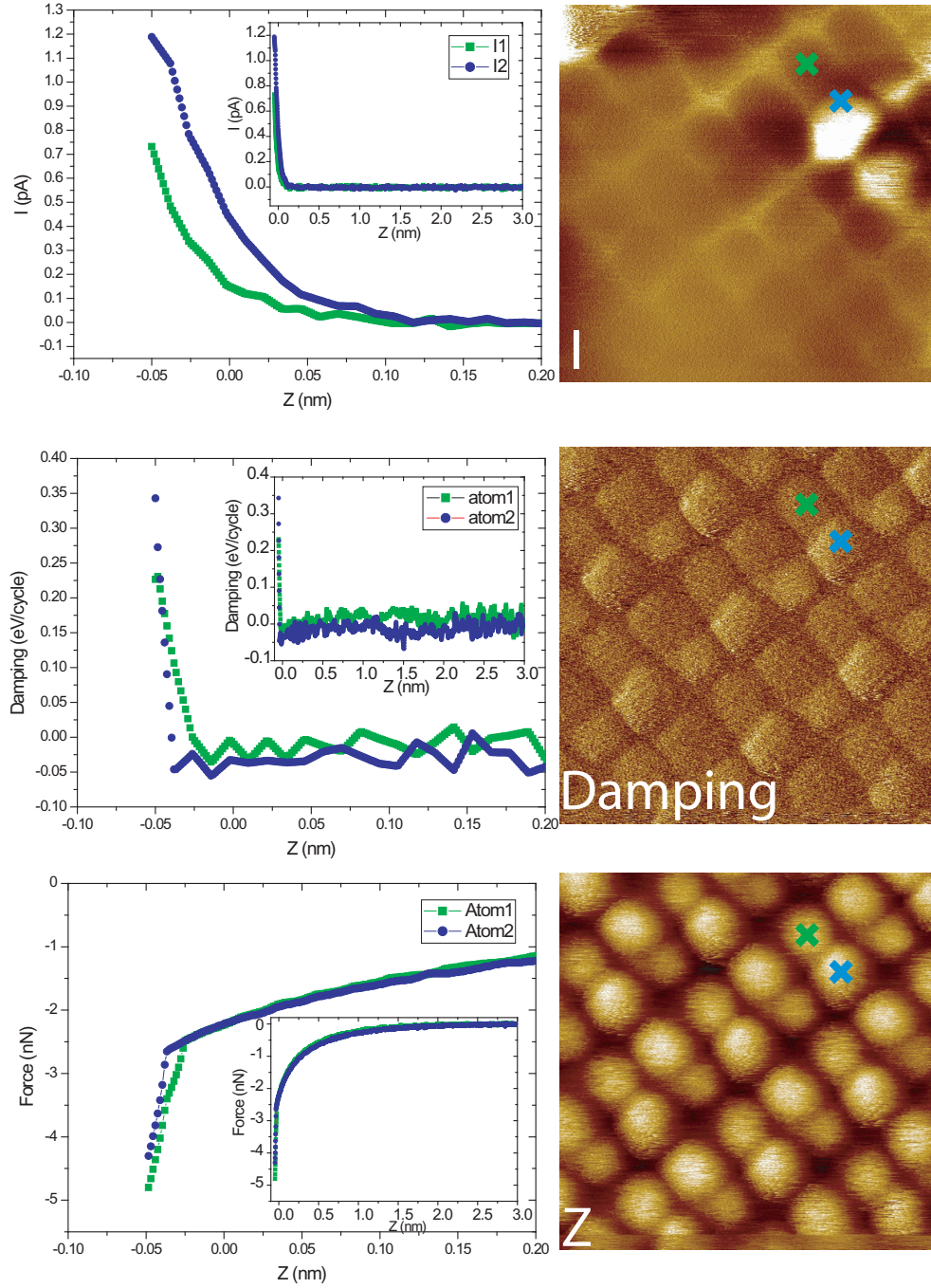


Figure 5.29: Spectroscopic data taken from the same image sequence as Fig. 5.19, showing tunnel current (top), damping (middle) and force (bottom). Each curve is an average of three spectroscopy points. Dissipation is recorded over both atoms, with (unexpectedly) higher peak dissipation over the 'up' atom. (Insets: graphs showing long-range behaviour).

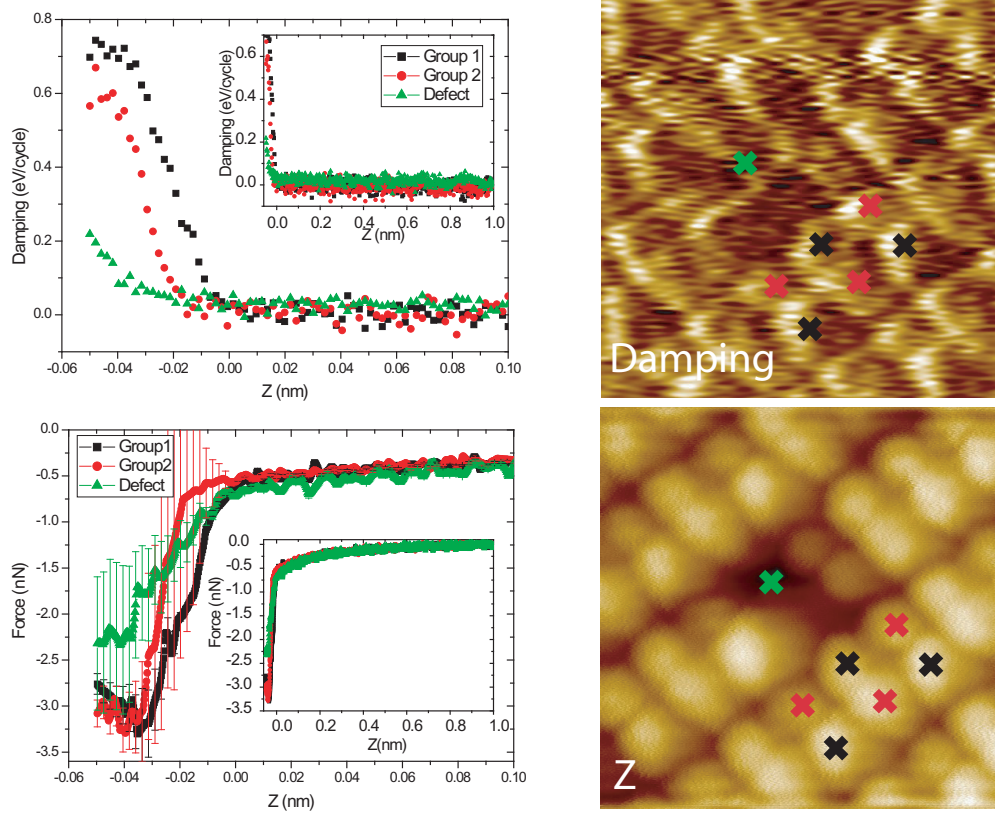


Figure 5.30: Spectroscopic data taken from the same image sequence as Fig. 5.21, showing force and damping data. Since in this data set it was not possible to clearly identify “down” atoms, groups of spectroscopy points were taken over atoms that should be in the same configuration assuming a buckled structure. The forces are uniformly smaller, but the dissipation higher than Fig. 5.29. The damping image has been FFT filtered to improve contrast. (Inset graphs showing long-range behaviour).

In Fig. 5.30 it was difficult to determine from the data which atoms were originally up and down (see earlier setpoint sequence in Fig. 5.21 and discussion). If, however, we assume a buckled structure then we can assume that all of the atoms in “group 1” are in the same state, and all the atoms in “group 2” are in the same (but different from group 1) state. Again, similar to Fig. 5.29, we see that one group experiences a sudden increase in force slightly sooner than the other. In this experiment the probe was brought slightly closer to the surface, and it appears to enter the repulsive regime. Force spectroscopy

points taken over the defect region show a different behaviour, with a much lower force gradient and maximum force. The trend of the damping signal also appears similar to Fig. 5.29 as well, with group 1 seeing an increase slightly before group 2, but with group 2 experiencing a sudden sharp increase closer to the surface (although here the absolute value does not exceed that of group 1). Similar to the force measurements the signal associated with the defect is much smaller. Note, however that the quantitative values for the damping are radically different from Fig. 5.29 - most likely due to the very different tip state. Comparing Fig. 5.29 and Fig. 5.30 it might be thought reasonable to presume that the data associated with “group 1” may be that of atoms originally in a “down” state. We note however that in this instance the spread of absolute values in each group was large, and, as indicated by the representative error bars, it is impossible to conclusively assign the grouped spectroscopic points to any particular atom state.

Fig. 5.31 shows spectroscopy data taken from scans that did not show a buckled to p(2x1) transition, possibly due to a blunt tip. Also, due to thermal drift during the scan the positioning of the spectroscopy points does not allow for a simple “grouping” as with the previous figure. However we can see that each point does seem to experience a sudden increase in force (although we cannot associate this data easily with up and down atoms). Examining the damping signal, it is striking to note that the amount of damping seems to *reduce* as the tip approaches the surface. It is difficult to interpret how an increasing interaction with the surface would cause an associated reduction in the damping signal in each position, but it should also be noted that the absolute value of the damping is an order of magnitude less than that observed in Fig. 5.29 and Fig. 5.30. An unexpected drop in dissipation has previously been observed during force measurements on the Si(100) surface during the experiments using sub angstrom oscillations with dynamic STM feedback [214]. However, this drop in dissipation only occurred in the repulsive regime and it should also be noted that this experiment was conducted at room temperature, and also observed anomalously high tip - sample interaction forces. As such, a degree of caution must be used when comparing the two sets of data

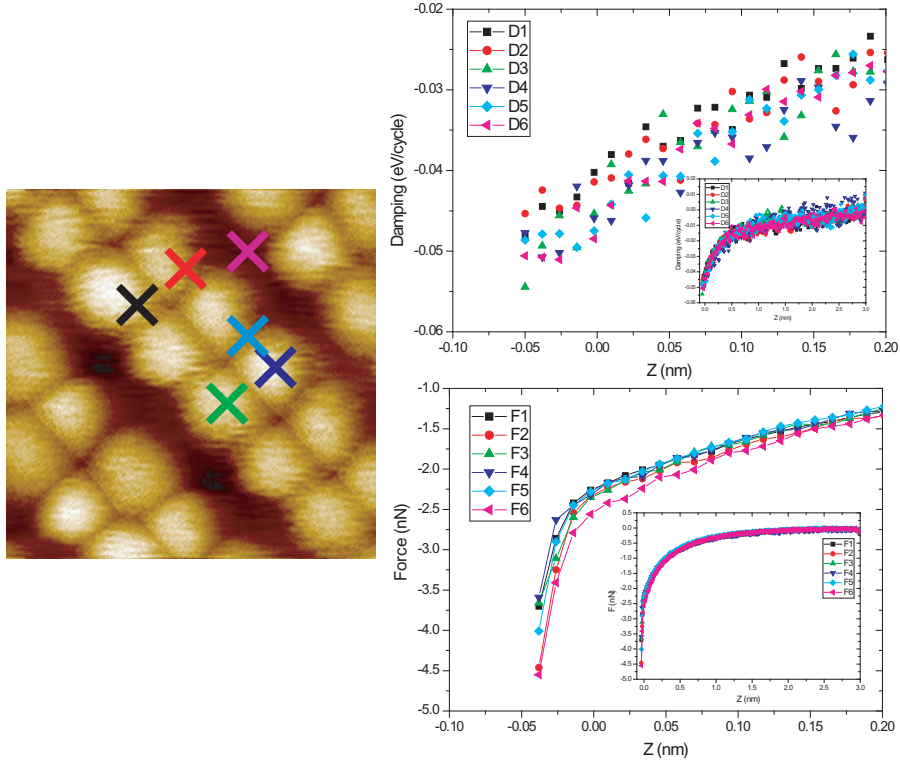


Figure 5.31: Spectroscopic data taken from the same image sequence as Fig. 5.22. While the forces are quantitatively similar to Fig. 5.29, the damping is unusual, being both an order of magnitude smaller, and apparently showing a *decrease* on approach to the sample. (Inset graphs showing long-range behaviour).

5.8 Imaging of C_{60} on Si(100)

Recent work by Gross et al [25] has demonstrated the striking ability of qPlus NC-AFM to probe the structure of individual isolated molecules with unprecedented resolution. Previously, sub-molecular resolution using conventional NC-AFM had been demonstrated on either monolayer coverages or islands of molecules [212], or relatively large isolated nanostructures such as carbon nanotubes [215]. However, imaging non-planar molecules is expected to present an additional challenge due to complications involved in SPM of high aspect ratio systems. Nonetheless theoretical work indicates that NC-AFM should be able to image sub-molecular features for C_{60} molecules bonded to the Si(100) surface, and, of even greater interest, perform controlled mechanical manip-

ulation [168]. Therefore, attempts were made to image C_{60} on the Si(100) substrate as a first step towards possible NC-AFM based molecular manipulation experiments. Here we present preliminary results on this topic.

5.8.1 Preparation

The clean Si(100) surface was prepared as described above. C_{60} was placed in a simple tantalum boat that was subsequently degassed in the preparation chamber. A current was passed through the tantalum foil until C_{60} molecules began to sublime, giving a low to moderate flux. The Si(100) surface was then introduced into the molecular beam for between 10 to 20 seconds in order to produce a low coverage giving isolated molecules. The surface was investigated in STM mode to check coverage and to prepare the tip - a typical image is shown in Fig. 5.32. It should be noted that tip preparation was significantly more challenging on a surface with absorbed C_{60} due to the high probability of one, or more, C_{60} molecules adhering to the tip. For later experiments involving the heating of the silicon with absorbed C_{60} , the sample was removed from the STM head and heated to around 500°C using the same the equipment as used to prepare the clean surface.

5.8.2 Imaging

Fig. 5.33 and Fig. 5.34 demonstrate imaging of the C_{60} molecule using small amplitude NC-AFM at 77 K. In both images sub-molecular features are clearly resolved, however the features of the underlying substrate are not. In Fig. 5.33 the molecule was imaged without an applied bias, in principle to remove the possibility of any crosstalk between the tunnel current/damping signal and the topography. Although none of our data thus far indicate any crosstalk it was felt important to demonstrate “pure” topographic imaging was possible and a fortuitous tip configuration with the appropriate contact potential difference made this possible. At high setpoints, however, a careful analysis of the tunnel current and damping images appears to show a very faint signal. Although a signal in the damping image is not unexpected, the presence of the tunnel current signal with zero applied bias is somewhat concerning (see discussion

in following section).

In Fig. 5.34, by contrast, a relatively large (+0.5 V) bias was applied, and in addition to the topographic signal and damping a significant tunnel current signal was detected. It is worth noting that the tunnel current signal differs somewhat from the topography, but has a very strong correlation with the damping image. The scan direction also seems to affect the imaging, again possibly due to an asymmetry of the tip.

In Fig. 5.33 it is clear that the molecule is being disturbed by the action of the scan. In general, imaging of the molecule with sub-molecular resolution was extremely difficult, and in addition to carefully controlled set point parameters, it was found that extremely slow scan speeds (very much less than 1 nm per second) were required to image the molecule in even the best case. Fig. 5.35 shows an example of the most common occurrence when attempt-

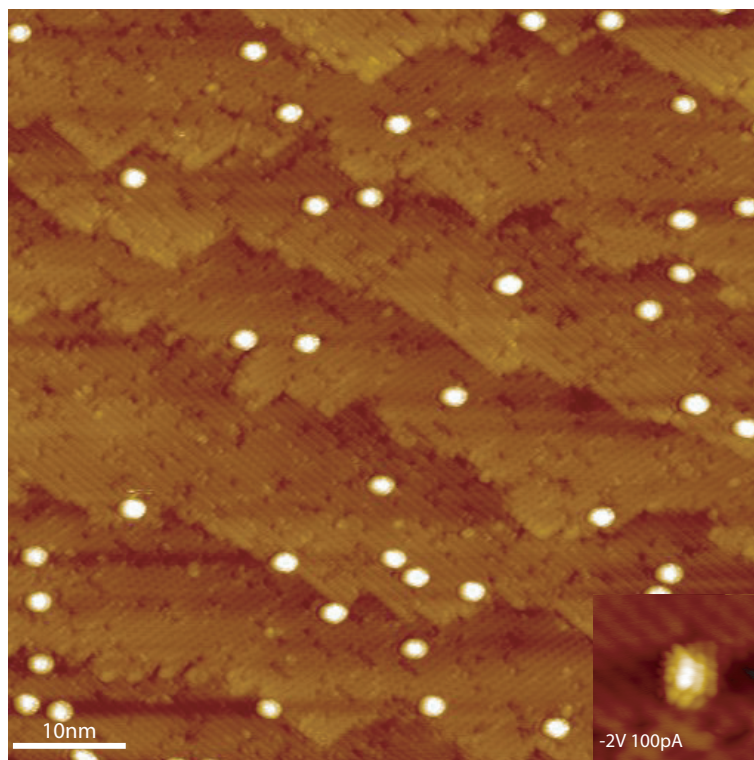


Figure 5.32: Large-scale STM image of the Si(100) surface after C_{60} deposition showing low coverage. (Inset) High resolution STM image of an individual C_{60} molecule taken with a different tip structure. Both images at -2V/100 pA.

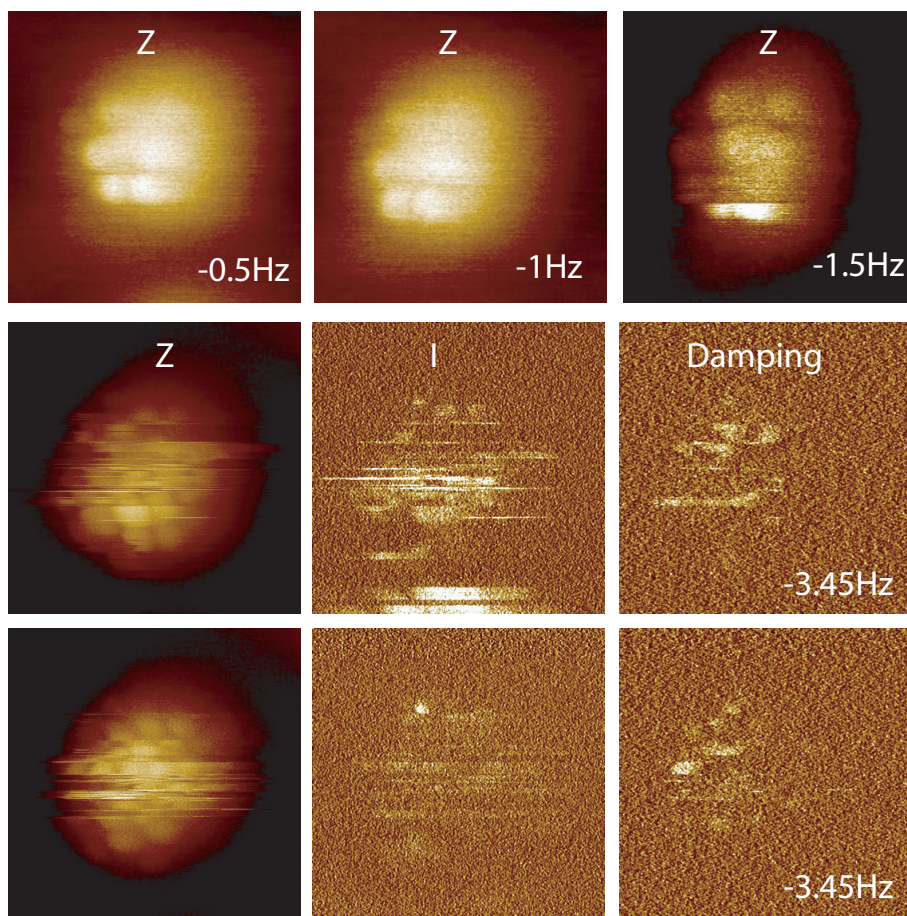


Figure 5.33: Image of a single C_{60} molecule taken using small oscillation amplitude showing sub-molecular resolution. At higher setpoints “scratching” was observed, most likely indicating movements of the molecule due to strong tip sample interaction. These “scratches” persisted despite careful adjustment of scan parameters, and slow ($\ll 1\text{nm s}^{-1}$) scan speeds. Curiously, at high setpoints images are detected in the tunnel current despite a lack of bias voltage. Intermittent imaging in the damping signal is also visible. $A_0 = 0.35\text{ nm}$, $V_{\text{gap}} = 0\text{ V}$.

ing to image an individual molecule – the molecule is clearly disturbed and displaced along the substrate. In other cases (data not shown) the molecule would apparently disappear from the scan, followed by an abrupt change in imaging. The most likely interpretation of this is that the C_{60} molecule was vertically manipulated from the surface onto the tip, although it is also possible that there was a tip-molecule interaction that simply caused a catastrophic tip

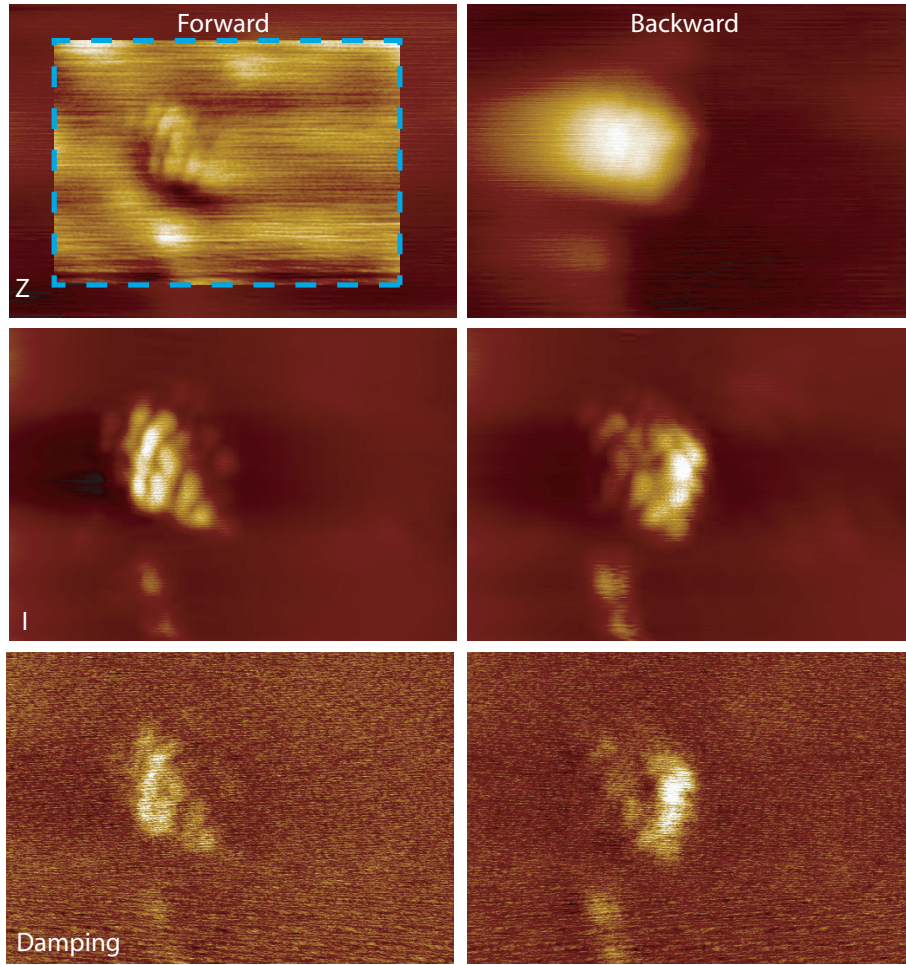


Figure 5.34: Image of a single C_{60} molecule with sub-molecular resolution with a different tip showing different contrast. Differences in forward and backward traces are most likely the result of tip asymmetry, or inadequate feedback, despite careful parameter tuning and slow ($\ll 1 \text{ nm s}^{-1}$) scan speeds. The forward trace has been high pass filtered to reveal fine detail. $df = -7 \text{ Hz}$, $A_0 = 0.25 \text{ nm}$, $V_{gap} = +0.5 \text{ V}$.

change resulting in a complete loss of resolution. The "dark spot" apparent in the middle of the C_{60} molecule has been previously reported, both for C_{60} adsorbed on silicon substrates and TiO_2 [170,212]. Previously, this inversion was ascribed to a jump to the repulsive regime, but more recent work suggests inversion is observed due to crossing points in the frequency shift-distance curve unrelated to the onset of the repulsive regime [212]. During our experiments it

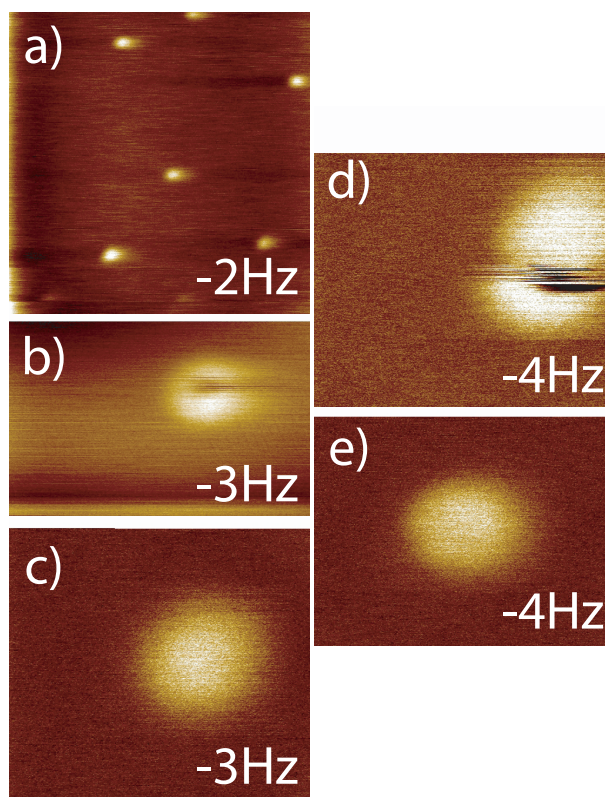


Figure 5.35: Series of images demonstrating initial imaging of C_{60} . a) large-scale image showing multiple molecules, b) individual molecule with “dark patch” in the centre, c) individual molecule with low resolution, d) accidental manipulation of molecule during imaging at higher setpoint, e) same molecule successfully imaged at the same setpoint with reduced scan speed. $A_0 = 0.35$ nm, $V_{gap} = 0$ V.

was noted that the dark halo was critically dependent on the feedback parameters, by reducing scan speed and/or setpoint the inversion could sometimes be eliminated. It was also noted that the appearance of this inversion was a strong indicator of a upcoming uncontrolled manipulation event.

It is known that annealing the Si(100) substrate with C_{60} absorbed at $\sim 500^\circ\text{C}$ causes the molecules to migrate from their usual adsorption positions in between the dimers onto the top of the rows [163,171], and further annealing causes them to ‘sink’ into the surface itself. In an attempt to improve imaging stability this procedure was performed, and Fig. 5.36 shows a series of images taken after annealing. It is important to note that we again see a

very strong correlation between the tunnel current signal and the damping, with the topography appearing quite different from either. Importantly, in the middle of the sequence, we start to see evidence of the dimer rows in the damping and tunnel current. The last two topographic images have been high pass filtered (original data inset) and it is clear that not only is sub-molecular detail resolved within the molecule itself, but, in addition, the dimer rows of the silicon substrate can also be seen. It should be noted that in this final scan despite extremely slow scan speeds and carefully tuned scan parameters the molecule itself was still manipulated just after the section of the scan shown, causing a sudden loss of the imaging, and so only approximately half of the molecule is shown in the final image.

5.8.3 Force spectroscopy of C₆₀

Although imaging of C₆₀ was significantly more difficult than imaging the bare Si(100) substrate, it was nonetheless possible to obtain a small number of force spectroscopy points during imaging. Fig. 5.37 shows a low resolution image of a C₆₀ molecule, and spectroscopy points taken both on and off the molecule. A clear difference is observed, with seemingly a slightly larger force being detected over the C₆₀ molecule itself. At smaller distances, however, the forces appeared to be converging. The probe was not approached close enough to the surface to detect any sudden increase, or the repulsive region, as the primary concern was to prevent the manipulation of the molecule or any sudden tip change.

Fig. 5.38 shows spectroscopy on silicon and C₆₀ taken after the sample had been annealed in an attempt to increase the bonding between the molecule and the surface. Since the detail on the substrate is only poorly resolved (and only then in the tunnel current and damping) it is possible that one or more of the spectroscopy points was taken over a surface feature such as a defect, rendering it qualitatively different from the previous points taken on silicon. Despite these difficulties, a key point to note is that the force needed to image the sub-molecular features on the C₆₀ is much lower than the force needed to image atomic features on the silicon surface (at least with this tip configuration).

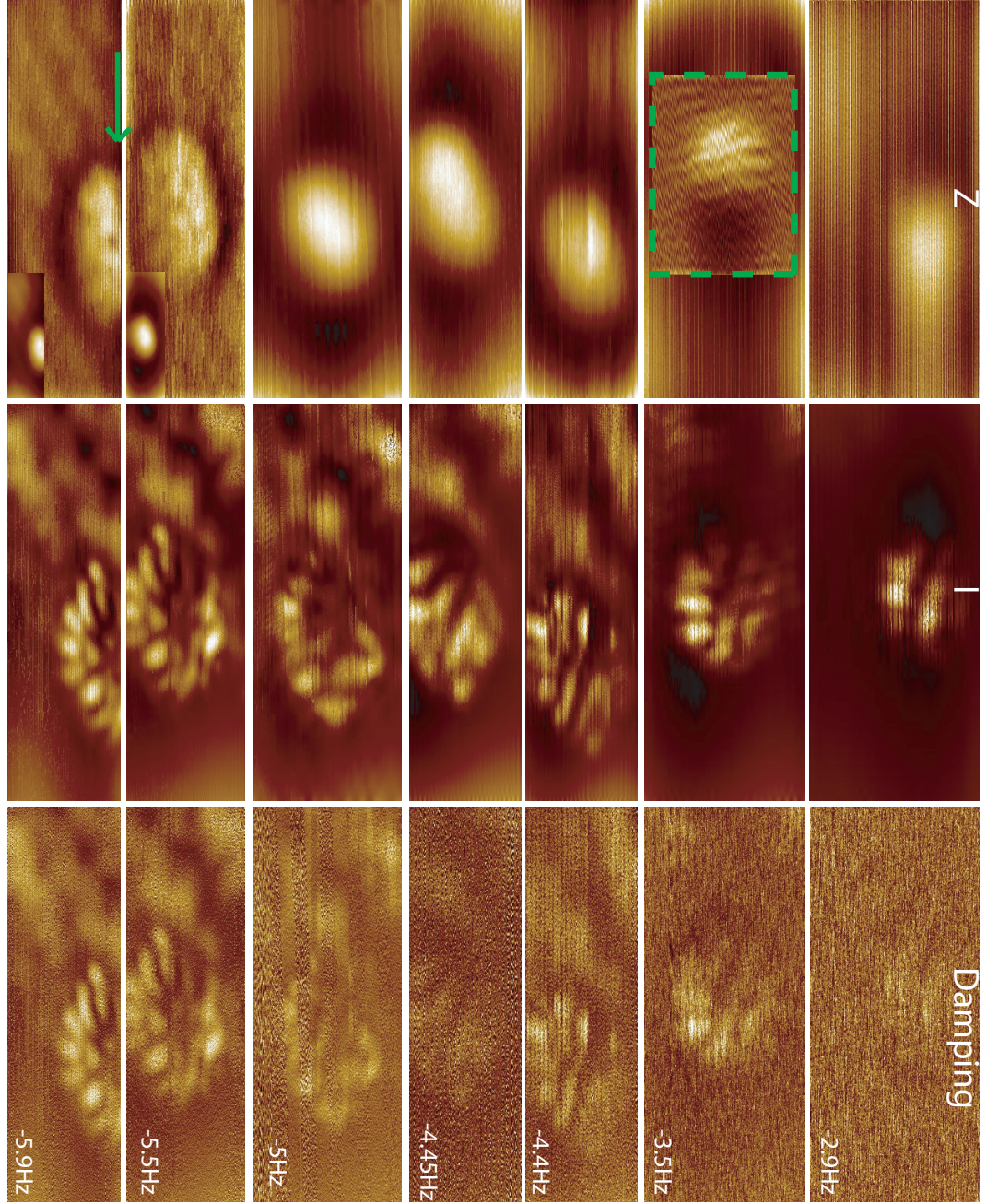


Figure 5.36: Setpoint dependent imaging of an individual C_{60} molecule. At low setpoints sub-molecular features are resolved in the tunnel current and damping, but not in topography. High pass filtering (-3.5Hz, -5.5Hz and -5.9Hz) reveals sub-molecular features in the topography, and in the final image details of the substrate are visible in the topography - arrow indicates point at which the molecule was manipulated. (Inset) unfiltered topographic images. $A_0 = 0.25$ nm, $V_{gap} = +0.5$ V.

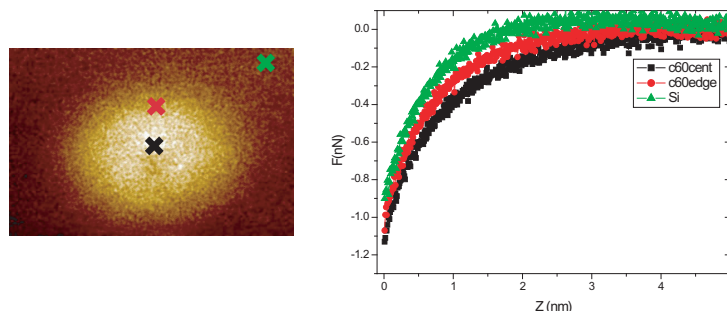


Figure 5.37: Force spectroscopy over a single C_{60} molecule. The maximum force appears to be slightly larger over the C_{60} molecule than the surrounding silicon. Taken from the same image sequence as Fig. 5.36. Note the force data here has been smoothed using a 5x interpolate in ORIGIN.

There is some debate even theoretically as to whether the setpoints required to acquire atomic resolution on the silicon surface might necessarily be so large as to cause a natively adsorbed C_{60} molecule to move and therefore prevent simultaneous sub-molecular and substrate topographic imaging. Very recent virtual NC-AFM simulations comparing the force required to image the Si(100) surface with that needed to image a natively adsorbed C_{60} molecule [216] using ‘conventional’ AFM parameters indicate that this is indeed the case. In that study (using the same tip and parameters) peak tip-sample forces of ~ 1.5 nN were required to resolve the Si(100) surface, whilst ~ 0.3 nN would cause a tip-molecule event in the case of C_{60} . These preliminary calculations appear to support our results which only demonstrated substrate/sub-molecular resolution post-anneal. These data are, to our knowledge, the first attempts to directly measure the forces involved during imaging of this system.

5.8.4 Signal coupling in the Omicron qPlus implementation

In general it was extremely difficult to produce a tip state that allowed for atomic resolution topographic imaging and atomic resolution tunnel current imaging at the same time, possibly partly due to the fact that the contact potential difference between the tip and the surface was usually between 0V and +0.4 V, well within the bandgap for the samples used. However Fig. 5.39

shows a topographic scan showing atomic resolution with the $p(2\times 1)$ periodicity, and a corresponding tunnel current scan showing an apparent inverted buckled structure. However the applied tip bias for this scan was $0V$ (Note that a similar effect was noted during the imaging of C_{60} (see Fig. 5.33)). In both cases the tunnel current variation recorded was $\sim 0.5pA$, smaller than the values recorded during normal imaging ($\sim 2-3pA$), but still a significant fraction.

Obviously if both the tip and sample are truly at the same potential then

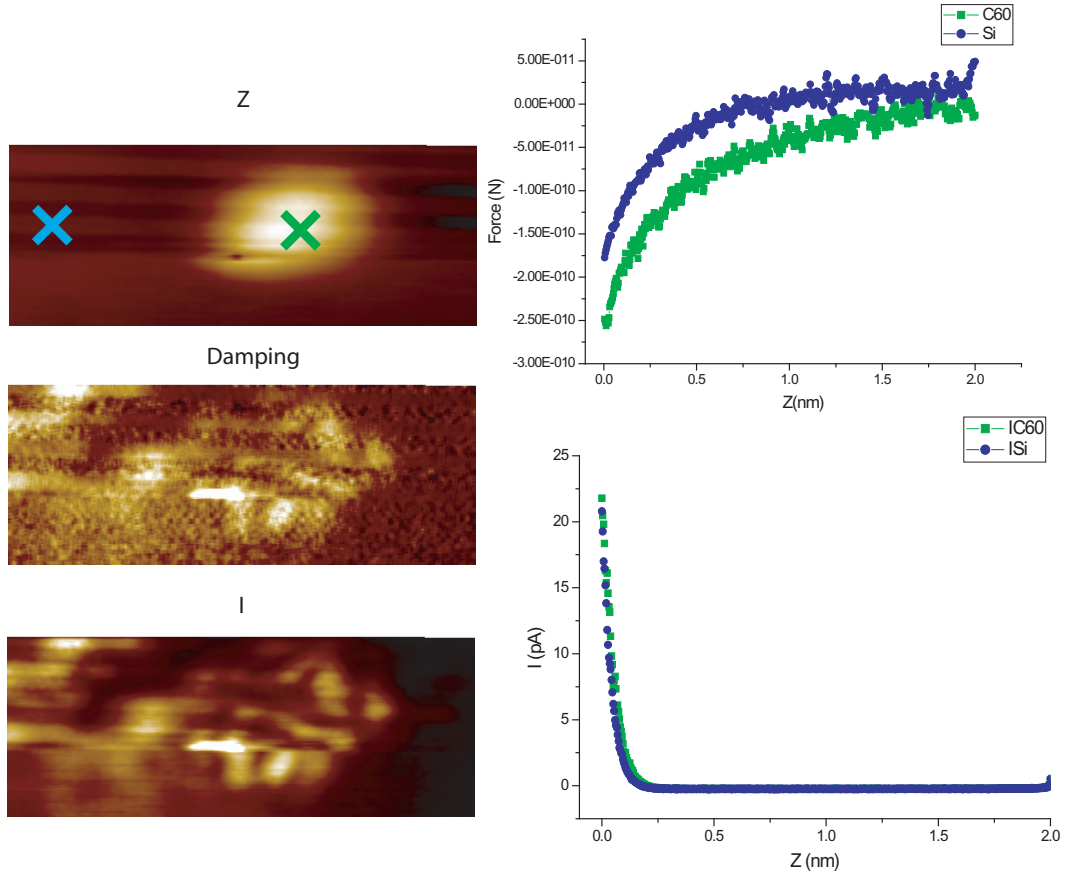


Figure 5.38: Spectroscopic data over a single C_{60} molecule with a different tip. Similar to Fig. 5.37 a greater maximum force is detected over the C_{60} molecule compared to the silicon. The qualitative behaviour of the tunnel current dependence is very similar over both. Image taken from the same sequence as Fig. 5.36

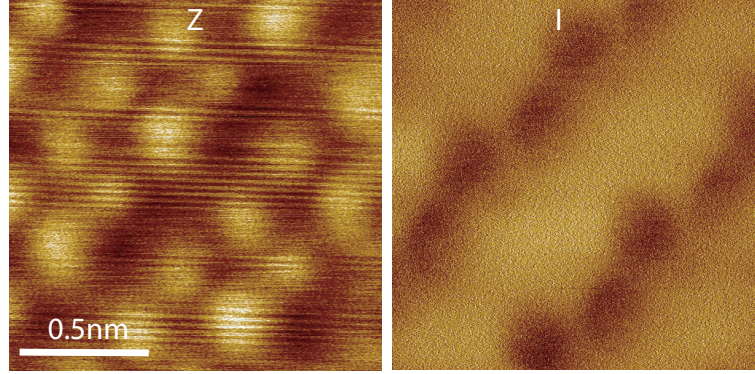


Figure 5.39: p(2x1) topography and inverted c(4x2) tunnel current image taken at (nominally) 0V bias. Such imaging may indicate either a crosstalk between the AFM df /damping/tunnel current channels. $df = -13.5$ Hz, $A_0 = 0.25$ nm, $V_{gap} = 0$ V.

this image becomes extremely hard to interpret. We have estimated, based on information from Omicron, that a offset of ~ 2 mV could have been present at ‘0V’ during this experiment, but note that tunnelling at this bias seems unlikely on a semiconductor. Ignoring the possibility of major instrument malfunction, one possibility is electronic crosstalk between one of the data channels and the tunnel current. In light of the other data collected that shows very clear separation of topography, damping and tunnel current this seems unlikely. Similarly in this instance where no contrast was observed in the damping, and the topography and tunnel current are very different, it is difficult to immediately see how crosstalk can be responsible. This said it is known that the Omicron implementation of the qPlus setup uses a proprietary ‘bandwidth decoupling’ method to separate the signal paths. The exact methodology is propriety and not available for inspection, despite requests by our group. We are currently in communication with Omicron as regards this issue.

5.9 Conclusions and analysis

In this chapter we have successfully demonstrated imaging of the p(2x1), p(2x2), and c(4x2) periodicities at 77 K for the first time using qPlus NC-AFM. We have also demonstrated the first simultaneous measurement of topography

and tunnel current on the Si(100) surface at low-temperature and presented the first analysis of several defect structures using the same technique. In addition we presented extended work confirming the setpoint dependent imaging of the Si(100) surface at low-temperature and also noted the critical dependence of the tip apex on the qualitative appearance of the transition from buckled to symmetric. Likewise, we have shown evidence that suggests an asymmetric tip can result in scan direction specific modification of the dimer configuration. Simultaneous tunnel current measurements have shown intriguing, and as yet not well understood, differences between the topography and the average tunnel current at low biases. We demonstrated imaging of defects and compared NC-AFM results with currently accepted models and STM based data. In general we found good agreement with many aspects but our data contain features that the currently accepted models cannot adequately explain.

The results of quantitative force spectroscopy experiments are broadly in agreement with previous work in the literature, and have demonstrated quantitative differences between atoms in up and down positions, at least for some tip apex structures. Nonetheless we are forced to conclude that some data, especially regarding the mechanism of dissipation, remain open to interpretation. We have also performed (to our knowledge) the first NC-AFM imaging of the C₆₀ molecule on the Si(100) surface and demonstrated what we believe to be the first examples of sub-molecular resolution on this molecule using NC-AFM.

5.10 Further work

It is clear from the data presented that a number of open questions remain regarding NC-AFM and the study of the Si(100) surface. A number of obvious avenues for further exploration therefore present themselves. A clear near-term goal must be to repeat the experiments performed in this chapter at 5K where the reduced thermal energy of the system should make interpreting the images and tunnel current/damping data significantly easier. Specifically, it will be of great interest to perform constant height “force mapping” experiments, in conjunction with force spectroscopy experiments, and to investigate the

possibility of individual dimer manipulation and patterning using chemical bonding forces.

A longer term goal must be to combine these experimental results with detailed theoretical investigations to understand the role the tip apex can play in imaging, and modifying, the surface. In particular, models examining tunnel current signals on Si(100) in the near contact regime and the effects of asymmetric tips should be a high priority.

As regards imaging of absorbed molecules, a possible avenue of exploration is to combine STM-based manipulation with the use of dynamic STM in order to directly measure the forces during manipulation. Controlled manipulation experiments of this kind may also provide the possibility of deliberately manipulating a molecule into a defect, or against a step edge, which may increase the stability of the molecule on the surface and aid in more reproducible imaging.

Chapter 6

NC-AFM and KPFM of spun cast nanoparticle networks

“Creationists make it sound as though a ‘theory’ is something you dreamt up after being drunk all night.”

Isaac Asimov

In the previous chapter we looked at atomic resolution NC-AFM of Si(100) surfaces using qPlus NC-AFM. In this chapter we increase the scale by several orders of magnitude and present results pertaining to the imaging of gold nanoparticle networks using conventional NC-AFM. We show the first high resolution AFM images of spun-cast thiol passivated gold nanoparticles on SiO₂ surfaces in UHV alongside spectroscopy data measuring both force profiles and differences in contact potential above the bare silicon and the nanoparticle networks. Differences in the imaging of these networks using different experimental techniques are discussed. Finally, we compare conventional AFM imaging to imaging carried out using dynamic contact potential adjustment i.e. using Kelvin probe force microscopy (KPFM).

6.1 Topographic imaging

Although spun- and drop-cast networks of thiol passivated gold nanoparticles have been extensively investigated using ambient TM-AFM techniques

[185, 189, 190, 193] to our knowledge these systems have not been investigated with NC-AFM techniques either in ambient conditions or in UHV. Also, since extensive work has been carried out measuring, and modelling [189] the $I(V)$ characteristics for these networks an obvious goal is to attempt to directly image the associated charge flow through these networks using scanning probe techniques. As a first step towards this goal a wide array of NC-AFM imaging techniques were used to investigate the networks and examine contact potential differences (CPD) between the substrate and network in order to develop the basis for later work.

The nanoparticle networks investigated in this chapter were created by spin casting 2 nm (core size) gold nanoparticles (capped with either octanethiol (C8) or dodecanethiol (C12) suspended in hexane) onto silicon wafers at approximately 4000 rpm for 20 to 30 seconds. The silicon wafers either had 300 nm thermally grown oxide (topographic imaging) or 2 nm native oxide (Kelvin probe imaging). All sample preparation was carried out by Andrew Stannard, School of Physics and Astronomy, University of Nottingham. In the case of UHV experiments the samples were then mounted onto standard Omicron sample plates and introduced into vacuum without further treatment. All measurements (UHV and ambient) were carried out at room temperature.

Initial imaging of the networks using the cantilever based VT FM-AFM Omicron system (see section 2.4.1) was successful. Fig. 6.1 appears to show features that may be interpreted as arising from single nanoparticle resolution, but care must be taken in the interpretation of such images as the nominal radius of curvature of the tips used (NSC-16 standard silicon cantilevers with nominal radius of curvature 10 nm) is larger than the diameter of the nanoparticles that make up the network (between 2 and 5 nm depending on how the diameter is defined – see later sections for a detailed discussion). Although a sharp asperity smaller than the radius of curvature is not uncommon it is difficult to separate the effects of convolution due to the tip, especially on less well characterised inhomogeneous samples such as these. Even with this caveat it is clear that the resolution obtained is far superior to images so far acquired in our group in ambient conditions - see, in comparison, Fig. 6.2.

Although the high lateral resolution scans were of interest, another, more

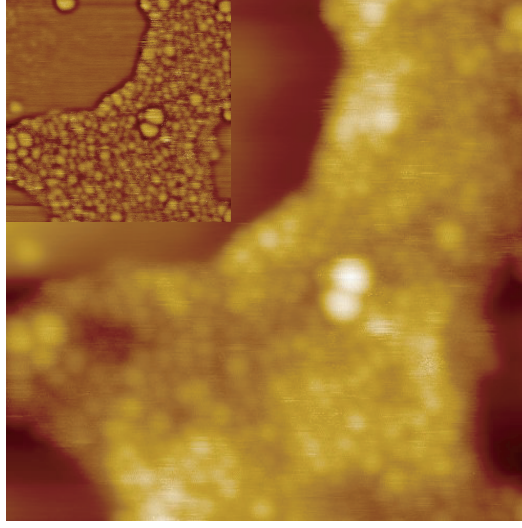


Figure 6.1: High resolution NC-AFM image of spun-cast C8 passivated Au nanoparticles on a SiO₂ surface demonstrating nanoparticle sized features (Inset: High pass filtered image). Imaged using an Omicron VT-AFM in UHV using FM mode. $V_{gap}=+0.8V$, $A_0=16nm$, $df=-150Hz$, $100nm \times 100nm$. Image courtesy of Subhashis Gangopadhyay

important feature was noted during these investigations – the apparent height of the network above the SiO₂ surface was significantly higher than that previously measured during extensive tapping mode ambient investigations carried out within our group [178,190]. In addition, the presence of an apparent “sub-layer” was noted in some images. In contrast to clear overlayers of nanoparticles occasionally seen previously in tapping mode investigations the apparent height of this feature made it difficult to interpret its origin, especially in the light of the different height measurements of the network itself. Therefore a systematic investigation of the apparent height of the nanoparticle networks under different imaging modes was carried out and forms the basis of the next section.

6.2 Apparent height of nanoparticle networks

In this section we compare images of the networks using FM-AFM and Kelvin probe FM-AFM in UHV with SPM data acquired in ambient conditions using

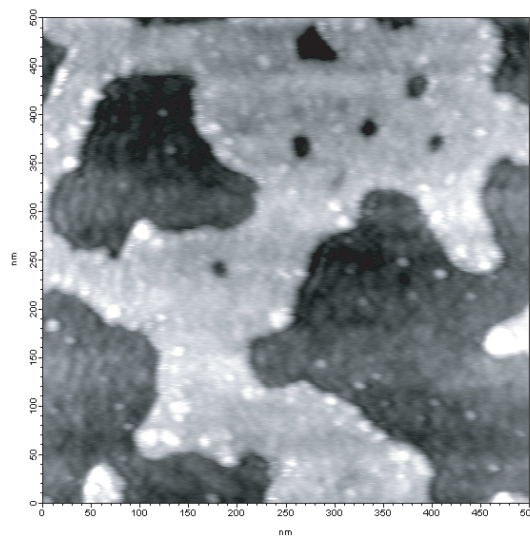


Figure 6.2: Comparable high resolution image of same sample type as Fig. 6.1 taken using Asylum AFM in ambient conditions using AM mode. 500nm x 500nm.

both amplitude modulated (AM) noncontact and tapping mode (TM) AFM. As mentioned in the previous section the key points that instigated the investigation were the apparent “sub-layer” feature and unexpected network height measurements. One initial hypothesis was the possibility that the entire network was itself formed of a double layer of nanoparticles. However this ran contrary to currently accepted models for the network formation [185] and so understanding both of these features in conjunction became an important goal.

We first consider the qualitative differences in the imaging. Fig 6.3 shows a collection of high resolution scans taken with various tips and scan parameters demonstrating that the apparent “sub-layer” was a common feature during imaging. Some regions demonstrating the feature are highlighted and Fig 6.3 (e) and (f) show magnified images of the clearest examples. This repeated presence in high quality imaging confirmed it was not a tip artifact but did not explain its origin. Fig 6.3 (c) also shows a small region of overlayer as has previously been imaged in ambient conditions.

In light of these observations it was thought prudent to re-investigate the samples using ambient techniques in order to establish if the features were in some way related to imaging in UHV. Fig. 6.4 shows an image taken of a

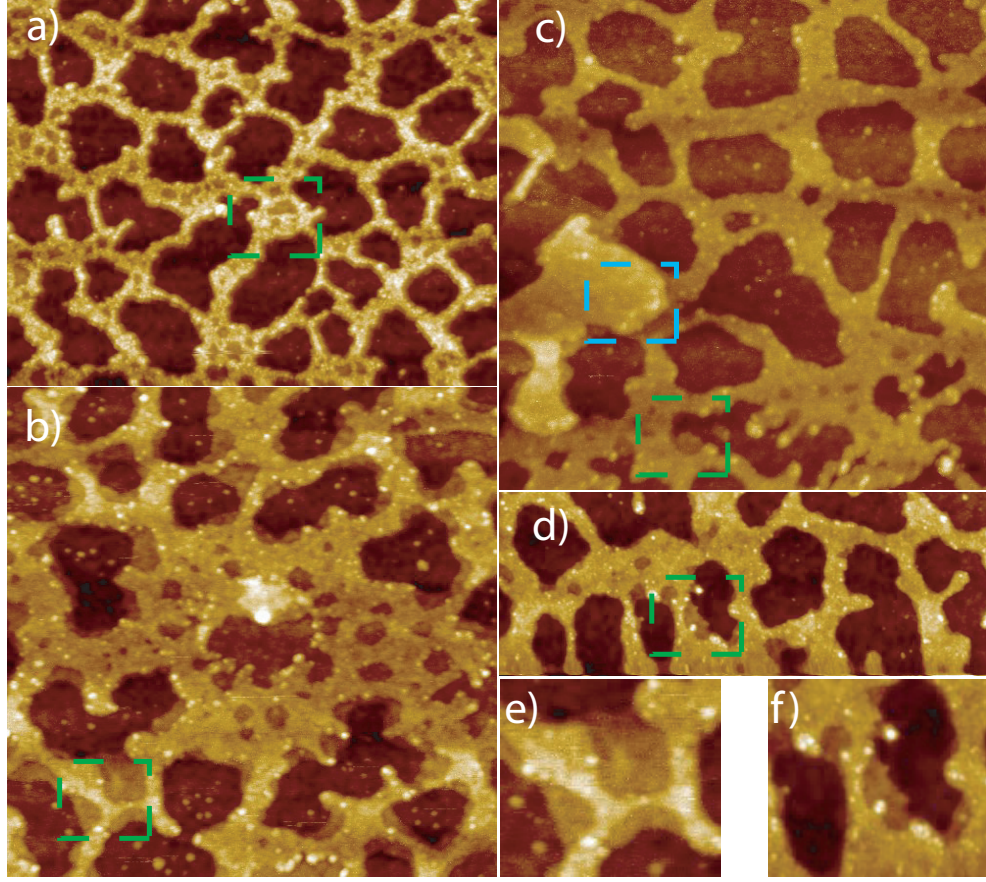


Figure 6.3: NC-AFM images of spun cast C8 passivated Au nanoparticles on a SiO₂ surface demonstrating apparent “sub-layer” (highlighted regions). a) $V_{gap}=+1.2V$, $A_0=8nm$, $df=-15Hz$, $1000nm \times 785nm$, b) $V_{gap}=0V$, $A_0=16nm$, $df=-15Hz$, $1000nm \times 1000nm$, c) $V_{gap}=+1.2V$, $A_0=8nm$, $df=-15Hz$, $1000nm \times 1000nm$, d) $V_{gap}=0V$, $A_0=17.6nm$, $df=-20Hz$, $1000nm \times 312nm$, e) Zoom of b), f) Zoom of d).

similar sample in ambient conditions using amplitude modulated NC-AFM. Although the resolution is not as good as Fig. 6.3 the network is clearly resolved. Critically, a number of regions that look similar to the “sub-layer” areas seen under UHV conditions are also seen. Utilising the ability of the Asylum system to operate in both NC-AM and TM, Fig. 6.5 shows an image of the same region taken soon afterwards using tapping mode. By identifying the same regions in both images we can see that regions of “sub-layer” image only faintly in the topography (in fact the apparent height is of the order of

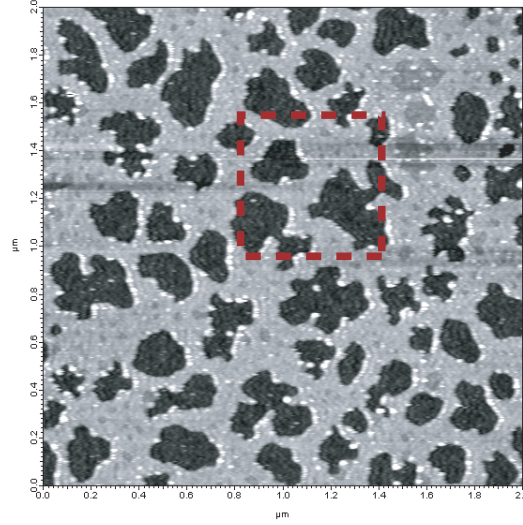


Figure 6.4: Image of spun cast nanoparticle network taken using Asylum AFM in ambient conditions using AM mode. Highlighted region shows the areas in Fig. 6.2 and Fig. 6.5. 2000nm x 2000nm

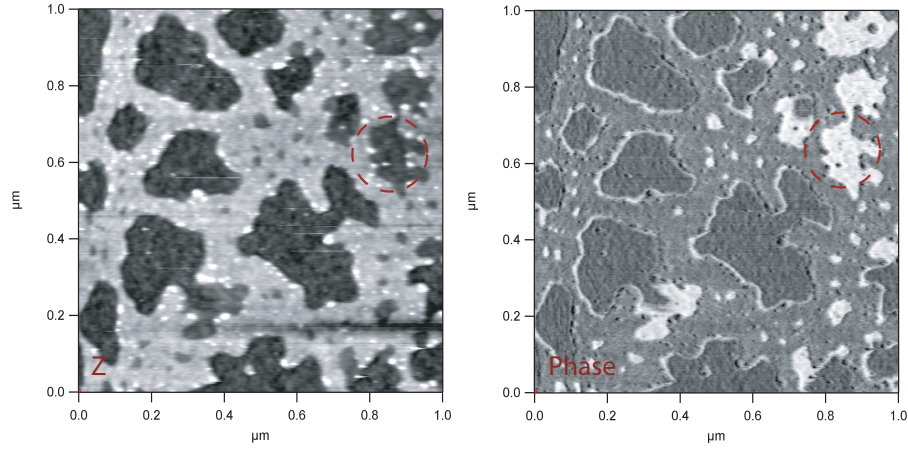


Figure 6.5: (left) Image of spun cast nanoparticle network taken using Asylum AFM in ambient conditions using tapping mode. (Right) Corresponding phase image. 1000nm²

the recorded variation over the SiO₂). However, the same regions demonstrate a striking signature in the phase image. It is worth noting that no effect was noted on the phase in attractive mode, or the damping signal acquired during FM-AFM imaging.

This imaging of the same samples with both modes allows us to make a

direct comparison between the observed features. Table 6.1 shows a systematic comparison of the heights of different regions of the sample as measured using different techniques.

In this table “Normal network” is defined as the bulk of the nanoparticles, “sub-layer” is defined as regions that appear lower than the normal network and are not the result of any obvious tip artefact, “High area” is defined as small patches in the network that clearly appear topographically higher than the rest of the network and the “double layer” refers to areas where an additional layer can clearly be seen on top of the existing nanoparticle network.

As detailed in the Experimental Methods chapter one possible cause of inaccurate topographic measurements in AFM profiling can be differences in contact potential between two regions of different material. In standard UHV experiments a compromise is reached by applying a tip bias that results in the same of frequency shift due to the electrostatic potential over both regions. Therefore, although the electrostatic force is not minimised on either material, the effect is nominally the same and therefore it is assumed that the detected topography is due to the resulting van der Waals attractive force which may be more confidently ascribed to changes in the ‘actual’ topography. However, the preferred solution is generally considered to be the use of an automatically compensating system i.e. to use Kelvin probe force microscopy. The detail of the Kelvin probe experiments are described in a later section, but the height

Technique	Sample area	Apparent height (nm)
FM-AFM	Normal Network	3.4 ± 0.1
KPFM-AFM	Normal Network	3.0 ± 0.1
KPFM-AFM*	Normal Network	2.5 ± 0.6
AM-AFM	Normal Network	3.2 ± 0.1
TM-AFM	Normal Network	2.3 ± 0.1
FM-AFM	“sub-layer”	2.0 ± 0.1
AM-AFM	“sub-layer”	2.2 ± 0.1
AM-AFM	High Area	4.8 ± 0.3
FM-AFM	High Area	4.6 ± 0.1
FM-AFM	Double Layer	5.9 ± 0.1

Table 6.1: Table of network heights measured by different AFM techniques.
*Measured using KPFM setup without KPFM feedback engaged

measurements of the C8 capped nanoparticle networks are included here for continuity in the discussion.

The most immediately striking point to note in these data is the wide variation in the apparent height of the networks depending on the type of imaging technique used. There is an approximate 50 per cent variation in the apparent height of the network between the lowest value (for tapping mode) and the highest value (for FM-AFM). The clearest distinction is between the attractive mode (both ambient amplitude modulated and vacuum frequency modulated) techniques and the repulsive mode techniques. Although the attractive mode techniques do not quite agree within error they all lie between 3 and 3.5 nm, while the repulsive mode technique suggests heights of around 2.3 nm. This value is close to, but still larger than, the estimated core gold nanoparticle diameter of 1.8nm [187]. The attractive mode techniques indicate a radius greater than the core nanoparticle, but less than the maximum possible radius that could be achieved by having the thiols of the nanoparticle fully extended (i.e. the free solution radius, estimated to be around 4.3 nm). Also of interest is that the “sub-layer” in attractive mode is comparable to the height of the network itself in tapping mode.

6.2.1 Analysis of apparent heights

The origin of the apparent height differences of the nanoparticles networks between different imaging lines is not yet fully understood. We can, however, consider the validity of the most plausible mechanisms.

In earlier work on mechanically driven coarsening of nanoparticle networks, Blunt et al [190] noted an increase in apparent height of the networks from ~ 2 nm to ~ 4.3 nm during coarsening. This increase in height was ascribed to the change in packing density of the networks. When thiol-passivated nanoparticles are allowed to dry slowly into well ordered arrays, it has been observed the equilibrium configuration tends towards maximum interdigitation of the thiols [177, 217–221], that is to say that the nanoparticles in the array are spaced by the length of one thiol chain. However, in other formation conditions arrays have been observed with almost no interdigitation [222], i.e. the nanoparti-

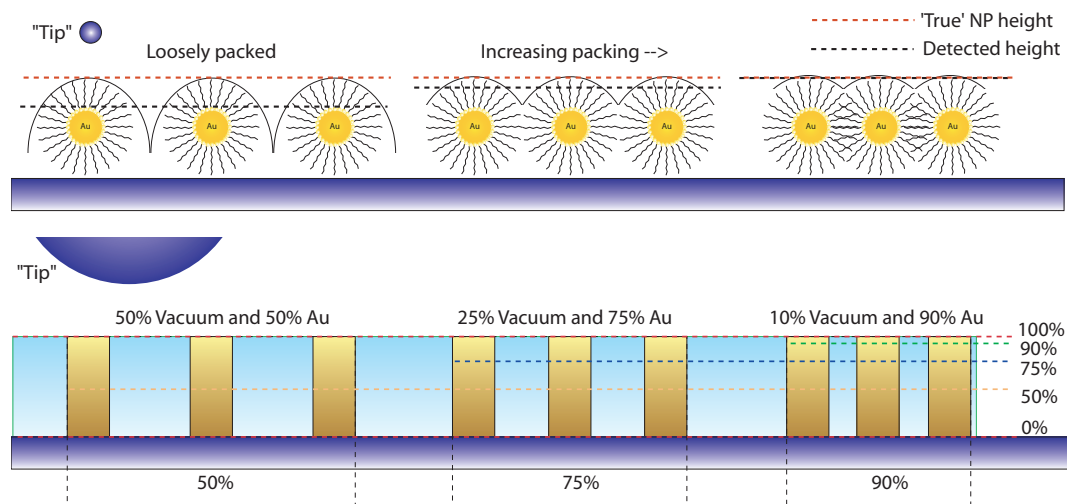


Figure 6.6: Top, change in apparent height of a nanoparticle array when imaging at low resolution with a sharp tip. Apparent height increases with packing density. Bottom, as the fraction of gold in the ‘layer’ increases, so the effective interaction with the tip increases and results in a change in detected height.

cles are separated by two thiol chain lengths. The exact packing density of the spun cast networks used in this study is not well known, but we might expect them not to be fully interdigitated as the drying takes place extremely rapidly. Therefore, the nanoparticles may not have time to reach the equilibrium configuration. Consequently, it is plausible that the packing density of the particles is able to increase during mechanical coarsening. This process is shown schematically in Fig. 6.6. This interpretation implicitly assumes, however, that the tip apex is sharp enough to detect the spacing between the particles. If the tip apex is very blunt with respect to the spacing of the particles, then, by simple convolution arguments, a flat surface with the maximum height as shown in Fig. 6.6 will be detected.

However, there is a route by which this mechanism may still influence the apparent height even with a blunt tip, as recently proposed by Stannard [223] (and shown schematically in Fig. 6.6). If we consider a thin layer of fixed height and assume a long-range diffuse interaction that cannot sense the “fine detail” of the film then the fraction of the film composed of nanoparticles will effect what we might term the “effective Hamaker constant” of the layer. Therefore,

the influence of the film on the tip at a given height will change depending on the packing density *even if the tip is too blunt to sense the individual gaps and particles*. A quantitative analysis of how large this effect might be has not yet been presented.

However, based on results presented in this thesis, there is another possibility that we must consider: that of the interaction of the probe with the particle itself. On the basis that tapping mode of normal networks obtains a height close to that of the gold core, and that noncontact techniques obtain a value significantly larger, but less than the free solution radius (and, critically, less than the height detected in tapping mode studies of *coarsened* networks) then we can hypothesise that the interaction of the thiols with the tip and surface strongly influence the apparent height. In a simplified view of the situation we might imagine that tapping mode, which involves the repulsive regime of tip-sample interaction, effectively “compresses” the thiols as shown in Fig. 6.7. Molecular dynamics studies of thiol passivated gold nanoparticles physisorbed on inert surfaces [224, 225] have shown that the degree to which the thiols separate the gold core from the substrate depends critically, and nonlinearly, on the length of the thiol chain.

W. D. Luedtke and Uzi Landman [224, 225] found in their simulations that, counterintuitively, longer thiol chains could actually *reduce* the metal core to substrate distance due to the increased tendency of the longer chains to flex, and interact with the surface. They also found the thiol – substrate interaction strength also dramatically altered the separation, with almost 100% variation between a weakly interacting (HOPG) and strongly interacting (metal) substrate. This dramatic length variation is in contrast to the observed behaviour of the same type of thiols in self assembled monolayers (SAMs.), where numerous studies (including ellipsometry [226], small angle x-ray scattering [227], and AFM [228], [226]) have found that short to medium length thiols are almost uniformly straight and angled at between 20 to 35° normal to the surface in order to maximise the van der Waals interaction between the thiol chains (with no observed compression during AFM studies).

We therefore might offer another explanation that accounts for not only the variation between tapping mode and noncontact mode AFM studies, but also

the increase in observed height during coarsening experiments. Here we assume that during tapping mode experiments the thiols are indeed “compressed” and we recover a height of the nanoparticles slightly larger than the metal core diameter. In attractive mode we interact less strongly with the thiols, but the overall height of the nanoparticles is reduced from their free solution radius as a result of the thiol - surface interactions as detailed in [224]. In the coarsening experiments we follow the outline in [190] and assume that the particles are indeed packed close together, but ascribe the increase in height to the increased thiol - thiol interaction between the now closepacked nanoparticles which forces them into a “SAM-like” configuration, both increasing the core to surface distance and providing a stiff surface in response to the AFM tip. This is shown schematically in Fig. 6.7.

Unfortunately, detailed experimental, and theoretical studies of the behaviour of closely interacting thiol passivated nanoparticles in close proximity to a surface, and, critically, the thiol - thiol interaction are not yet available in the literature, and the computational cost of introducing an AFM tip interaction into the studies is expected to be high. Nonetheless, it seems that an extended molecular dynamics study along the lines of [224,225] could confirm certain aspects of this hypothesis. Additionally, it would seem that imaging coarsened networks using both TM-AFM and AM-AFM might also provide an experimental route by which to determine which of these theories (or if indeed some combination of these effects) might successfully explain the observed results.

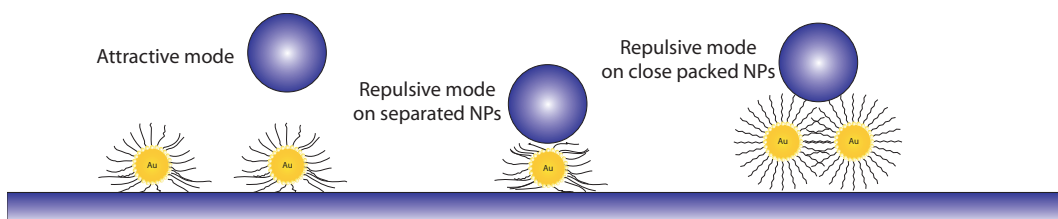


Figure 6.7: (left) Cartoon of possible tip - thiol interaction in repulsive and attractive modes. (right) Nanoparticle packing may increase thiol - thiol interactions and modify the effective height

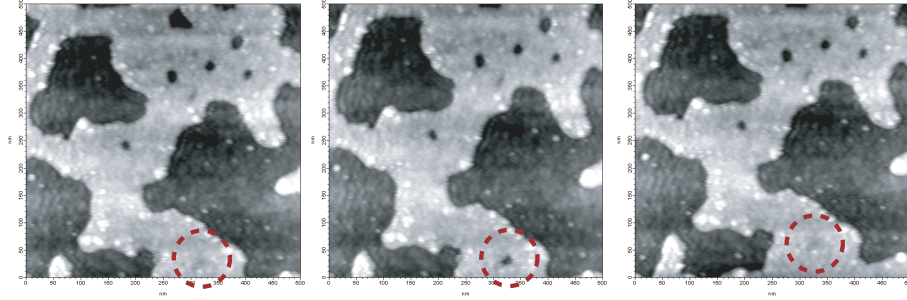


Figure 6.8: Image sequence showing zoom in of Fig. 6.4 showing apparent sample modification due to repeated scanning. Taken using Asylum AFM in ambient conditions using AM mode. 500nm x 500nm

6.2.2 Network modification

It has been well established that during typical tapping mode scans the nanoparticles are highly mobile either due to being moved along the surface or being transferred from sample to tip and vice versa [190]. It is thought that operating in attractive mode should reduce the tip sample interaction.

Although we did not observe the large scale network coarsening observed by Blunt et al. [190] in attractive mode, the process of scanning was capable of causing modifications to areas of “sub-layer”. Fig. 6.8 shows a series of scans taken in the same region as Fig. 6.4 and Fig. 6.5. The highlighted region clearly shows holes opening up and closing within the network as the surface is scanned. This behaviour was not observed during FM-AFM scans in UHV, although whether this is because of a reduced tip sample interaction, or because the absorbed water layer is removed in UHV conditions is not clear.

6.2.3 Origin of the “sub-layer”

We are now in a position to summarise some of the key features of the “sub-layer”

- i Images with a height of approximately 2 nm using noncontact techniques.
- ii Has almost no topographic signature in tapping mode, but has a clear signal in the phase.

- iii Is visible in both ambient and UHV conditions
- iv Appears to be mobile under the influence of the tip in ambient conditions during noncontact imaging

A direct comparison of imaging and line profiles taken over network and “sub-layer” in the 3 imaging modes is shown in Fig. 6.9. These features strongly suggest that the “sub-layer” is not composed of nanoparticles. Although the height in noncontact mode is comparable to the observed height of the nanoparticles in tapping mode, the lack of topographic imaging in tapping mode and contrast in the phase suggests that these regions are both compressible, and mechanically different from the network. Secondly, the apparent mobility during attractive mode imaging suggests these areas are mechanically weaker than the network.

If the “sub-layer” is not composed of nanoparticles, then we have to consider other likely candidates. The two most likely contenders are either excess thiol, or residual tetraoctylammonium bromide (TOAB) left over from the synthesis process. The presence of these substances has been noted in previous nanoparticle synthesis experiments by this group.

Unfortunately, given the degree of ambiguity in height measurements previously noted, and the danger of ascribing chemical identity based on purely topographic imaging, it is difficult to determine which of these is most likely. Based purely on the topographic information collected in noncontact mode either is a possibility. Although C8 only has a length of approximately 1.3 nm, NC-AFM experiments on islands of thiols absorbed on self assembled monolayers on Au(111), indicate that thiols can easily form bilayers with effective heights lying somewhere between one and two (upright) absorbed layers [226, 228]. Information derived from TEM studies of TOAB capped nanoparticles suggests that TOAB could have an effective length of between 2 and 4 nm [220]. As such, depending on the packing, and tip interaction, either could conceivably fit the topographic data presented. Likewise, their susceptibility to manipulation and mechanical differences from the nanoparticle network could be indicative of either molecule.

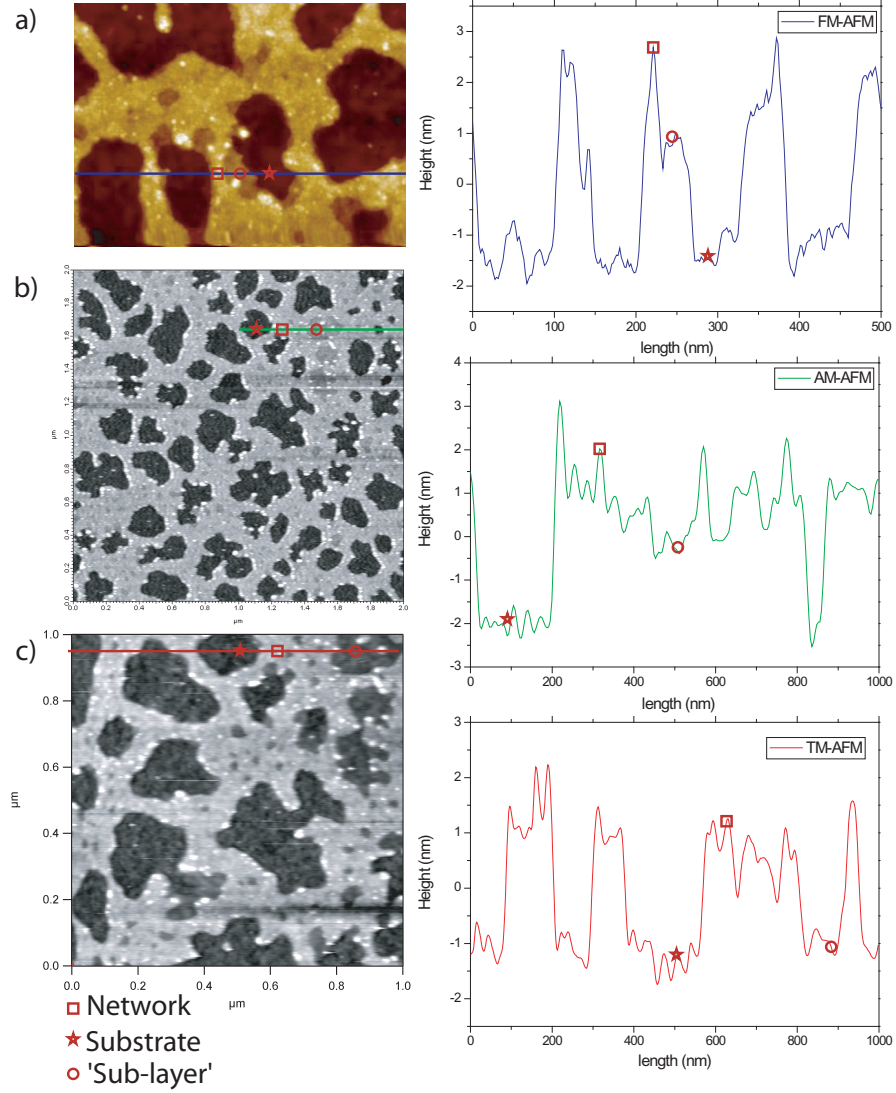


Figure 6.9: (a) image and line profile taken using FM-AFM in UHV. Network height ~ 4 nm, “sub-layer” ~ 2.2 nm, (b) image and line profile taken using AM-AFM in ambient conditions. Network height ~ 3.5 nm, “sub-layer” ~ 2.5 nm; (c) image and line profile taken using TM-AFM in ambient conditions (same region as (b) Network height ~ 2.5 nm, “sub-layer” ~ 0.2 nm.

In conclusion, we have presented results showing both high resolution scans of the nanoparticle networks and investigated apparent height differences in the imaging of the networks between the various modes. The presence of an apparent “sub-layer” has been noted for the first time, as has its manipula-

tion during scanning. The chemical composition of the “sub-layer” cannot be conclusively determined using the scanning probe techniques use, but is likely due to excess surfactant in the form of thiols or TOAB.

6.3 Force spectroscopy

In addition to basic topographic imaging, a limited number of force spectroscopy experiments were conducted. In the previous chapter (on Si(100)), force profiles were presented taken at single points on the image or as an average of a few points taken over the same location. In experiments on the nanoparticle networks a different technique was used - so called “grid spectroscopy”. In this technique the topographic image is subdivided into a grid of spectroscopy points (each point being typically 10 x 10 pixels). As the scan is performed, a single spectroscopy point is performed in each of these grid points. As a result, for a typical 500 x 500 pixel topographic scan approximately 2500 spectroscopy points will be taken. Consequently, with typical scan parameters these experiments can take between four and eight hours to complete. The advantage of this technique, apart from obviously generating a large amount of data for analysis, is that the spectroscopy grid points can then themselves be converted into an image format, and the frequency shift difference imaged at different distances above the surface. Related techniques have recently been used to analyse in detail the force maps of various surfaces and molecules with atomic resolution (see for example [25,220,229]). Although the images presented here are on a much larger scale and in general of lower resolution, some parallels may be drawn. In Fig. 6.10 images at four different distances from the surface are shown alongside the simultaneously acquired topography image. Shown below are the corresponding force versus distance graphs for the two areas indicated.

First, there is a clear double crossover between the force profiles for the SiO₂ and the network. Second, despite penetrating a significant distance past the turning point, the force gradient in the repulsive regime is much smaller than expected, and, interestingly, almost the same over both the network and substrate. This is especially unusual given that we would expect the thiols and

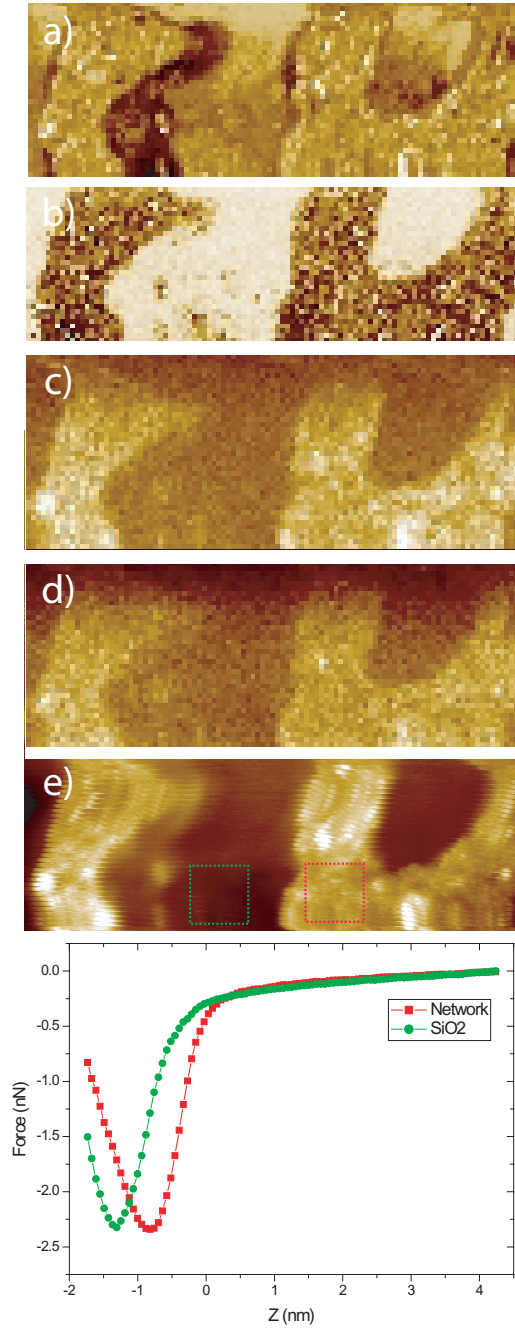


Figure 6.10: Frequency shift images imaged at a) -1.8 nm, b) -0.45 nm, c) +0.6nm, and d) +3nm. e) Topographic image. Force vs. tip-sample separation graph deconvolved from the averaged frequency shift curves of the regions highlighted in e). $V_{gap}=0V$, $A_0=20nm$, $df=-20Hz$, $333nm \times 114nm$

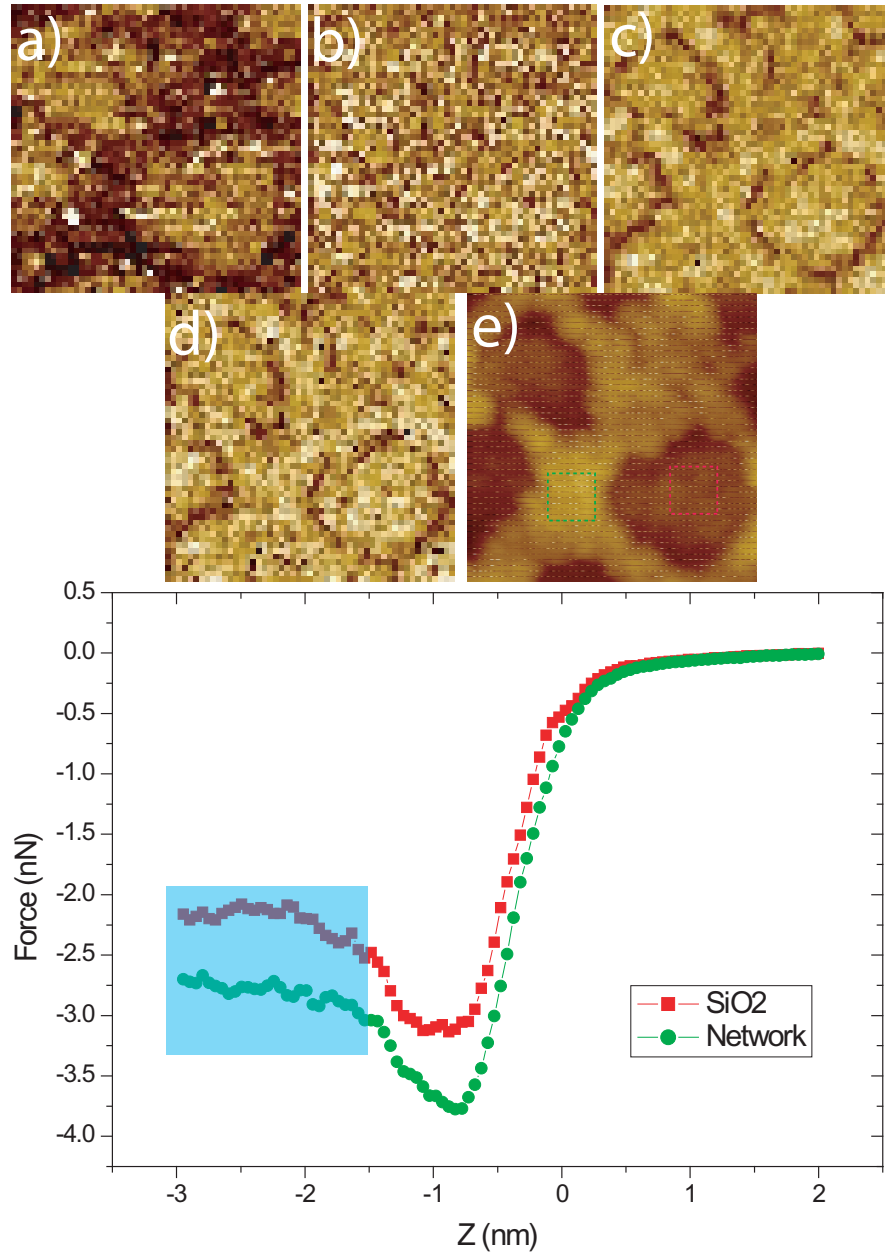


Figure 6.11: Frequency shift images imaged at a) -3 nm, b) -0.4 nm, c) +0.6nm and d) + 3nm. e) Topographic image. Force vs. tip-sample separation graph deconvolved from the averaged frequency shift curves of the regions highlighted in e). The shaded region in the force curves its most likely due to an instrumental artifact (see main text for discussion). $V_{gap}=0V$, $A_0=20nm$, $df=-25Hz$, $200nm^2$

the silicon oxide to show significantly different mechanical properties. Third, the turning points of the two regions are offset by about 0.5 nm. This indicates that for a given frequency shift setpoint the actual ‘true’ distance above the network and the silicon oxide is significantly different. The crossover of the force profiles indicates that contrast inversion may be possible during topographic imaging, and indeed the setpoint imaging demonstrates a contrast inversion as observed in the force profiles. It should be noted that we did not observe a contrast inversion during constant frequency shift setpoint imaging with this tip. The failure to observe a steep repulsive regime can be indicative of a soft tip [230]. Given that we also observe very similar force gradients over both regions, one possibility is that the apex of the tip is formed from a cluster of absorbed nanoparticles that were picked up during previous imaging, and that we are recovering mechanical properties of the absorbed cluster rather than probing differences in the surface. Ambient tapping mode experiments have demonstrated that the nanoparticles are highly mobile between the tip and sample, and given the probability of accidental tip collision a similar transfer is perhaps not unexpected in this case.

It should be made explicit that a very wide variety of force profiles were observed depending on the tip. Fig. 6.11 shows a set of force profile data observed with a different tip on the same sample. With this tip we do not see the large offset in the turning points of the different regions. The attractive force over the network, however, is almost uniformly larger than that over the substrate. In an attempt to recover a strong repulsive regime the tip was driven closer to the surface than for the data shown in Fig. 6.10. Instead of an increase in the repulsive interaction, however, the force began to level off. As noted for Fig. 6.10 it may be that we have a soft tip, terminated with a nanoparticle cluster that is deformed upon indentation. However, another possible explanation for this reduction in the force gradient is that as we push into the surface the amplitude regulator is no longer able to maintain a constant oscillation amplitude. This would show up clearly in damping, or amplitude error signals, but unfortunately neither of these data channels were recorded during this experimental run. Consequently, it may be unwise to ascribe the highlighted features to the mechanical properties of the tip or sample.

In general, the wide variety of force profiles observed for different tips prevent us making any strong quantitative conclusions regarding the tip-sample interaction. Nevertheless, the smaller than expected force gradient in the repulsive regime and similar force gradients in the attractive regime over different regions may suggest that in general the tip is terminated with a nanoparticle cluster rather than a hard silicon apex.

6.4 Contact potential difference measurements

In this section we present the results concerned with the measurement and imaging of the contact potential difference (CPD) across the substrate and the network. We first present results obtained using grid voltage spectroscopy taken on the same system as the topographic results in the first section, and then look at Kelvin probe measurements conducted at the CEA in Grenoble, France.

6.4.1 Voltage spectroscopy

Fig. 6.12 and Fig. 6.13 show the results of grid voltage spectroscopy experiments. These images highlight a couple of important points. First, they demonstrate that, by the correct choice of gap voltage, the electrostatic difference between two regions with different contact potentials can be effectively nulled out so as to allow accurate topographic imaging (as detailed in [85]). Second, by taking the difference in minima of each curve we can measure the contact potential difference between the tip and both regions of the sample. We also show the very strong tip dependence on both the qualitative and quantitative nature of the shape of the curves and the absolute values recorded. Images from grid spectroscopy (as described in the previous section) are shown alongside the topography. It is clear that at the extremes of the spectra a very strong contrast is observed between the substrate and the network, but that by imaging close to the voltage at which the two curves coincide (i.e. at a point at which a given voltage has the same the frequency shift on both regions) any electrostatic difference in the force is effectively minimised.

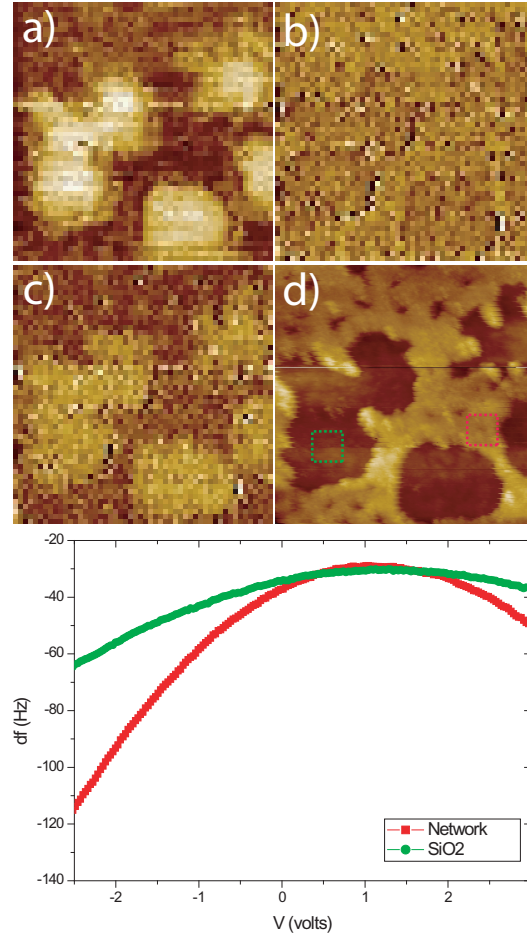


Figure 6.12: Frequency shift images imaged at a) -3V, b) +0.5V, c) +3V, d) topographic image. Averaged voltage versus frequency shift curves of the regions highlighted in d). $V_{gap}=+1V$, $A_0=16nm$, $df=-30Hz$, $500nm^2$. CPD \sim 160mV

It should also be noted that in principle two such points exist for curves in the configuration shown (i.e. two intersection points). It is generally assumed that in such instances it is preferable to pick the lower voltage so as to reduce any field related effects on the tip and/or sample. It is curious to note that not only are the voltage spectra radically different in qualitative shape (as we might expect between different tips), but also critically the *difference* (in CPD) between the network and the substrate in each case is significantly different. We discuss the origin of differences in contact potential measurement in detail in the next section.

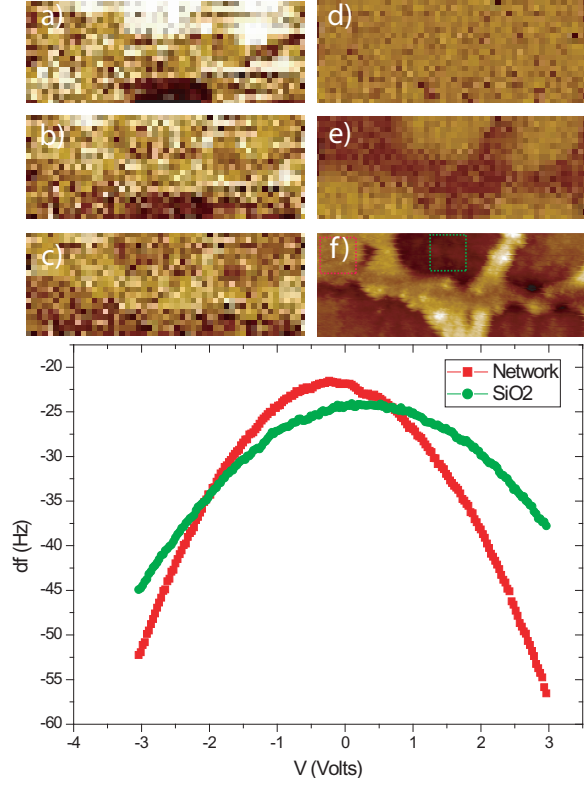


Figure 6.13: Frequency shift images imaged at a) -3V, b) -2V, c) -0.7V, d) +0.9V E) +3V f) topographic image. Averaged voltage versus frequency shift curves of the regions highlighted in f). $V_{gap}=0V$, $A_0=16nm$, $df=-25Hz$, $500nm \times 188nm$. $CPD \sim 470mV$

6.4.2 Kelvin probe

In the previous section, a voltage was applied to the tip during scanning based on the results of voltage spectroscopy points taken before and during the scans. As we have seen, this is an effective method for reducing the effect of electrostatic differences between the two regions. There are, however, a number of limitations to this approach. For example, if there are three or more different regions, it is in general impossible to choose a tip voltage that will allow accurate topography to be recovered [85]. In addition, during an experimental run itself it may not be possible to determine the gap voltage with high accuracy. Third, this method is unable to cope with changes in the tip state; strictly, in the event of any change in the tip the voltage must be re-checked. Finally,

the effect of ramping a large voltage across the tip-sample junction can be unpredictable and can in itself result in damage to the tip. For these reasons, and where possible, it is preferable to implement an automatic contact potential difference compensation technique – i.e. Kelvin probe force microscopy (KPFM). In this section we detail (to our knowledge) the first results of scanning Kelvin probe microscopy of colloidal gold nanoparticle arrays on SiO₂ substrates. It should be noted that in the previous sections all experiments were performed on thermal (300 nm) SiO₂, whilst these experiments were carried out on native SiO₂ (approximately 2 nm thick), and so care must be taken when making any direct comparison between the two data sets.

Sample preparation and introduction processes were effectively identical to those previously described. The only important difference is that in this case EFM-50 Pt-Ir (platinum iridium) coated tips (radius of curvature ~ 25 nm) were used rather than bare silicon cantilevers. The dither voltage (~ 500 mV) was applied at the second eigenfrequency of the cantilever in order to enhance sensitivity [87].

Fig. 6.14 shows an initial topographic scan carried out using a Pt-Ir coated tip on a sample similar to those detailed in the previous section (C8 capped Au nanoparticles). The nanoparticle assemblies are clearly observed, but are in general blurry and indistinct. Fig. 6.15 shows the same region imaged with the Kelvin probe feedback engaged and at a slightly higher setpoint.

It is clear from comparison of the two images that the resolution and clarity of the scan is greatly improved by the constant correction of the gap voltage. In addition, the Kelvin probe signal is recorded simultaneously and shows excellent resolution, comparable to that of the topography. It should be noted that strong damping signals were observed when the Kelvin probe compensation was engaged. During conventional NC-AFM (in both systems) very little damping was observed. A higher resolution image is shown in Fig. 6.16.

It was observed that during Kelvin probe scans of this sample, additional, apparent “subsurface” features were seen in the Kelvin probe image as seen in Fig. 6.17. The most likely origin of these is that they are the influence of step edges on the silicon surface buried underneath the native oxide layer. It has been shown on some surfaces that step edges can have a strong effect on

the local contact potential difference [207] and that this influence can extend through an insulating layer. This effect is likely to be more pronounced in amplitude modulated Kelvin probe force microscopy which is more sensitive to long-range forces than frequency modulated mode. The lack of any strong topographic or damping signal that corresponds to these features also strongly supports the likelihood of a subsurface origin.

6.5 C12 capped nanoparticles

After imaging of the C8 thiol-capped nanoparticles, a more extensive Kelvin probe study was carried out on C12 thiol-capped nanoparticles, and the effect of annealing the networks in vacuum.

An initial topographic image of the C12 nanoparticle network is shown in Fig. 6.18 and immediately shows striking differences as compared to the features previously observed. In this image the electrostatic difference between the substrate and network has caused a complete image inversion, with the substrate imaging apparently 8 nm higher than the network. This provides an excellent example of why compensating the electrostatic force is so important

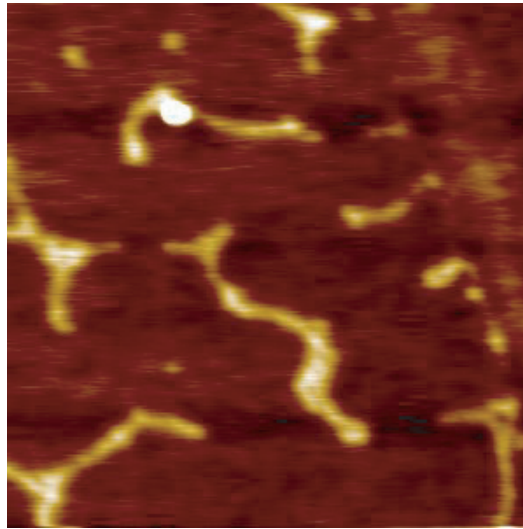


Figure 6.14: Image taken of spun cast C8 spun cast nanoparticle assemblies using a Pt-Ir tip. $V_{gap}=0V$, $A_0 = 38nm$, $df=-10Hz$, $1000nm^2$

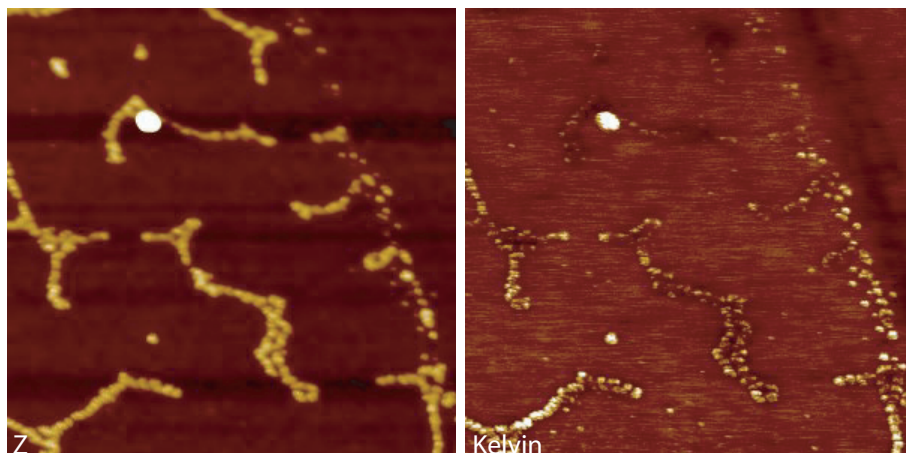


Figure 6.15: (Left) Image taken of spun cast C8 spun cast nanoparticle assembly using a Pt-Ir tip of the same area as Fig. 6.14 with Kelvin probe compensation engaged. (Right) simultaneous Kelvin image. $A_0 = 38\text{nm}$, $df = -15\text{Hz}$, $1000\text{nm} \times 1000\text{nm}$

in obtaining accurate topography images.

Fig. 6.19 and Fig. 6.20 show two subsequent scans with the Kelvin probe compensation engaged. In the first large-scale image (taken at lower setpoint) the network is clearly resolved in topography and Kelvin images. An interesting feature is that there are certain areas of the network which initially appear brighter than others in the Kelvin image. Upon zooming in and increasing the setpoint, however, the contrast changed slightly with high resolution topography and Kelvin images obtained (Fig. 6.20). The slightly brighter areas now appear to correspond to topographic features of the same size. The apparent change in the number of bright areas in the Kelvin image seems to indicate that this is a setpoint dependent effect – i.e. there is a variation in the absolute contact potential difference detected based on how close the tip is to the sample (see later sections for discussion). As expected, approaching closer to the sample increases the resolution in both images.

6.5.1 In situ annealing and imaging

Previous studies have been performed to examine the feasibility of using spun cast nanoparticle networks as a template for nanowire networks [187]. As part

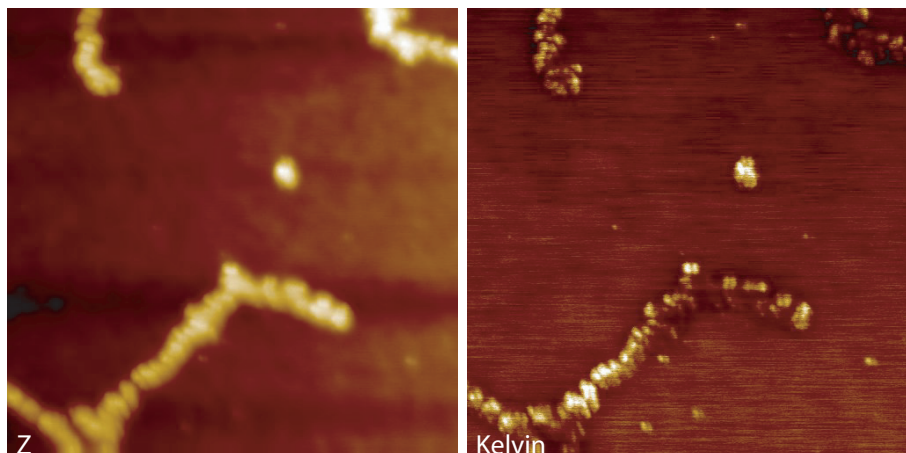


Figure 6.16: (Left) High-resolution image of part of the assemblies shown in Fig. 6.15 with Kelvin probe compensation engaged. (Right) simultaneous Kelvin image. $A_0 = 38\text{nm}$, $df = -15\text{Hz}$, $500\text{nm} \times 500\text{nm}$

of these experiments the networks were annealed in situ and the change in their valence band spectra observed using UPS. In those experiments, however, it was not possible to scan the nanoparticles in situ or with high resolution. Instead, low resolution tapping mode images, prior to and after annealing, indicated that the networks appeared to be broadly similar, but with a detectable degree of sintering post anneal. In order to expand on this work, nanoparticle samples were investigated in vacuum using Kelvin probe, then annealed to remove the thiols from the gold nanoparticles and then rescanned in the same system. In all annealing experiments presented here, C12 capped nanoparticles were used.

Fig. 6.21 shows an initial topographic scan taken of the same sample as Fig. 6.20 after having been annealed in vacuum at a temperature of approximately 250°C for around ten minutes. We observe the general topography of the network remains the same, in broad agreement with previous work [187]. Here, however, we are able to resolve much more detail than was possible in previous work, and we can see that the nanoparticles have indeed sintered together into larger granules. Unfortunately, in subsequent imaging after engaging the Kelvin probe a tip event occurred resulting in a clear tip artefact during imaging of the network (see Fig. 6.22), most likely due to accidental

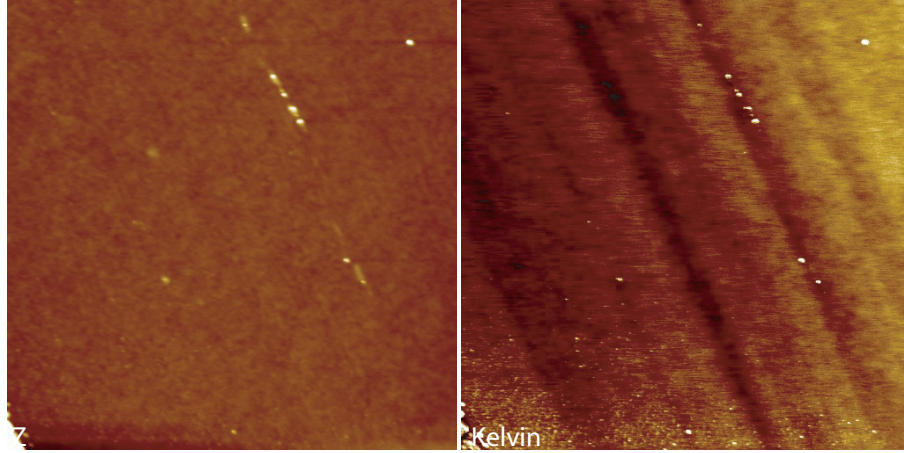


Figure 6.17: (Left) topography of bare SiO₂ region close to the area shown in Fig. 6.15 (Right) simultaneous Kelvin image showing apparent subsurface features. $A_0 = 38\text{nm}$, $df=-20\text{Hz}$, $1500\text{nm} \times 1500\text{nm}$

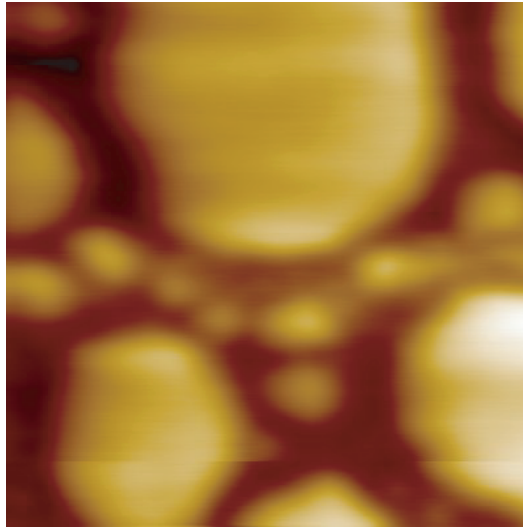


Figure 6.18: Topographic scan of C12 capped nanoparticle spun cast network taken with Pt-Ir tip showing contrast inversion. $V_{gap} = 0\text{V}$, $A_0 = 38\text{nm}$, $df=-20\text{Hz}$, $1500\text{nm} \times 1500\text{nm}$

transfer of nanoparticles from the sample to the tip. Despite this change high-resolution images were still possible, although the influence of the tip shape during imaging is clear.

The same sample was then subsequently annealed again at the same temperature/time in order to examine if there were any further changes in the

topography or work function. Although the topography appeared to remain qualitatively the same as for the first anneal (see Fig. 6.23) a significant change in the recorded work function did occur. Confusingly, however, in terms of absolute values, the change appears to have occurred over the substrate rather than the network as might be expected - Fig. 6.24) shows a zoomed-in scan of the same area. As previously noted it is clear that annealing to remove the thiols does introduce breaks in the network due to sintering at these coverage levels. It is also curious to note “dark regions” in between the sintered gold areas which image as much darker than either the gold, or the substrate. As well as obvious changes in the structure of the network, a careful analysis of the images before and after annealing shows that the imaging of the substrate has also changed (Fig. 6.25) (see later sections for discussion on both these points).

In light of the unexpected changes in contact potential observed during the second anneal, the experiment was repeated using a different sample and tip. In this second experimental run the image quality was significantly lower (see Fig. 6.26), most likely due to an inferior tip. In addition, the quantitative and qualitative detail of the contact potential differences measured was different to the first run, with a much smaller variation between the first and second

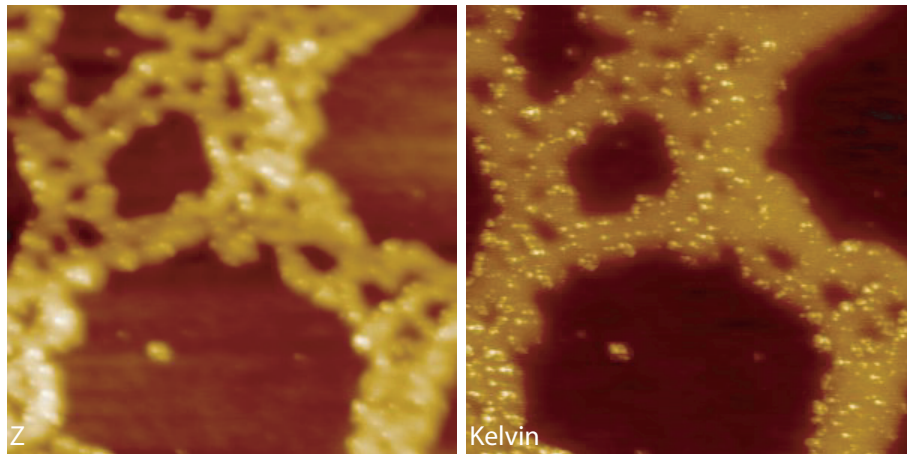


Figure 6.19: (Left) zoom in of the same region in a shown in Fig. 6.18 with Kelvin probe compensation engaged. (Right) simultaneous Kelvin image. $A_0 = 38\text{nm}$, $df = -24\text{Hz}$, $500\text{nm} \times 500\text{nm}$

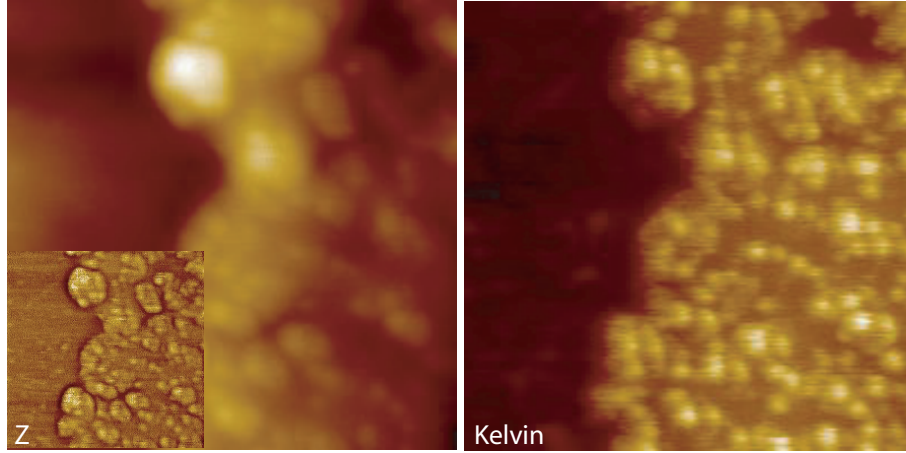


Figure 6.20: (Left) high-resolution scan showing zoom in region shown in Fig. 6.19 (inset) high pass filtered image. (Right) simultaneous Kelvin image. $A_0 = 38\text{nm}$, $df = -31\text{Hz}$, $100\text{nm} \times 100\text{nm}$

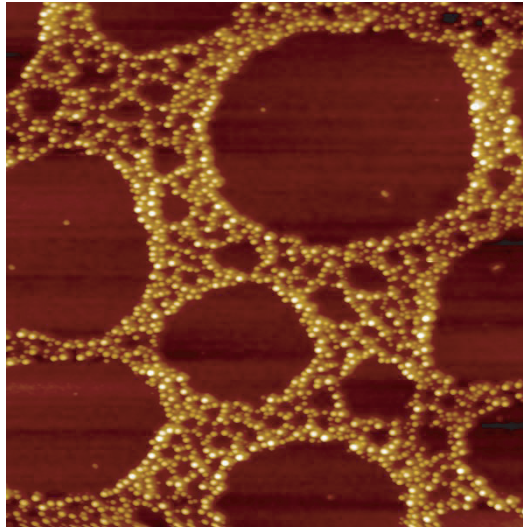


Figure 6.21: Topographic image of nanoparticle network after being annealed at $250\text{ }^\circ\text{C}$ for approximately 10 minutes. $V_{gap} = +0.6\text{V}$, $A_0 = 38\text{nm}$, $df = -10\text{Hz}$, $1500\text{nm} \times 1500\text{nm}$

anneal (see Fig. 6.27), and Fig. 6.28). As with the first run the absolute value of both the network and the silicon varied but to a much reduced degree.

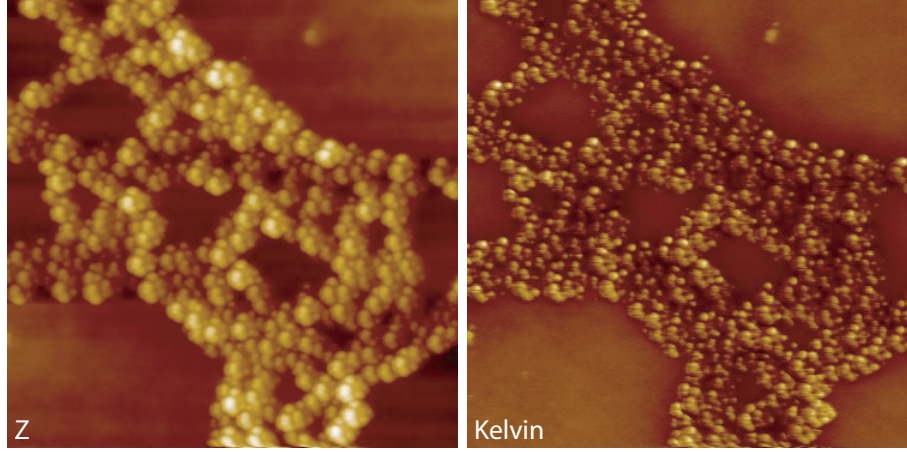


Figure 6.22: Zoom in of similar region to Fig. 6.21 with Kelvin probe compensation engaged. Note that there is an obvious tip artefact. $A_0 = 38\text{nm}$, $df = -14\text{Hz}$, $500\text{nm} \times 500\text{nm}$

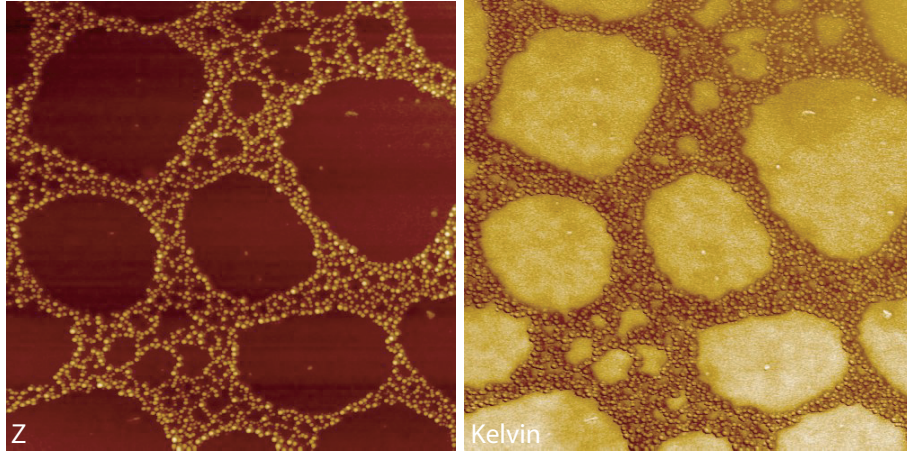


Figure 6.23: Topographic image of nanoparticle network after being annealed at 250°C for a second time. $V_{\text{gap}} = +0.6\text{V}$, $A_0 = 38\text{nm}$, $df = -10\text{Hz}$, 500nm^2
 $A_0 = 38\text{nm}$, $df = -13\text{Hz}$, 1500nm^2

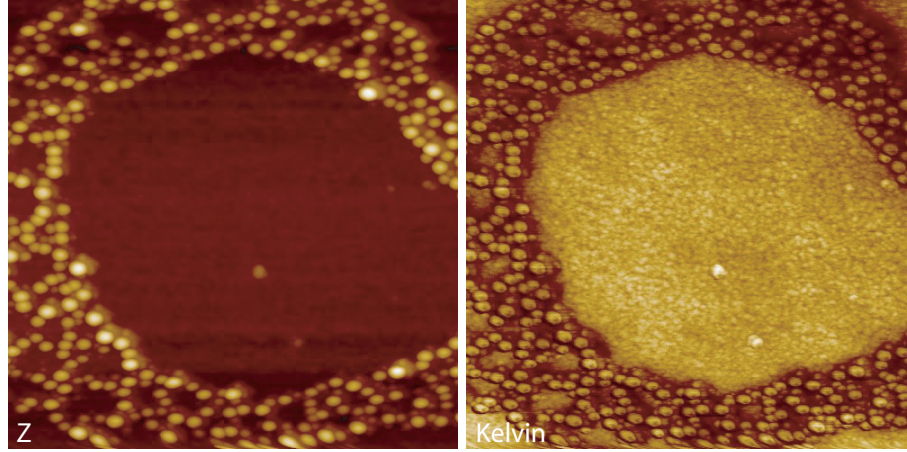


Figure 6.24: Zoom in of similar region to Fig. 6.23 with Kelvin probe compensation engaged. $A_0 = 38\text{nm}$, $df = -10\text{Hz}$, 500nm^2

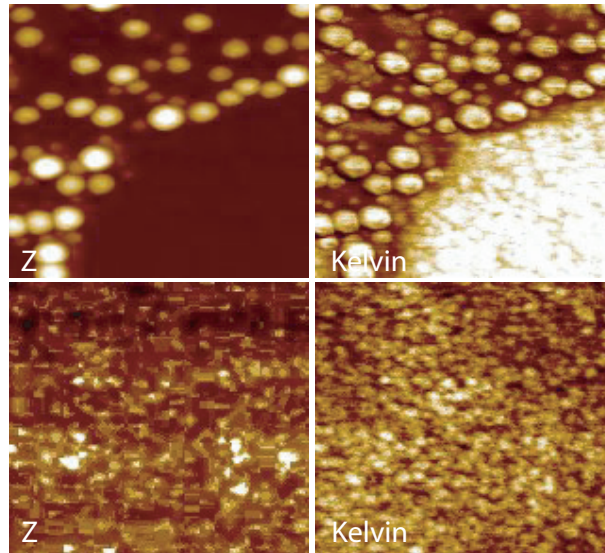


Figure 6.25: Zoom of network and substrate in Fig. 6.24 $A_0 = 38\text{nm}$, $df = -10\text{Hz}$, $157\text{nm} \times 157\text{nm}$

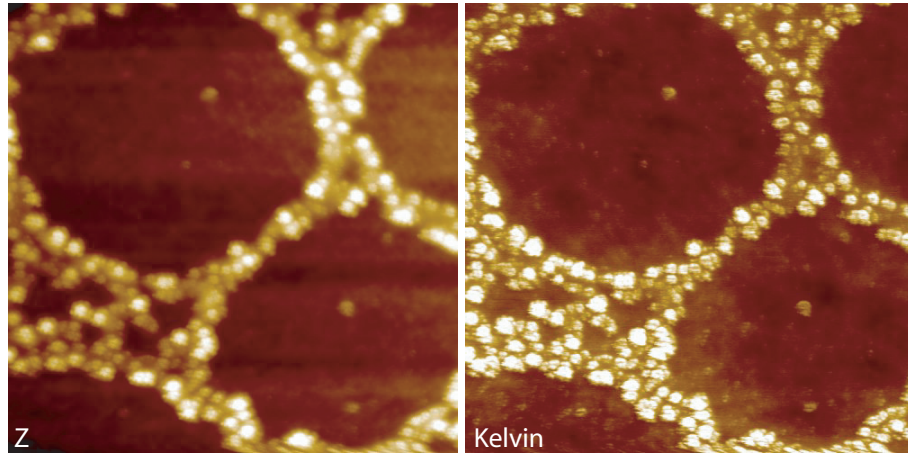


Figure 6.26: Topographic image of second C12 capped nanoparticle network sample with Kelvin probe engaged, image courtesy Evan Spadafora. Image $A_0 = 38\text{nm}$, $df = -15\text{Hz}$, $500\text{nm} \times 500\text{nm}$

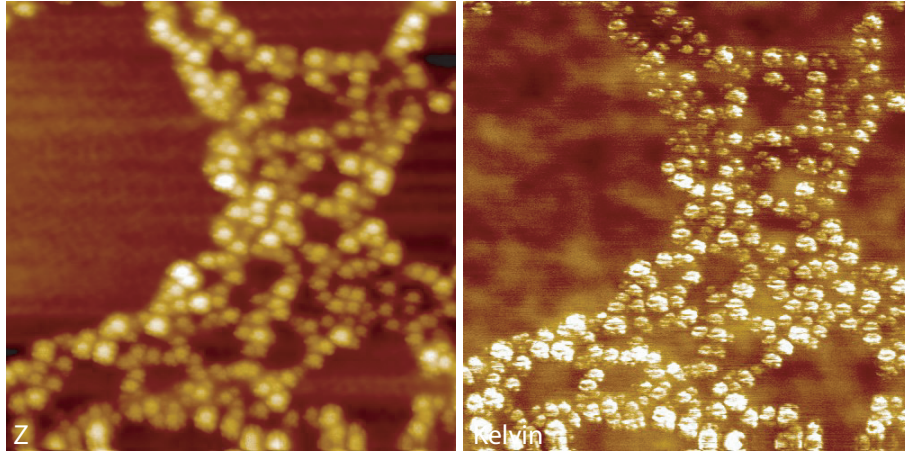


Figure 6.27: Topographic image of second nanoparticle network sample after being annealed at 250 °C for approximately 10 minutes. Image courtesy Evan Spadafora. $A_0 = 38\text{nm}$, $df = -15\text{Hz}$, $500\text{nm} \times 500\text{nm}$

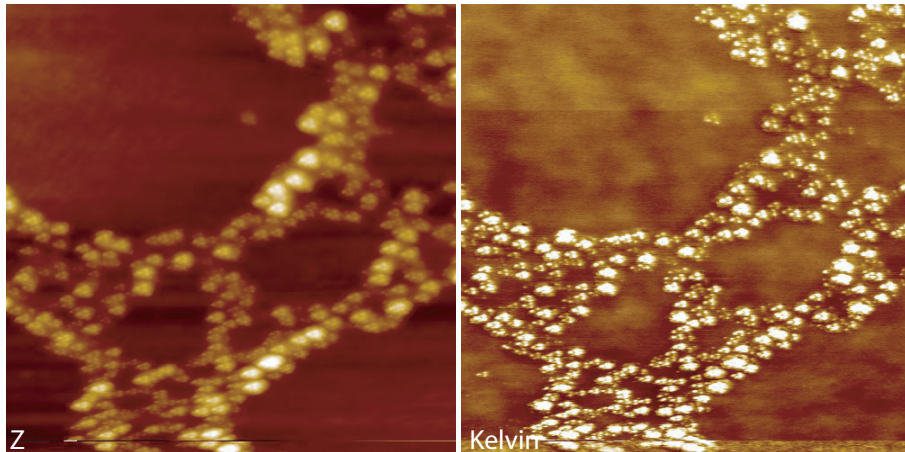


Figure 6.28: Topographic image of second nanoparticle network sample after being annealed at 250 °C for a second time. Image courtesy Evan Spadafora. $A_0 = 38\text{nm}$, $df = -15\text{Hz}$, $500\text{nm} \times 500\text{nm}$

6.5.2 Analysis of measured CPD

In this section we present quantitative data on the measured contact potential differences obtained from both voltage spectroscopy and Kelvin probe experiments and comment on the validity of the measurements and the possible origins of the features observed. Table 6.2 and Table 6.3 show data collected from the Kelvin probe and voltage spectroscopy experiments respectively.

An important aspect of this analysis is that in general we do not expect to recover the same absolute values of CPD between different tips, or between tip changes. The CPD is most simply thought of as the difference in work function between the tip and the sample, and, as such, if the tip undergoes a structural or compositional change then the CPD between it and a region of the surface may of course change. By careful calibration (see [231] for example) it is possible to perform qualitative Kelvin probe experiments. However, in the first approximation it is assumed that for a *given* tip then the *difference* in CPD measured between two regions should remain constant even if the absolute values vary, i.e. if we are measuring the contact potential difference of two regions A and B, with a given tip, then

$$\phi_{tip} - \phi_A = CPD_{tip-A} \quad (6.1)$$

$$\phi_{tip} - \phi_B = CPD_{tip-B} \quad (6.2)$$

$$CPD_{tip-A} - CPD_{tip-B} = \Delta\phi_{AB} \quad (6.3)$$

$$\Delta\phi_{AB} = \phi_A - \phi_B \quad (6.4)$$

Sample	Network(mV)/Dark areas	SiO2(mV)	Δ CPD/ Δ CPD Dark Area(mV)
C8	-471	-584	-113 (± 15)
C12	-638	-880	-243 (± 15)
C12 Anneal 1	-472/-690	-562	-90/+123 (± 15)
C12 Anneal 2	-426/-685	-347	+79/+336 (± 40)
C12 # 2	-281	-418	-137 (± 20)
C12 # 2 Anneal 1	-295	-438	-143 (± 20)
C12 # 2 Anneal 2	-70	-260	-196 (± 25)
C12 (TM)*	Data from E.Spadafora	-	160

Table 6.2: CPD values recorded for both substrate and network using Kelvin probe. *Data collected in ambient conditions in Tapping mode

i.e. the contact potential difference between A and B can be determined independently of the absolute value of the work function of the tip.

Nonetheless, we in fact see a wide range of CPD values. For C8 passivated particles we record values between 30 and 470 mV, and for C12 passivated particles values between 137 and 243 mV. However, three of the measurements on C8 networks agree with in error (values between 113 mV and 160 mV) with two outliers. Likewise on the un-annealed C12 two of the measurements (sample number two, and the sample investigated using tapping mode by E.Spadofoa) also seem to agree (137 mV and 160 mV). Although there are insufficient data to conduct a statistical analysis, this seems to suggest that again that the quality of the tip plays a strong role in determining the value we measure. However, this then in turn casts doubt on our assumption that we should be able to accurately recover *differences* in CPD irrespective of the absolute value of the tip. We discuss issues relating to the validity of CPD measurements in the next section.

6.5.3 Comments on the determination of absolute and relative CPD by AM-KPFM

The variation we observed in the CPD measured between the network and silicon suggested that the simple, and often applied, interpretation of Kelvin probe data could not explain our results. In addition, we observed a number of instances during scanning where parameter, or tip, changes suggested that we could not take the difference in CPD between the two regions as being constant. In Fig. 6.29, for example, we observe a sudden change in the CPD observed over the substrate, but no apparent change over the network. We

Sample	Network(V)	SiO2(V)	Δ CPD(mV)
C8	1.9	1.76	130 (\pm 60)
C8	2.47	2.44	30 (\pm 30)
C8	0.26	-0.25	470 (\pm 300)
C8	1.12	1.06	160 (\pm 30)

Table 6.3: CPD values recorded for both substrate and network using grid voltage spectroscopy on native oxide samples.

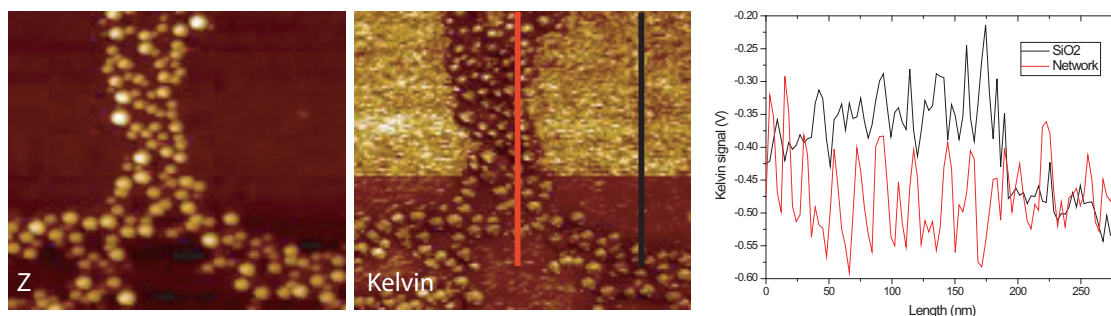


Figure 6.29: Image showing sudden change in Kelvin signal over SiO_2 but not over network. Note there is no apparent change in the topography.

also do not appear to observe a change in the topography.

In Fig.6.30 we observed the same region imaged at two different setpoints. In addition to increased resolution at higher setpoint, an analysis of the absolute values detected over the silicon and the network reveals that the recorded difference in CPD between the two changed by approximately 90 mV.

The variation we observed in CPD studies of the spun cast nanoparticle networks was unexpected, but nonetheless certain aspects may be explained by a combination of different effects noted in the literature. First, the unexpected variation in the appearance and absolute value of the substrate after anneal could have several origins. Although in terms of removing the oxide the system is stable at the temperatures used, previous studies have found that there could be significant modification of the silicon/silicon oxide interface, trapping states at the surface and therefore affecting the work function that might be recorded during Kelvin probe measurements. Alternatively, it was found during quantitative Kelvin probe studies on HOPG [231] that annealing a nominally clean unreactive surface introduced from atmosphere could result in significant changes in detected work function of the order of 200 meV, a change they ascribed to the removal of residual adsorbates.

The variation in the difference in CPD recorded between different tips and samples may also have a number of origins. Several groups [231–233] have documented variation in the detected CPD as a function of the height of the tip above the surface. The origin of these variations is a matter of some debate, with some groups assigning it to band bending in semiconduct-

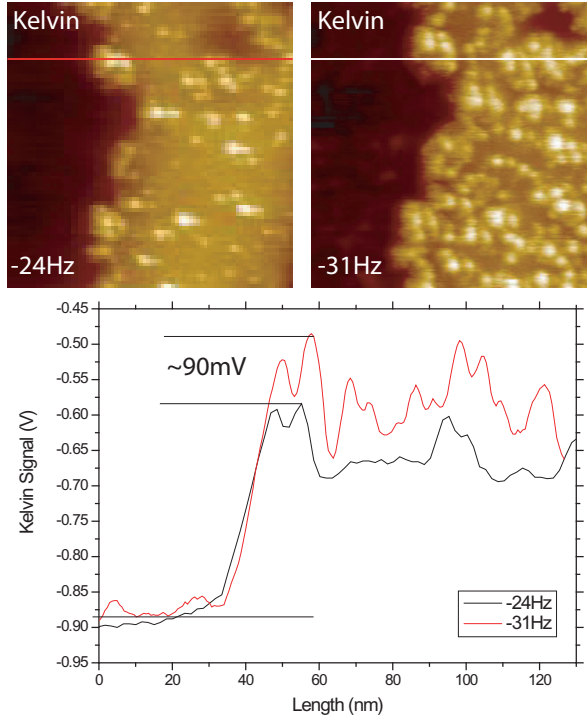


Figure 6.30: Image showing sudden change in change in the difference in Kelvin signal between substrate and network with setpoint. Absolute values have been offset to align the substrate values.

ing tips and/or surfaces [234]. Although this is no doubt an important effect, other groups using metallic tips have noted similar variations, and critically, noted that recorded variations differ depending on the Kelvin probe method used (i.e. whether using amplitude-modulated, or frequency-modulated Kelvin probe signal detection). Glatzel [232] et al performed a systematic experimental and theoretical study which showed that variations in the absolute value, and critically the *difference* in contact potential differences measured between two regions could be the result of artefacts associated with the operation of amplitude modulated Kelvin probe. They also found that the amplitude modulated mode consistently underestimated the difference in CPD compare to the values determined by UPS. Zerweck [233] also noted in a comparison of frequency modulated and amplitude modulated Kelvin probe differences in the recorded difference in work function depending on the detection method.

The “dark regions” observed after the second anneal of the first sample has

previously been noted by [232] on gold islands on HOPG, an effect that they assigned to dipoles located at the edges of metallic surfaces – and which is also found on step edges (which would correspond to the “subsurface” features we noted pre-anneal). The failure to observe these dark regions following the second anneal may be due to a different structuring of the gold network, or tip structure.

In addition to the apparent Z dependence, it should be noted that tip changes have been shown to affect the recorded difference in CPD between two regions [235]. Of course any tip change will cause a modification of the force profile between the tip and sample and implicitly cause a crosstalk into the Kelvin probe signal (in constant frequency shift feedback) as the physical distance between tip and sample will change after the tip event. Nonetheless, in the example presented above we see a change in the Kelvin signal *without any apparent change in the topography*.

6.6 Conclusions

In this chapter we have successfully demonstrated the imaging of spun cast thiol-passivated gold nanoparticle networks on silicon oxide substrates using a variety of AFM-based techniques. As well as demonstrating high resolution NC-AFM imaging in UHV, we have for the first time noted important quantitative differences in the apparent height of the networks imaged using different AFM modes and explored possible avenues of explanation. We have also performed preliminary force spectroscopy experiments that suggest that during imaging in UHV our tip apex was formed from a cluster of adsorbed nanoparticles, but also noted large qualitative differences between different tips. In addition to the topography we have also investigated the electronic properties of the networks using both conventional voltage spectroscopy and Kelvin probe studies. Although we routinely obtained high contrast topographic and Kelvin probe images, analysis reveals that quantitative measurement of the work function, especially with regard to networks annealed in situ, requires a painstaking and time-consuming study so that a statistical appraisal of results with different tips and samples can be performed.

6.7 Future work

Future work developing from the results in this chapter can be split into two broad topics, topographic imaging and CPD imaging. As regards the topography, the most immediately accessible short term experiments must be NC-AM and TM investigations on coarsened networks (especially at the boundary between the two). This should help resolve the issue as to the origin of the height differences observed in different modes, and if combined with further experiments with different chain lengths, and MD simulations, could reveal a great deal of information regarding the nanoparticle-nanoparticle and nanoparticle-surface/tip interactions. Extending work on the CPD measurements using Kelvin probe will be more arduous. It seems essential that not only are multiple well-characterised tips used, but also that both AM and FM KPFM feedback modes are engaged, and that the experiments are combined with explicit measurement of the variation in the CPD with Z (i.e. CPD(Z) “spectroscopy”). Only then will there be sufficient evidence to confidently make quantitative statements as to the variation of the work function over these samples.

Chapter 7

Electrokinetic assembly of nanoparticles in solution

“For me, it is far better to grasp the Universe as it really is than to persist in delusion, however satisfying and reassuring.”

Carl Sagan

In this chapter we present details of experiments investigating the growth of microwire super-structures from gold nanoparticles in solution via self organisation under the influence of dielectrophoretic (DEP) and AC electro-osmotic (ACEO) forces. We explore the effect of applied voltage and applied frequency on the type of structures formed and note how these parameters affect the dynamics of structure formation. In addition, we present (to our knowledge) the first investigation of how electrochemical phenomena can affect the structures even in the high frequency alternating current regime, and how under certain conditions these effects can be used to controllably and reproducibly remove and regrow the microwire structures in situ.

7.1 Experimental preparation

Experiments in this section were conducted using the setup described in section 3.5.1. To recap briefly, the electrode arrays were mounted onto the PCB

and electrically connected by microbonding. The PCB was then fixed onto the microscope stage and the connections made to a signal generator and oscilloscope (where appropriate). A small droplet ($\sim 1\mu\text{L}$) of nanoparticle solution (20nm diameter charge stabilised gold in water) was placed over the electrode of interest and the microscope objective lowered to obtain a clear image of the electrode gap (typically this involved contact with the droplet). The image capture software was then initiated and the experiment started by the application of the required signal. In all images presented in this chapter the electrode gap is approximately $10\mu\text{m}$ and the electrodes are approximately $30\mu\text{m}$ wide.

7.2 Frequency variation

An initial goal of the investigation was to find parameters that enabled ready growth of the microwire structures for our particular experimental setup. A wide variety of experimental parameters have been used in previous experiments carried out by other groups [37, 90, 92, 93, 98, 99, 197] depending on the precise combination of electrode material, electrode shape, substrate type, nanoparticle type, solution composition and electrode gap size among others. During preliminary experiments it was found that wire growth occurred most readily between 100 kHz and 1 MHz when a series resistor of $1\text{ K}\Omega$ and an applied voltage of 20 V peak-to-peak were used. We observed, however, an unexpected variation in the morphology of the wires with frequency. At the time it was not understood where the origin of this morphological change lay as it was not expected that the dielectrophoretic force would vary for metallic nanoparticles over the frequency range investigated. Therefore, we began a systematic investigation of the microstructures formed between 100 kHz and 1 MHz. The structures were observed in situ using optical microscopy, and, where possible, also imaged at high resolution ex situ using SEM as described in section 3.

A representative sample of the optical and SEM micrographs from these experiments are shown in Fig. 7.1 and Fig. 7.2. There is a great deal of variation in the morphology and number of wires grown from sample to sample. The

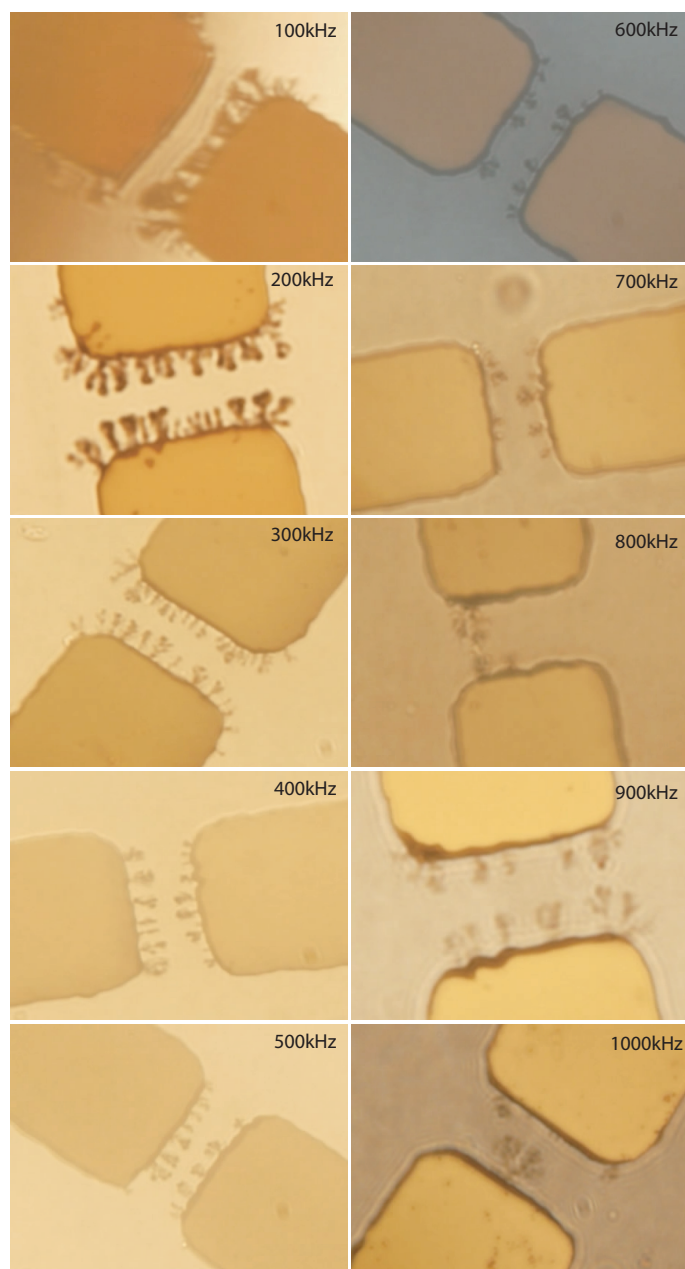


Figure 7.1: in situ optical micrographs of microwire growth in the range of 100 kHz to 1 MHz. A notable change in morphology is observed as the frequency is changed (most notably in the 100 - 600Khz range). We also observed a wide variation between different electrodes at the same frequency, but note that, in general, a larger number of denser appearing wires were observed lower frequencies. Poor contrast in the examples shown at 400 and 500Khz is due to “clouding” (see later sections)

degree of variation is most likely due to microscopic differences in the electrode surfaces producing very different field gradients between different electrodes, but, despite this, a number of clear reproducible qualitative trends were observed. Primarily it appeared that at the lower end of the frequency range more wires were grown, and that the wires grown appeared to be “thicker” and to be more branched than those grown at higher frequencies. The origin and effects of the different morphology are discussed in later sections.

It should be noted that SEM imaging of the samples was not entirely straightforward, as the wires were occasionally damaged during the drying process. It is, however, perhaps surprising that, given the high capillary forces expected during drying, as many of the wires survived and produced good quality images as was observed. Second, the imaging of conductive samples on highly insulating substrates such as silicon oxide or glass can be problematic in SEM due to charging effects which can cause distortion of the image. Third, contamination due to residual citrate from the solution was often observed (see Fig. 7.3) either as what appeared to be a thick coating or “crystalline” precipitation. In order to reduce this contamination a careful rinsing/drying procedure was initiated. After the experiments had been carried out, small (10 μ l) droplets of DI water were placed on to the substrate and then carefully drawn off using a micro pipette and clean room tissue. This procedure was repeated three times in order to draw off as much of the residual citrate as possible, without damaging the assembled structures. Although not completely reliable, this method seemed to result in a higher proportion of nominally clean samples.

7.3 Growth dynamics

In addition to changes in morphology, there appeared to be differences in the observed growth rate and dynamics of the wires at different frequencies. Consequently, further analysis was performed on videos recorded during the growth observations. The videos were broken down into individual frames, and processed using standard image processing software [236] in order to allow quantitative measurements of the wire positions during the growth process.

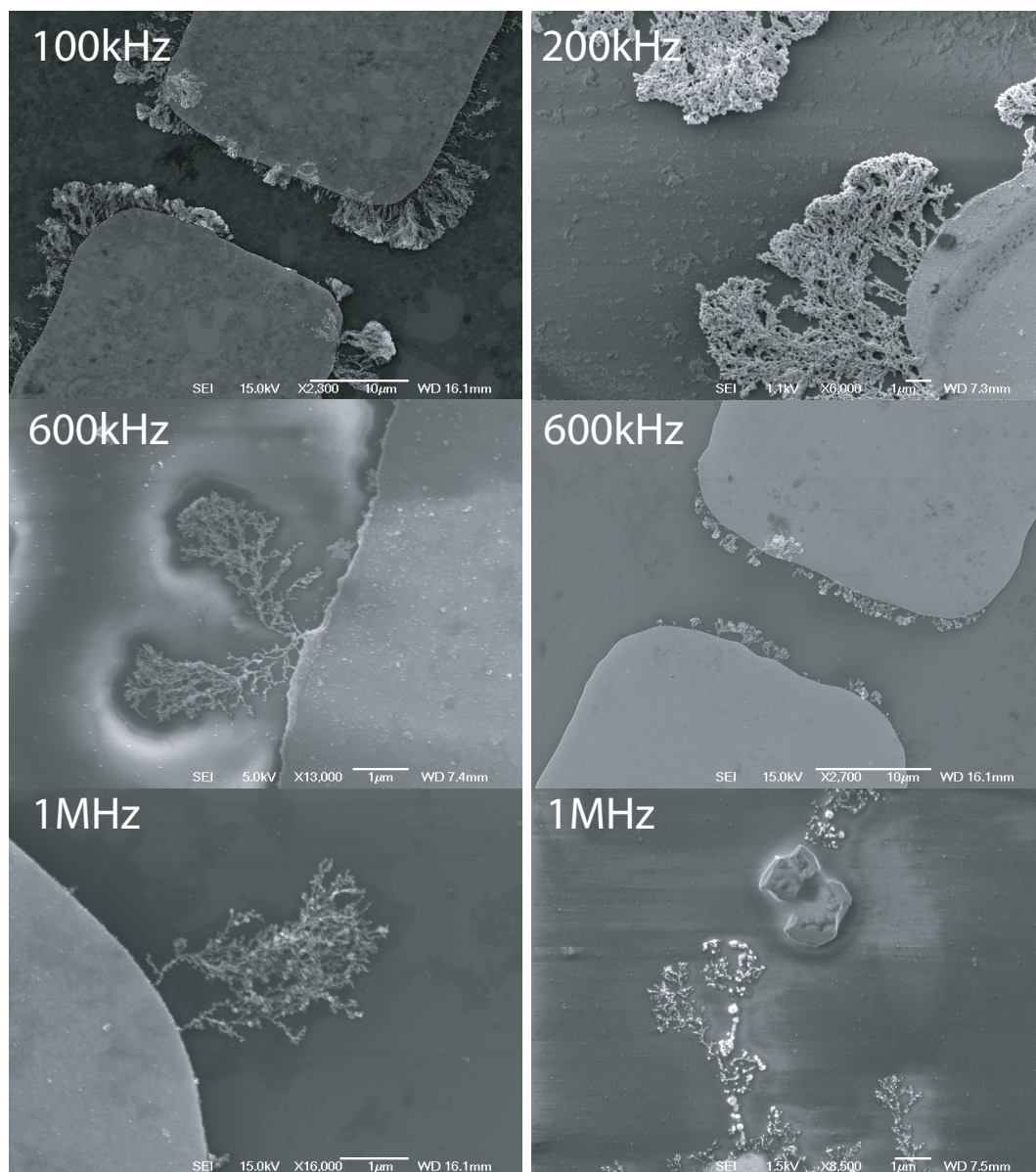


Figure 7.2: Representative SEM micrographs of microwires grown over a frequency range of 100 kHz to 1 MHz on both SiO₂ and glass substrates.

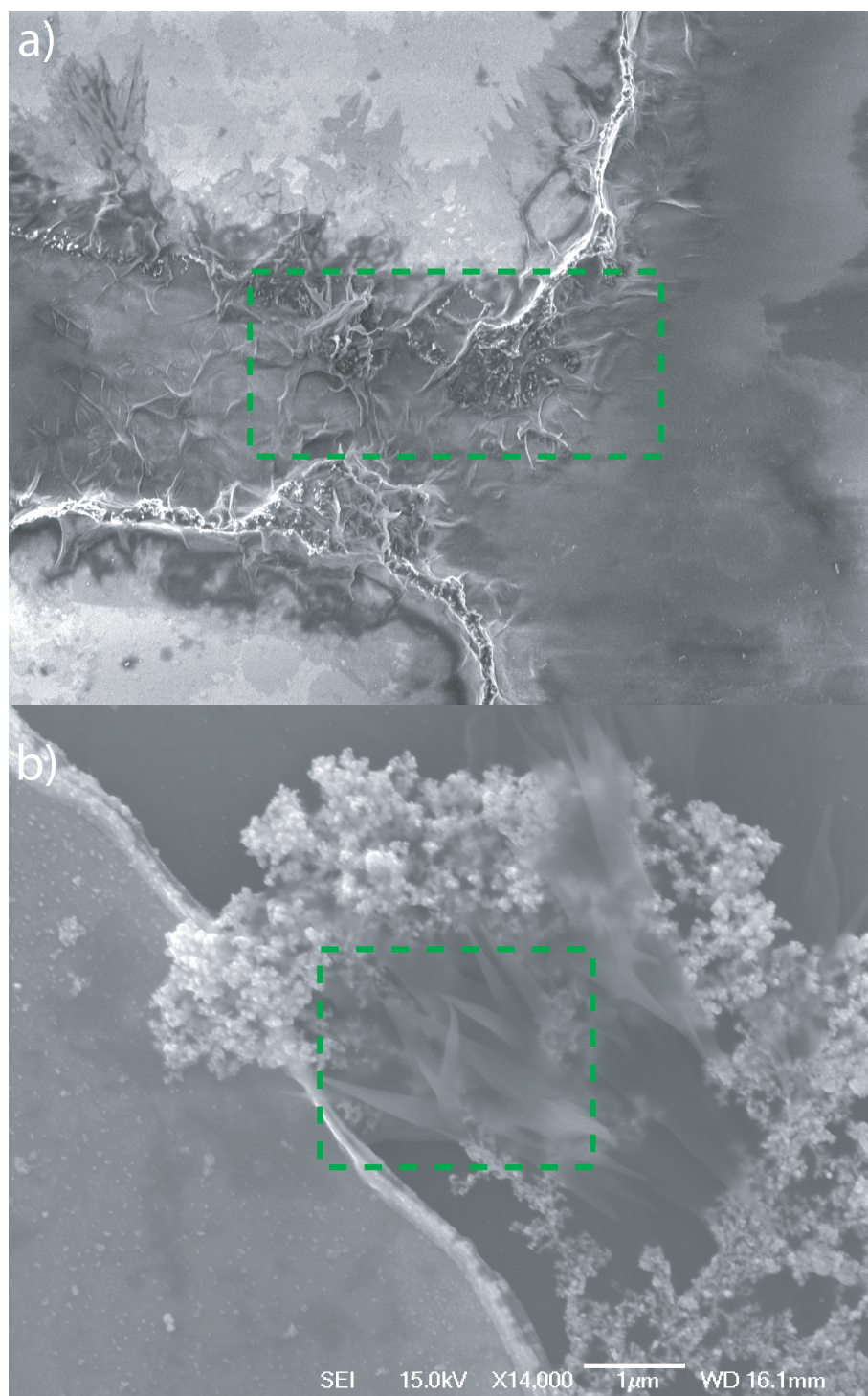


Figure 7.3: Examples of different contamination structures due to residual citrate observed during SEM micrographs: a) “coating”, b) “crystalline”.

Representative samples of the data collected are shown in Fig. 7.4. As with the qualitative observations of morphology there is a wide variation from sample to sample. Nonetheless, it is clear that there is a quantitative difference between the wire growth dynamics observed at low frequencies, and those at high frequencies – with a somewhat noisy continuum in between.

At high frequencies growth appeared to be approximately linear within the resolution and error of the measurements. At low frequencies, however, the growth rate appears to significantly reduce as the wires approach each other, and then to plateau/stall as the wires get very close (approximately 2 μm apart). This behaviour was not only unexpected, but also entirely counterintuitive. When the wires grow extremely close together, the electric field gradient should be much stronger than during the initial stages of growth, as not only is the aspect ratio of the wires higher than that of the electrode edge, but the effective distance between the electrodes has been reduced. Therefore, one would expect the growth rate to increase (if the dielectrophoretic force is the limiting factor) or at the least remain constant if other factors (such as diffusive particle delivery) limit the growth rate. However, the situation is much more complex than this rather naive analysis suggests and is discussed further in the following sections.

7.4 Growth thresholds

In addition to observing changes in the morphology and growth dynamics, data were collated in order to construct a basic “phase diagram” for the threshold growth of the microwires across the voltage/frequency range investigated. The results are shown in Fig. 7.5. Approximately twenty to thirty separate experimental runs were used in order to construct these diagrams but again, it must be stressed that there is a great deal of variability from sample to sample. One plausible explanation for this is that the roughness of the electrodes undoubtedly plays a large role in initiating growth. This roughness is essentially not well controlled, because in the method used to construct the electrodes the 10 μm gap is itself at the resolution limit of the optical masking process. The fine structure of the electrodes themselves is mainly governed by the final lift-off

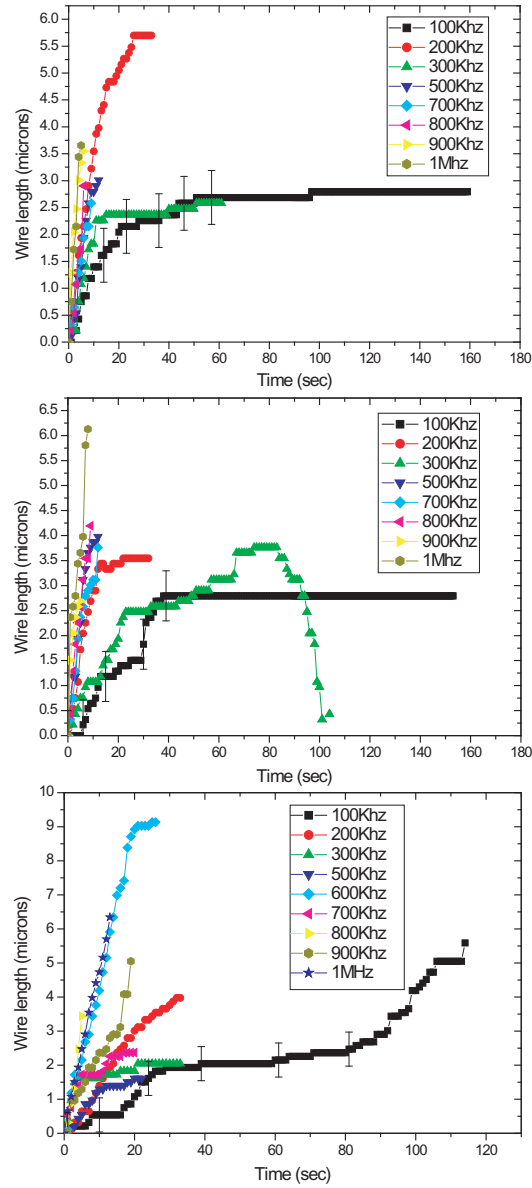


Figure 7.4: Plots of wire growth taken from in situ videos. In general there is a wide variation of growth rates and dynamics, but lower frequencies (100 to 300 kHz) generally have lower growth rates than those at high frequencies (600 kHz to 1 MHz). Note that at low frequency there are numerous examples of “plateaus”. Representative error bars are included on one dataset of each graph. One example of “spontaneous” retraction is captured (centre graph, 300kHz data)

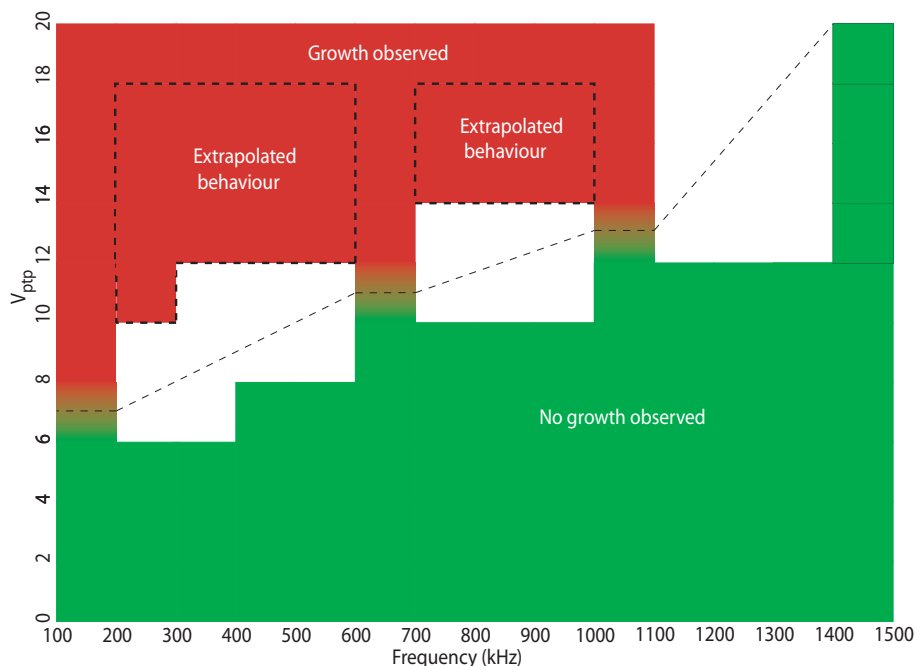


Figure 7.5: Phase diagram of frequency versus applied voltage demonstrating the threshold regime for growth starting with bare electrodes. White regions indicate where there is insufficient experimental data to precisely define the transition. Dotted line is included as a guide to the eye only, the trend may not be linear in these regions. Extrapolated behavior indicates regions where we have no direct experimental data, but in which we can confidently predict growth

process and sonication. Even with this caveat in place it is nonetheless clear that a trend can clearly be observed. As the frequency is increased the voltage required appears to increase – although the resolution of the phase diagram is not good enough to quantitatively determine the exact nature of the trend-line. Growth data below 100 kHz could not be obtained systematically and reproducibly due to problems with damage to the electrodes.

7.5 Wire retraction

In addition to the wide variety of morphologies, dynamics and thresholds observed for growth in the experiments, unusual and intriguing phenomena were sometimes observed. For low frequencies (100-400kHz), and in approximately

10% of cases, as the wires approached and came close to connecting they would “stall” (see Fig. 7.4). Importantly, in a number of cases, the wires would not then connect, but instead the solution would become cloudy and the assembled wires would appear to “retract” from the tips back towards the electrodes (see Fig. 7.6 and Fig. 7.7). This retraction would then sometimes continue to progress back onto the bulk electrode itself, typically stripping away the gold but leaving behind most of the titanium adhesion layer. While spontaneous retraction was not observed above 600kHz the “clouding” of the solution was observed after successful wire connection, even at higher frequencies.

Understanding these observations was further complicated by results obtained whilst trying to grow wires of different morphologies on the same sample. Initially, an attempt was made to grow long high aspect ratio wires at a high frequency, followed by a switch to a lower frequency in order to grow thicker, more branched wires on the tips. When this experiment was attempted, however, the wires appeared to retract, and then growth would proceed at the low frequency as normal from the bulk electrode (see Fig. 7.8, Fig. 7.9 and Fig. 7.10). Further investigations revealed that this sequence could be cycled on one electrode, i.e. wires could be grown at high frequency, “withdrawn” at low frequency and, if the power was then turned off and reengaged at high frequency, the cycle could be repeated. Although this appeared to offer the exciting possibility of controlled growth and retraction of the wires in situ it was not initially understood how this controlled retraction related to the changes in morphologies and thresholds, or the apparent “spontaneous” retraction observed at low frequencies (or even if the phenomena were related). Consequently, a systematic investigation of the phenomenon was carried out.

Initially of interest were the thresholds at which this controlled retraction would occur. First, it was determined that it was not any “transient” behaviour, such as a voltage spike or the voltage slew rate, that caused the retraction. This was confirmed by performing experiments that featured a direct transition from one frequency to another, and then repeating the experiments with an extended “rest” period in between turning off the high frequency signal and reapplying the low frequency signal. These experiments were also performed using two different frequency generators [237,238] in order to ensure

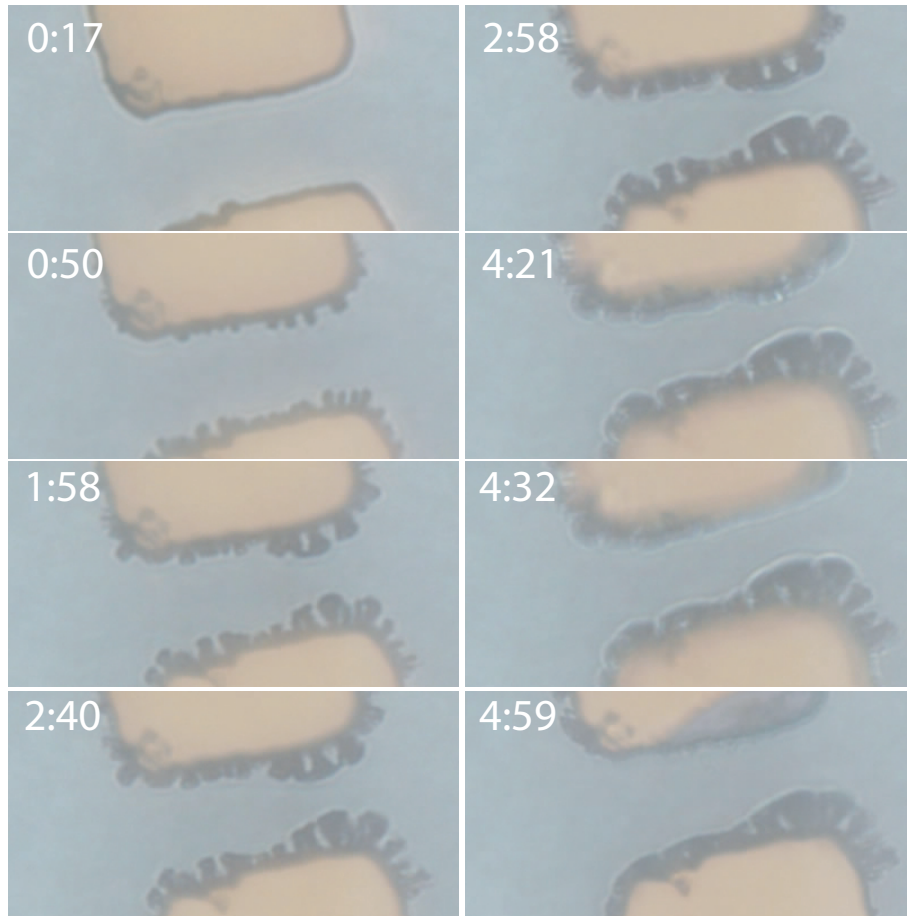


Figure 7.6: Image sequence showing growth at 100 kHz and subsequent “spontaneous” retraction and electrode damage. Note that in this particular example the wires on the “live” electrode suffered more significant retraction than on the “grounded” electrode.

it was not some inherent property of the frequency generator that was causing the retraction. In addition, measurements taken using a triggered oscilloscope appeared to show that the signal generator used did not have any “transient behaviour” when switching between frequency ranges. Finally, the retraction was sometimes observed to proceed on the time scale of several seconds – far longer than any expected transient behaviour might be expected to propagate. In addition, switching off the applied signal, and then reapplying it at the same (or higher) frequency, did not seem to cause any further retraction, but rather growth continued unabated.

Given that transient behaviour did not seem to be the primary cause of the phenomenon it seemed prudent to investigate the thresholds for this apparent retraction. As noted, reapplying a signal at the same frequency did not seem to cause retraction. This suggested that there was some upper threshold above which retraction would not take place, and instead further growth would occur. Unfortunately, it was also clear that wires could be grown at low frequencies, and that subsequently switching off the power, then reapplying (on those wires) would cause regrowth at the self-same frequencies that caused retraction (when applied to wires grown at higher frequencies). This causes a vast expansion in the parameter space to be explored, as not only must we take into account the parameters used in order to cause retraction, but also the *initial* parameters used to grow the wire in the first place. This vastly increased parameter space precluded a complete systematic investigation, but it was possible to sample a subset. The chosen procedure was to use wires grown at 600 kHz 20 V peak-to-peak as a standard “testbed” wire for initial growth as this was found to be close to an optimum configuration for growing wires in the initial systematic frequency investigation. An investigation of frequencies and voltages to be

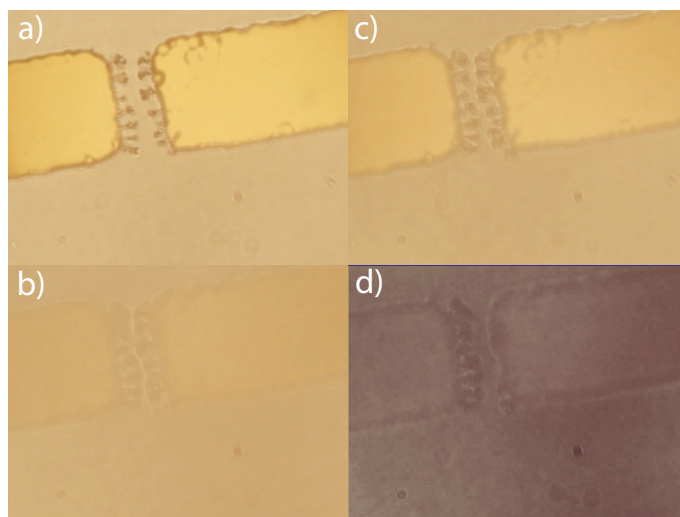


Figure 7.7: Example of “spontaneous” retraction that demonstrates heavy “clouding” of the solution at 300 kHz. Note that contrast is almost lost. In (d) clear retraction is observed on the live electrode. The final image has been contrast enhanced.

switched to after initial growth at these parameters could then be attempted. These results are summarised schematically in Fig. 7.11.

It was clear that not only is there a frequency limit, but also a voltage threshold for instigating retraction. The results indicate a combination of high voltage and low frequency were required in order to cause retraction of the grown wires. It was expected from preliminary experiments that using

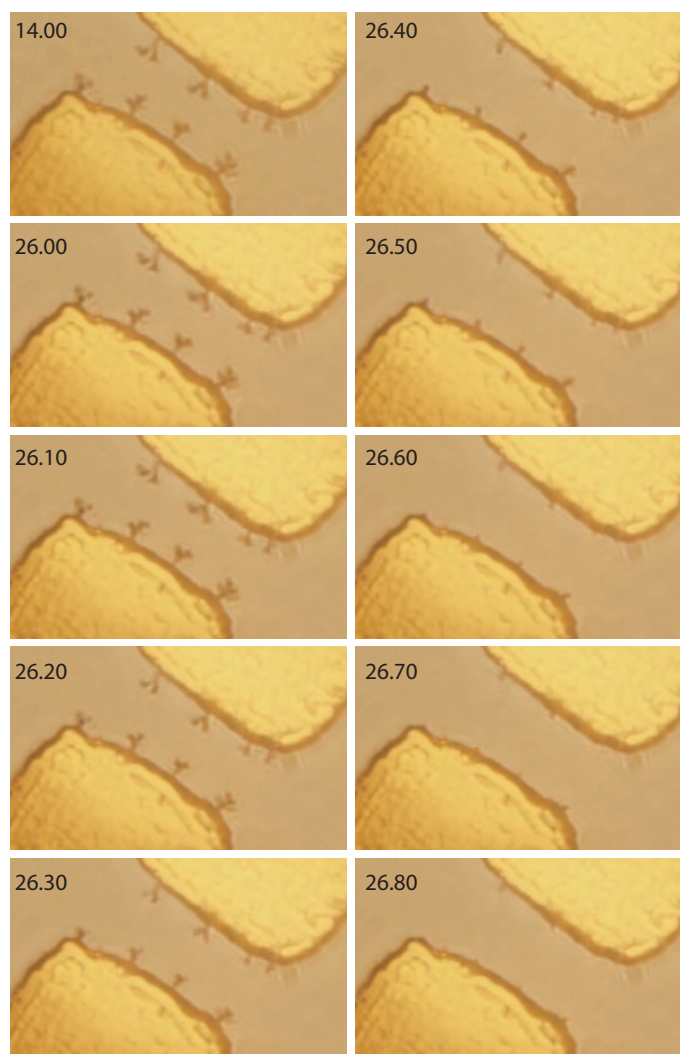


Figure 7.8: Controlled reaction due to a frequency change from 600 kHz to 100 kHz. Wires were grown at 600 kHz and the signal removed – the wires were stable during the period when no signal was applied. Time index of 26.1 to 26.9 shows rapid retraction of wires upon application of signal at 100 kHz.

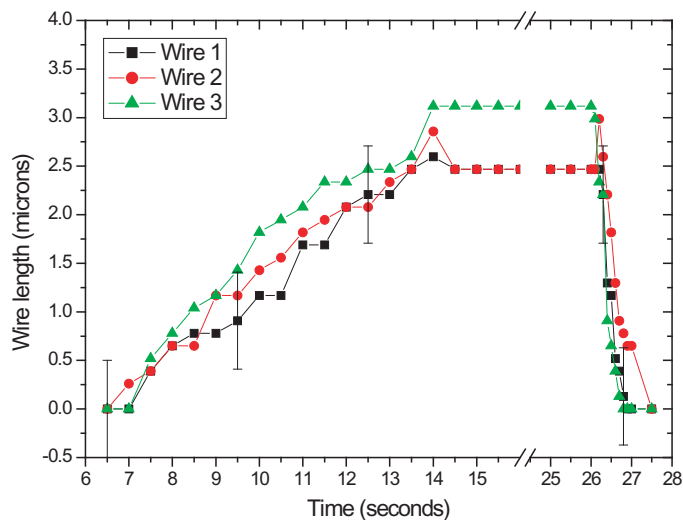


Figure 7.9: Plots of wire growth of three wires from the sequence shown in Fig. 7.8 during normal growth at 600 kHz, showing subsequent stability with no applied signal, and rapid retraction upon application of 100 kHz signal.

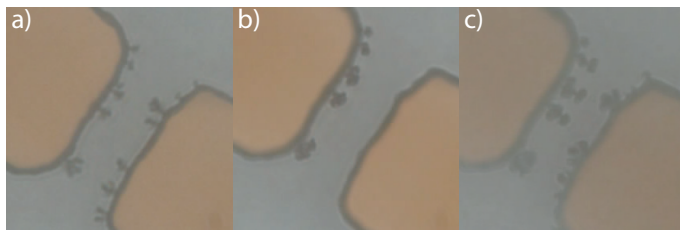


Figure 7.10: Image sequence showing controlled retraction and subsequent regrowth. (a) growth at 600 kHz. (b) immediately after application of 100 kHz signal showing complete retraction on live electrode (c) subsequent regrowth at 100 kHz.

even lower frequencies will also cause ready retraction, but it was difficult to perform a systematic investigation in this region due to the aforementioned electrode damage that was present even during growth experiments. This tendency for retraction to occur at high voltages and low frequencies again suggested a connection to the “spontaneous” retraction that was sometimes observed at lower frequencies (see previous section). Additional experiments also showed that careful choice of parameters could yield quite a high degree of control – for example in Fig. 7.12 initially a 200 kHz signal is used to grow the

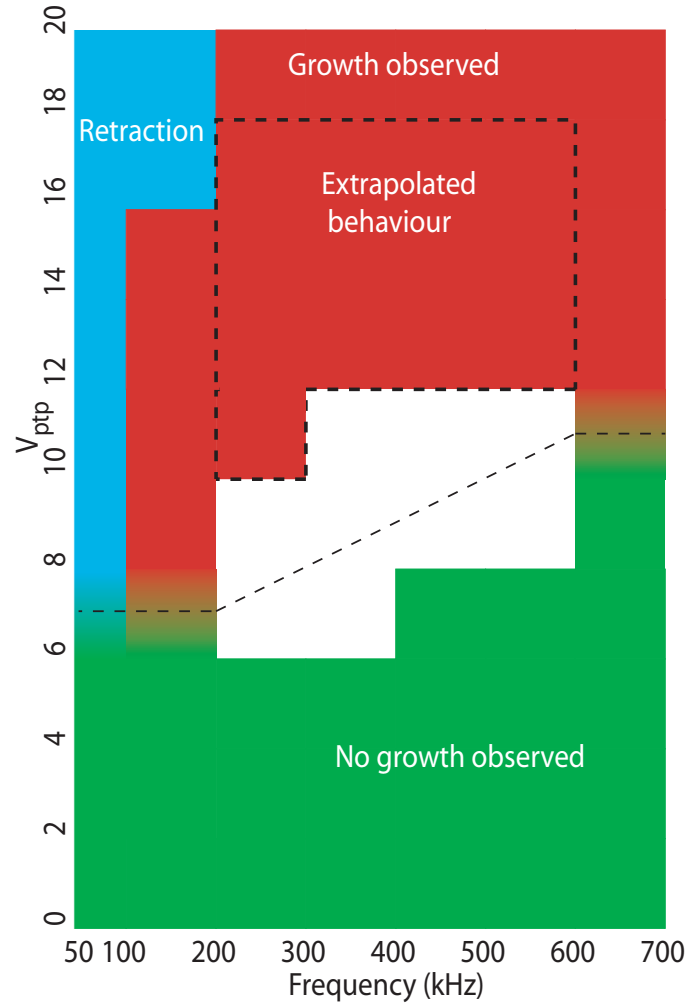


Figure 7.11: Phase diagram of frequency versus applied voltage showing where growth, no growth, or retraction was observed when applied to wires grown at 600 kHz, 20 V_{pk-pk} . White regions indicate where there is insufficient experimental data to precisely define the transition. Dotted line serves as a guide to the eye only. Extrapolated behavior indicates regions where we have no direct experimental data, but in which we can confidently predict growth

initial structures, the power is then turned off and a 700 kHz signal applied. This caused continued growth at the higher frequencies. The power is then again switched off, and this time an even lower frequency signal (at 100 kHz), is applied causing the complete retraction of both the wires grown at 200 kHz, and those grown at 700 kHz.

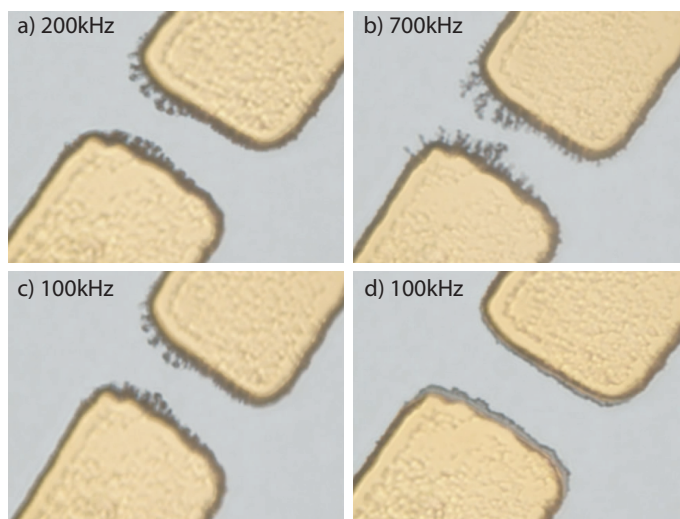


Figure 7.12: a) Growth at 200 kHz, b) subsequent continued growth at 700 kHz, c) - d) retraction of all wires after application of signal at 100 kHz.

One additional facet of the parameter space which we have not mentioned is the initial growth *voltage* of the wires. All experiments mentioned thus far involved growth of wires at 20 V peak-to-peak. In the previous sections we noted that the threshold voltage for wire growth was usually below this, dependent on the frequency applied. In one set of experiments wires growing at 100 kHz at 10 V peak-to-peak had the power switched off, and then the signal was reapplied at 100 kHz 20 V peak-to-peak. Surprisingly, rather than continued growth at 100 kHz, the wires *retracted*. These experiments demonstrated that it was not some purely frequency-dependent phenomenon that made a wire susceptible, but rather some complicated behaviour based on an interaction of both the frequency and the applied voltage that rendered some structures susceptible to retraction and others not.

At this juncture although the mechanism behind the retraction was still not clear, two primary candidates presented themselves. It was known from the work of Gierhart and Bahukudumbi [92,93,95] that the most likely cause for the changes in the assembled structure morphology was variations in the ACEO (AC electroosmotic) force, whereas our observations of “spontaneous retraction” proceeding back on to the bulk electrode suggested an electrochemical effect. In light of this, a concerted effort was made to preserve wires in

the midst of both the “controlled” and the “spontaneous” retraction such that they could be investigated using high resolution SEM. Despite the difficulties involved in stopping the retraction process at the correct time, cleaning the sample, and transferring the wires intact into the SEM, it was on occasion possible to obtain high resolution images, as shown in Fig. 7.13 ((e) and (f)) and Fig. 7.14.

The most immediately striking feature is that it appears that nanoparticles in the wires have sintered despite not coming into direct electrical contact, see in particular Fig. 7.13 (f). This finding was particularly surprising given previous publications [98] where much attention had been paid to the need to include a limiting resistor and complex “fast switch off” mechanisms in order to preserve wires that connect so as to prevent damage caused by excess current flowing through the wires. However, we reproducibly found that the individual nanoparticle nature of the wires was lost *prior* to connection in our experimental setup. As well as being an unexpected observation in its own right it also suggested that one possible mechanism for the retraction – that of enhanced fluid flow “disassembling” the wires from the tip nanoparticle by nanoparticle – was not plausible as the wires already appeared to have formed solid metallic structures. While an enhanced fluid flow might be able to break the wires off at the base it did not explain the retraction from the tip in the controlled way that we observed. Furthermore, the sintering lends support to an electrochemical or electrothermal explanation for the retraction itself. As regards images of microstructures in the midst of “spontaneous” retraction - as can be seen in Fig. 7.14 - an extreme degree of sintering is immediately apparent, with the entire “front” of the nanoparticle structures having been melted/etched away. It should be noted that even structures in areas that were not seen to withdraw optically are still sintered together even though they have not experienced wholesale deformation at their tips. This observation of sintering in both cases seemed to confirm that the ACEO force, although most likely responsible for the large changes in morphology observed over the frequency range investigated, could not be responsible for the retraction events that we observed.

It is worth noting that are valid concerns about the effect of the electron

beam on the imaging of nanostructures when using SEM. We found, however, that under the imaging conditions used we were regularly able to obtain nanoparticle resolution without sintering of nanoparticles. Fig. 7.15 provides

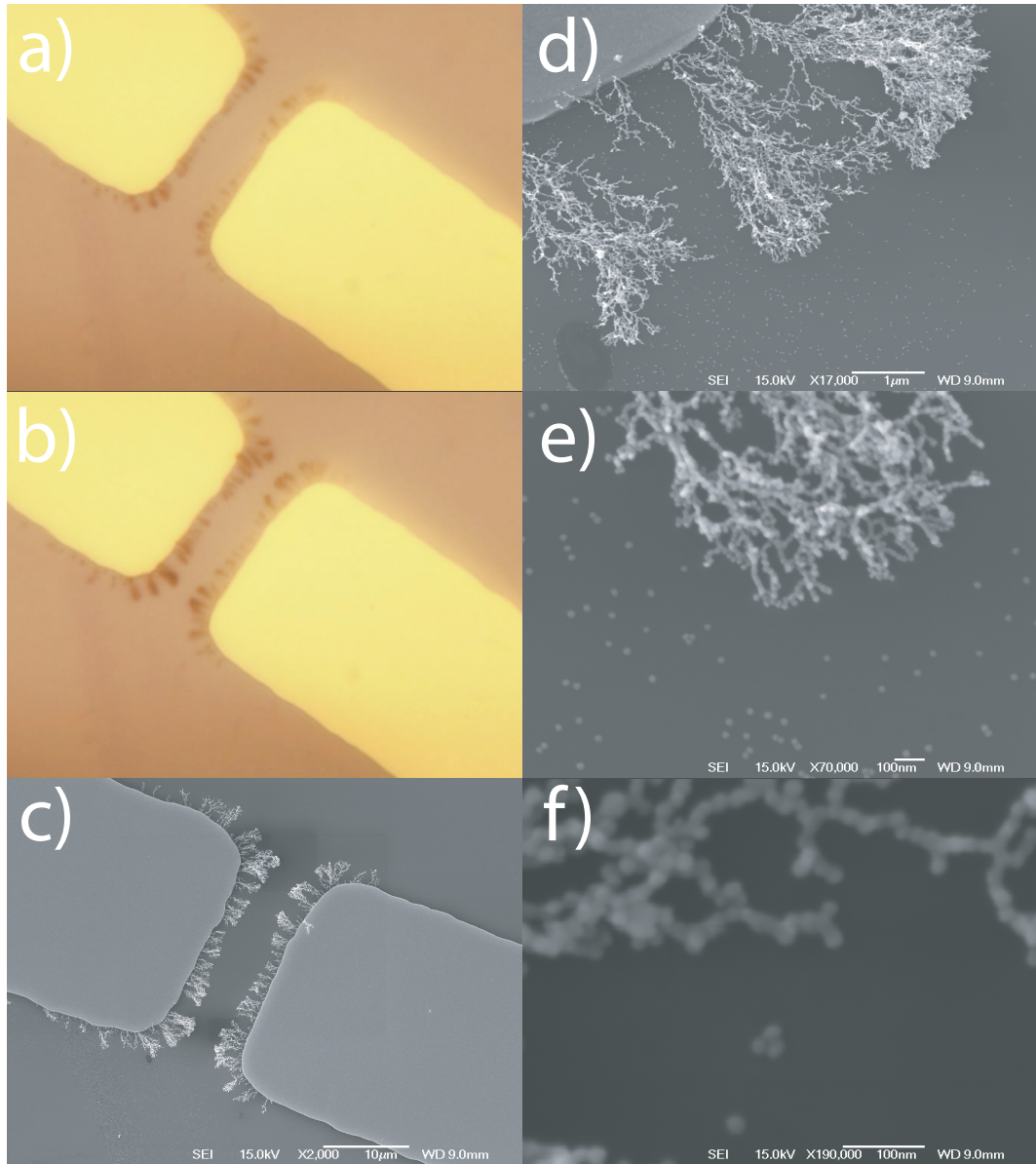


Figure 7.13: Growth of wires at 600 kHz showing the same regions in both optical microscopy ((a), (b)) and SEM and subsequent high resolution imaging showing that wires have sintered before connection (note that small clusters of *unsintered* nanoparticles are observed on the substrate).

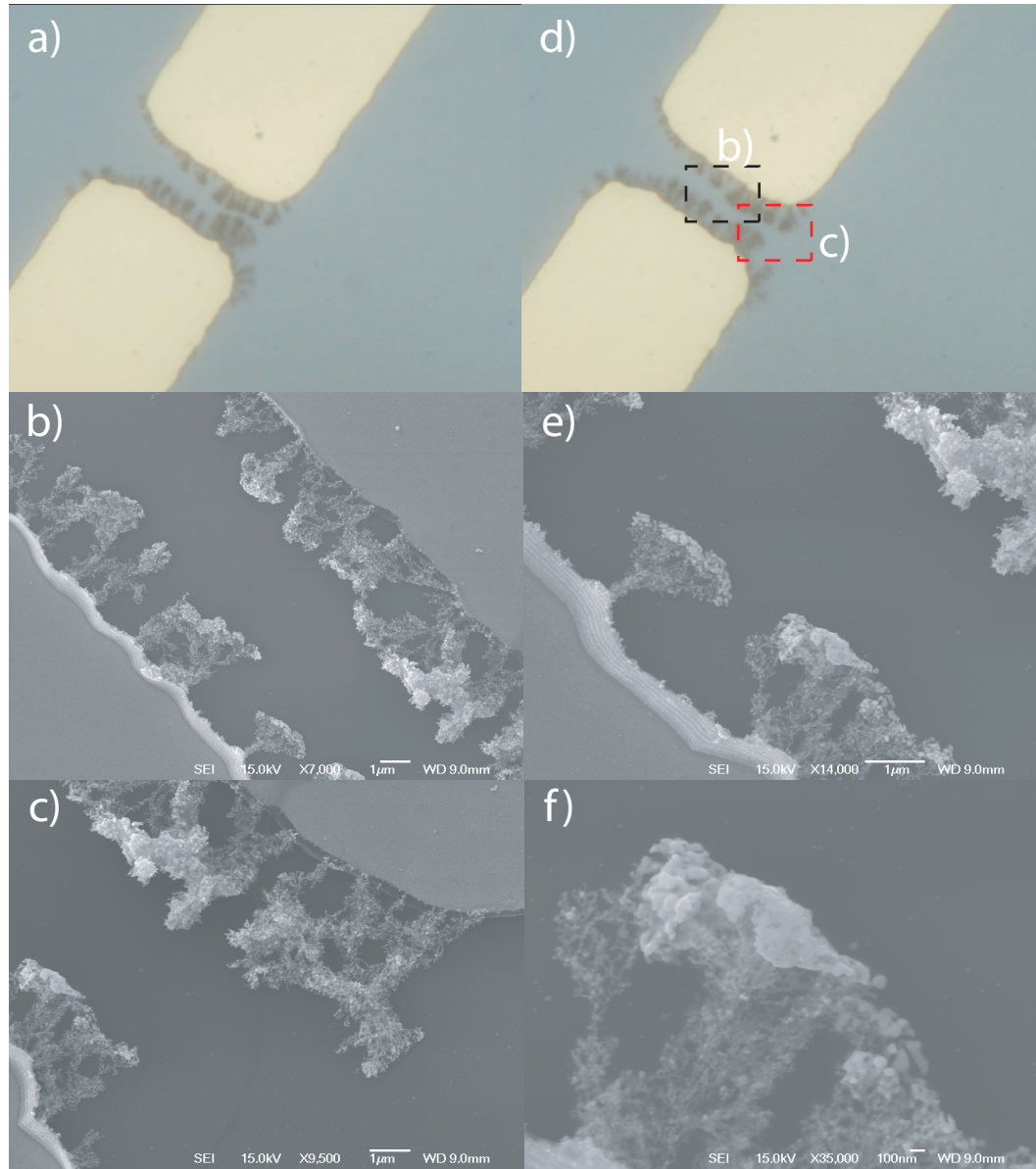


Figure 7.14: a) Optical microscope image capture of Au nanoparticles during growth, (d) after spontaneous retraction began signal was turned off and wires preserved. Highlighted regions correspond to high resolution SEM of wires captured in the middle of “spontaneous” retraction in (b) and (c). (e) and (f) high-resolution SEM scans showing large scale sintering both sides.

an example of a high-resolution image of nanoparticles on the silicon oxide surface. The individual nanoparticles are clearly imaged and no beam induced

sintering is apparent.

Although ACEO now seemed unlikely as the primary cause of the retraction events, it was still necessary to confirm that it was in fact the primary phenomenon underlying the formation of different wire morphologies. To this end, experiments were conducted with latex tracer sphere solution (300 nm charge stabilised in D. I. water) [239] further diluted in a 200:1 ratio in D. I. water to produce a dilute suspension. Experiments were then conducted both with the latex tracer solution, and also by introducing small quantities into nanoparticle solutions. Experiments with the latex tracer solution indicated qualitative changes in the flow dynamics around the electrodes between 100 kHz and 1 MHz, although it should be stressed that the DEP force variation for latex spheres in this range is itself somewhat complicated [95]. In experiments where the tracer spheres were added to the nanoparticle solutions qualitative differences were also noted. Measurements in our system using a small quantity of diluted 300 nm latex tracer spheres solution added to the nanoparticle solution, allow us to make a reasonable estimate as to the changes in fluid flow. We found that at 600 kHz flows in the gap of approximately 100 μm per second were observed at 20 V peak-to-peak applied voltage. For the same electrode setup at 100 kHz with the same applied voltage, flows in excess of 400 μm per second were observed. It should be noted that the time resolution of the videos prevents more accurate estimations of the upper velocity with the setup used. Introducing the latex sphere solution will no doubt alter the properties of the nanoparticle suspension, but these figures should provide a rough estimate of how the fluid velocity varies with frequency.

7.6 Electrochemistry/Electrode damage

Although gold is usually thought of as relatively inert, it has been shown that reactions can take place at gold electrodes in electrochemical cells and, indeed, some nanoparticle synthesis techniques use gold electrodes in order to synthesise nanoparticles, nanocubes or nanorods [116–118]. One of the acknowledged advantages of DEP, however, is that it is insensitive to the use of DC or AC fields and allows operation at frequencies where electrochemical

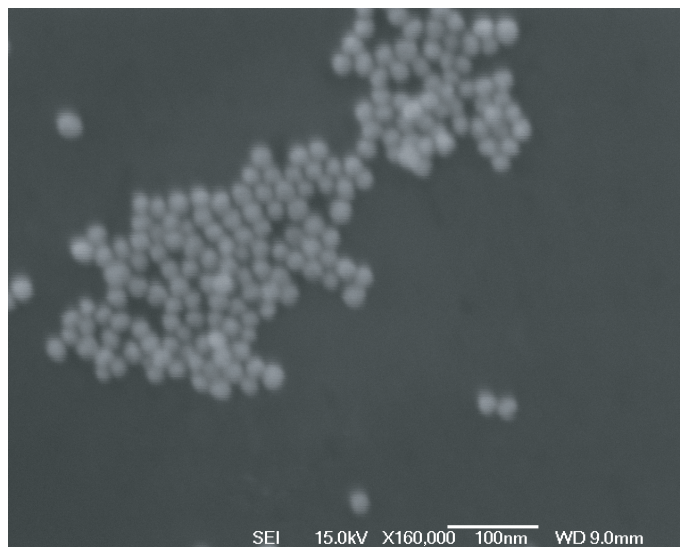


Figure 7.15: High resolution SEM showing closepacked arrays of charge stabilised gold nanoparticles on SiO_2 substrate demonstrating stability under typical SEM imaging conditions.

effects are not thought to be important. Indeed, in general, it does not seem intuitive that electrochemical effects would play a strong role at frequencies that are a good fraction of one megahertz. In these electrochemical schemes it is thought the bulk gold metal is converted from the anode to form gold nanoparticles, most likely at the interfacial region of the cathodic surface and within the electrolytic solution [116,117,240]. Nonetheless, the authors of these papers specifically state that the exact details of the growth mechanism are still not well understood. In the case of a rapidly fluctuating AC potential without the benefit of a control electrode the situation is likely to be more complicated still.

7.6.1 Estimation of permittivity and conductivity

A key parameter in dielectrophoresis, ACEO, and electrochemistry is the conductivity of the solutions being used. Although accurate measurements of permittivity and conductivity of electrolytic solutions can be difficult, an accurate estimate may be made if the molar concentrations and molar conductivity of the constituent components of the solution are known. Calculations of the

conductivity of the nanoparticle solutions based on concentration information supplied by Sigma Aldrich [183] indicated conductivities of between 50 and 60 mS per metre. This corresponds well to literature values for conductivity measurements of similar solutions of between 20 and 60 mS per metre [92] [241]. The permittivity of electrolytic solutions also varies with electrolytic concentration, but over a much smaller range than the conductivity. While extremely pure D. I. water has a permittivity around $80\epsilon_0$, even moderately high concentrations of salts only reduce this to around $60\epsilon_0$ [242]. Therefore, a realistic estimate for the permittivity of the solution is most likely between 70 and $80\epsilon_0$. It should be noted that there are questions as to the validity of treating colloidal suspensions as being separate from the solution itself when the length scale of the colloids reaches the nanometre scale. However, since all of the experiments reported here feature nanoparticles of at least 20 nm diameter we will not discuss these considerations further.

In order to try to isolate the origin of the retraction events, a number of control solutions were made to ascertain whether the presence of the nanoparticles themselves contributed to the phenomenon. These included a degassed deionised water solution, a pH controlled solution of tannic acid and sodium citrate at the same concentration as is estimated for the nanoparticles solution, a pH controlled sodium citrate only solution, and a 0.1M NaCl solution. With the deionised water there did not appear to be any effect on the electrodes at high frequencies, although dielectrophoresis of suspended contaminants was observed. With the tannic acid and sodium citrate control no effect was observed at 100 kHz. Reducing the applied frequency by an order of magnitude to 10 kHz (at 20 V peak-to-peak), however, resulted in stripping of the gold from the electrodes, and, interestingly, apparent wire assembly from the dissolved/stripped gold. Lower frequencies resulted in even more dramatic etching of the electrodes. Similar effects were noted with the sodium citrate only control solution, indicating that the presence of the tannic acid appeared to have little effect. It was also noted that removing the 1 k Ω current limiting resistor seemed to increase the probability of electrode damage events, and indeed had been noted to increase the likelihood of micro-wire growth when

using the nanoparticle solutions. Electrode damage was also noted at slightly higher frequencies (between 50 and 100 kHz) when tests were carried out with the sodium chloride control solutions.

An interesting observation was obtained during experiments using a sodium citrate control solution at lower frequencies (1 kHz) – at these lower frequencies electrode damage occurred readily and over a greater area of electrode than at 100 kHz. Critically, a large scale investigation of the electrode after the experiment revealed a striking colouration far back from the electrode tip on the bulk contact (see Fig. 7.16). This striking range of colours was indicative of a range of nanoparticle sizes, as it is well known that the colour of nanoparticles is determined by their size. Investigation of similar electrodes under high-resolution SEM confirm this hypothesis with areas demonstrating colouration appearing to have a wide variety of “nano-sized” metallic flakes scattered on the surface. It should be noted that there was no possibility of nanoparticle solution contamination on the sample as separate wafers and pipettes were used. Although these images were obtained at much lower frequencies than those used in the growth experiments with the nanoparticle solutions they do demonstrate that nano sized metallic objects may be generated using high-frequency alternating currents in microelectrode systems such as the ones in use here. The size distribution of these objects, though not well characterised, might also explain the “clouding” sometimes observed during spontaneous retraction which would seem to indicate the release into solution of objects capable of scattering of light at visible wavelengths, but too small to be resolved individually. Of course great care must be taken when comparing data from low frequency/high concentration experiments to the relatively high frequency/low concentration conditions in most of the experiments. Nonetheless these results do provide a plausible ‘proof of concept’ when considered in light of the other evidence collected during the nanoparticle solution experiments.

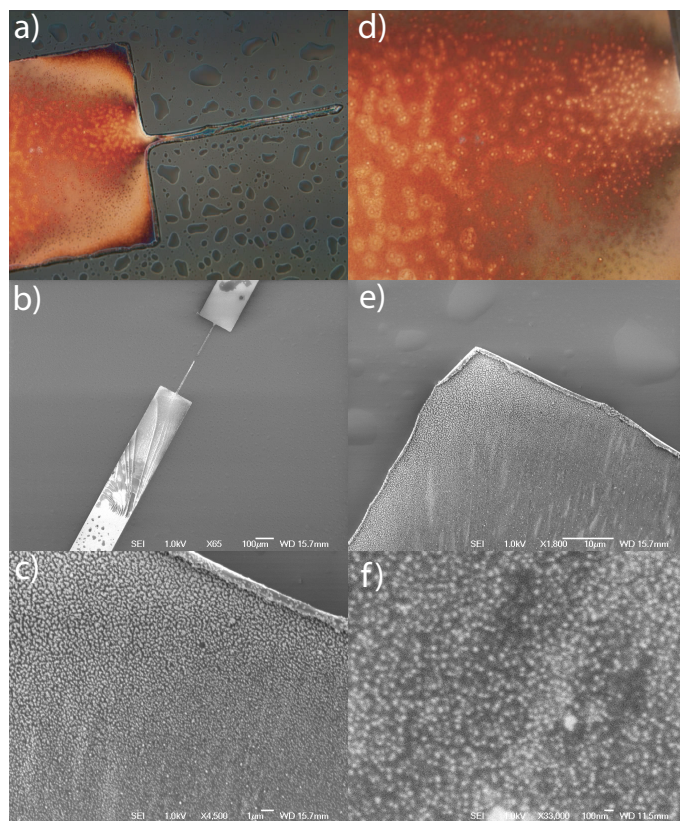


Figure 7.16: a) and b) Optical and c) - f) high-resolution SEM micrographs showing large-scale damage and discoloration to electrodes upon application of 1 kHz signal to a 0.5M sodium citrate solution. The colouration in the optical micrographs is suggestive of nanoscale fragments. This hypothesis is supported by the high-resolution SEM micrographs.

7.6.2 Electrical measurements

A range of experiments were carried out in an attempt to measure the voltage drop and the current flow across the gap. However, it was found overwhelmingly that with standard lab equipment (i.e. an oscilloscope with standard or high impedance probes) that the parasitic capacitance of the leads and, critically, the oscilloscope itself modified the experimental setup so as to make the results unusable. In addition, the sensitivities required to monitor currents on the milliamp scale, with high accuracy at the frequencies required were not possible. Therefore, as detailed in the experimental method section a high impedance, high gain amplifier designed by [243] to allow these

measurements to be performed. A range of experiments were carried out on the electrodes during microwire assembly at various frequencies and voltages, but no detectable change in the current flow was detected – we found that typically between 1 and 2 milliamps flowed across the electrode gap prior to connection, irrespective of the density of microwires, and apparently independent of the applied frequency. The current also seemed to remain constant during controlled dissolution experiments, although we were unable to obtain measurements during “spontaneous” dissolution. We found in agreement with previous work [244] that if the wires were allowed to connect, the current through the circuit would spike and be limited by the series resistor (in the case of the majority of the experiments to around 20 mA, limited by the 1 K Ω series resistor).

This apparent lack of variation may initially appear to be counterintuitive but is consistent with the results obtained by [245] who noted that in microwire assembly experiments (using gold nanorods) the bulk of the current flows through the solution rather than the wires up until the moment of actual ohmic connection. In order to accurately measure the current flowing through the wires in their experiments they were forced to construct a complex two electrode control system, such that the effects of current flow through the fluid were effectively nulled out by monitoring a control electrode, and any variations in the measured current could be ascribed to the growth of the wires at the electrode. This complicated lock in setup would appear to be necessary to determine the current flowing through the wires, but was unfortunately not available with the electrode setup we used. We noted that in previous experiments on nanoparticle microwires assembled by DEP [98], and subsequently recovered from solution, that currents of between one and 2 milliamps were required (DC potential *ex situ*) to cause the wires to melt. However, given the aforementioned likelihood of electrochemical reactions, it may be difficult to separate sintering due to current flow from electrochemical effects also causing sintering at the nanowire/solution interface. Therefore we must be careful in ascribing the sintering observed as being due to Joule heating effects in the wires as, although the currents measured are sufficient, we do not know the ratio of current flowing through the wire to that flowing through the bulk

solution.

7.7 Origin of morphological changes

As noted in [92, 93], morphological changes in assembled microwire structure from nanoparticles via DEP assembly have been ascribed to changes in ACEO flows caused by changes in the behaviour of the double layer around the electrodes and the wires themselves. As yet, however, no quantitative picture relating the morphologies to the flow dynamics has been proposed, and indeed such an undertaking is likely to be a significant body of work in and of itself. With that caveat in place, it is possible to speculate on how higher flows may qualitatively affect the assembled structures. In keeping with the findings of [92, 93] we find that at lower frequencies the assembled structures were much denser, although quantitative differences in the crossover frequencies compared with our data are most likely explained by significant differences in experimental setup and applied potentials. At lower frequencies where the ACEO flow is much higher (as observed in our system, see previous sections) it is plausible that the available flux of nanoparticles incident on the area around wire growth is much higher, and that, in addition, localised flows around the tips of the wires during growth will be turbulent. Quantitatively understanding how these flows disrupt wire formation will undoubtedly be an active area of future research, but it may be that a qualitative understanding can be obtained from such disparate sources as works on seaweed growth [246, 247] where it is observed that growth in turbulent waters can dramatically affect the structure of otherwise identical seaweed varieties. While the exact mechanism is undoubtedly different, intriguing possibilities for cross-disciplinary research present themselves.

7.7.1 Double layer effects: ACEO flow/Electrochemistry

The most plausible explanation for the retardation of growth at low frequencies is that of increasingly high field gradients, and changes in the double layer. First, the effective field strength as the wires approach each other is expected to

increase by at least an order of magnitude simply due to the effective reduction of the distance between the electrodes (in actual fact the increase may be even higher due to aspect ratio effects). This increase in the field gradient may be further augmented by changes in the potential dropped across the double layer. Following the model put forth by Ramos et al [95] it can be shown that the potential dropped across the double layer varies strongly with distance from the centre of the electrode gap. Fig. 7.17 shows the results of calculations performed using typical values for the experimental setup used. Using;

$$\phi_{DL}(x) = \frac{V_0}{2 + i\omega\pi\kappa(\epsilon/\sigma)x} \quad (7.1)$$

where the conductivity of the solution $\sigma \sim 60\text{mS m}^{-1}$, the permittivity $\epsilon \sim 70\epsilon_0$, the Debye length $\kappa^{-1} \sim 3\text{nm}$ and ω and x are the applied frequency and distance from the centre of the gap respectively. It is clear that there are dramatic changes in the fraction of the potential dropped across the double layer as we approach the centre of the gap. Although most likely an oversimplification for the complex system under consideration, it shows that at least in principle we might expect an increase in the ion concentration/voltage drop in the double layer as the wires approach each other, even excluding effects such as electrochemical reactions. Therefore we may expect effects that occur at lower frequencies to start occurring at higher frequencies as the wires approach. It is interesting to note that the region where we expect the double layer to at least partially form (i.e. between 10 kHz and 100 kHz) is the region where we experience damage to the electrodes and unexpected retraction events. Therefore, it seems likely that some combination of increased electrolyte concentration near the electrodes and the higher field gradients associated with the potential being dropped across the double layer, are in some way responsible not only for the dramatic reduction in growth rate, but also at least related to the observed retraction events.

7.7.2 Origin of the controlled retraction

If we conclude that enhanced ion concentration in the double layer and increased field gradient is the most likely trigger for the observed phenomenon

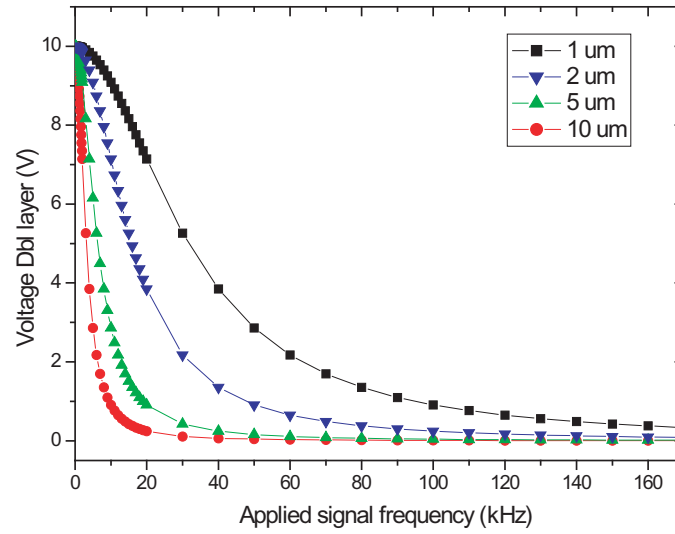


Figure 7.17: Graph showing results of calculations based on the model of Ramos et al. showing how the voltage dropped across the double layer at the electrode (for an applied field of 20 V peak to peak) varies with frequency for a range of electrode gaps.

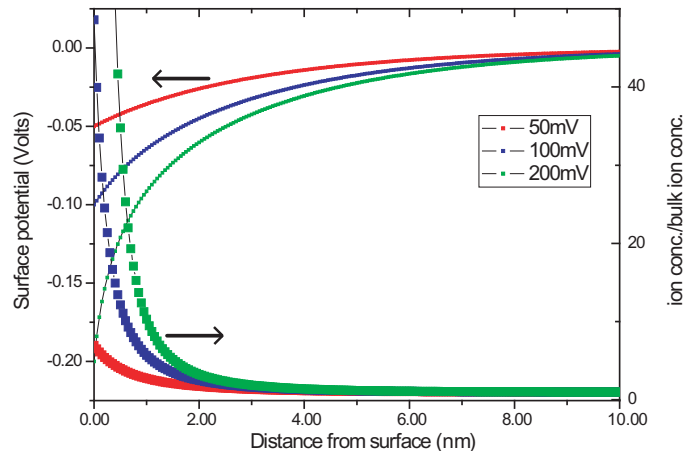


Figure 7.18: Calculations based on the model of Ramos et al. showing how the surface potential and double layer ion concentration (as a fraction of the bulk ion concentration) vary with distance from the surface at a range of DC surface potentials. Note that the ion concentration increases dramatically with applied potential. The expected potential at the electrode in our experiments is expected to be two orders of magnitude higher.

then we can begin to form a hypothesis as to the mechanism behind the retraction events observed. First considering the “controlled” retraction events, which are probably of more interest from an applications point of view, then it is plausible to imagine that when the applied (lower) frequency is reduced, the ion concentration and field gradient near the tips is dramatically increased compared to the conditions during growth. As such, we might hypothesise an increased rate of electrochemical reaction is able to rapidly etch the wire back towards the electrodes. However, this does not then explain why a wire grown at 600 kHz will retract at 100 kHz, and why wires grown at lower frequencies are less likely to. Nor does it explain why a wire grown at 10 V and 100 kHz retracts when a signal of 20 V and 100 kHz is applied. In both cases we see an increase in the field gradient and ion concentration - see Fig. 7.18 – at the tip, but the key issue is how the wires grown at these other frequencies vary from the wires grown “natively” at 20 V, 100 kHz. A plausible argument is that wires grown in these “more demanding” conditions are only able to propagate if they assume certain characteristics, i.e. by growing in a much denser, more branched configuration. It suggests that under some conditions the balance between corrosion by electrochemical effects and assembly by DEP and ACEO is a delicate one and dependent on the pre-existing morphology of the wire.

7.7.3 Origin of the spontaneous retraction

We must also consider the spontaneous retraction events and how they may be related to the controlled events. The key difference here is that even if the field gradient and ion concentration increases as the wires approach each other, this only in itself explains why the growth mode changes, not why the wires continue to retract back past their original positions, and then in some cases to affect the bulk electrode. If we continue to accept that a change in the ion concentration is the most likely candidate, then the obvious conclusion is that the local electrolyte concentration of the solution has changed. In our experimental configurations this is perhaps not surprising as under these conditions an extremely large quantity of material is locally being deposited into the solution. Although optical and SEM data seem to suggest at least some of

this material is being deposited in nanoparticle size quantities, undoubtedly a good proportion of it is being dissolved into the solution as charged species, and so under these conditions of large-scale wire/electrode disintegration we cannot expect the local solution to remain identical to that of the bulk, nor for assumptions as to its local conductivity to remain valid. Therefore if we push the experimental conditions to a point at which electrode dissolution starts, we might expect it to become a self-sustaining/positive feedback reaction as observed. This hypothesis is supported by observations of droplet drying with an applied field that resulted in sudden and severe electrode damage as the droplet thinned to a film (and presumably the salt concentration of the remaining solution becomes extremely high).

7.8 Origin of dynamics/plateau

While the origin of morphological changes might be reasonably explained by changes in the ACEO flow, the unusual dynamics observed require a somewhat more complex analysis. While we might expect the amount of fluid flow to alter the growth rate of a wire (either due to the flow disrupting formation, or, conversely, delivering a greater flux of nanoparticles to a wire apex) it is not clear how the flow could cause the non-linear effects observed in Fig. 7.4. Unfortunately a definitive answer must be the subject of more detailed future investigations – but we can critically consider the likely candidates.

7.8.1 Fractal nature

As noted, the wires grown at lower frequencies tended to be more branched, and of higher density than those grown at high frequencies. Therefore, as a simple approximation, for a wire to extend a unit distance towards the opposing electrode, a proportionally higher number of nanoparticles is required compared to a simple high aspect ratio wire. Determining the degree to which this will retard the growth would depend on accurate measurements of the fractal dimension/wire density for both types of wires under high-resolution SEM. Unfortunately, the three-dimensional nature of the wires precludes a simple

“top-down” fractal analysis, but we do note that previous studies have found that in their experimental set-ups the limiting factor of growth was diffusive delivery of nanoparticles to the tip apices [37]. In our set-up, diffusive flow is likely to be completely overwhelmed by hydrodynamic flow, and, although some retardation is plausible, it seems improbable that this factor alone could prevent wire connection for the long periods of time observed.

7.8.2 Depletion

A phenomenon related to the change in branching might be possible nanoparticle depletion in the small gap between two opposing wire front assemblies. If the nanoparticles could be excluded via some DEP or ACEO phenomenon growth would obviously be retarded. However, as we have seen, the DEP force on the nanoparticles in the frequency range investigated is expected to be uniformly positive, and the ACEO flow should increase the flow of particles from the bulk into the gap and in fact offset any diffusion limited depletion. Other less dominant effects (such as electrothermal hydrodynamics) are similarly unlikely to be important in this respect due to their smaller magnitudes [92, 95]. As such, there seems no plausible mechanism for nanoparticle exclusion in the gap on the basis of the dominant forces in this scenario.

7.8.3 Electrochemical

Given the observation of retraction events of apparently electrochemical origin, and that these events appear to depend not only on the voltage and frequency applied, but also on the voltage and frequency used to initially grow the wires, it is an obvious leap to speculate that related effects could account for the unusual growth dynamics. One hypothesis might be that as thick clusters of wires approach each other the balance between electrochemical ‘etching’ and growth by DEP and ACEO becomes extremely close, and that as fast as nanoparticles can be delivered to the tips, so they are etched away. This direct, and delicate, competition between electrokinetic assembly and electrochemical disassembly would provide an aesthetically pleasing compliment to the controlled and spontaneous retraction events, but we cannot categorically

confirm this on the basis of the data collected so far.

7.8.4 Origin of high frequency cutoff

As noted previously, the size and magnitude of the DEP force is not thought to significantly change in the frequency range investigated (for metallic nanoparticles). Therefore, in addition to the morphological changes described previously, we must also consider the origin of the apparent high frequency cutoff in growth. The answer, as alluded to in [92] most likely lies in the phenomena behind the change in the ACEO force with frequency, i.e. the change in the structure of the electrical double layer. As [92] noted, as the frequency increases, the charges in the solution find it increasingly difficult to respond to the changing field, until above a certain frequency they are unable to effectively respond and the thickness of the double layer falls to zero. Consequently, the proportion of the field dropped across the double layer (as opposed to in the bulk of the solution) varies strongly with frequency. Calculations based on a model proposed by Ramos et al. [104] (Fig. 7.18) indicate that for the solutions used in our experiments the potential dropped across the double layer has fallen by over 50 per cent at around 5 kHz, with an even smaller (but still significant) voltage drop still present around 20 kHz. It should be noted that certain approximations made in the model (i.e. infinitely wide and infinitely long electrodes, with no electrochemical reactions), are not met when applied to our system. It should also be noted that, although on the basis of these calculations we would expect the counter-ions in the solution to be insensitive to the effects of the applied field above 100 kHz, we still note significant fluid flows in frequency range from 100 kHz to 1 MHz, and previous work at lower field strengths [92] noted that the fluid velocity does not drop to zero even at 1 MHz, suggesting that the model is approximate at best. Nonetheless, and qualitatively, we expect the field gradient near the electrodes to be smaller if the field is dropped linearly over the 10 μm gap, rather than sharply over a few tens of nanometres close to each electrode, with a corresponding drop in the dielectrophoretic force. This reduction in the effect of the double layer most likely explains the increasingly higher voltages needed to initiate growth

with higher frequency, and why growth could not be initiated reliably above 1 MHz.

7.9 Conclusions

In this chapter we have successfully investigated the effect of varying frequency and potential on the assembly of microwire structures from a solution of gold nanoparticles. We have confirmed reports in the literature showing that the ACEO flow can produce dramatic changes in the morphology of the assembled wires and also noted effects on the dynamics of growth. We have also, for the first time, observed, and utilised, what appear to be electrochemical effects in order to controllably modify the wires in situ. By utilising in situ optical microscopy and ex situ high resolution SEM we have also been able to demonstrate significant sintering of the structures prior to ohmic connection. An exploration of the parameter space has revealed that a delicate balance between DEP, ACEO and electrochemical/Joule heating appears to determine whether the wire structures are dynamically stable at a given frequency and applied potential, but we note that in our experimental setup there are significant variations between different nominally identically fabricated electrodes.

7.10 Future Work

In this chapter we have investigated a system with a vast parameter space, and a number of competing forces. Consequently it is unlikely that any immediate near-term set of experiments will conclusively answer all questions. Nonetheless, there are obvious avenues for exploration that could greatly enhance our understanding of the system. The most obvious step would be to redesign the electrode arrays used, and use a more conventional parallel, or interdigitated finger design, and combine this with a dedicated flow chamber. This would not only greatly enhance the ease by which the experiments may be carried out (as the setup used had a number of practical failings), but the use of a dedicated flow set up could help eliminate issues related to changes in the concentration of the solution, as well as aid in the successful recovery of the wires for ex situ

investigation. Additionally implementing a “parallel control electrode” would allow for high sensitivity, impedance controlled, electrical measurements to be made during growth and conclusively determine whether current flow through unconnected wires, or electrochemical effects, are responsible for pre-connect sintering observed.

With these improvements in setup design, a more thorough investigation of the parameter space, specifically as regards the susceptibility of wires grown in different conditions to retraction, could be undertaken, along with collaboration with groups specialising in simulation of electro-hydrodynamic systems.

Chapter 8

Conclusions

“Instead of filling with questions, empty of questions. Continue to empty. Questions confine answers. When there are no longer questions, answers are no longer bound by them.”

Lao Tzu

In this chapter we present a short summary of the work carried out in the course of this thesis.

8.1 Conclusions

In the final analysis, it is clear that we have probed a wide range of forces and interactions. In UHV we have investigated the effect of chemical bond formation on an unstable semiconductor surface at low-temperature, and been forced to consider the variations in bonding and tunnel current over oscillation cycles with amplitudes of under a nanometre. Our experiments have shown how unique tip apex configurations can radically change the interaction with the surface even in the highly controlled UHV and low temperature environments used. We have proposed, and are in the process of carrying out a series of experiments that should allow us to answer some of the key questions with regards to the system in the near future.

Our investigation of nanoparticle arrays using similar methods was primarily concerned with the vdW and electrostatic interactions, but has revealed

that even for a well studied system such as gold nanoparticles, there are still unanswered questions as to the exact mechanisms underlying the tip – sample interaction. Again, building on earlier work carried out within the group we have identified a (relatively) simple experimental pathway that should allow us to determine the relevant mechanisms in the near future. Measurements of the contact potential difference between the nanoparticles and the substrate demonstrated clear high-resolution contrast, but analysis has shown that the techniques used must be carefully reconsidered in order to allow for quantitative measurements.

Experiments with nanoparticles in solution have revealed a hitherto unexplored mechanism for dynamic control of nano wires in situ. It is hoped that improvement in the experimental setup, along with collaborations with theoretical groups, may allow us to move beyond our current tentative conclusions into a more fully realised understanding of the system.

Bibliography

- [1] Brian O'Regan and Michael Gratzel. A low-cost, high-efficiency solar cell based on dye-sensitized colloidal TiO₂ films. *Nature*, 353(6346):737–740, October 1991.
- [2] Didier Astruc. *Nanoparticles and Catalysis*. Wiley VCH, October 2007.
- [3] Nanotechnology: What it can do for drug delivery. <http://www.ncbi.nlm.nih.gov/pmc/articles/PMC1949907/>, July 2007.
- [4] Jason Valentine, Jensen Li, Thomas Zentgraf, Guy Bartal, and Xiang Zhang. An optical cloak made of dielectrics. *Nat Mater*, 8(7):568–571, July 2009.
- [5] Lyman J. *Electronics*, 58:36, 1985.
- [6] Tobey A.C. *Electronics*, 52:169, 1979.
- [7] Chris Mack. *Fundamental Principles of Optical Lithography: The Science of Microfabrication*. Wiley, illustrated edition edition, 2008.
- [8] <http://www.intel.com/products/processor/index.htm>.
- [9] Jim Gray. http://research.microsoft.com/gray/moore_law.html.
- [10] <http://www.ipfrontline.com/depts/article.asp?id=19365&deptid=5>.
- [11] http://www.almaden.ibm.com/st/nanoscale_st/nano_fabrication/ebeam/projects/.
- [12] <http://www.news.cornell.edu/releases/july97/guitar.ltb.html>.

- [13] Smalley Drexler. Drexler and smalley make the case for and against 'molecular assemblers'. *C & EN*, 81:37, 2003.
- [14] G. Binnig, H. Rohrer, Ch. Gerber, and E. Weibel. 7 x 7 reconstruction on si(111) resolved in real space. *Physical Review Letters*, 50(2):120, 1983. Copyright (C) 2009 The American Physical Society; Please report any problems to prola@aps.org.
- [15] D. M. Eigler and E. K. Schweizer. Positioning single atoms with a scanning tunnelling microscope. *Nature*, 344(6266):524–526, April 1990.
- [16] M. F. Crommie, C. P. Lutz, and D. M. Eigler. Imaging standing waves in a two-dimensional electron gas. *Nature*, 363(6429):524–527, June 1993.
- [17] Franz J. Giessibl. Atomic resolution of the silicon (111)-(7x7) surface by atomic force microscopy. *Science*, 267(5194):68–71, 1995.
- [18] Franz J. Giessibl, S. Hembacher, H. Bielefeldt, and J. Mannhart. Subatomic features on the silicon (111)-(7x7) surface observed by atomic force microscopy. *Science*, 289(5478):422–425, July 2000.
- [19] A. J. Heinrich, C. P. Lutz, J. A. Gupta, and D. M. Eigler. Molecule cascades. *Science*, 298(5597):1381–1387, November 2002.
- [20] Noriaki Oyabu, scar Custance, Insook Yi, Yasuhiro Sugawara, and Seizo Morita. Mechanical vertical manipulation of selected single atoms by soft nanoindentation using near contact atomic force microscopy. *Physical Review Letters*, 90(17):176102, May 2003. Copyright (C) 2009 The American Physical Society; Please report any problems to prola@aps.org.
- [21] Yoshiaki Sugimoto, Masayuki Abe, Shinji Hirayama, Noriaki Oyabu, Oscar Custance, and Seizo Morita. Atom inlays performed at room temperature using atomic force microscopy. *Nat Mater*, 4(2):156–159, February 2005.
- [22] Yoshiaki Sugimoto, Pablo Pou, Oscar Custance, Pavel Jelinek, Masayuki Abe, Ruben Perez, and Seizo Morita. Complex patterning by vertical

- interchange atom manipulation using atomic force microscopy. *Science*, 322(5900):413–417, October 2008.
- [23] Yoshiaki Sugimoto, Pablo Pou, Masayuki Abe, Pavel Jelinek, Ruben Perez, Seizo Morita, and Oscar Custance. Chemical identification of individual surface atoms by atomic force microscopy. *Nature*, 446(7131):64–67, March 2007.
 - [24] Markus Ternes, Christopher P. Lutz, Cyrus F. Hirjibehedin, Franz J. Giessibl, and Andreas J. Heinrich. The force needed to move an atom on a surface. *Science*, 319(5866):1066–1069, February 2008.
 - [25] Leo Gross, Fabian Mohn, Nikolaj Moll, Peter Liljeroth, and Gerhard Meyer. The chemical structure of a molecule resolved by atomic force microscopy. *Science*, 325(5944):1110–1114, August 2009.
 - [26] K. Eric Drexler. *Nanosystems: Molecular Machinery, Manufacturing and Computation*. John Wiley & Sons, November 1992.
 - [27] Eric Drexler. *Engines of Creation: The Coming Era of Nanotechnology*. Anchor, October 1987.
 - [28] Michael Crichton. *Prey*. HarperCollins, 1st edition, November 2002.
 - [29] J. Pethica. Invited lecture spm 2009, npl, uk. 2009.
 - [30] M. Nonnenmacher, M. P. O’Boyle, and H. K. Wickramasinghe. Kelvin probe force microscopy. *Applied Physics Letters*, 58(25):2921–2923, June 1991.
 - [31] E. Gnecco, R. Bennewitz, T. Gyalog, Ch. Loppacher, M. Bammerlin, E. Meyer, and H.-J. Gntherodt. Velocity dependence of atomic friction. *Physical Review Letters*, 84(6):1172, February 2000. Copyright (C) 2009 The American Physical Society; Please report any problems to prola@aps.org.
 - [32] Y. Martin and H. K. Wickramasinghe. Magnetic imaging by “force microscopy” with 1000 [Å-ring] resolution. *Applied Physics Letters*, 50(20):1455–1457, May 1987.

- [33] Christopher P. Martin, Matthew O. Blunt, Emmanuelle Pauliac-Vaujour, Andrew Stannard, Philip Moriarty, Ioan Vancea, and Uwe Thiele. Controlling pattern formation in nanoparticle assemblies via directed solvent dewetting. *Physical Review Letters*, 99(11):116103–4, 2007.
- [34] <http://www.howtoons.com/>.
- [35] James A. Theobald, Neil S. Oxtoby, Michael A. Phillips, Neil R. Champness, and Peter H. Beton. Controlling molecular deposition and layer structure with supramolecular surface assemblies. *Nature*, 424(6952):1029–1031, 2003.
- [36] Matthew O. Blunt, James C. Russell, Maria del Carmen Gimenez-Lopez, Juan P. Garrahan, Xiang Lin, Martin Schroder, Neil R. Champness, and Peter H. Beton. Random tiling and topological defects in a Two-Dimensional molecular network. *Science*, 322(5904):1077–1081, November 2008.
- [37] Kevin D. Hermanson, Simon O. Lumsdon, Jacob P. Williams, Eric W. Kaler, and Orlin D. Velev. Dielectrophoretic assembly of electrically functional microwires from nanoparticle suspensions. *Science*, 294(5544):1082–1086, November 2001.
- [38] Guanglu Ge and Louis Brus. Evidence for spinodal phase separation in Two-Dimensional nanocrystal Self-Assembly. *The Journal of Physical Chemistry B*, 104(41):9573–9575, October 2000.
- [39] C. J. Kiely, J. Fink, M. Brust, D. Bethell, and D. J. Schiffrin. Spontaneous ordering of bimodal ensembles of nanoscopic gold clusters. *Nature*, 396(6710):444–446, December 1998.
- [40] G. Binnig, H. Rohrer, Ch. Gerber, and E. Weibel. Surface studies by scanning tunneling microscopy. *Physical Review Letters*, 49(1):57, July 1982. Copyright (C) 2009 The American Physical Society; Please report any problems to prola@aps.org.

- [41] G. Binnig, H. Rohrer, Ch. Gerber, and E. Weibel. Tunneling through a controllable vacuum gap. *Applied Physics Letters*, 40(2):178–180, 1982.
- [42] Erwin W. Mller. Das feldionenmikroskop. *Zeitschrift fr Physik A Hadrons and Nuclei*, 131(1):136–142, March 1951.
- [43] G. Binnig, C. F. Quate, and Ch. Gerber. Atomic force microscope. *Physical Review Letters*, 56(9):930, March 1986. Copyright (C) 2009 The American Physical Society; Please report any problems to prola@aps.org.
- [44] Roland Wiesendanger. *Scanning probe microscopy and spectroscopy*. Cambridge University Press, November 1994.
- [45] C. Julian Chen. *Introduction to Scanning Tunneling Microscopy*. OUP Oxford, 2 edition, September 2007.
- [46] Joseph A. Stroscio and William J. Kaiser. *Scanning Tunneling Microscopy*. Academic Press Inc, new edition edition, October 1994.
- [47] J. Tersoff and D. R. Hamann. Theory of the scanning tunneling microscope. *Physical Review B*, 31(2):805, 1985. Copyright (C) 2009 The American Physical Society; Please report any problems to prola@aps.org.
- [48] J. Bardeen. Tunnelling from a many-particle point of view. *Phys. Rev. Lett.*, 6(2):57–59, Jan 1961.
- [49] Stefan Hembacher, Franz J. Giessibl, Jochen Mannhart, and Calvin F. Quate. Revealing the hidden atom in graphite by low-temperature atomic force microscopy. *Proceedings of the National Academy of Sciences of the United States of America*, 100(22):12539–12542, October 2003.
- [50] R. M. Feenstra, Joseph A. Stroscio, J. Tersoff, and A. P. Fein. Atom-selective imaging of the GaAs(110) surface. *Physical Review Letters*, 58(12):1192, March 1987. Copyright (C) 2009 The American Physical Society; Please report any problems to prola@aps.org.

- [51] M. Herz, F. J. Giessibl, and J. Mannhart. Probing the shape of atoms in real space. *Physical Review B*, 68(4):045301, July 2003. Copyright (C) 2009 The American Physical Society; Please report any problems to prola@aps.org.
- [52] M. Herz, Ch. Schiller, F. J. Giessibl, and J. Mannhart. Simultaneous current-, force-, and work-function measurement with atomic resolution. *Applied Physics Letters*, 86(15):153101–3, April 2005.
- [53] Gerhard Meyer and Nabil M. Amer. Simultaneous measurement of lateral and normal forces with an optical-beam-deflection atomic force microscope. *Applied Physics Letters*, 57(20):2089–2091, November 1990.
- [54] M. Fritz, M. Radmacher, N. Petersen, and H. E. Gaub. Visualization and identification of intracellular structures by force modulation microscopy and drug induced degradation. In *The 1993 international conference on scanning tunneling microscopy*, volume 12, pages 1526–1529, Beijing, China, May 1994. AVS.
- [55] Amar S. Basu, Shamus McNamara, and Yogesh B. Gianchandani. Scanning thermal lithography: Maskless, submicron thermochemical patterning of photoresist by ultracompliant probes. In *The 48th International Conference on Electron, Ion, and Photon Beam Technology and Nanofabrication*, volume 22, pages 3217–3220, San Diego, California (USA), November 2004. AVS.
- [56] J. M. R. Weaver and David W. Abraham. High resolution atomic force microscopy potentiometry. *Journal of Vacuum Science & Technology B: Microelectronics and Nanometer Structures*, 9(3):1559–1561, May 1991.
- [57] Franz J. Giessibl. Advances in atomic force microscopy. *Reviews of Modern Physics*, 75(3):949, July 2003. Copyright (C) 2009 The American Physical Society; Please report any problems to prola@aps.org.
- [58] F. J. Giessibl and B. M. Trafton. Piezoresistive cantilevers utilized for scanning tunneling and scanning force microscope in ultrahigh vacuum. *Review of Scientific Instruments*, 65(6):1923–1929, June 1994.

- [59] N. Suehira, Y. Tomiyoshi, Y. Sugawara, and S. Morita. Low-temperature noncontact atomic-force microscope with quick sample and cantilever exchange mechanism. *Review of Scientific Instruments*, 72(7):2971–2976, July 2001.
- [60] Satoru Fujisawa, Masahiro Ohta, Takefumi Konishi, Yasuhiro Sugawara, and Seizo Morita. Difference between the forces measured by an optical lever deflection and by an optical interferometer in an atomic force microscope. *Review of Scientific Instruments*, 65(3):644–647, March 1994.
- [61] A. Oral, R. A. Grimsdale, H. O. Ozer, and J. B. Pethica. High-sensitivity noncontact atomic force microscope/scanning tunneling microscope (nc AFM/STM) operating at subangstrom oscillation amplitudes for atomic resolution imaging and force spectroscopy. *Review of Scientific Instruments*, 74(8):3656–3663, 2003.
- [62] O. Wolter, Th. Bayer, and J. Greschner. Micromachined silicon sensors for scanning force microscopy. In *Proceedings of the Fifth International Conference on Scanning Tunneling Microscopy/Spectroscopy*, volume 9, pages 1353–1357, Baltimore, Massachusetts (USA), March 1991. AVS.
- [63] AFM tips - schematics and specifications. http://www.nanoscience.com/products/AFM_tips.html.
- [64] MikroMasch - main -. <http://www.spmtips.com/>.
- [65] Franz J. Giessibl. Atomic resolution on si(111)-(7 x 7) by noncontact atomic force microscopy with a force sensor based on a quartz tuning fork. *Applied Physics Letters*, 76(11):1470–1472, March 2000.
- [66] S. Morita, R. Wiesendanger, and E. Meyer. *Noncontact Atomic Force Microscopy*. Springer, 1 edition, September 2002.
- [67] Seizo Morita, Franz J. Giessibl, and Roland Wiesendanger. *Noncontact Atomic Force Microscopy: Volume 2*. Springer, 1 edition, September 2009.

- [68] F. Ohnesorge and G. Binnig. True atomic resolution by atomic force microscopy through repulsive and attractive forces. *Science*, 260(5113):1451–1456, June 1993.
- [69] L. Howald, R. Lthi, E. Meyer, P. Gthner, and H. -J. Gntherodt. Scanning force microscopy on the si(111)77 surface reconstruction. *Zeitschrift fr Physik B Condensed Matter*, 93(3):267–268, 1994.
- [70] M. Guggisberg, M. Bammerlin, Ch. Loppacher, O. Pfeiffer, A. Abdurixit, V. Barwich, R. Bennewitz, A. Baratoff, E. Meyer, and H.-J. Gntherodt. Separation of interactions by noncontact force microscopy. *Physical Review B*, 61(16):11151, April 2000. Copyright (C) 2009 The American Physical Society; Please report any problems to prola@aps.org.
- [71] Kenji Okamoto, Kentaro Yoshimoto, Yasuhiro Sugawara, and Seizo Morita. KPFM imaging of si(1 1 1)-Sb surface for atom distinction using NC-AFM. *Applied Surface Science*, 210(1-2):128–133, March 2003.
- [72] Shin’ichi Kitamura, Katsuyuki Suzuki, Masashi Iwatsuki, and C. B. Mooney. Atomic-scale variations in contact potential difference on Au/Si(111) 77 surface in ultrahigh vacuum. *Applied Surface Science*, 157(4):222–227, April 2000.
- [73] Q. Zhong, D. Inniss, K. Kjoller, and V.B. Elings. Fractured polymer/silica fiber surface studied by tapping mode atomic force microscopy. *Surface Science*, 290(1-2):L688–L692, June 1993.
- [74] F.J. Giessibl, S. Hembacher, H. Bielefeldt, and J. Mannhart. Imaging silicon by atomic force microscopy with crystallographically oriented tips. *Applied Physics A: Materials Science & Processing*, 72(7):S15–S17, March 2001.
- [75] T. R. Albrecht, P. Grutter, D. Horne, and D. Rugar. Frequency modulation detection using high-Q cantilevers for enhanced force microscope sensitivity. *Journal of Applied Physics*, 69(2):668–673, 1991.

- [76] Franz J. Giessibl. Forces and frequency shifts in atomic-resolution dynamic-force microscopy. *Physical Review B*, 56(24):16010, December 1997. Copyright (C) 2009 The American Physical Society; Please report any problems to prola@aps.org.
- [77] M. Heyde, M. Sterrer, H.-P. Rust, and H.-J. Freund. Frequency modulated atomic force microscopy on MgO(001) thin films: interpretation of atomic image resolution and distance dependence of tip-sample interaction. *Nanotechnology*, 17(7):S101–S106, 2006.
- [78] S. Alireza Ghasemi, Stefan Goedecker, Alexis Baratoff, Thomas Lenosky, Ernst Meyer, and Hans J. Hug. Ubiquitous mechanisms of energy dissipation in noncontact atomic force microscopy. *Physical Review Letters*, 100(23):236106–4, June 2008.
- [79] M. A. Lantz, H. J. Hug, R. Hoffmann, P. J. A. van Schendel, P. Kappenberger, S. Martin, A. Baratoff, and H.-J. Guntherodt. Quantitative measurement of Short-Range chemical bonding forces. *Science*, 291(5513):2580–2583, March 2001.
- [80] John E. Sader and Suzanne P. Jarvis. Accurate formulas for interaction force and energy in frequency modulation force spectroscopy. *Applied Physics Letters*, 84(10):1801–1803, March 2004.
- [81] F. J. Giessibl. A direct method to calculate tip-sample forces from frequency shifts in frequency-modulation atomic force microscopy. *Applied Physics Letters*, 78(1):123–125, 2001.
- [82] Dr. Mathew Suddards. School of Physics, University of Nottingham.
- [83] Dr. rer. nat. Franz J. Giessibl. *PROGRESS IN ATOMIC FORCE MICROSCOPY Habilitationsschrift*. PhD thesis, November 2000.
- [84] http://www.physik.uni-regensburg.de/forschung/giessibl/neu/research/qplus-sensor_e.phtml.

- [85] Sascha Sadewasser and Martha Ch. Lux-Steiner. Correct height measurement in noncontact atomic force microscopy. *Physical Review Letters*, 91(26):266101, December 2003. Copyright (C) 2009 The American Physical Society; Please report any problems to prola@aps.org.
- [86] C. Schnenberger and S. F. Alvarado. Observation of single charge carriers by force microscopy. *Physical Review Letters*, 65(25):3162, December 1990. Copyright (C) 2009 The American Physical Society; Please report any problems to prola@aps.org.
- [87] A. Gil, J. Colchero, J. Gomez-Herrero, and A. M. Baro. Electrostatic force gradient signal: resolution enhancement in electrostatic force microscopy and improved kelvin probe microscopy. *Nanotechnology*, 14(2):332–340, 2003.
- [88] H. Pohl. *Dielectrophoresis*. Cambridge University Press, 1978.
- [89] Herbert A. Pohl. The motion and precipitation of suspensoids in divergent electric fields. *Journal of Applied Physics*, 22(7):869–871, July 1951.
- [90] Orlin D. Velev, Sumit Gangwal, and Dimitar N. Petsev. Particle-localized AC and DC manipulation and electrokinetics. *Annual Reports Section "C" (Physical Chemistry)*, 105:213–246, 2009.
- [91] At the time of writing approximately 150 unique citations.
- [92] Brian C Gierhart, David G Howitt, Shiahn J Chen, Rosemary L Smith, and Scott D Collins. Frequency dependence of gold nanoparticle superassembly by dielectrophoresis. *Langmuir: The ACS Journal of Surfaces and Colloids*, 23(24):12450–12456, November 2007. PMID: 17963407.
- [93] Pradipkumar Bahukudumbi, W. Neil Everett, Ali Beskok, Michael A. Bevan, Gregory H. Huff, Dimitris Lagoudas, and Zoubeida Ounaies. Colloidal microstructures, transport, and impedance properties within

- interfacial microelectrodes. *Applied Physics Letters*, 90(22):224102–3, May 2007.
- [94] Thomas B. Jones. *Electromechanics of Particles*. Cambridge University Press, October 1995.
- [95] Morgan. *AC Electrokinetics: Colloids and Nanoparticles (and references therein)*. Research Studies Press, July 2001.
- [96] Joseph Priestley. *The history and present state of electricity*. Printed for C. Bathurst, and T. Lowndes ... J. Rivington, and J. Johnson ... S. Crowder, G. Robinson, and R. Baldwin ... T. Becket, and T. Cadell, 1775.
- [97] S.H Hong. *Jour. of Korean Physical Society*, 45:665, 2004.
- [98] Robert Kretschmer and Wolfgang Fritzsche. Pearl chain formation of nanoparticles in microelectrode gaps by dielectrophoresis. *Langmuir*, 20(26):11797–11801, December 2004.
- [99] S. J. Papadakis, Z. Gu, and D. H. Gracias. Dielectrophoretic assembly of reversible and irreversible metal nanowire networks and vertically aligned arrays. *Applied Physics Letters*, 88(23):233118–3, June 2006.
- [100] A. S. Bahaj and A. G. Bailey. Dielectrophoresis of microscopic particles. *Journal of Physics D: Applied Physics*, 12(10):L109–L112, 1979.
- [101] H. A. Pohl and J. P. Schwar. Factors affecting separations of suspensions in nonuniform electric fields. *Journal of Applied Physics*, 30(1):69–73, 1959.
- [102] A. Chiabrera. *Interactions Between Electromagnetic Fields and Cells*. Springer, 1 edition, December 1985.
- [103] L. Benguigui and I. J. Lin. More about the dielectrophoretic force. *Journal of Applied Physics*, 53(2):1141–1143, February 1982.

- [104] Antonio Ramos, Hywel Morgan, Nicolas G. Green, and Antonio Castellanos. AC Electric-Field-Induced fluid flow in microelectrodes. *Journal of Colloid and Interface Science*, 217(2):420–422, September 1999.
- [105] A. Gonzlez, A. Ramos, N. G. Green, A. Castellanos, and H. Morgan. Fluid flow induced by nonuniform ac electric fields in electrolytes on microelectrodes. II. a linear double-layer analysis. *Physical Review E*, 61(4):4019, April 2000. Copyright (C) 2009 The American Physical Society; Please report any problems to prola@aps.org.
- [106] N. G. Green, A. Ramos, A. Gonzlez, H. Morgan, and A. Castellanos. Fluid flow induced by nonuniform ac electric fields in electrolytes on microelectrodes. i. experimental measurements. *Physical Review E*, 61(4):4011, April 2000. Copyright (C) 2009 The American Physical Society; Please report any problems to prola@aps.org.
- [107] N. G. Green, A. Ramos, A. Gonzlez, H. Morgan, and A. Castellanos. Fluid flow induced by nonuniform ac electric fields in electrolytes on microelectrodes. III. observation of streamlines and numerical simulation. *Physical Review E*, 66(2):026305, 2002. Copyright (C) 2009 The American Physical Society; Please report any problems to prola@aps.org.
- [108] Jacob N. Israelachvili. *Intermolecular and Surface Forces*. Academic Press Inc, 3rd edition edition, February 2007.
- [109] P. Attard. *Electrolytes and the electric double layer*, volume 92. 1996.
- [110] Robert J. Hunter. *Foundations of Colloid Science*. Oxford University Press, USA, 2 edition, February 2001.
- [111] J. Lyklema. *Fundamentals of interface and colloid science*. Academic Press, May 2005.
- [112] Martin Z. Bazant, Mustafa Sabri Kilic, Brian D. Storey, and Armand Ajdari. Towards an understanding of induced-charge electrokinetics at large applied voltages in concentrated solutions. *Advances in Colloid*

- and Interface Science (and references therein)*, 152(1-2):48–88, November 2009.
- [113] S Gawad, L Schild, and P H Renaud. Micromachined impedance spectroscopy flow cytometer for cell analysis and particle sizing. *Lab on a Chip*, 1(1):76–82, September 2001. PMID: 15100895.
- [114] Masato Suzuki, Tomoyuki Yasukawa, Yoshiaki Mase, Daisuke Oyamatsu, Hitoshi Shiku, and Tomokazu Matsue. Dielectrophoretic micropatterning with microparticle monolayers covalently linked to glass surfaces. *Langmuir*, 20(25):11005–11011, December 2004.
- [115] Seungkyung Park and Ali Beskok. Alternating current electrokinetic motion of colloidal particles on interdigitated microelectrodes. *Analytical Chemistry*, 80(8):2832–2841, April 2008.
- [116] Manfred T. Reetz and Wolfgang Helbig. Size-Selective synthesis of nanostructured transition metal clusters. *Journal of the American Chemical Society*, 116(16):7401–7402, 1994.
- [117] Yu, Ser-Sing Chang, Chien-Liang Lee, and C. R. Chris Wang. Gold nanorods: Electrochemical synthesis and optical properties. *The Journal of Physical Chemistry B*, 101(34):6661–6664, 1997.
- [118] Chien-Jung Huang, Yeong-Her Wang, Pin-Hsiang Chiu, Ming-Chang Shih, and Teen-Hang Meen. Electrochemical synthesis of gold nanocubes. *Materials Letters*, 60(15):1896–1900, July 2006.
- [119] Emmanuelle Pauliac-Vaujour. *Patterns and Instabilities in Colloidal Nanoparticle Assemblies*. PhD thesis, University of Nottingham, 2009.
- [120] UK University of Edinburgh.
- [121] R. E. Schlier and H. E. Farnsworth. Structure and adsorption characteristics of clean surfaces of germanium and silicon. *The Journal of Chemical Physics*, 30(4):917–926, April 1959.

- [122] R. J. Hamers, R. M. Tromp, and J. E. Demuth. Scanning tunneling microscopy of si(001). *Physical Review B*, 34(8):5343, October 1986. Copyright (C) 2009 The American Physical Society; Please report any problems to prola@aps.org.
- [123] D. J. Chadi. Atomic and electronic structures of reconstructed si(100) surfaces. *Physical Review Letters*, 43(1):43, July 1979. Copyright (C) 2009 The American Physical Society; Please report any problems to prola@aps.org.
- [124] Masakazu Kubota and Yoshitada Murata. Streak patterns in low-energy electron diffraction on si(001). *Physical Review B*, 49(7):4810, February 1994. Copyright (C) 2009 The American Physical Society; Please report any problems to prola@aps.org.
- [125] Y. Kondo, T. Amakusa, M. Iwatsuki, and H. Tokumoto. Phase transition of the si(001) surface below 100 k. *Surface Science*, 453(1-3):L318–L322, May 2000.
- [126] Takashi Yokoyama and Kunio Takayanagi. Anomalous flipping motions of buckled dimers on the si(001) surface at 5 k. *Physical Review B*, 61(8):R5078, February 2000. Copyright (C) 2009 The American Physical Society; Please report any problems to prola@aps.org.
- [127] T. Mitsui and K. Takayanagi. Extrinsic structure changes by STM at 65 k on si(001). *Physical Review B*, 62(24):R16251, December 2000. Copyright (C) 2009 The American Physical Society; Please report any problems to prola@aps.org.
- [128] Robert A. Wolkow. Direct observation of an increase in buckled dimers on si(001) at low temperature. *Physical Review Letters*, 68(17):2636, April 1992. Copyright (C) 2009 The American Physical Society; Please report any problems to prola@aps.org.
- [129] M. Matsumoto, K. Fukutani, and T. Okano. Low-Energy electron diffraction study of the phase transition of si(001) surface below 40 k. *Physical*

- Review Letters*, 90(10):106103, March 2003. Copyright (C) 2009 The American Physical Society; Please report any problems to prola@aps.org.
- [130] Masanori Ono, A. Kamoshida, N. Matsuura, E. Ishikawa, T. Eguchi, and Y. Hasegawa. Dimer buckling of the si(001)2 x 1 surface below 10 k observed by low-temperature scanning tunneling microscopy. *Physical Review B*, 67(20):201306, May 2003. Copyright (C) 2009 The American Physical Society; Please report any problems to prola@aps.org.
- [131] Yan Jun Li, Hikaru Nomura, Naoyuki Ozaki, Yoshitaka Naitoh, Masami Kageshima, Yasuhiro Sugawara, Chris Hobbs, and Lev Kantorovich. Origin of p(2 x 1) phase on si(001) by noncontact atomic force microscopy at 5 k. *Physical Review Letters*, 96(10):106104–4, March 2006.
- [132] Y. Kondo, T. Amakusa, M. Iwatsuki, and H. Tokumoto. Phase transition of the si(001) surface below 100 k. *Surface Science*, 453(1-3):L318–L322, May 2000.
- [133] Lev Kantorovich and Chris Hobbs. Probing the si(001) surface with a si tip: An ab initio study. *Physical Review B (Condensed Matter and Materials Physics)*, 73(24):245420–12, June 2006.
- [134] K. Hata, Y. Sainoo, and H. Shigekawa. Atomically resolved local variation of the barrier height of the Flip-Flop motion of single buckled dimers of si(100). *Physical Review Letters*, 86(14):3084, April 2001. Copyright (C) 2009 The American Physical Society; Please report any problems to prola@aps.org.
- [135] M. T. Yin and Marvin L. Cohen. Theoretical determination of surface atomic geometry: Si(001)-(2 x 1). *Physical Review B*, 24(4):2303, 1981. Copyright (C) 2009 The American Physical Society; Please report any problems to prola@aps.org.
- [136] John E. Northrup. Electronic structure of si(100)c(4 x 2) calculated within the GW approximation. *Physical Review B*, 47(15):10032, April 1993. Copyright (C) 2009 The American Physical Society; Please report any problems to prola@aps.org.

- [137] Kenji Hata, Satoshi Yasuda, and Hidemi Shigekawa. Reinterpretation of the scanning tunneling microscopy images of si(100)-(2 x 1) dimers. *Physical Review B*, 60(11):8164, 1999. Copyright (C) 2009 The American Physical Society; Please report any problems to prola@aps.org.
- [138] Keisuke Sagisaka and Daisuke Fujita. Emergence of p (2 x 2) on highly doped n -type si(100) surfaces: A scanning tunneling microscopy and spectroscopy study. *Physical Review B*, 71(24):245319, June 2005. Copyright (C) 2009 The American Physical Society; Please report any problems to prola@aps.org.
- [139] Kawai H and Narikiyo O. Vibration of the dimer on si(001) surface excited by STM current. *J Phys Soc Jpn*, 73(2):417–422, 2004.
- [140] Shoji Yoshida, Tomohiko Kimura, Osamu Takeuchi, Kenji Hata, Haruhiro Oigawa, Toshihiko Nagamura, Hiroshi Sakama, and Hidemi Shigekawa. Probe effect in scanning tunneling microscopy on si (001) low-temperature phases. *Physical Review B*, 70(23):235411, December 2004. Copyright (C) 2009 The American Physical Society; Please report any problems to prola@aps.org.
- [141] Keisuke Sagisaka, Daisuke Fujita, and Giyuu Kido. Phase manipulation between c(4 x 2) and p(2 x 2) on the si(100) surface at 4.2 k. *Physical Review Letters*, 91(14):146103, October 2003. Copyright (C) 2009 The American Physical Society; Please report any problems to prola@aps.org.
- [142] Seizo Morita and Yasuhiro Sugawara. Atomically resolved imaging of si(100)2 x 1, 2 x 1:h and 1 x 1:2h surfaces with noncontact atomic force microscopy. *Japanese Journal of Applied Physics*, 41(Part 1, No. 7B):4857–4862, 2002.
- [143] T. Uozumi, Y. Tomiyoshi, N. Suehira, Y. Sugawara, and S. Morita. Observation of si(1 0 0) surface with noncontact atomic force microscope at 5 k. *Applied Surface Science*, 188(3-4):279–284, March 2002.
- [144] Daisuke Sawada, Takashi Namikawa, Masuhiro Hiragaki, Yoshiaki Sugimoto, Masayuki Abe, and Seizo Morita. High-spatial-resolution topo-

- graphic imaging and dimer distance analysis of si(100)-(2×1) using non-contact atomic force microscopy. *Japanese Journal of Applied Physics*, 47(7):6085–6087, 2008.
- [145] R. J. Hamers and U. K. Köhler. Determination of the local electronic structure of atomic-sized defects on si(001) by tunneling spectroscopy. *Journal of Vacuum Science & Technology A: Vacuum, Surfaces, and Films*, 7(4):2854–2859, 1989.
- [146] R. M. Tromp, R. J. Hamers, and J. E. Demuth. Si(001) dimer structure observed with scanning tunneling microscopy. *Physical Review Letters*, 55(12):1303, 1985. Copyright (C) 2009 The American Physical Society; Please report any problems to prola@aps.org.
- [147] Pavel Sobotk and Ivan Otdal. Transformations of c-type defects on si(100)-2 × 1 surface at room temperature STM/STS study. *Surface Science*, 602(17):2835–2839, September 2008.
- [148] O. Warschkow, S. R. Schofield, N. A. Marks, M. W. Radny, P. V. Smith, and D. R. McKenzie. Water on silicon (001): C defects and initial steps of surface oxidation. *Physical Review B (Condensed Matter and Materials Physics)*, 77(20):201305–4, May 2008.
- [149] Jing Wang, T. A. Arias, and J. D. Joannopoulos. Dimer vacancies and dimer-vacancy complexes on the si(100) surface. *Physical Review B*, 47(16):10497, April 1993. Copyright (C) 2009 The American Physical Society; Please report any problems to prola@aps.org.
- [150] H. J. W. Zandvliet, H. K. Louwsma, P. E. Hegeman, and Bene Poelsema. Energetics of ni-induced vacancy line defects on si(001). *Phys. Rev. Lett.*, 75(21):3890–3893, Nov 1995.
- [151] S. R. Schofield, N. J. Curson, J. L. O'Brien, M. Y. Simmons, R. G. Clark, N. A. Marks, H. F. Wilson, G. W. Brown, and M. E. Hawley. Split-off dimer defects on the si(001)2 x 1 surface. *Physical Review B*, 69(8):085312, February 2004. Copyright (C) 2009 The American Physical Society; Please report any problems to prola@aps.org.

- [152] T. Komeda and Y. Nishioka. Atomic configuration of segregated b on si(001) surface. *Applied Physics Letters*, 71(16):2277–2279, October 1997.
- [153] M. A. Kulakov, Z. Zhang, A. V. Zotov, B. Bullemer, and I. Eisele. Structure of the B/Si(100) surface at low boron coverage studied by scanning tunnelling microscopy. *Applied Surface Science*, 103(4):443–449, December 1996.
- [154] Zhenghui Liu, Zhaohui Zhang, and Xing Zhu. Atomic structures of boron-induced protrusion features on si(100) surfaces. *Physical Review B (Condensed Matter and Materials Physics)*, 77(3):035322–5, 2008.
- [155] M. J. Butcher, J. W. Nolan, M. R. C. Hunt, P. H. Beton, L. Dunsch, P. Kuran, P. Georgi, and T. J. S. Dennis. Adsorption and manipulation of endohedral and higher fullerenes on si(100)-2 x 1. *Physical Review B*, 67(12):125413, March 2003. Copyright (C) 2009 The American Physical Society; Please report any problems to prola@aps.org.
- [156] N. Martsinovich, C. Hobbs, L. Kantorovich, R. H. J. Fawcett, M. J. Humphry, D. L. Keeling, and P. H. Beton. Manipulation of c₆₀ on the si(001) surface: Experiment and theory. *Physical Review B (Condensed Matter and Materials Physics)*, 74(8):085304–12, 2006.
- [157] Alexey Y. Ganin, Yasuhiro Takabayashi, Yaroslav Z. Khimyak, Serena Margadonna, Anna Tamai, Matthew J. Rosseinsky, and Kosmas Prasad. Bulk superconductivity at 38[thinsp]K in a molecular system. *Nat Mater*, 7(5):367–371, May 2008.
- [158] Tomihiro Hashizume, Xiang-Dong Wang, Yuichiro Nishina, Hisanori Shinohara, Yahachi Saito, Young Kuk, and Toshio Sakurai. Field ion-scanning tunneling microscopy study of c₆₀ on the si(100) surface. *Japanese Journal of Applied Physics*, 31(Part 2, No. 7A):L880–L883, 1992.
- [159] D. Klyachko and D. M. Chen. Ordering of c₆₀ on anisotropic surfaces. *Physical Review Letters*, 75(20):3693, November 1995. Copyright (C)

- 2009 The American Physical Society; Please report any problems to prola@aps.org.
- [160] Kazuyuki Sakamoto, Masashi Harada, Daiyu Kondo, Akio Kimura, Akito Kakizaki, and Shozo Suto. Bonding state of the c60 molecule adsorbed on a si(111)-(7 x 7) surface. *Physical Review B*, 58(20):13951, November 1998. Copyright (C) 2009 The American Physical Society; Please report any problems to prola@aps.org.
 - [161] Kazuyuki Sakamoto, Daiyu Kondo, Yoshimitsu Ushimi, Masashi Harada, Akio Kimura, Akito Kakizaki, and Shozo Suto. Thermal induced transition in the bonding nature of c60 molecules adsorbed on a si(111)-(7x7) surface. *Journal of Electron Spectroscopy and Related Phenomena*, 101-103:413–418, June 1999.
 - [162] P. H. Beton, A. W. Dunn, and P. Moriarty. Manipulation of c[sub 60] molecules on a si surface. *Applied Physics Letters*, 67(8):1075–1077, 1995.
 - [163] P. Moriarty, Y. R. Ma, M. D. Upward, and P. H. Beton. Translation, rotation and removal of c60 on si(100)-(2 x 1) using anisotropic molecular manipulation. *Surface Science*, 407(1-3):27–35, June 1998.
 - [164] X.-D. Wang, T. Hashizume, H. Shinohara, Y. Saito, Y. Nishina, and T. Sakurai. Adsorption of c60 and c84 on the si(100)2 x 1 surface studied by using the scanning tunneling microscope. *Physical Review B*, 47(23):15923, June 1993. Copyright (C) 2009 The American Physical Society; Please report any problems to prola@aps.org.
 - [165] S. Gangopadhyay, R.A.J. Woolley, R. Danza, M.A. Phillips, K. Schulte, Li Wang, V.R. Dhanak, and P.J. Moriarty. C60 submonolayers on the si(111)-(7 x 7) surface: Does a mixture of physisorbed and chemisorbed states exist? *Surface Science*, 603(18):2896–2901, September 2009.
 - [166] Dong Chen and Dror Sarid. An STM study of c60 adsorption on si(100)-(2 x 1) surfaces: from physisorption to chemisorption. *Surface Science*, 329(3):206–218, May 1995.

- [167] File:C60a.png - wikipedia, the free encyclopedia.
<http://en.wikipedia.org/wiki/File:C60a.png>.
- [168] N. Martsinovich and L. Kantorovich. Modelling the manipulation of c60 on the si(001) surface performed with NC-AFM. *Nanotechnology*, 20(13):135706, 2009.
- [169] Chris Hobbs and Lev Kantorovich. Non-contact AFM images of a c60 molecule adsorbed on the si(0 0 1) surface: An ab initio method. *Surface Science*, 600(3):551–558, February 2006.
- [170] Kei Kobayashi, Hirofumi Yamada, Toshihisa Horiuchi, and Kazumi Matsushige. Investigations of c60 molecules deposited on si(111) by noncontact atomic force microscopy. *Applied Surface Science*, 140(3-4):281–286, February 1999.
- [171] A. V. Hamza and M. Balooch. The chemisorption of c60 on si(100)-(2 1). *Chemical Physics Letters*, 201(5-6):404–408, 1993.
- [172] I. Borgia, B. Brunetti, I. Mariani, A. Sgamellotti, F. Cariati, P. Fermo, M. Mellini, C. Viti, and G. Padeletti. Heterogeneous distribution of metal nanocrystals in glazes of historical pottery. *Applied Surface Science*, 185(3-4):206–216, 2002.
- [173] E. Bontempi, P. Colombi, L.E. Depero, L. Cartechini, F. Presciutti, B.G. Brunetti, and A. Sgamellotti. Glancing-incidence x-ray diffraction of ag nanoparticles in gold lustre decoration of italian renaissance pottery. *Applied Physics A: Materials Science & Processing*, 83(4):543–546, June 2006.
- [174] M. Faraday. The Bakerian Lecture: Experimental Relations of Gold (and Other Metals) to Light. *Royal Society of London Philosophical Transactions Series I*, 147:145–181, 1857.
- [175] Richard B.M. Schasfoort. *Handbook of Surface Plasmon Resonance*. Royal Society of Chemistry, 1 edition, April 2008.

- [176] Wolfgang J. Parak, Daniele Gerion, Teresa Pellegrino, Daniela Zanchet, Christine Micheel, Shara C. Williams, Rosanne Boudreau, Mark A. Le Gros, Carolyn A. Larabell, and A. Paul Alivisatos. Biological applications of colloidal nanocrystals. *Nanotechnology*, 14(7):R15–R27, 2003.
- [177] L. Motte, F. Billoudet, E. Lacaze, J. Douin, and M. P. Pileni. Self-Organization into 2D and 3D superlattices of nanosized particles differing by their size. *The Journal of Physical Chemistry B*, 101(2):138–144, 1997.
- [178] P. Moriarty, M. D. R. Taylor, and M. Brust. Nanostructured cellular networks. *Physical Review Letters*, 89(24):248303, November 2002. Copyright (C) 2009 The American Physical Society; Please report any problems to prola@aps.org.
- [179] E. Verrelli, D. Tsoukalas, K. Giannakopoulos, D. Kouvatsos, P. Normand, and D. E. Ioannou. Nickel nanoparticle deposition at room temperature for memory applications. *Microelectron. Eng.*, 84(9-10):1994–1997, 2007.
- [180] John Turkevich, Peter Cooper Stevenson, and James Hillier. A study of the nucleation and growth processes in the synthesis of colloidal gold. *Discussions of the Faraday Society*, 11:55–75, 1951.
- [181] G. Frens. Particle size and sol stability in metal colloids. *Colloid & Polymer Science*, 250(7):736–741, July 1972.
- [182] Mathias Brust, Merryl Walker, Donald Bethell, David J. Schiffrin, and Robin Whyman. Synthesis of thiol-derivatised gold nanoparticles in a two-phase Liquid-Liquid system. *Journal of the Chemical Society, Chemical Communications*, (7):801–802, 1994.
- [183] G1402 gold colloid ~0.01% H₂AuCl₄, ~1a520 units/mL, 3.0-5.5nm mean particle size (monodisperse), 5nm particle size. www.sigmaaldrich.com.
- [184] Emmanuelle Pauliac-Vaujour and Andrew Stannard.

- [185] Christopher P. Martin, Matthew O. Blunt, and Philip Moriarty. Nanoparticle networks on silicon: Self-Organized or disorganized? *Nano Letters*, 4(12):2389–2392, December 2004.
- [186] Matthew O. Blunt, Milovan Suvakov, Fabio Pulizzi, Christopher P. Martin, Emmanuelle Pauliac-Vaujour, Andrew Stannard, Andrew W. Rushforth, Bosiljka Tadic, and Philip Moriarty. Charge transport in cellular nanoparticle networks: Meandering through nanoscale mazes. *Nano Letters*, 7(4):855–860, April 2007.
- [187] J. N. O’Shea, M. A. Phillips, M. D. R. Taylor, P. Moriarty, M. Brust, and V. R. Dhanak. Colloidal particle foams: Templates for au nanowire networks? *Applied Physics Letters*, 81(26):5039–5041, December 2002.
- [188] Klara E. Mueggenburg, Xiao-Min Lin, Rodney H. Goldsmith, and Heinrich M. Jaeger. Elastic membranes of close-packed nanoparticle arrays. *Nat Mater*, 6(9):656–660, 2007.
- [189] Matthew O. Blunt, Milovan Suvakov, Fabio Pulizzi, Christopher P. Martin, Emmanuelle Pauliac-Vaujour, Andrew Stannard, Andrew W. Rushforth, Bosiljka Tadic, and Philip Moriarty. Charge transport in cellular nanoparticle networks: Meandering through nanoscale mazes. *Nano Letters*, 7(4):855–860, April 2007.
- [190] BluntM. O., MartinC. P., Ahola-TuomiM., Pauliac-VaujourE., SharpP., Nativop., BrustM., and MoriartyP. J. Coerced mechanical coarsening of nanoparticle assemblies. *Nat Nano*, 2(3):167–170, March 2007.
- [191] E. Pauliac-Vaujour, A. Stannard, C. P. Martin, M. O. Blunt, I. Nottingher, P. J. Moriarty, I. Vancea, and U. Thiele. Fingering instabilities in dewetting nanofluids. *Physical Review Letters*, 100(17):176102–4, May 2008.
- [192] U. Thiele, I. Vancea, A. J. Archer, M. J. Robbins, L. Frastia, A. Stannard, E. Pauliac-Vaujour, C. P. Martin, M. O. Blunt, and P. J. Moriarty. Modelling approaches to the dewetting of evaporating thin films

- of nanoparticle suspensions. *Journal of Physics: Condensed Matter*, 21(26):264016, 2009.
- [193] Blunt Matthew O. Martin Christopher P. Stannard Andrew See Thesis: Pauliac-Vaujour, Emmanuelle. PhD thesis, University of Nottingham Nanoscience Group.
- [194] Orlin D. Velev and Ketan H. Bhatt. On-chip micromanipulation and assembly of colloidal particles by electric fields. *Soft Matter*, 2(9):738–750, 2006.
- [195] Sanjeev Kumar, Seok-Hwang Yoon, and Gil-Ho Kim. Bridging the nanogap electrodes with gold nanoparticles using dielectrophoresis technique. *Current Applied Physics*, 9(1):101–103, 2009.
- [196] Seok-Hwang Yoon, Sanjeev Kumar, Gil-Ho Kim, Young-Suk Choi, T.W. Kim, and Saiful I. Khondaker. Dielectrophoretic assembly of single gold nanoparticle into nanogap electrodes. *Journal of Nanoscience and Nanotechnology*, 8:3427–3433, July 2008.
- [197] J. J. Boote and S. D. Evans. Dielectrophoretic manipulation and electrical characterization of gold nanowires. *Nanotechnology*, 16(9):1500–1505, 2005.
- [198] S. Evoy, N. DiLello, V. Deshpande, A. Narayanan, H. Liu, M. Rieglman, B. R. Martin, B. Hailer, J. -C. Bradley, W. Weiss, T. S. Mayer, Y. Gogotsi, H. H. Bau, T. E. Mallouk, and S. Raman. Dielectrophoretic assembly and integration of nanowire devices with functional CMOS operating circuitry. *Microelectronic Engineering*, 75(1):31–42, July 2004.
- [199] Sumit Gangwal, Olivier J. Cayre, and Orlin D. Velev. Dielectrophoretic assembly of metallodielectric janus particles in AC electric fields. *Langmuir*, 24(23):13312–13320, December 2008.
- [200] Daisuke Sawada, Yoshiaki Sugimoto, Ken ichi Morita, Masayuki Abe, and Seizo Morita. Simultaneous measurement of force and tunneling

- current at room temperature. *Applied Physics Letters*, 94(17):173117–3, April 2009.
- [201] Pavel Jelinek, Martin Svec, Pablo Pou, Ruben Perez, and Vladimir Chab. Tip-Induced reduction of the resonant tunneling current on semiconductor surfaces. *Physical Review Letters*, 101(17):176101–4, October 2008.
- [202] G. W. Brown, H. Grube, M. E. Hawley, S. R. Schofield, N. J. Curson, M. Y. Simmons, and R. G. Clark. Imaging charged defects on clean si(100)-(2 x 1) with scanning tunneling microscopy. *Journal of Applied Physics*, 92(2):820–824, July 2002.
- [203] Masayasu Nishizawa, Leonid Bolotov, and Toshihiko Kanayama. Scanning tunneling microscopy observation of individual boron dopant atoms beneath si(001)-2 x 1 surfaces. *Japanese Journal of Applied Physics*, 44(48):L1436–L1438, 2005.
- [204] Geoffrey W. Brown, Holger Grube, and Marilyn E. Hawley. Observation of buried phosphorus dopants near clean si (100) - (2 x 1) surfaces with scanning tunneling microscopy. *Physical Review B*, 70(12):121301, 2004. Copyright (C) 2009 The American Physical Society; Please report any problems to prola@aps.org.
- [205] Yoshitaka NAITOH, Hikaru NOMURA, Masami KAGESHIMA, Yan Jun LI, and Yasuhiro SUGAWARA. Influence of surface stress on the phase change in a si(001) step measured by lt-nc-afm. *Hyomen Kagaku*, 28(8):421–427, 2007.
- [206] Masashi Ishii and Bruce Hamilton. Electron trapping at the si (111) atomic step edge. *Applied Physics Letters*, 85(9):1610–1612, 2004.
- [207] Th. Glatzel, S. Sadewasser, R. Shikler, Y. Rosenwaks, and M. Ch. Lux-Steiner. Kelvin probe force microscopy on III-V semiconductors: the effect of surface defects on the local work function. *Materials Science and Engineering B*, 102(1-3):138–142, September 2003.

- [208] K. Hata, S. Ozawa, Y. Sainoo, K. Miyake, and H. Shigekawa. Electronic structure of the c defects of si(001) measured by scanning tunneling spectroscopy at room and low temperature (80 k). *Surface Science*, 447(1-3):156–164, February 2000.
- [209] S. Ihara, S. L. Ho, T. Uda, and M. Hirao. Ab initio molecular-dynamics study of defects on the reconstructed si(001) surface. *Physical Review Letters*, 65(15):1909, October 1990. Copyright (C) 2009 The American Physical Society; Please report any problems to prola@aps.org.
- [210] T. Arai and M. Tomitori. Bias dependence of si(111)77 images observed by noncontact atomic force microscopy. *Applied Surface Science*, 157(4):207–211, April 2000.
- [211] H. Ozgur Ozer, Simon J. O’Brien, and John B. Pethica. Local force gradients on si(111) during simultaneous scanning tunneling/atomic force microscopy. *Applied Physics Letters*, 90(13):133110–3, March 2007.
- [212] Felix Loske, Philipp Rahe, and Angelika Kuhnle. Contrast inversion in non-contact atomic force microscopy imaging of c60 molecules. *Nanotechnology*, 20(26):264010, 2009.
- [213] P. Rahe, R. Bechstein, J. Schutte, F. Ostendorf, and A. Kuhnle. Repulsive interaction and contrast inversion in noncontact atomic force microscopy imaging of adsorbates. *Physical Review B (Condensed Matter and Materials Physics)*, 77(19):195410–6, May 2008.
- [214] H. zgr zer, Mehrdad Atabak, and Ahmet Oral. Ultra-small oscillation amplitude nc-AFM/STM imaging, force and dissipation spectroscopy of si(100)(21). *Solid State Communications*, 124(12):469–472, December 2002.
- [215] Makoto Ashino, Dirk Obergfell, Miroslav Haluska, Shihe Yang, Andrei N. Khlobystov, Siegmair Roth, and Roland Wiesendanger. Atomic-resolution three-dimensional force and damping maps of carbon nanotube peapods. *Nanotechnology*, 20(26):264001, 2009.

- [216] Lev Kantorovitch; Natalia Martsinovich. Unpublished work.
- [217] L. Motte, F. Billoudet, and M. P. Pileni. Self-Assembled monolayer of nanosized particles differing by their sizes. *The Journal of Physical Chemistry*, 99(44):16425–16429, November 1995.
- [218] Hakan Rensmo, Andrea Ongaro, Declan Ryan, and Donald Fitzmaurice. Self-assembly of alkane capped silver and silica nanoparticles. *Journal of Materials Chemistry*, 12(9):2762–2768, 2002.
- [219] Hakan Rensmo, Karin Westermarck, Donald Fitzmaurice, and Hans Siegbahn. Studies of dodecanethiol capped ag and au nanoparticles using synchrotron radiation based photoelectron spectroscopy. *Langmuir*, 18(26):10372–10378, December 2002.
- [220] Aaron E. Saunders, Michael B. Sigman, and Brian A. Korgel. Growth kinetics and metastability of monodisperse tetraoctylammonium bromide capped gold nanocrystals. *The Journal of Physical Chemistry B*, 108(1):193–199, 2004.
- [221] C. Jiang, S. Markutsya, H. Shulha, and V.V. Tsukruk. Freely suspended gold nanoparticle arrays. *Advanced Materials*, 17(13):1669–1673, 2005.
- [222] Venugopal Santhanam, Jia Liu, Rajan Agarwal, and Ronald P. Andres. Self-Assembly of uniform monolayer arrays of nanoparticles. *Langmuir*, 19(19):7881–7887, 2003.
- [223] A. Stannard. *PhD Thesis (Submitted)*. PhD thesis, School of Physics and Astronomy, Nottingham University, 2009.
- [224] W. D. Luedtke and Uzi Landman. Structure, dynamics, and thermodynamics of passivated gold nanocrystallites and their assemblies. *The Journal of Physical Chemistry*, 100(32):13323–13329, 1996.
- [225] W. D. Luedtke and Uzi Landman. Structure and thermodynamics of Self-Assembled monolayers on gold nanocrystallites. *The Journal of Physical Chemistry B*, 102(34):6566–6572, 1998.

- [226] Jing-Jiang Yu, Johnpeter N. Ngunjiri, Algernon T. Kelley, and Jayne C. Garino. Nanografting versus solution Self-Assembly of γ -Alkanedithiols on au(111) investigated by AFM (and references therein). *Langmuir*, 24(20):11661–11668, October 2008.
- [227] Marc D. Porter, Thomas B. Bright, David L. Allara, and Christopher E. D. Chidsey. Spontaneously organized molecular assemblies. 4. structural characterization of n-alkyl thiol monolayers on gold by optical ellipsometry, infrared spectroscopy, and electrochemistry. *Journal of the American Chemical Society*, 109(12):3559–3568, June 1987.
- [228] John T. Woodward, Marlon L. Walker, Curtis W. Meuse, David J. Vanderah, G. E. Poirier, and Anne L. Plant. Effect of an oxidized gold substrate on alkanethiol Self-Assembly. *Langmuir*, 16(12):5347–5353, June 2000.
- [229] Boris J. Albers, Todd C. Schwendemann, Mehmet Z. Baykara, Nicolas Pilet, Marcus Liebmann, Eric I. Altman, and Udo D. Schwarz. Three-dimensional imaging of short-range chemical forces with picometre resolution. *Nat Nano*, 4(5):307–310, May 2009.
- [230] B Such et al. 3d force spectroscopy of kbr(001). *JVST B*, In Press 2009.
- [231] Ch. Sommerhalter, Th. W. Matthes, Th. Glatzel, A. Jager-Waldau, and M. Ch. Lux-Steiner. High-sensitivity quantitative kelvin probe microscopy by noncontact ultra-high-vacuum atomic force microscopy. *Applied Physics Letters*, 75(2):286–288, July 1999.
- [232] Th. Glatzel, S. Sadewasser, and M. Ch. Lux-Steiner. Amplitude or frequency modulation-detection in kelvin probe force microscopy. *Applied Surface Science*, 210(1-2):84–89, March 2003.
- [233] Ulrich Zerweck, Christian Loppacher, Tobias Otto, Stefan Grafstrm, and Lukas M. Eng. Accuracy and resolution limits of kelvin probe force microscopy. *Physical Review B*, 71(12):125424, March 2005. Copyright (C) 2009 The American Physical Society; Please report any problems to prola@aps.org.

- [234] Ch. Sommerhalter, Th. Glatzel, Th. W. Matthes, A. Jger-Waldau, and M. Ch. Lux-Steiner. Kelvin probe force microscopy in ultra high vacuum using amplitude modulation detection of the electrostatic forces. *Applied Surface Science*, 157(4):263–268, April 2000.
- [235] G. H. Enevoldsen, T. Glatzel, M. C. Christensen, J. V. Lauritsen, and F. Besenbacher. Atomic scale kelvin probe force microscopy studies of the surface potential variations on the TiO₂(110) surface. *Physical Review Letters*, 100(23):236104–4, June 2008.
- [236] Ifranview image software. <http://www.irfanview.com>.
- [237] Stanford research DS345 30MHz Synthesized function Generator.
- [238] T g 210. *TTL*.
- [239] UK Polymer laboratories. Technical report.
- [240] Ser-Sing Chang, Chao-Wen Shih, Cheng-Dah Chen, Wei-Cheng Lai, and C. R. Chris Wang. The shape transition of gold nanorods. *Langmuir*, 15(3):701–709, February 1999.
- [241] Hackley. Nist report 2002.
- [242] J. B. Hasted. *Aqueous Dielectrics*. John Wiley & Sons, Incorporated, 1973.
- [243] Bob chettle. *University of Nottingham, School of Physics and Astronomy*.
- [244] L. Bernard, M. Calame, S. J. van der Molen, J. Liao, and C. Schonenberger. Controlled formation of metallic nanowires via au nanoparticle ac trapping. *Nanotechnology*, 18(23):235202, 2007.
- [245] Matthew S Marcus, Lu Shang, Bo Li, Jeremy A Streifer, Joseph D Beck, Edward Perkins, Mark A Eriksson, and Robert J Hamers. Di-electrophoretic manipulation and real-time electrical detection of single-nanowire bridges in aqueous saline solutions. *Small (Weinheim an*

Der Bergstrasse, Germany), 3(9):1610–1617, September 2007. PMID: 17705314.

- [246] Jaap A. Kaandorp and Janet E. Kbler. *The algorithmic beauty of seaweeds, sponges, and corals*. Springer, 2001.
- [247] Christopher S. Lobban and Paul James Harrison. *Seaweed ecology and physiology*. Cambridge University Press, 1994.

List of Figures

1.1	Illustrative representation of some of the important forces at the nanoscale: a) short-range Pauli repulsion between two atoms, b) chemical bonding between electron shells, c) mutual induced dipole interaction (van der Waals), d) electrostatic interaction due to a net difference in charge between two surfaces.	3
1.2	Examples of “top-down” methods of fabrication: (a) A commercial Intel “Xeon” chip created using UV lithography imaged by SEM [10]; (b) microscale girder fabricated using focused ion beam (FIB) [11]; (c) “the world’s smallest guitar” fabricated using electron beam lithography [12].	4

1.3	A potted history of the rise of the scanning probe microscope: (from top to bottom) the first real space image of the Si(111) 7 x 7 reconstruction taken by STM [14], atomically precise manipulation of individual atoms by STM [15], observation of standing electron waves enclosed in a artificially constructed “quantum corral” [16], first true atomic resolution in NC-AFM [17], “subatomic” resolution achieved using small amplitude NC-AFM [18], an operational logic gate system constructed from individual CO molecules by STM [19], vertical manipulation of an individual silicon atom by chemical forces [20], atomically precise lateral manipulation in NC-AFM [21], atomically precise vertical interchange by NC-AFM [22], chemical identification of individual atoms using NC-AFM [23], direct measurement of the force needed to move an atom by NC-AFM [24], atomic resolution within individual molecules with small amplitude NC-AFM and STM [25]	5
1.4	Complex behaviour at the breakfast table. Self-assembly and self-organisation are ubiquitous on many length scales, but engineering molecules or nanoparticles to self-assemble into a useful structures remains a challenge for researchers in the field. From [34]	8
1.5	self-organisation on a range of length scales relevent to nanotechnology: (a) microwires self organising out of a colloidal suspension under the influence of an inhomogeneous electric field [37], (b) cellular networks formed from a spun cast solution of thiol passivated nanoparticles [38], (c) a close packed network of metallic nanoparticles using two different sizes to create the packing arrangement [39], (d) self-assembly of PTCDI and melamine molecules into a supramolecular network in UHV conditions via hydrogen bonding [35].	9

2.1	Block diagram showing the major electronic components of a modern STM system. Other features such as the vacuum chamber and vibration isolation have been omitted for clarity.	13
2.2	Schematic diagram showing a wave incident on a one-dimensional barrier. In region a) we have a travelling wave, in region b) an exponentially decaying wave function, and in region c) a travelling wave, but with diminished amplitude. Note that the associated energy of the electron does not change, only the wave function amplitude, and therefore the probability of finding the electron on the other side of the gap.	15
2.3	Cartoon showing different regions of a tip and their effects. Region A, comprising of only the last few atoms of the tip is primarily responsible for most of the short-range chemical bonding and Pauli repulsion. A slightly larger region (labelled B) is responsible for the bulk of the tunnel current flowing between tip and sample. Region C indicates the region where the long-range van der Waals force due to the bulk of the tip originates. T (labelled inset on the graph) shows the total force modelled by a Lennard-Jones potential as a result of A and C. D shows an asperity demonstrating the effect of a double tip. Although a double tip may not produce a noticeable effect imaging a flat surface, if a larger feature, such as a step edge, is approached, its influence may become apparent.	18
2.4	Conventional STM image of the Si(111) 7 x 7 reconstruction taken at -0.3 V, 500 pA. Image size 15 x 15 nm.	19
2.5	Conventional STM image of the same region on the Si(100) surface taken at -1.5 V (left) and +1.5 V (right) at 77 Kelvin. Note the strong differences in both the appearance of the dimer rows and the defects.	20

2.6	Conventional STM image of the gallium arsenide surface at +1.9V (left) and -1.9V (right) taken from [50]. At positive bias only the Ga atoms are visible, while at negative bias only the As atoms are visible. The square box shows the same unit cell in both images.	20
2.7	Schematic diagram showing the tunnelling between a metallic tip and a sample with a bandgap and complex density of states. In a) the Fermi levels align and no net tunnelling takes place. In b) the sample is biased negatively by -V and electrons tunnel out of the occupied (filled) sample states into the tip. In c) the sample is biased positively by +V and a net flow of electrons tunnel out of the tip into the unoccupied (empty) states of the sample.	21
2.8	Graphs showing the Lorentzian response of a free, and a coupled oscillator. Coupling the oscillator causes a shift in the resonant frequency as described in the text. If we continue to apply a drive frequency at the same initial value, then the amplitude response of the oscillator will be changed as we are “sitting” in a different region of the slope. This is the basic principle by which AM-AFM operates. FM-AFM directly tracks the change in frequency using a phase locked loop.	28
2.9	Conventional (cantilever based) FM-AFM image taken at the Si(111) 7 x 7 reconstruction over a step edge. $df = -30$ Hz with an effective sample bias of -0.3 V	30
2.10	Conventional (cantilever based) FM-AFM image taken of the Si(111) 7 x 7 reconstruction showing a different contrast. $df = -50$ Hz with an effective sample bias of -0.3 V.	30

2.11	Block diagram showing at the major components of a modern FM-AFM system. Additional regions marked qPlus and Kelvin probe indicate features that are only present on the respective modifications to the basic template. Note, for example, the lack of a laser-based deflection system in the qPlus setup and the additional feedback regulation necessary for Kelvin probe. In some systems STM feedback may also be included as an additional regulator branch.	33
2.12	Photograph of qPlus sensor design take from [84]. This sensor setup is similar, though not identical to that implemented in the Omicron qPlus system used to acquire results for this thesis.	39
2.13	Example of a $df(V)$ voltage spectroscopy measurement. In this case the contact potential difference is approximately +1.2V. . .	40
2.14	Schematic showing how an inappropriate choice of bias voltage can adversely affect topographic imaging during NC-AFM when scanning over regions of a sample with different work functions. The topographic feature has height A, and if we choose a contact potential difference such that the frequency shift is the same over both regions we recover this accurately (trace B). If the tip bias is chosen incorrectly the topography may be exaggerated (trace C) or we may even experience contrast inversion (trace D). . . .	41
2.15	Photograph of the Omicron VT STM/AFM used during investigation of the spun cast nanoparticle networks.	42
2.16	Photograph of the VT STM/AFM head. Note that in this image an STM tip is mounted rather than in AFM cantilever.	44
2.17	Photograph of the Omicron LT system used during investigation of the Si(100) surface.	45
2.18	Photograph inside the chamber of the LT system showing the heat shields of the cryostat that surround the STM/AFM head during normal low-temperature operation.	46
2.19	Photograph of the Asylum system MFP 3D AFM unit used to obtain images of nanoparticle networks in ambient conditions. .	47

3.1	Representation of the torque on a small dipole in a uniform electric field	52
3.2	Representation of the net force on a small dipole in a nonuniform electric field	53
3.3	Interactions of different particles with electric fields.. From left to right – a conducting particle in a uniform field, an insulating particle in a uniform field, a conducting particle in an inhomogeneous field. Note that for the conducting particle in an inhomogeneous field the result of the DEP force is that it will be drawn towards regions of higher field intensity.	61
3.4	Side view of the electrode array on insulating surface (after [104]) showing Ramos et al’s model treating the solution and the double layer as a series of C-R-C circuits. The effect of the double layer is represented by the capacitors while the impedance of the bulk solution is represented by the resistors.	66
3.5	Side view of electrodes on an insulating substrate immersed in an electrolyte showing both field lines, the movement of charge and the bulk fluid flow resulting from the ACEO effect due to an inhomogeneous electric field (after [104]).	68
3.6	(Left) AutoCAD representation of the electrode mask used in DEP experiments. (Right) High contrast photograph taken of gold electrodes on a glass substrate after lithography and lift-off process.	72
3.7	Side view of electrode on an insulating substrate with a nanoparticle solution droplet over the gap and optical microscope objective lens brought into contact with the droplet. (Inset) 3D representation of the electrodes and nanoparticle growth in solution.	72
3.8	Photograph of Olympus BX51 optical microscope used for in situ investigation of microwire self organisation.	73
3.9	Photograph of electrode array from Fig. 3.6 mounted onto PCB (second iteration).	74

3.10	Photograph of electrode array mounted on third-generation PCB with improved electrical connections and integral high bandwidth, high gain amplifier for electrical measurements. . . .	74
3.11	Circuit diagram for amplifier integrated into third-generation PCB, circuit design by Robert Chettle, School of Physics and Astronomy electronics workshop.	75
4.1	The different surface reconstruction units cells of Si(100) viewed from above and along the surface. A: The 1x1 ‘bulk-like’ surface (not observed), B: Symmetric p(2x1), C: Asymmetric p(2x1), D: In phase buckling p(2x2), E: Out of phase buckling c(4x2). . . .	78
4.2	Si(100)-p(2x1) imaged at +1.5V, 0.5nA at 77K in conventional STM. Rectangle indicates unit cell. Image courtesy S. Gangopadhyay.	81
4.3	Conventional STM image of Si(100) at 77 K (taken with a qPlus tip) showing different features of the surface, including the orthogonal row directions over a step edge. A: c(4x2), B: p(2x2), C: ‘flicker’ dimers, D: 1DV (dimer vacancy) defect, E: 1+2DV defect, F: Boron induced defect.	84
4.4	Simplified view of the scheme from [131,133]. a) At low setpoints the probe does not perturb the surface. b) At high setpoints ‘down’ atoms are pulled into a ‘up’ position. c) Each subsequent down atom is pulled up, resulting in a apparent p(2x1) image. . .	86
4.5	Structure of the most common ‘native’ defects on Si(100). From left to right, the 1DV, 2DV and 1+2DV defects shown using the currently accepted re-bonding model.	88
4.6	Most recent model [154] for the substitutional boron defect shown in plane and side view. Red atoms indicate substitutional boron.	89
4.7	Simple ball and stick model of the C ₆₀ molecule, after [167] . . .	91

4.8	Cartoon representation of different gold nanoparticle structures. Top: thiol passivated (sulphur headgroups attached to the gold); Bottom: Citrate (charge) stabilised with citrate coating sur- rounded by counter-ion ‘cloud’	95
5.1	Conventional high resolution STM image of the clean Si(100) surface taken using a qPlus sensor Scan condititions: -2V effec- tive sample bias; setpoint 1 nA.	100
5.2	First successful NC-AFM imaging of the Si(100) substrate using a qPlus sensor at 77 K. $df = -2.4$ Hz, $A_0 = 8$ nm, $V_{gap} = +0.15$ V	101
5.3	Imaging across a step edge using large amplitude showing the p(2x1) phase on the upper and lower terraces. $df = -0.5$ Hz, A_0 $= 5$ nm, $V_{gap} = 0$ V.	102
5.4	Image of the p(2x2) and c(4x2) phases using large amplitude. Note the faint appearance of the lower atoms in the topography, and the very weak (~ 0.1 pA peak current) simultaneous tunnel current signal. $df = -5.9$ Hz, $A_0 = 5$ nm, $V_{gap} = +0.2$ V. . . .	102
5.5	dI/dV measurement of the Si(100) c(4x2) surface at 77K show- ing a lack of states between 0V and 0.25V obtained using a 100mV dither during a scan at +1.5V / 2.5nA. [Data taken by Subhashis Gangopadhyay]	103
5.6	Imaging using large oscillation amplitudes showing clear differ- ences between the contrast in Z / damping / I signals. Contrast is enhanced in the tunnel current around a number of the defects on the surface, while the B-Si ad-dimer defects demonstrate en- hanced contrast in the damping. $df = -4.8$ Hz, $A_0 = 5$ nm, V_{gap} $= +0.1$ V	104

5.7	Large-scale imaging using large oscillation amplitude with simultaneous tunnel current imaging. Note that due to an apparent difference in tip-sample interaction, resolution on the lower terrace was poor and has been thresholded out. The topography shows a uniformly p(2x1) periodicity, while the tunnel current data shows a mix of buckled and symmetric dimers along with bright regions associated with charging of defects. The overlay demonstrates that the buckled and symmetric dimers in the tunnel current image correspond to the topography. $df = -4.9$ Hz, $A_0 = 5$ nm, $V_{gap} = +0.1$ V.	105
5.8	Charge around defect imaged at +1.3 V sample bias (at room temperature). Tunneling current 0.2 nA. Image taken from [202]	106
5.9	High resolution NC-AFM image showing details of two key types of defect on the Si(100) surface. To the left is a boron induced defect, and to the right a complex of 1+2 DV defects. The damping shows strong contrast over the boron defect ad-dimers, while the tunnel current shows an anomalously high tunnel current signal over one of the split off dimers. $df = -5.9$ Hz, $A_0 = 5$ nm, $V_{gap} = +0.2$ V.	107
5.10	qPlus NC-AFM image of the Si(100) surface using small oscillation amplitude. Both the c(4x2) and the p(2x2) periodicities are observable, and demonstrate a difference in the apparent intensity of the lower atoms. $df = -10.9$ Hz, $A_0 = 0.35$ nm, $V_{gap} = +0.3$ V.	108
5.11	Detail of the defect structures shown in Fig. 5.9 b) and c) show line profiles over the boron induced defect and 1+2 DV defect respectively. In c) a comparison with the currently accepted model [149] is shown with the anomalous “recessed” dimer position labelled R.	111

5.12	Ball and stick model of the most recently proposed structure for the boron induced defect. In the side on view a comparison between experimentally measured and theoretically predicted heights for atoms in the structure is given showing good quantitative agreement. Ball and stick model and atomic position information courtesy of [154]	112
5.13	Small amplitude imaging of the boron induced defect showing internal structure of the defect, and strong tip - sample interaction in the damping over the Si-B ad-dimers. $df = -18$ Hz $A_0 = -0.25$ nm, $V_{gap} = + 0.2$ V.	112
5.14	Frequency shift (df) setpoint dependent imaging of the B-induced defect with simultaneous tunnel current. At low df diffuse rows appear in Z with a buckled structure in tunnel current. At high df a symmetric structure is imaged in the topography, while a mix of symmetric and buckled dimers appears in the tunnel current similar to images taken at large oscillation amplitudes (see Fig. 5.7). The circle highlights the same dimers throughout, but note this area has drifted out of frame in some of the images. The topographic imaging of the defect appears qualitatively similar to high positive bias STM imaging, while the tunnel current image has appearance closer to low positive, or negative bias imaging (see Fig. 5.15). $A_0 = 0.25$ nm, $V_{gap} = + 0.3$ V.	114
5.15	Conventional STM of boron induced defects at various bias voltages. Setpoint 500pA. Images courtesy of Subhashis Gangopadhyay	115
5.16	Additional image of boron defects taken with small oscillation amplitude. At low setpoint only poor resolution is observed in the topography, but a clear buckled structure is observed in the tunnel current image, confirming a buckled structure around the defects in the absence of a strong tip sample interaction. $df = -6$ Hz, $A_0 = 0.35$ nm, $V_{gap} = + 0.35$ V	115

5.17	Very high tunnel current setpoint imaging of the 1+2 DV in dual bias STM. a) -1.5 V 17 nA, b) + 1.5 V 17 nA. The “recessed” dimer is clearly visible at positive bias voltage, but apparently invisible at negative bias voltages. Image appears courtesy of Subhashis Gangopadhyay.	116
5.18	Setpoint dependent imaging at low oscillation amplitude of the 1+2 DV defect confirming observation of the “recessed” dimer. Final image has been 3x3 low pass filtered. $A_0 = 0.25$ nm, $V_{gap} = + 0.4$ V.	117
5.19	Series of images demonstrating the effect of increasing setpoint during imaging. At low setpoints (-26 Hz) a buckled structure is observed in the topography. With increasing setpoint the lower atom intensity increases, as does contrast in the damping and tunnel current signals. X’s indicate the same atoms in each image $A_0 = 0.25$ nm, $V_{gap} = + 0.8$ V for all images.	119
5.20	Simulated NC-AFM scans of the c(4x2) structure with high setpoint resulting in an apparent p(2x1) structure at 0K (left) and 100K (right). Note the residual asymmetry at 100K. Image taken from [133]	120
5.21	Series of images with a different tip showing the buckled to symmetric transition with increasing setpoint. In this instance the transition is less clear, and it is difficult to pinpoint the transition of the lower atoms into the symmetric structure (Inset final image: damping signal after applying 3x3 low pass filter). X’s indicate the same atoms in each image. $A_0 = 0.25$ nm, $V_{gap} = + 0.4$ V	121
5.22	Setpoint dependent imaging of the same region with two different oscillation amplitudes failing to show a buckled to symmetric transition. Although a p(2x1) symmetric structure is imaged at high setpoints, at low setpoints the buckled structure is not observed, possibly due to a blunt tip. $V_{gap} = + 0.2$ V for all images.	123

- 5.23 Series of images with a tip showing the topographic and tunnel current imaging with increasing setpoint. Note the ‘diffuse buckled’ structure at low setpoint. Due to drift there is a small shift in the observed region. X’s indicate the same atoms in each image. $A_0 = 0.25$ nm, $V_{gap} = +0.3$ V 124
- 5.24 Tip event showing a dramatic change from clear symmetric p(2x1) to low resolution buckled p(2x2) structure indicating a strong change in the tip – sample interaction. The corresponding tunnel current data also indicates a large change in the electronic structure of the tip. $df = -7.5$ Hz, $A_0 = 0.35$ nm, $V_{gap} = +0.35$ V 126
- 5.25 Rare example of a sudden tip change causing image inversion, and subsequent setpoint dependent imaging. Initially the symmetric p(2x1) structure was imaged, after tip change an inverted c(4x2) appeared. Subsequent setpoint increases show a “intermittent” phase, but eventually recover the p(2x1) periodicity. At high setpoints a transition from c(4x2) to p(2x1) is also observed in the damping. $A_0 = 0.25$ nm, $V_{gap} = +0.2$ V 127
- 5.26 Example of asymmetric imaging, clear atomic resolution is observed in the backwards scan, but only a diffuse structure is observed in the forward scan. The diffuse imaging suggests a poorly resolved buckled structure. $df = -4.9$ Hz, $A_0 = 5$ nm, $V_{gap} = +0.1$ V. 128
- 5.27 Asymmetric imaging with atomic resolution in both directions at large oscillation amplitude, showing p(2x1) in the forward trace, and a buckled structure in the reverse. Curiously on the upper terrace the imaging is approximately the same in forward and reverse with a p(2x1) structure in both. $df = -0.5$ Hz, $A_0 = 5$ nm, $V_{gap} = 0$ V. 129

5.28	Asymmetric imaging observed at small oscillation amplitude with simultaneous tunnel current imaging. At low setpoints a buckled structure is observed in both the topography and tunnel current. At higher setpoints, however, a symmetric structure is observed in the reverse trace in topography and tunnel current, while a mix of buckled and symmetric dimers is seen in the forward trace. Curiously “flicker” noise is observed over some dimers in the tunnel current. $A_0 = 0.35$ nm, $V_{gap} = + 0.35$ V. . .	130
5.29	Spectroscopic data taken from the same image sequence as Fig. 5.19, showing tunnel current (top), damping (middle) and force (bottom). Each curve is an average of three spectroscopy points. Dissipation is recorded over both atoms, with (unexpectedly) higher peak dissipation over the ‘up’ atom. (Insets: graphs showing long-range behaviour).	132
5.30	Spectroscopic data taken from the same image sequence as Fig. 5.21, showing force and damping data. Since in this data set it was not possible to clearly identify “down” atoms, groups of spectroscopy points were taken over atoms that should be in the same configuration assuming a buckled structure. The forces are uniformly smaller, but the dissipation higher than Fig. 5.29. The damping image has been FFT filtered to improve contrast. (Inset graphs showing long-range behaviour).	134
5.31	Spectroscopic data taken from the same image sequence as Fig. 5.22. While the forces are quantitatively similar to Fig. 5.29, the damping is unusual, being both an order of magnitude smaller, and apparently showing a <i>decrease</i> on approach to the sample. (Inset graphs showing long-range behaviour).	135
5.32	Large-scale STM image of the Si(100) surface after C_{60} deposition showing low coverage. (Inset) High resolution STM image of an individual C_{60} molecule taken with a different tip structure. Both images at -2V/100 pA.	137

- 5.33 Image of a single C_{60} molecule taken using small oscillation amplitude showing sub-molecular resolution. At higher setpoints “scratching” was observed, most likely indicating movements of the molecule due to strong tip sample interaction. These “scratches” persisted despite careful adjustment of scan parameters, and slow ($\ll 1\text{nm s}^{-1}$) scan speeds. Curiously, at high setpoints images are detected in the tunnel current despite a lack of bias voltage. Intermittent imaging in the damping signal is also visible. $A_0 = 0.35\text{ nm}$, $V_{gap} = 0\text{ V}$ 138
- 5.34 Image of a single C_{60} molecule with sub-molecular resolution with a different tip showing different contrast. Differences in forward and backward traces are most likely the result of tip asymmetry, or inadequate feedback, despite careful parameter tuning and slow ($\ll 1\text{nm s}^{-1}$) scan speeds. The forward trace has been high pass filtered to reveal fine detail. $df = -7\text{ Hz}$, $A_0 = 0.25\text{ nm}$, $V_{gap} = +0.5\text{ V}$ 139
- 5.35 Series of images demonstrating initial imaging of C_{60} . a) large-scale image showing multiple molecules, b) individual molecule with “dark patch” in the centre, c) individual molecule with low resolution, d) accidental manipulation of molecule during imaging at higher setpoint, e) same molecule successfully imaged at the same setpoint with reduced scan speed. $A_0 = 0.35\text{ nm}$, $V_{gap} = 0\text{ V}$ 140
- 5.36 Setpoint dependent imaging of an individual C_{60} molecule. At low setpoints sub-molecular features are resolved in the tunnel current and damping, but not in topography. High pass filtering (-3.5Hz , -5.5Hz and -5.9Hz) reveals sub-molecular features in the topography, and in the final image details of the substrate are visible in the topography - arrow indicates point at which the molecule was manipulated. (Inset) unfiltered topographic images. $A_0 = 0.25\text{ nm}$, $V_{gap} = +0.5\text{ V}$ 142

5.37	Force spectroscopy over a single C ₆₀ molecule. The maximum force appears to be slightly larger over the C ₆₀ molecule than the surrounding silicon. Taken from the same image sequence as Fig. 5.36. Note the force data here has been smoothed using a 5x interpolate in ORIGIN.	143
5.38	Spectroscopic data over a single C ₆₀ molecule with a different tip. Similar to Fig. 5.37 a greater maximum force is detected over the C ₆₀ molecule compared to the silicon. The qualitative behaviour of the tunnel current dependence is very similar over both. Image taken from the same sequence as Fig. 5.36	144
5.39	p(2x1) topography and inverted c(4x2) tunnel current image taken at (nominally) 0V bias. Such imaging may indicate either a crosstalk between the AFM df /damping/tunnel current channels. $df = -13.5$ Hz, $A_0 = 0.25$ nm, $V_{gap} = 0$ V.	146
6.1	High resolution NC-AFM image of spun-cast C8 passivated Au nanoparticles on a SiO ₂ surface demonstrating nanoparticle sized features (Inset: High pass filtered image). Imaged using an Omicron VT-AFM in UHV using FM mode. $V_{gap}=+0.8$ V, $A_0=16$ nm, $df=-150$ Hz, 100nm x 100nm. Image courtesy of Subhashis Gangopadhyay	150
6.2	Comparable high resolution image of same sample type as Fig. 6.1 taken using Asylum AFM in ambient conditions using AM mode. 500nm x 500nm.	151
6.3	NC-AFM images of spun cast C8 passivated Au nanoparticles on a SiO ₂ surface demonstrating apparent “sub-layer” (highlighted regions). a) $V_{gap}=+1.2$ V, $A_0=8$ nm, $df=-15$ Hz, 1000nm x 785nm, b) $V_{gap}=0$ V, $A_0=16$ nm, $df=-15$ Hz, 1000nm x 1000nm, c) $V_{gap}=+1.2$ V, $A_0=8$ nm, $df=-15$ Hz, 1000nm x 1000nm, d) $V_{gap}=0$ V, $A_0=17.6$ nm, $df=-20$ Hz, 1000nm x 312nm, e) Zoom of b), f) Zoom of d).	152

6.4	Image of spun cast nanoparticle network taken using Asylum AFM in ambient conditions using AM mode. Highlighted region shows the areas in Fig. 6.2 and Fig. 6.5. 2000nm x 2000nm . . .	153
6.5	(left) Image of spun cast nanoparticle network taken using Asylum AFM in ambient conditions using tapping mode. (Right) Corresponding phase image. 1000nm ²	153
6.6	Top, change in apparent height of a nanoparticle array when imaging at low resolution with a sharp tip. Apparent height increases with packing density. Bottom, as the fraction of gold in the ‘layer’ increases, so the effective interaction with the tip increases and results in a change in detected height.	156
6.7	(left) Cartoon of possible tip - thiol interaction in repulsive and attractive modes. (right) Nanoparticle packing may increase thiol - thiol interactions and modify the effective height	158
6.8	Image sequence showing zoom in of Fig. 6.4 showing apparent sample modification due to repeated scanning. Taken using Asylum AFM in ambient conditions using AM mode. 500nm x 500nm	159
6.9	(a) image and line profile taken using FM-AFM in UHV. Network height ~ 4 nm, “sub-layer” ~ 2.2 nm, (b) image and line profile taken using AM-AFM in ambient conditions. Network height ~ 3.5 nm, “sub-layer” ~ 2.5 nm; (c) image and line profile taken using TM-AFM in ambient conditions (same region as (b) Network height ~ 2.5 nm, “sub-layer” ~ 0.2 nm.	161
6.10	Frequency shift images imaged at a) -1.8 nm, b) -0.45 nm, c) +0.6nm, and d) + 3nm. e) Topographic image. Force vs. tip-sample separation graph deconvolved from the averaged frequency shift curves of the regions highlighted in e). $V_{gap}=0$ V, $A_0=20$ nm, $df=-20$ Hz, 333nm x 114nm	170

6.11	Frequency shift images imaged at a) -3 nm, b) -0.4 nm, c) +0.6nm and d) + 3nm. e) Topographic image. Force vs. tip-sample separation graph deconvolved from the averaged frequency shift curves of the regions highlighted in e). The shaded region in the force curves its most likely due to an instrumental artifact (see main text for discussion). $V_{gap}=0V$, $A_0=20nm$, $df=-25Hz$, $200nm^2$	171
6.12	Frequency shift images imaged at a) -3V, b) +0.5V, c) +3V, d) topographic image. Averaged voltage versus frequency shift curves of the regions highlighted in d). $V_{gap}=+1V$, $A_0=16nm$, $df=-30Hz$, $500nm^2$. CPD~160mV	172
6.13	Frequency shift images imaged at a) -3V, b) -2V, c) -0.7V, d) +0.9V E) +3V f) topographic image. Averaged voltage versus frequency shift curves of the regions highlighted in f). $V_{gap}=0V$, $A_0=16nm$, $df=-25Hz$, $500nm \times 188nm$. CPD~470mV	173
6.14	Image taken of spun cast C8 spun cast nanoparticle assemblies using a Pt-Ir tip. $V_{gap}=0V$, $A_0 = 38nm$, $df=-10Hz$, $1000nm^2$. .	174
6.15	(Left) Image taken of spun cast C8 spun cast nanoparticle assembly using a Pt-Ir tip of the same area as Fig. 6.14 with Kelvin probe compensation engaged. (Right) simultaneous Kelvin image. $A_0 = 38nm$, $df=-15Hz$, $1000nm \times 1000nm$	174
6.16	(Left) High-resolution image of part of the assemblies shown in Fig. 6.15 with Kelvin probe compensation engaged.(Right) simultaneous Kelvin image. $A_0 = 38nm$, $df=-15Hz$, $500nm \times 500nm$	175
6.17	(Left) topography of bare SiO ₂ region close to the area shown in Fig. 6.15 (Right) simultaneous Kelvin image showing apparent subsurface features. $A_0 = 38nm$, $df=-20Hz$, $1500nm \times 1500nm$.	175
6.18	Topographic scan of C12 capped nanoparticle spun cast network taken with Pt-Ir tip showing contrast inversion. $V_{gap} = 0V$, $A_0 = 38nm$, $df=-20Hz$, $1500nm \times 1500nm$	176

6.19	(Left) zoom in of the same region in a shown in Fig. 6.18 with Kelvin probe compensation engaged. (Right) simultaneous Kelvin image. $A_0 = 38\text{nm}$, $df = -24\text{Hz}$, $500\text{nm} \times 500\text{nm}$	176
6.20	(Left) high-resolution scan showing zoom in region shown in Fig. 6.19 (inset) high pass filtered image. (Right) simultaneous Kelvin image. $A_0 = 38\text{nm}$, $df = -31\text{Hz}$, $100\text{nm} \times 100\text{nm}$	177
6.21	Topographic image of nanoparticle network after being annealed at 250°C for approximately 10 minutes. $V_{gap} = +0.6\text{V}$, $A_0 = 38\text{nm}$, $df = -10\text{Hz}$, $1500\text{nm} \times 1500\text{nm}$	177
6.22	Zoom in of similar region to Fig. 6.21 with Kelvin probe compensation engaged. Note that there is an obvious tip artefact. $A_0 = 38\text{nm}$, $df = -14\text{Hz}$, $500\text{nm} \times 500\text{nm}$	178
6.23	Topographic image of nanoparticle network after being annealed at 250°C for a second time. $V_{gap} = +0.6\text{V}$, $A_0 = 38\text{nm}$, $df = -10\text{Hz}$, 500nm^2 $A_0 = 38\text{nm}$, $df = -13\text{Hz}$, 1500nm^2	178
6.24	Zoom in of similar region to Fig. 6.23 with Kelvin probe compensation engaged. $A_0 = 38\text{nm}$, $df = -10\text{Hz}$, 500nm^2	179
6.25	Zoom of network and substrate in Fig. 6.24 $A_0 = 38\text{nm}$, $df = -10\text{Hz}$, $157\text{nm} \times 157\text{nm}$	179
6.26	Topographic image of second C12 capped nanoparticle network sample with Kelvin probe engaged, image courtesy Evan Spadafora. Image $A_0 = 38\text{nm}$, $df = -15\text{Hz}$, $500\text{nm} \times 500\text{nm}$. . .	180
6.27	Topographic image of second nanoparticle network sample after being annealed at 250°C for approximately 10 minutes. Image courtesy Evan Spadafora. $A_0 = 38\text{nm}$, $df = -15\text{Hz}$, $500\text{nm} \times 500\text{nm}$	181
6.28	Topographic image of second nanoparticle network sample after being annealed at 250°C for a second time. Image courtesy Evan Spadafora. $A_0 = 38\text{nm}$, $df = -15\text{Hz}$, $500\text{nm} \times 500\text{nm}$. . .	181
6.29	Image showing sudden change in Kelvin signal over SiO_2 but not over network. Note there is no apparent change in the topography.	184
6.30	Image showing sudden change in change in the difference in Kelvin signal between substrate and network with setpoint. Absolute values have been offset to align the substrate values. . . .	185

7.1	in situ optical micrographs of microwire growth in the range of 100 kHz to 1 MHz. A notable change in morphology is observed as the frequency is changed (most notably in the 100 - 600Khz range). We also observed a wide variation between different electrodes at the same frequency, but note that, in general, a larger number of denser appearing wires were observed lower frequencies. Poor contrast in the examples shown at 400 and 500Khz is due to “clouding” (see later sections)	190
7.2	Representative SEM micrographs of microwires grown over a frequency range of 100 kHz to 1 MHz on both SiO ₂ and glass substrates.	191
7.3	Examples of different contamination structures due to residual citrate observed during SEM micrographs: a) “coating”, b) “crystalline”.	192
7.4	Plots of wire growth taken from in situ videos. In general there is a wide variation of growth rates and dynamics, but lower frequencies (100 to 300 kHz) generally have lower growth rates than those at high frequencies (600 kHz to 1 MHz). Note that at low frequency there are numerous examples of “plateaus”. Representative error bars are included on one dataset of each graph. One example of “spontaneous” retraction is captured (centre graph, 300kHz data)	193
7.5	Phase diagram of frequency versus applied voltage demonstrating the threshold regime for growth starting with bare electrodes. White regions indicate where there is insufficient experimental data to precisely define the transition. Dotted line is included as a guide to the eye only, the trend may not be linear in these regions. Extrapolated behavior indicates regions where we have no direct experimental data, but in which we can confidently predict growth	195

7.6	Image sequence showing growth at 100 kHz and subsequent “spontaneous” retraction and electrode damage. Note that in this particular example the wires on the “live” electrode suffered more significant retraction than on the “grounded” electrode. . .	197
7.7	Example of “spontaneous” retraction that demonstrates heavy “clouding” of the solution at 300 kHz. Note that contrast is almost lost. In (d) clear retraction is observed on the live electrode. The final image has been contrast enhanced.	198
7.8	Controlled reaction due to a frequency change from 600 kHz to 100 kHz. Wires were grown at 600 kHz and the signal removed – the wires were stable during the period when no signal was applied. Time index of 26.1 to 26.9 shows rapid retraction of wires upon application of signal at 100 kHz.	199
7.9	Plots of wire growth of three wires from the sequence shown in Fig. 7.8 during normal growth at 600 kHz, showing subsequent stability with no applied signal, and rapid retraction upon application of 100 kHz signal.	200
7.10	Image sequence showing controlled retraction and subsequent regrowth. (a) growth at 600 kHz. (b) immediately after application of 100 kHz signal showing complete retraction on live electrode (c) subsequent regrowth at 100 kHz.	200
7.11	Phase diagram of frequency versus applied voltage showing where growth, no growth, or retraction was observed when applied to wires grown at 600 kHz, 20 V_{pk-pk} . White regions indicate where there is insufficient experimental data to precisely define the transition. Dotted line serves as a guide to the eye only. Extrapolated behavior indicates regions where we have no direct experimental data, but in which we can confidently predict growth	201
7.12	a) Growth at 200 kHz, b) subsequent continued growth at 700 kHz, c) - d) retraction of all wires after application of signal at 100 kHz.	202

7.13	Growth of wires at 600 kHz showing the same regions in both optical microscopy ((a), (b)) and SEM and subsequent high resolution imaging showing that wires have sintered before connection (note that small clusters of <i>unsintered</i> nanoparticles are observed on the substrate).	203
7.14	a) Optical microscope image capture of Au nanoparticles during growth, (d) after spontaneous retraction began signal was turned off and wires preserved. Highlighted regions correspond to high resolution SEM of wires captured in the middle of “spontaneous” retraction in (b) and (c). (e) and (f) high-resolution SEM scans showing large scale sintering both sides.	205
7.15	High resolution SEM showing closepacked arrays of charge stabilised gold nanoparticles on SiO ₂ substrate demonstrating stability under typical SEM imaging conditions.	206
7.16	a) and b) Optical and c) - f) high-resolution SEM micrographs showing large-scale damage and discoloration to electrodes upon application of 1 kHz signal to a 0.5M sodium citrate solution. The colouration in the optical micrographs is suggestive of nanoscale fragments. This hypothesis is supported by the high-resolution SEM micrographs.	210
7.17	Graph showing results of calculations based on the model of Ramos et al. showing how the voltage dropped across the double layer at the electrode (for an applied field of 20 V peak to peak) varies with frequency for a range of electrode gaps.	213
7.18	Calculations based on the model of Ramos et al. showing how the surface potential and double layer ion concentration (as a fraction of the bulk ion concentration) vary with distance from the surface at a range of DC surface potentials. Note that the ion concentration increases dramatically with applied potential. The expected potential at the electrode in our experiments is expected to be two orders of magnitude higher.	214